Neue Entwicklungen auf dem Gebiet der Zirkonium-basierten Metall-organischen Gerüstverbindungen in Bezug auf Cluster-, Netzwerktransformation und Liganden

Kumulative Dissertation

zur Erlangung des Doktorgrades der
Mathematisch-Naturwissenschaftlichen Fakultät der
Heinrich-Heine-Universität Düsseldorf

vorgelegt von

Bahareh Nateghi

aus Teheran, Iran

Düsseldorf, November 2019

aus dem Institut für Anorganische Chemie und Strukturchemie I
der Heinrich-Heine-Universität Düsseldorf

Gedruckt mit der Genehmigung der
Mathematisch-Naturwissenschaftlichen Fakultät der
Heinrich-Heine-Universität Düsseldorf

Berichterstatter:

1. Prof. Dr. Christoph Janiak

2. Prof. Dr. Christian Ganter

Tag der mündlichen Prüfung: 23. Januar 2020

Eidesstattliche Erklärung

Ich versichere an Eides statt, dass die Dissertation von mir selbstständig und ohne unzulässige fremde Hilfe unter Beachtung der „Grundsätze zur Sicherung guter wissenschaftlicher Praxis“ an der Heinrich-Heine-Universität Düsseldorf erstellt worden ist. Die aus fremden Quellen direkt oder indirekt übernommenen Gedanken sind als solche kenntlich gemacht. Die Arbeit wurde bisher weder im Inland noch im Ausland in gleicher oder ähnlicher Form einer anderen Prüfungsbehörde vorgelegt. Es wurden keine früheren erfolglosen Promotionsversuche unternommen.

……..... …….....

Ort, Datum Unterschrift

Danksagung

Mein besonderer Dank gilt Herrn Prof. Dr. Christoph Janiak für die Möglichkeit meine Promotion in seinem Arbeitskreis anzufertigen. Außerdem danke ich ihm für die Möglichkeit einer freien Forschungs- und Projektwahl.

Herrn Prof. Dr. Christian Ganter danke ich herzlich für die Übernahme des Koreferats und die zahlreichen Anregungen in meinen Seminarvorträgen.

Ein weiterer besonderer Dank geht an Herrn Dr. Ishtvan Boldog für die umfangreiche wissenschaftliche Unterstützung sowie hilfreichen Denkanstöße.

Des Weiteren möchte ich mich bei Frau Birgit Tommes, Frau Maria Breuer, Herrn Dr. Peter Tommes und Herrn Ralf Bürgel für die analytischen Untersuchungen bedanken.

Frau Claudia Schäfer, Frau Jutta Bourgeois, Frau Annette Ricken und Herrn Marcell Demandt danke ich für die stete Ansprechbarkeit.

Ein weiterer besonderer Dank geht an Olga Koikolainen für die Korrektur der vorliegenden Dissertation. Außerdem danke ich ihr für die freundliche Unterstützung, hilfreichen Tipps sowie für die vielen netten Gespräche.

Darüber hinaus möchte ich bei allen Mitarbeitern der beiden Arbeitskreise für die freundliche Aufnahme, gute und positive Laune sowie ihre Hilfsbereitschaft bedanken.

Mein allergrößter Dank gilt meiner Familie und vor allem meinen Eltern für ihre Unterstützung, die Liebe und den Rückhalt während meiner gesamten Studienzeit. Ohne diese Grundlage wäre diese Arbeit nicht möglich gewesen.

Inhaltsverzeichnis

I. Publikationsliste

Christian Heering, Bahareh Nateghi, Christoph Janiak; „Charge-Assisted Hydrogen-Bonded Networks of $NH_4^+$and $[Co(NH)_6)]^{3+}$ with the New Linker Anion of 4-Phosphono-Biphenyl-4'-Carboxylic Acid"

Crystals, **2016**, *6*(3), 22. DOI: 10.3390/cryst6030022

Christian Heering, Biju Francis, Bahareh Nateghi, Gamall Makhloufi, Steffen Lüdeke, Christoph Janiak; „Syntheses, structures and properties of group 12 element (Zn, Cd, Hg) coordination polymers with a mixed-functional phosphonate-biphenyl-carboxylate linker"

CrystEngComm, **2016**, *18*, 5209–5223. DOI: 10.1039/C6CE00587J

Bahareh Nateghi, Ishtvan Boldog, Konstiantyn V. Domasevitch, Christoph Janiak; "More versatility than thought: Large $\{Zr_{26}\}$ oxocarboxylate cluster by corner-sharing of standard octahedral subunits"

CrystEngComm, **2018**, *20*, 5132–5136. DOI: 10.1039/C8CE01064A

Bahareh Nateghi, Kostiantyn V. Domasevitch, Roman Bulánek, Christoph Janiak*****, Ishtvan Boldog*****; „Ligand Excess "Inverse-Defected" Zr_6 Tetrahedral Tetracarboxylate Framework and its Thermal Transformation"
Inorg. Chem. **2019**, *58*, 12786–12797. DOI: 10.1021/acs.inorgchem.9b01721

Bahareh Nateghi, Christoph Janiak; „Synthesis and characterization of two bifunctional pyrazole-phosphonic acid ligands"
Z. Naturforsch. B, **2019**, accepted. DOI: 10.1515/znb-2019-0170

II. Kurzzusammenfassung

Die vorliegende Arbeit beschäftigt sich mit drei Forschungsschwerpunkten. Im ersten Teil wird der neue {Zr_{26}}-Cluster als größter bisher bekannter Zirkonium-Carboxylat-Cluster vorgestellt. Die supramolekularen Cluster dieser Größenordnung werden mit Hilfe von oktaedrischem Zr_6-Cluster als Standardbaustein beschrieben. Die etablierten Methoden zum Ligandenaustausch unter milden Bedingungen könnten zur Bildung von porösen Koordinationspolymeren führen, wobei die supramolekularen Cluster als sekundäre Bausteine (SBUs) dienen könnten.

Im zweiten Teil dieser Arbeit wird ein neues poröses Koordinationspolymer, **ZRTE-10**, basierend auf einer tetraedrischen ((Adamantan-1,3,5,7-tetrayl)tetra(phen-4-yl))tetracarbonsäure (H_4L^4) beschrieben. Unerwarteterweise zeigt [$Zr_6(\mu_3\text{-}O)_4(\mu_3\text{-}OH)_4(L^4)(HL^4)_2(OH)_2(H_2O)_2$] eine niedrige Symmetrie (C_2/c). Die Struktur basiert auf einem seltenen Metallknoten mit zehnfacher Konnektivität und besitzt eine signifikante Porosität. Zwei Drittel der Liganden tragen hierbei eine nicht-deprotonierte Carboxylgruppe. Das Gerüst weist ein komplexes trinodales {$4^{14}.6^{24}.8^7$}{4^3}$_2${$4^5.6$}-Netz auf. Die überkritische Trocknung mit CO_2 und milde Entgasung bei 120 °C ergab ein poröses Material mit einer BET-Oberfläche von 1190 m^2g^{-1}. Beim Erhitzen auf ~ 200 °C wandelte sich **ZRTE-10** in ein anderes kristallines Gerüst **ZRTE-11** um. Es wurde festgestellt, dass die Topologie von **ZRTE-11** mit der erwarteten Fluorit-Topologie übereinstimmt, die zuvor für andere literaturbekannte MOFs, basierend auf tetraedrischen Liganden, beobachtet wurde. **ZRTE-11** mit einer hohen Symmetrie (*I*4/m) besitzt achtfach-verknüpfte Metallknoten und hat die Formel [$Zr_6(\mu_3\text{-}O)_4(\mu_3\text{-}OH)_4(OH)_4(L^4)_2$]. Die thermisch induzierte Umwandlung von **ZRTE-10** verläuft durch Entfernung eines Liganden pro Zr_6-Knoten in den Poren des Gerüsts, was zur einer relativ niedrigen BET-Oberfläche von 585 m^2g^{-1} für das aktivierte **ZRTE-11** führt. Ein *mixed-Linker*-Ansatz für **ZRTE-10,11** wurde folglich unter Verwendung von ((Adamantan-1,3,5-triyl)tri(phen-4-yl))tricarbonsäure-Linker (H_3L^3) versucht, welcher ein gestutztes Analogon (*truncated analog*) zum H_4L^4 ist. Röntgenpulverdiffraktogramme der erhaltenen Materialien zeigen die Bildung semi-amorpher Materialien. Die thermische Behandlung dieser Materialien erhöht ihre Kristallinität. Jedoch liegen die BET-Oberflächen für die Ansätze mit H_3L^3 im Bereich von 400 bis 550 m^2g^{-1}.

Im letzten Teil dieser Arbeit werden zwei neue bifunktionelle Verbindungen beschrieben. 3,5-Dimethyl-4-(4-phosphonophenyl)-1*H*-pyrazol und 4-(4-Phosphonophenyl)-1*H*-pyrazol wurden mittels einer Suzuki-Miyaura Kreuzkupplung, ausgehend von einem Boc-geschützten Pyrazolyl-boronsäureester und Iodo-arylphosphonat, synthetisiert. Beide Verbindungen

kristallisieren jeweils mit HCl-Molekülen als Pyrazolium-chlorid Salze. Die Strukturen der isolierten Produkte weisen supramolekulare Netzwerke auf, die durch H-Brückenbindungen ausgebildet werden. Die Reaktion fand in Gegenwart von Pd(dppf)Cl_2-Katalysator und Cs_2CO_3-Base in trockenem 1,4-Dioxan als Lösungsmittel statt, wobei keine Co-Liganden eingesetzt wurden. Die alternativen Wege, sowohl die Umsetzung von Iodarylpyrazol als auch die von Iodarylphosphonat mit Acetylaceton in einer Arbuzov-Reaktion, erwiesen sich als ineffizient.

III. Abstract

The work consists of three main parts. In the first part the novel {Zr_{26}}-cluster, which is the largest zirconium carboxylate cluster known to date, is described. The structure of the ´supercluster´ is rationalized as a union of `standard´ {Zr_6} octahedral clusters. The extra-large cluster might serve as a secondary building unit (SBU) in porous coordination polymers, *via* introduction by established methods of ligand exchange under mild conditions.

In the second part of this work a new porous coordination polymer, **ZRTE-10**, based on a tetrahedral 1,3,5,7-tetra(carboxyphenyl)benzene ligand (H_4L^4) was reported. Unexpectedly, $[Zr_6(\mu_3\text{-}O)_4(\mu_3\text{-}OH)_4(L^4)(HL^4)_2(OH)_2(H_2O)_2]$ shows a low symmetry (C_2/c). The structure, based on a unusual 10 connected Zr_6 cluster, has a significant proven porosity (up to 1190 m^2g^{-1}). Two-thirds of the ligands bear one nondeprotonated carboxy group, and the framework has a complex trinodal $\{4^{14}.6^{24}.8^7\}\{4^3\}_2\{4^5.6\}$, underlying net. Supercritical CO_2 drying and mild degassing at 120 °C yielded a porous material with SBET = 1190 m^2g^{-1}. When heated up to ~ 200 °C, **ZRTE-10** converts to another crystalline framework, **ZRTE-11**. The latter was identified to be identical to the expected fluorite (*flu*) observed previously for other tetrahedral ligands. The high symmetry (I_4/m) framework is built upon 8-connected Zr_6 clusters and has a formula of $[Zr_6(\mu_3\text{-}O)_4(\mu_3\text{-}OH)_4(OH)_4(L^4)_2]$. The thermally induced conversion of **ZRTE-10** proceeds with expulsion of one ligand per Zr_6 node in the pores of the framework, resulting in a relatively low S_{BET} = 585 m^2g^{-1} for the activated **ZRTE-11**. A mixed ligand approach for **ZRTE-10,11** was attempted using 1,3,5-tetra(carboxyphenyl)benzene (H_3L^3), which is a truncated analog of H_4L^4 with one missing branch. The monocrystalline sample of **ZRTE-10** obtained in small yields demonstrated only minor inclusion of H_3L^3. However, the high-yielding (~ 80%) procedure with HCl as a modulator allows near proportional incorporation of the ligands. The formed materials are semiamorphous with powder XRDs intermediary between pure **ZRTE-10** and **-11**. Thermal treatment of the semiamorphous materials increases their crystallinity and allows S_{BET} = 400–550 m^2g^{-1} surface areas to be reached for pure H_3L^3.

In the last part of this work the bifunctional compounds 3,5-dimethyl-4-(4-phosphonophenyl)-1*H*-pyrazole and 4-(4-phosphonophenyl)-1*H*-pyrazole were reported, which were synthesized via Suzuki-Miyaura coupling, starting from a Boc-protected pyrazolylboronic acid ester and iodoarylphosphonate. The target compounds were isolated after acidic hydrolysis in the form of the hydrochloride salts. The structures of the isolated hydrochloride salts feature H-bonded networks involving the chloride anions. $Pd(dppf)Cl_2$ was found to be superior to $Pd(PPh_3)_4$ as a catalyst; dry 1,4-dioxane as a solvent, Cs_2CO_3 as a base, and no co-ligands were the best found conditions. The alternative routes through iodoarylphosphonate of iodoarylpyrazole, with

the crucial steps based on the copper-catalyzed coupling with acetylacetone or the Arbuzov reaction were proven inefficient.

IV. Abkürzungsverzeichnis

Å	Ångström (1 Å = 10^{-10} m)
BDC	*benzene dicarboxylat* (Terephthalat)
BET	Brunauer-Emmett-Teller
Boc	*tert*-Butyloxycarbonyl
COF	*Covalent organic framework*
CUSs	*Coordinatively unsaturated sites*
DMF	Dimethylformamid
ESI	*Elektrospray-Ionisation*
et al.	*et alia* (und andere)
H_3BPPA	4-Phosphono-biphenyl-4´-carbonsäure
HKUST	*Hong Kong University of Science and Technology*
HSAB	*Hard and Soft Acids and Bases*
IR	Infrarot
IRMOF	*isoreticular metal organic framework*
IUPAC	*International Union of Pure and Applied Chemistry*
MALDI	*Matrix-assisted laser desorption/ionization*
MIL	*Matériaux de l'Institute Lavoisier*
MOF	*Metal organic framework* (Metall-organische Gerüstverbindung)
nm	Nanometer (1 nm = 10^{-9} m)
NMR	*Nuclear magnetic resonance* (Kernspinresonanzspektroskopie)
PCPs	*porous coordination polymers*
POMs	*Polyoxometalates*
PSM	*Post synthetic modification*
P-XRD	*Powder X-Ray diffraction* (Pulver-Röntgendiffraktometrie)
SBUs	*Secondary building units*
SC-XRD	*Single Crystal X-ray Diffraction* (Einkristall-Röntgendiffraktometrie)
TGA	*Thermogravimetric analysis*
UiO	*Universitet i Oslo* (Universität in Oslo)

1. Einleitung

1.1. Metall-organische Gerüstverbindungen

In den letzten Jahrzehnten sind poröse Materialien sowohl für Chemiker als auch für Physiker und Materialwissenschaftler von besonderem Interesse, da sie durch Wechselwirkung mit anderen Atomen, Molekülen und Ionen eine (spezifische) Einlagerungsfähigkeit aufweisen und sie in hohen Mengen aufnehmen können.[1] Es besteht auch kommerzielles Interesse an ihrer Anwendung in der Stofftrennung, der Speicherung und der heterogenen Katalyse. Bis Mitte der 90er Jahre gab es grundsätzlich zwei Arten von porösen Materialien, nämlich anorganische Materialien und Kohlenstoffmaterialien. Bei anorganischen Feststoffen sind die beiden Unterklassen mit definierten Porengrößenverteilung bzw. die Aluminosilicate und Aluminophosphate zu nennen. Eine weitere Klasse stellen die Kohlenstoffmaterialien dar, wie Aktivkohle und kovalente organische Netzwerke (COF, *covalent organic framework*).[2,3] Nach einer IUPAC-Definition werden poröse Materialien anhand ihres Porendurchmessers in mikroporös (< 2 nm), mesoporös (2–50 nm) und makroporös (> 50 nm) klassifiziert.[4] Innerhalb der jeweiligen Porengröße werden Porensysteme nach geordneten wie z.B. Zeolithe und ungeordneten, wie bei Aktivkohle, unterteilt.[3] Neben klassischen porösen Materialien stellen molekulare organisch-anorganische Hybridverbindungen in jüngster Zeit eine neue Stoffklasse hochporöser Materialien dar (Abbildung 1).

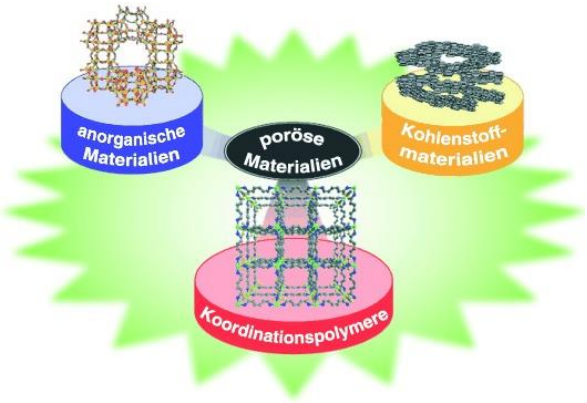

Abbildung 1 Verschiedene Klassen der porösen Materialien. Nachdruck mit Genehmigung aus Lit. 2, © 2004, WILEY-VCH Verlag GmbH & Co. KGaA, Weinheim.

Poröse Koordinationspolymere (PCPs) zeichnen sich durch eine perfekte Regelmäßigkeit und potenziell eine hohe Porosität aus. Sie lassen sich unter milden Bedingungen synthetisieren und bestehen aus Metallionen, welche über organische Liganden (Linker) zu ein-, zwei- und dreidimensionalen Strukturmotiven verbunden werden können (Abbildung 2).[5]

Der Begriff des *metal-organic framework*s, auch als Metall-organische Gerüstverbindung oder kurz MOF bezeichnet, wurde erstmals von Yaghi im Jahr 1995 in einer Publikation verwendet.[6] Die zu Beginn meist verwendeten organischen Linker beziehen sich auf multifunktionelle Carbonsäuren, die durch Deprotonierung der Carboxylat-Gruppen ergeben und nun zu den Metallionen eine koordinative Bindung ausbilden können. Bekannteste Vertreter in diesem Kontext sind das kubische MOF-5 [$Zn_4O(1,4\text{-}BDC)_3$] mit Terephthalsäure als Linker und HKUST-1 [$Cu_3(BTC)_2(H_2O)_3$] mit einer bekannten *paddle-wheel* Struktur (Schaufelrad-Cluster) von Kupferacetat.[7,8] Im Allgemeinen liegt die Stärke der Metall-organischen Gerüstverbindungen in der hohen Porosität. Hierbei können die Porengröße über die Länge des Linkers sowie die Funktionalität über zusätzliche funktionelle Gruppen (z.B. Amino-, Alkohol-, oder Säuregruppen) gesteuert werden, um spezifische Interaktionen mit Molekülen hervorzurufen. Man kann die Funktionalisierung *in situ* durchführen oder aber auch eine bereits existierende Substanz, post-synthetisch funktionalisieren und damit diese Substanzklassen für spezielle Anwendungen anfertigen.[9,10,11] Aufgrund ihrer Größen- und Formselektivität finden diese Materialien Anwendung in Trennverfahren und der Katalyse.

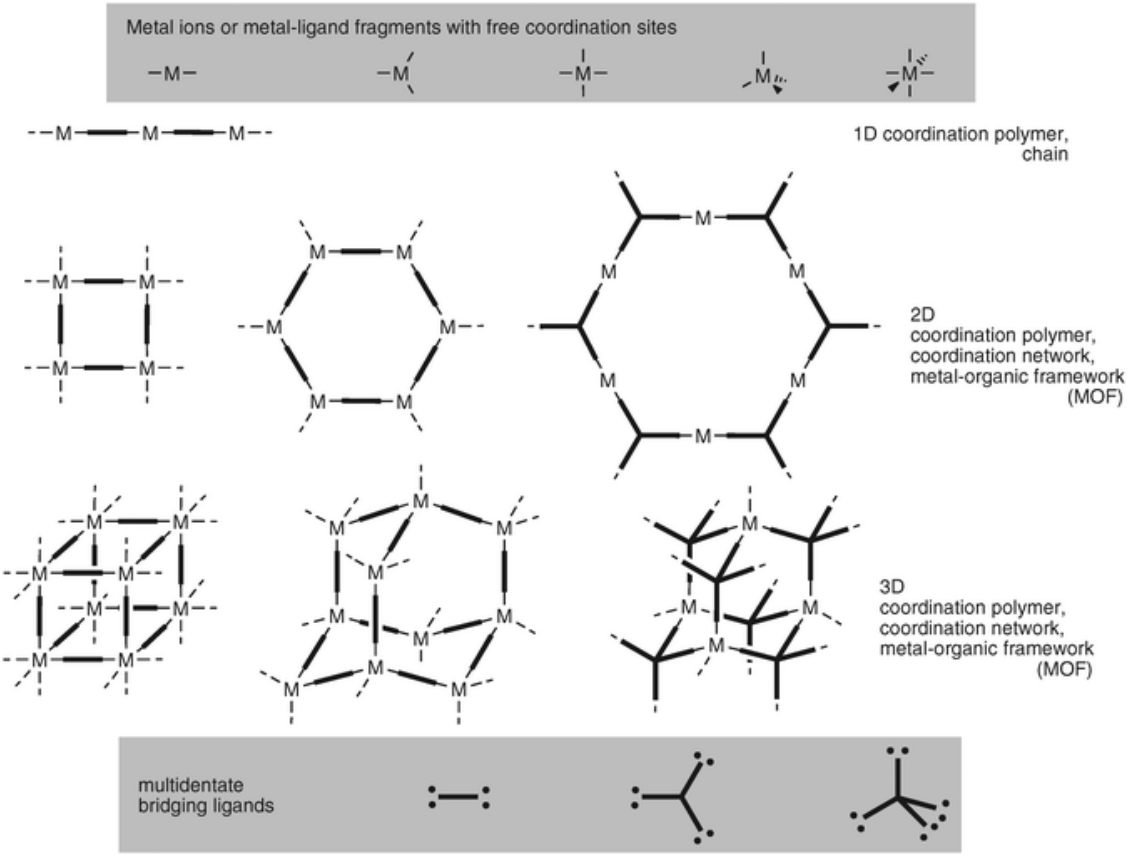

Abbildung 2 Schematische Darstellung des Aufbaus von Koordinationspolymeren und MOFs aus SBUs und organischen Liganden. Nachdruck mit Genehmigung aus Lit. 5, © 2010, Royal Society of Chemistry (RSC).

MOFs sind Koordinationsnetzwerke, welche häufig kristallin sind und aus organischen Liganden bestehen, die mittels Knoten (Metallionen oder Cluster) koordinativ miteinander verknüpft sind. Diese Metallionen oder Cluster werden auch als sekundäre Baueinheiten (*secondary building units*, SBUs) genannt. Durch Kombination der unterschiedlichen SBUs sowie Linker, ergeben sich verschiedene Geometrien in den resultierenden Koordinationspolymeren. Die Verwendung des SBUs dient als ein Konzept zur Klassifizierung der vielfältigen MOF-Strukturen in Bezug auf ihre Topologie.[12] Der grundlegende Aufbau von MOF und SBU kann exemplarisch anhand der Struktur von MOF-5, einer der am besten untersuchten MOF Struktur, vertieft werden. Die SBUs von MOF-5 bestehen aus Zn_4O^{6+}-Clustern, in denen ein O^{2-}-Ion tetraedrisch von vier Zn^{2+}-Ionen umgeben ist. Diese kationische Zn_4O^{6+}-SBUs sind durch anionische Benzodicarboxylat-Liganden zu einem kubisch primitiven Kristallgitter (**pcu**) der Formel $[Zn_4O(1,4\text{-BDC})_3]$ verknüpft. Die Topologie im MOF-5 stellt die anorganischen Einheiten $Zn_4O(CO_2)_6$ an Ausdehnungspunkte des Netzwerks und $–(C_6H_4)–$Linker an Kanten dar (Abbildung 3). Das dadurch entstehende Porensystem besitzt innere Oberfläche (BET) von etwa 2500 m^2/g.[13] MOF-177 besteht ebenfalls aus den gleichen Zn_4O Clustern, die durch Trimesinsäure verbunden sind, wodurch sich eine [6+3]-Koordination ergibt.[14] MOF-177 weist innere BET-Oberfläche von etwa 4500 m^2/g auf und ist aufgrund seiner Porengröße geeignet zur Einlagerung größerer Moleküle wie Brombenzol, 1-Bromnaphthalin, C_{60}, Farbstoffe wie Reichhardt Farbstoff (ein Farbstoffmolekül pro Zelle) und Astrazon orange R (16 Farbstoffmoleküle pro Zelle).

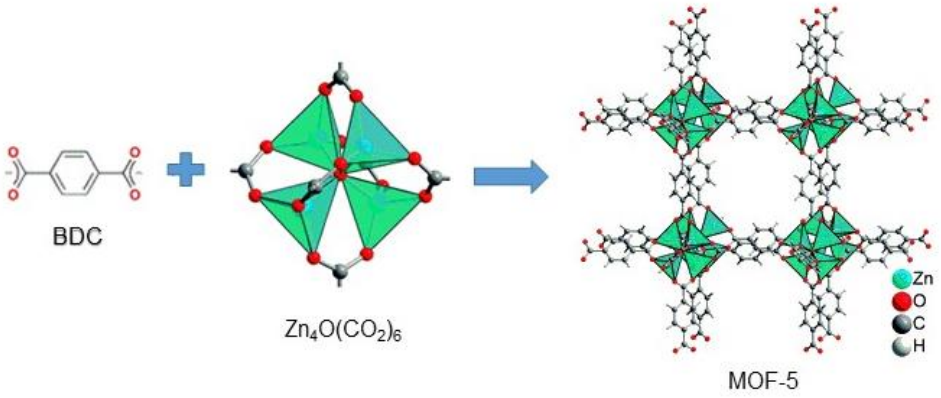

Abbildung 3 Aufbau von MOF-5 aus organischen Linkern und SBUs. Nachdruck mit Genehmigung aus Lit. 5, © 2010, Royal Society of Chemistry.

In den MOF-Verbindungen sind fast alle Übergangsmetalle und auch einige Hauptgruppenmetalle, wie Magnesium[15,16] oder Aluminium[17,18] integriert. Auch bei der Wahl der organischen Linker gibt es keine Beschränkung. Die verwendeten Liganden zur Synthese von MOFs können starr oder flexibel sein, wobei überwiegend starre Liganden verwendet werden.[19] Durch Einsatz der starren Linker können bestimmte Oberflächeneigenschaften

erhalten werden, wobei die Verwendung der flexiblen Linker zu einer geringen Oberfläche führen könnte. Diese Netzwerke können ebenfalls bei einer Aktivierung teilweise kollabieren und zu einer amorphen oder weniger kristallinen Verbindung umwandeln, wodurch Strukturtransformation stattfindet. Durch diese Flexibilität zeichnen solche MOFs eine Besonderheit aus, die in starren Systemen wie Zeolithen und Aktivkohle unmöglich ist. Diese sogenannten *breating stuctures* können ihre Poren dynamisch öffnen und schließen.[20] Dieser Effekt kann durch Druck, Temperatur oder Entfernung des Lösungsmittels sowie durch eine substituierte Gruppe ausgelöst werden. Der Druck, bei dem die Öffnung der Poren erfolgt, wird als *gate-pressure* bezeichnet. MOFs mit sogenanntem schaltbaren System sind gute Kandidaten für die Speicherung von Gasen und die Sensorik.[21,22]

Als Brückenliganden können zudem prinzipiell alle mindestens bifunktionelle Liganden mit verschiedenen Funktionalitäten eingesetzt werden. Ferner ist die Ladung ein bedeutender Faktor beim rationalen Aufbau von Koordinationspolymeren. Am häufigsten verwendeten organischen Liganden sind anionische oder neutrale Linker. Wenn die neutralen Liganden eingesetzt werden, da die meisten Übergangsmetall-Konnektoren Kationen sind, müssen zur Neutralisierung der Gesamtladung anionische Komponenten in die Koordinationspolymere eingebaut werden. Als häufig verwendete Anionen können schwach koordinierende Liganden wie ClO^{4-}, BF^{4-}, NO_3^- genannt werden, die in Form von terminalen Liganden vorliegen. Ebenfalls können hierzu starke Liganden wie z.B. CN^-, SO_4^{2-} verwendet werden, die auch als Brückenliganden vorkommen können. Allgemein treten Anionen in den Koordinationspolymeren als freie anionischen Gastmoleküle, terminal koordinierte Gegenionen oder Linker auf. Eine wichtige Besonderheit der anorganischen Anionen ist, dass ihre O- und F-Atome als Wasserstoffbrücken-Akzeptoren fungieren.

Es gibt aber auch einige Beispiele für kationische Liganden. Hier ist die Affinität der Linker zum Metallkation jedoch sehr gering. Kationische N-Arylpyridin- und Viologen-Derivate können hierbei als erfolgreich eingesetzte Liganden genannt werden.[23,24,25] Außerdem durch den Einsatz von unterschiedlichen Metallsalzen können verschiedene Gegenionen produziert werden, wodurch aufgrund ihres pH-Wertes und Redoxverhaltens die Struktur sowie Qualität von MOF-Strukturen beeinflusst werden können. Es wird ebenfalls in der Literatur über *Mixed*-Ligand-Ansatz berichtet. In diesem Kontext sind zwei Kombinationsmöglichkeiten für Linker bekannt: neutral-neutral und neutral-anionisch. Als Beispiel mit unterschiedlichen neutralen Liganden ist $\{[Cu(4,4'\text{-bpy})(pyz)(H_2O)_2]\cdot 2PF_6\}_n$ (4,4'-bpy = 4,4'-Bipyridin, pyz = Pyrazin) zu nennen.[26] Aufgrund des leicht möglichen Ladungsausgleiches sind Koordinationspolymere mit der Kombination der anionischen und neutralen Linker deutlich häufiger beschrieben. Dazu sind $[Cu_2(bpm)(ox)Cl_2]_n$ [27] (bpm = 2,2'-Bipyrimidin, ox = Oxalat) und $Cu_2(bpm)(suc)_{0.5}(ClO_4)_2(OH)(H_2O)_2]_n$ [28] (bpm = 2,2'-Bipyridin, suc = Succinat) zu nennen.

Basierend auf rationalem Design sowie retikulärer Synthese können neue MOFs synthetisiert werden. Die retikuläre Chemie befasst sich mit der Synthese von Verbindungen, die auf Basis von bekannten MOFs aus sekundären Baueinheiten (SBUs) gebildet werden, welche durch starke chemische Bindungen verknüpft sind.[29] Durch Einsatz dieser Strategie können hochsymmetrische Strukturen gebaut werden, wenn symmetrische SBUs über einfache Linker zusammengefügt werden.[30,31] Ein Vorteil dabei ist, dass aufgrund der Vorhersagbarkeit der Strukturen eine eindeutige Strukturbestimmung komplexer Kristalle durchgeführt werden kann. Zudem wird durch dieses Prinzip ermöglicht, die Porengeometrie und Funktionalitäten in den Poren auf molekularer Ebene für eine reversible Wirt-Gast-Wechselwirkung und mögliche Anwendungen gezielt zu gestallten. Die IRMOF-Reihe wurde durch Verlängerung oder Seitenfunktionalitäten der Linkerspezies entwickelt, wobei IR für isoretikulär (auf dem gleichen Netz basierend) steht. Die Methode eignet sich also, wenn eine anorganische Einheit beibehalten wird und nur die organischen Linker variiert werden. Yaghi *et al.* synthetisierten analog zu dem MOF-5 mit Terephthalsäure (1,4-BDC) als Ursprungslinker die IRMOF-Reihe.[8,32,33,34] Durch Verlängerung der aromatischen Kette zwischen den beiden Carbonsäure-Einheiten können so genannte interpenetrierenden MOFs generiert werden. Beispielsweise sind IRMOF-10 auf Basis von Biphenyl-4,4‘-dicarbonsäure und IRMOF-16 auf Basis von Triphenyl-4,4‘-dicarbonsäure zu nennen.[35] Ein großer Nachteil dieser interpenetierenden MOFs ist, dass ihre Poren von fremden Gerüsten gefüllt werden können.

Aufgrund des modularen Aufbaus der Porenwände von MOFs können chirale Gruppen und Funktionelle Gruppen an definierten Stellen positioniert werden, um spezifische Wechselwirkung mit dem Substrat zu gewinnen.[36,37] Es wurden unter anderem Halogen- (IRMOF-2), Aminogruppen (IRMOF-3), Alkoxygruppen (IRMOF-4,5) oder auch cyclische Substituenten (IRMOF-6,7) synthetisiert (Abbildung 4). Die Funktionalisierung findet bei präsynthetischer oder postsynthetischer Modifizierung (PSM) am MOF-Kristall oder Koordinationspolymer, im Sinne einer heterogenen Reaktion, statt. Postsynthetische Reaktionen können an SBUs durchgeführt werden, die durch Entfernung des Lösemittels MOFs mit freien Koordinationsstellen herstellen lassen, welche anschließend Liganden binden können.[38,39]

Deng *et al.* publizierten 2012 andere interessante Serie metallorganischer Netzwerke.[40] Das angewandte MOF dafür ist das MOF-74 mit eindimensionalen kettenförmigen SBUs, die durch Dioxidoterephthalatlinker in einem hexagonalen eindimensionalen Porensystem verknüpft sind. Hierbei wurden zusätzliche aromatischen Ringe in das Rückgrat des organischen Linkers eingeführt und dadurch den Porendurchmesser von etwa 10 Å auf 100 Å unter Erhalt der Gerüsttopologie erweitert. Dies weist somit den größten Porendurchmesser in metallorganischen Gerüstverbindungen auf, der in der bisherigen Literatur bekannt ist. Dies

deutet darauf hin, dass die isoretikuläre Synthese auch als Strategie zur gezielten Einstellung der Porengröße angesehen werden kann.

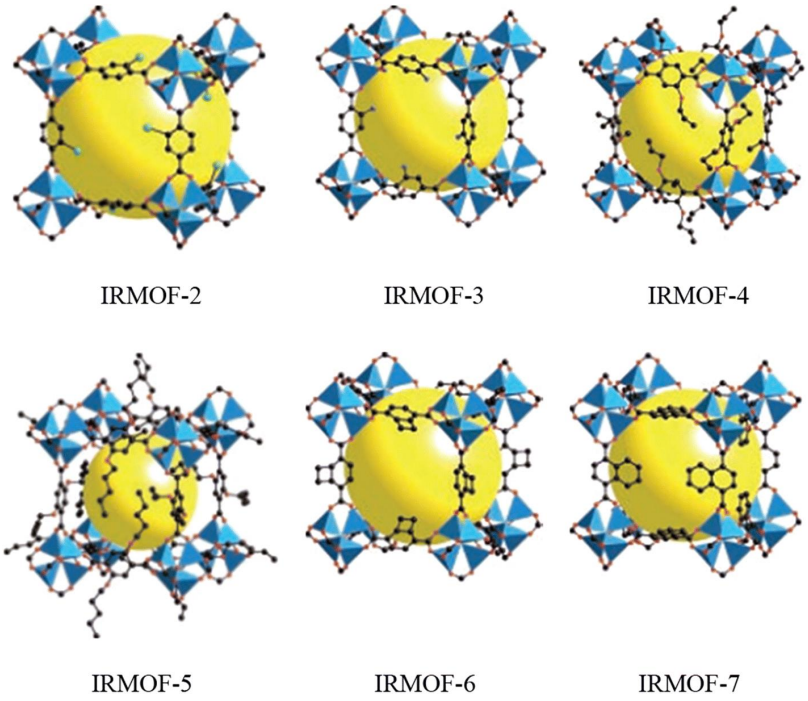

Abbildung 4 Substituierte IRMOFs. Nachdruck mit Genehmigung aus Lit. 35, © 2019, Springer Nature.

Wie bereits erwähnt, ist das rationale Design multidimensionaler und multifunktionaler molekularer Architekturen für die gezielte Synthese neuer Materialien von großer Bedeutung. Die hergestellten Netzwerke auf Basis des Konzeptes der retikulären Chemie (building units methodology) weisen neben hoher Porosität eine hohe strukturelle Stabilität auf. Eine Methode zur Verbesserung der Stabilität von MOFs besteht zudem in der Verwendung von hochvalenten Metallkationen und Carboxylatlinkern mit hoher Konnektivität.[41,42,43] Hochvalente Metallkationen mit hohen Ladungsdichten können bei gleichen Liganden und Koordinationsbedingungen stärkere Koordinationsbindungen und ein stabileres Gerüst ausbilden. Hierbei sind metallorganische Gerüste auf Metallbasis der Gruppe 4 (M^{IV}-MOFs), beziehungsweise Ti-, Zr- und Hf-basierte MOFs interessante Kandidaten zur Synthese einer Klasse von MOF, die einen breiten Anwendungsbereich aufweisen.[44,45] Zusätzlich zu den stärkeren Metall-Ligand-Bindungen benötigen diese 4+ Metallkationen mehr Liganden, um ihre Ladung auszugleichen. Daher weisen ihre anorganischen Knoten tendenziell eine hohe Konnektivität auf, welche die Stabilität des Gerüsts in gewissem Maße verbessert. Diese hohe Konnektivität kann zu einer Wasserstabilität hindeuten, wenn der Angriff von Gastmolekülen, in diesem Fall Wassermolekülen, verhindert werden kann.[46] Hierbei handelt es sich um ein relativ neues Gebiet, das in den letzten Jahren erhebliche Forschungsaufmerksamkeit erregt hat und zu großen Fortschritten bei Synthesen und Anwendungen geführt hat.

1.2. Zr-basierte MOFs

Das erste Zirkonium basierte MOF wurde erstmals von Lillerud *et al.* unter dem Namen UiO-66 (UiO = University of Oslo) beschrieben.[44] UiO-66 besteht aus Zr(IV)-Carboxylat-SBUs bzw. $[Zr_6(\mu_3\text{-}O)_4(\mu_3\text{-}OH)_4(COO)_{12}]$-Clustern mit einem linearen BDC-Linker (BDC = Terephthalsäure) und besitzt eine **fcu**-Topologie (Abbildung 5). Jede SBU ist aus sechs Zr(IV)-Ionen aufgebaut, die quadratisch antiprismatisch von jeweils acht Sauerstoffatomen koordiniert sind. Die SBUs sind über zwölf BDC-Liganden mit den benachbarten SBUs verknüpft. Das resultierende Gerüst bildet demnach eine kubisch dichteste Packung aus oktaedrischen und tetraedrischen Käfigen, welche über 6 Å große Fenster verbunden sind. Das Netzwerk besteht somit aus zwei Arten von Mikroporen mit einer BET-Oberfläche von ca. 1200 m^2g^{-1}, welche in Abhängigkeit von der Anzahl der Defektstellen ist.

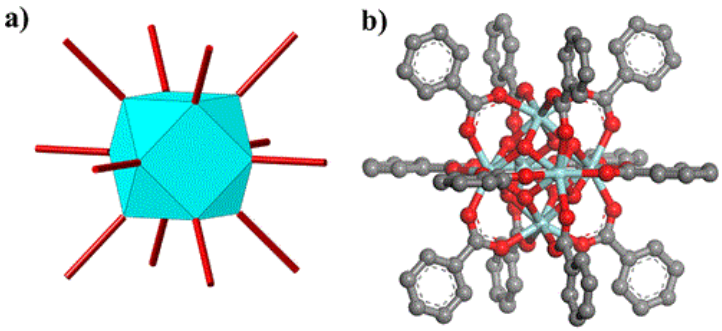

Abbildung 5 Darstellung des typischen Zr_6-Clusters mit 12 Metallknoten (a), und Struktur von $[Zr_6(\mu_3\text{-}O)_4(\mu_3\text{-}OH)_4(COOR)_{12}]$. Nachdruck mit Genehmigung aus Lit. 47, © 2016, American Chemical Society.

Das MOF UiO-66 besitzt thermisch (bis zu 500 °C), mechanisch, hydrolytisch sowie chemisch in sauren bzw. basischen Medien eine hohe Stabilität.[48] Die Stabilität von Zr_6-Cluster-basierten MOFs kann auf sowohl die hohe Oxophile des Zr^{IV} als auch ihre Coulomb-Wechselwirkung mit negativ geladenen Termini von Linkern zurückgeführt werden.[49] Zudem sind isoretikuläre Netzwerke von UiO-66 durch den Einsatz der verlängerten Liganden, nämlich UiO-67 und UiO-68, aufgebaut. Aufgrund der schnellen Komplexbildung bei der Synthese von Zr-basierten MOFs, welche zur Herstellung der mikrokristallinen sowie teilweise amorphen Verbindungen führt, werden hierbei sogenannte Modulatoren eingesetzt. Modulatoren mit der funktionalisierten terminalen Carbonsäure konkurrieren bei der Koordination am Metallion. Infolgedessen wird die Kristallwachstumsgeschwindigkeit herabgesetzt und hochkristalline Produkte erhalten.[50] Außerdem beeinflussen diese in einigen Fällen die Topologie.
In einem Lösungsmittelgemisch basiert auf DMF bilden sich mit einer hohen Vorhersagbarkeit Zr_6-Cluster.[51] Dies spielt eine große Rolle beim rationalen Design in MOFs. Nur einige

systematischen Ausnahmen, wie die MOF-140-Typen der isoretikulären-Reihe, besitzt eine eindimensionale Kette, aufgebaut aus ZrO_7-Polyedern mit gemeinsamen Kanten, die über lineare Liganden verbunden sind.[52] Weiterhin berichtete Clieffe *et al.* [$Zr_{12}(\mu_3\text{-}O)_8(\mu_3\text{-}OH)_8(\mu_2\text{-}OH)_6(COO)_{18}$]-Cluster, indem ein Paar Zr_6-Cluster durch μ_2-OH-Gruppen verbrückt wird.[53] Analog zu den Zr-MOFs wurden Hf-basierte MOFs synthetisiert. Infolgedessen zeigen Hf-MOFs ähnliche Strukturen sowie Anwendungen, da Hf^{4+} wie Zr^{4+} nahezu identische Ionenradien aufweisen.

1.2.1. Defekte in Zr-MOFs

Zr-MOFs weisen strukturelle Unregelmäßigkeiten oder Defekte auf. Dies stellt wiederum zusätzliche Möglichkeiten für die Integration neuer Eigenschaften zur Verfügung. Die Defekte können durch einen unvollständigen Kristallisationsprozess von MOF-Struktur entstehen,[54,55] aber auch kontrolliert und gezielt in MOFs eingebaut werden. Die Variabilität der Anzahl der Carboxylat-Gruppen im $\{Zr_6(\mu_3\text{-}O)_4(\mu_3\text{-}OH)_4(RCOO)_{12\text{-}n}(OH)_n(H_2O)_n\}$, wobei n = 0−4 die Anzahl der Defekte ist, bildet die Konnektivität des Zr_6-Clusters aus.

Neben den [$Zr_6(\mu_3\text{-}O)_4(\mu_3\text{-}OH)_4(COO)_{12}$]-Clustern mit zwölf Metallknoten können ebenfalls elf Metallknoten [$Zr_6(\mu_3\text{-}O)_4(\mu_3\text{-}OH)_4(OH)(H_2O)(COO)_{11}$],[56] oder zehn Metallknoten [$Zr_6(\mu_3\text{-}O)_4(\mu_3\text{-}OH)_4(OH)_2(H_2O)_2(COO)_{10}$][57], acht Metallknoten [$Zr_6(\mu_3\text{-}O)_4(\mu_3\text{-}OH)_4(OH)_4(H_2O)_4(COO)_8$][58] sowie selten sechs Metallknoten [$Zr_6(\mu_3\text{-}O)_4(\mu_3\text{-}OH)_4(OH)_6(H_2O)_6(COO)_6$][59] vorkommen, wobei jede fehlende Carboxylat-Gruppe für einen Ladungsausgleich mit einem terminalen Monocarboxylat-Ligand oder einem Paar von $\text{-}OH^-/H_2O$ Molekülen ersetzt wird. Ein prototypisches Beispiel dazu ist UiO-66, welches zahlreiche Linker-Leerstellen zeigen kann. Die dadurch entstehenden Strukturen sind praktisch unterschiedliche Verbindungen, die defektarme (**fcu**-Topologie) sowie defektreiche (z.B. **reo**-Topologie) Strukturen besitzen.[60,61]

Statisch, topologisch und dynamisch fehlgeordnete Koordinationspolymere wurden erstmals von Goodwin *et al.* anhand des Typs der Baueinheiten (SBUs), deren Konnektivitätsmuster und Periodizität sowie der Dynamik von Atomen/Einheiten definiert.[62,63] Strukturelle Unregelmäßigkeiten werden anhand ihrer Dimension in Punktdefekte (z.B. Leerstellen), Liniendefekte (z.B. Versetzungen), planare Defekte (z.B. Grenzflächen und Stapelungsfehler) und Volumendefekte in Meso- und Mikrodimensionen (z.B. Einschlüsse und Hohlräume) klassifiziert.[73] Weiterhin lassen sich die Defekte anhand ihrer Lage in äußere Oberflächendefekte und innere Defekte unterteilen. Für innere Defekte können beispielweise Fehlen von Metallknoten oder Linker genannt werden.

Außerdem zeigen einige MOFs die Bildung von reaktiven, koordinativ ungesättigten Metallzentren (*coordinatively unsaturated sites*, CUSs) innerhalb des molekularen Gerüstes. CUSs werden üblicherweise generiert, wenn Lösungsmittelmoleküle, die an Metallzentren

koordiniert sind, durch Waschen oder Aktivierung entfernt werden.[64] Es sind zahlreiche MOFs mit offenen zugänglichen Koordinationsstellen bekannt, in denen die Metallzentren als bevorzugte Adsorptionsplätze oder katalytisch aktive Zentren fungieren können. So eignet sich z.B. Vanadiumacetylacetonat als Gasphasenkatalysator für die oxidative Dehydrierung von Cyclohexan.[65] Zudem zeigten Jiang *et al.* mehr Lewis-acide CUSs an dem Zr_6-Cluster, die in Sulfat-MOF-808-Analogon eingebaut wurden. Diese besitzen katalytische Aktivität bei diversen Säure-katalysierten Reaktionen, wie z.B. Friedel-Crafts-Acylierung.[66] Die Entfernung von eingelagerten Edukten und Lösemittelmolekülen im Porenraum ermöglicht ebenfalls die Zugänglichkeit des Reagens für eine postsynthetische Modifikation (PSM). Dabei existiert die Möglichkeit der Koordination von organischen, Lewis-basischen Molekülen an die Metallzentren.[67] Dadurch können die katalytische Aktivität sowie Adsorptionsaufnahmekapazität im Porenraum erhöht werden.[68,69] Ein exemplarisches Beispiel für CUS kann bei MOF UiO-66 verdeutlicht werden. Die SBUs in UiO-66 können aufgrund der schwachen Bindungen der μ_3-OH Gruppen in der SBU reversibel dehydratisiert werden. Die dadurch entstehenden SBUs mit der Zusammensetzung $Zr_6(\mu_3\text{-}O)_6(CO_2)_{12}$ besitzen somit freie Koordinationsstellen.[70] Unter Berücksichtigung der Unterteilung der Defekte können ungesättigte Metallzentren somit als Punktdefekte bezeichnet werden. Zusätzlich, wie bereits die Verwendung von Modulatoren in Synthese von MOFs erwähnt wurde, führt der Einsatz von Carboxylat-funktionalisierten Modulatoren (z.B. Benzoesäure, Essigsäure oder Trifluoressigsäure) bei der Synthese von UiO-66 nicht nur auf die Kontrolle über die Kristallgröße zurück, sondern auch die Bildung von Defekten kann dadurch beeinflusst werden. Außerdem kann der Modulator in diesem Fall als gestutzter Linker betrachtet werden. Das bedeutet, dass die Defektkonzentration im erhaltenen MOF von der Konzentration des Modulators im Synthesegemisch abhängt. Dies ermöglicht eine kontrollierte Zunahme der Porosität.[71] Ferner haben Vermoortele *et al.* gezeigt, dass der Einsatz von TFA als Modulator mehr Lewis-Acide mCUSs an den Zr_6-Clustern öffnet und somit die Porosität von UiO-66 erhöht.[72] Durch Aktivierung konnte die TFA aus dem Netzwerk entfernt werden, wodurch die Zahl der Zr-CUSs weiter anstieg. Wu *et al.* berichteten, dass der Einsatz der Linker-Leerstellen zu einer signifikant verbesserten Porosität von UiO-66 führt.[73] Zudem zeigten diese Proben somit eine erhöhte katalytische Aktivität.[74]

1.2.2. Zr-Oxocluster

Des Weiteren können neben den Zr_6-Clustern andere Cluster bei kontrollierter Hydrolyse in nichtwässrigen Lösungsmitteln, besonders in alkoholischer Lösung aufgebaut werden. Diese Methode wurde bei der Synthese von $\{Zr_{18}\}$,[75] $[Zr_{18}O_{21}(OH)_2(RCOO)_{28}]$, der bis zum Jahr 2017

größte Zr-Oxocluster in der Literatur, durchgeführt, der Ursprung ist auf die Arbeit von Xu *et al.* zurückzuführen.

Das Feld der M(IV)-Oxoclustern ist benachbart mit dem Gebiet der klassischen Polyoxometallate, kurz POMs, mit der generellen Formel $[X_xM_aO_b]^-$.[76] Hierbei sind Atome M frühe Übergangsmetalle, wie Vanadium, Niob, Tantal, Molybdän oder Wolfram in ihren hohen bzw. höchsten Oxidationsstufen ($M^{IV,\ V,\ VI}$). Damit kann die hohe negative Ladung der Oxo-Anionen im Cluster kompensiert werden. Als weitere wichtige Beispiele im Bereich von MOF-SBUs können $M_3OX(RCOO)_6$ (M (III) = Fe, Cr, V, Al, In; X = OH, F) und $Zn_4O(RCOO)_6$ genannt werden, die sich ebenfalls in der Nachbarschaft der M(IV)-Oxoclustern befinden.[12]

Die bekannten Zr-Oxocluster sind typischerweise klein, auch die größten fullerenartigen $\{Ti_{42}\}$ und $\{Ti_{52}\}$, die kürzlich vorgestellt wurden.[77] Zr-Oxocluster lassen sich in folgenden Haupttypen unterteilen: der dreieckige $\{Zr_3\}$ ~ $(\{Zr_6\})_{1/2}$-,[78] der parallelogrammförmige $\{Zr_4\}$-,[79] der unvollständige oktaedrische $\{Zr_5\}$ ~ $\{Zr_{(6-1)}\}$-,[80] der archetypische oktaedrische $\{Zr_6\}$-,[81] der kubische $\{Zr_8\}$-,[82] der $\{Zr_9\}$ ~ $\{Zr_{(6-1+4)}\}$-,[83] der $\{Zr_{10}\}$ ~ $\{Zr_{(6+4)}\}$-,[77] der pseudo-$\{Zr_{12}\}$ ~ $\{Zr_6\}(COO)_4\{Zr_6\}$-, der instabile kubische $\{Zr_{13}\}$-[84] sowie der größte $\{Zr_{18}\}$-[77] Cluster. Für die Beschreibung all dieser Cluster ist der oktaedrische $\{Zr_6\}$-Cluster mit dem invariablen $\{Zr_6\ (\mu_3\text{-}O/OH)_8\}$-Kern von besonderer Bedeutung. Aus diesem Grund wurden auch große Aggregate mit Hilfe der archetypischen Zr_6-Cluster als Standardbaustein beschrieben, deren Ecken, Kanten oder Flächen geteilt sind (Abbildung 6). Ein ähnliches Bespiel gilt für größere Polyoxomolybdän-Cluster, welche sich durch Mo_8-Cluster als Grundbaustein dieser Struktur beschreiben lassen.[85]

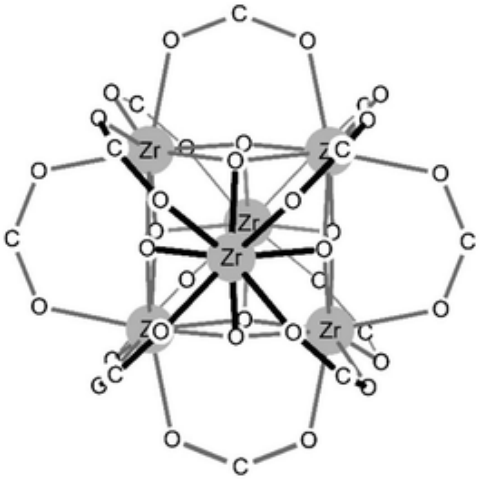

Abbildung 6 Der prototypische $\{Zr_6(\mu_3\text{-}O)_4(\mu_3\text{-}OH)_4(RCOO)_{12}\}$-Cluster. Nachdruck mit Genehmigung aus Lit. 86 © 2016, The Royal Society of Chemistry.

1.3. Carboxylat-basierte MOFs mit Schwerpunkt auf Zr-Verbindungen

Carboxylat-funktionalisierte Linker sind am häufigsten eingesetzte Linker zur Synthese von MOFs. Hierbei werden Liganden mit zwei Carboxylat-Gruppen am meisten zur MOF-Synthese verwendet. Es wurden ebenfalls viele Kristallstrukturen von Carboxylat-Komplexen veröffentlicht. Diese weisen eine permanente Porosität sowie eine hohe innere Oberfläche auf.[9,87] In Schema 1 sind einige Beispiele von Liganden auf Basis von Bi- bzw. Tricarbonsäure dargestellt. Carboxylate können in drei verschiedenen Koordinationsmodi vorkommen, da die Metallionen (als mono- und bidentater Ligand) verbrückend sowie durch Chelatisierung eines Metallzentrums koordinieren können.[88] Die Koordinationsart dieser Liganden hängt von der Metallionengröße sowie deren Ladung ab.[88]

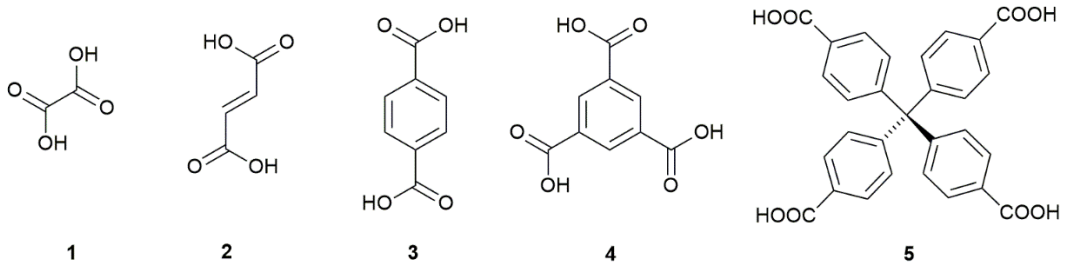

Schema 1 Darstellung einiger Beispiele von Carbonsäure-funktionalisierten Liganden, welche bei der Konstruktion von MOFs verwendet werden. Oxalsäure (1), Fumarsäure (2), Terephthalsäure (BDC, 3), Trimesinsäure (BTC, 4), Tetrakis(4-Carboxyphenyl)-Methan (5).

Hierbei ist Terephthalsäure (BDC) der am besten untersuchter und vielseitigter Linker bei der Synthese von porösen Koordinationspolymeren (PCPs) mit verschiedenen Stabilitäten und Oberflächen. Da Carboxylat-basierten PCPs eine hohe thermische Stabilität und Robustheit aufweisen, werden sie in zahlreichen Anwendungen eingesetzt.[89] Beispielsweise sind MIL (Matériaux de l'Institute Lavoisier) und UiO (Universitetet i Oslo) zu nennen, welche für ihre außergewöhnlich hohen Oberflächen bekannt sind.

Metall-organische Gerüstverbindungen, basiert auf Carboxylat-Linkern und Zr_6-Clustern haben große Aufmerksamkeit im Gebiet der MOFs erhalten, da sie eine Kombination aus hoher thermischen, chemischen, hydrolytischen Stabilität und Porosität, sowie den damit verbundenen Anwendungsmöglichkeiten aufweisen. Hierbei kann auch die Stabilität von MOFs durch kinetische Faktoren beeinflusst werden. Dichte und starre Gerüststrukturen, die durch stark verbundene Metall-Oxocluster und starre organische Linker gebildet werden, verbessern die Gesamtstabilität von MOFs, insbesondere die mechanische Stabilität. Dies erklärt auch teilweise die gute Stabilität von MOFs auf M^{4+}-Basis, da M^{4+}-Kationen mehr Liganden benötigen, um ihre Ladung auszugleichen.

Außerdem sind Caboxylat-basierten sowie Zr-Carboxylat-basierten MOFs bekannt für geringe Toxizität, optische Transparenz sowie Diamagnetismus (wichtig für die Verwendung als Matrix zur Aufnahme aktiver Spezies). Mögliche Anwendungen dieser Materialien sind in der Speicherung kleiner Moleküle,[90] Trennung[91] und gezielter Wirkstofffreisetzung,[92] sowie Katalyse[93] und Sensorik.[94]

Die strukturelle Vorhersagbarkeit der Zr-Carboxylaten ist ein wichtiger Vorteil bei der MOF-Forschung, welcher mit der hohen Stabilität des kuboktaedrischen {Zr_6 (μ_3-O)$_4$ (μ_3-OH)$_4$ ($RCOO)_{12}$}-Clusters verbunden ist. Für die thermodynamische Stabilität von MOFs spielt zudem die Metall-Ligand-Bindungsstärke eine wichtige Rolle. Basiert auf HSAB-Konzept (auch Pearson-Konzept) bilden sich starke Koordinationsbindungen zwischen harten-Lewis-Säuren und -Basen oder weichen-Lewis-Säuren und -Basen.[42,44] Carboxylat-funktionalisierte Liganden können aufgrund harter Oxo-Donorgruppen als relativ harte Basen angesehen werden, die mit Metallkationen der Gruppe 4 mit hoher Ladungsdichte stabile MOFs bilden.

Der Einsatz der retikulären Chemie ist weiterhin für Zr-Carboxylat-basierten MOFs sehr gut geeignet, im Vergleich zu den viel weniger stabilen Zink-Carboxylaten. Die Verfügbarkeit einer Reihe isoretikulärer MOFs mit einer großen Anzahl von Vertretern fokussiert sich nur auf die funktionelle Gruppe und Design dieser Materialien, weniger auf die grundlegenden strukturellen Aspekte. Die drei wichtigsten isoretikulären Reihen basieren auf (a) linearen Liganden, indem meiste Verbindungen mit einer **fcu**-Topologie (UiO-66-Typ[95]), (b) quadratförmigen Liganden,[96] die das **ftw**-Netz ergeben, und (c) tetraederförmigen Liganden,[97] die das **flu**-Netz erzeugen (Abbildung 7). Diese Liganden sind hierbei geeignet {$Zr_6(\mu_3\text{-}O)_4(\mu_3OH)_4(RCOO)_{12\text{-}n}(OH)_n(H_2O)_n$}-basierten Cluster zu bilden, der eine Konnektivität von zwölf (kuboktaedrische Einheit) bis acht (typischerweise eine kubische Einheit) zeigen kann.

Der Einsatz von einem tetraedrischen Linker bei der Konstruktion des Fluorit-Netzwerkes ist am Beispiel von PCN-521 in Abbildung 8 dargestellt. Es besteht aus Cluster mit acht Metallknoten und besitzt eine BET-Oberfläche von 3411 m^2g^{-1}. Weitere Beispiele sind PCN-222 (**csq**-Topologie)[58], PCN-224 (**she**-Topologie)[98] und PCN-225 (**sqc**-Topologie)[99].

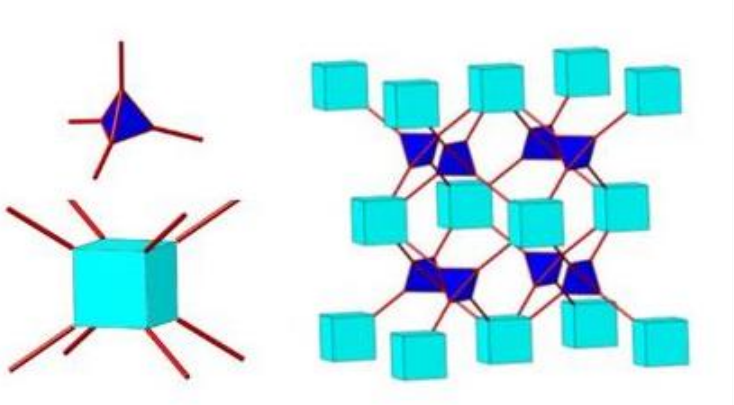

Abbildung 7 Darstellung der **flu**-Topologie. Das gebildete Netzwerk (rechts) besteht aus tetraerischen und kubischen Einheiten (links). Nachdruck mit Genehmigung aus Lit. 47, © 2016, American Chemical Society.

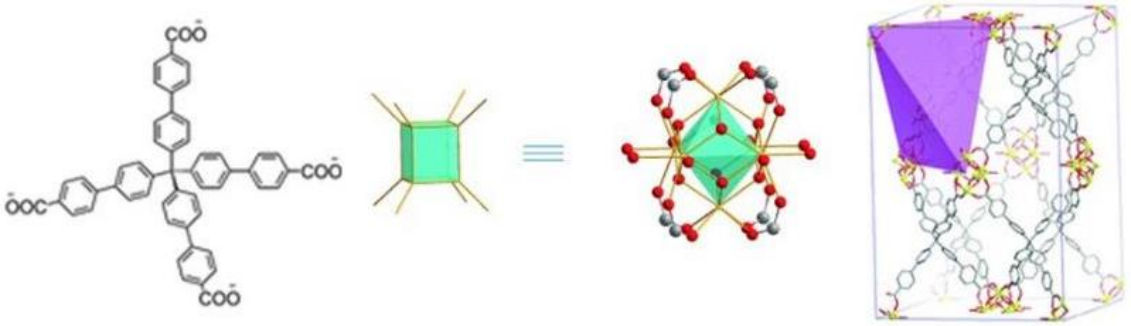

Abbildung 8 Darstellung des Linkers (links), Zr_6O_8-Cluster mit acht-Metallknoten in PCN-521 mit einer **flu**-Topologie (mitte), Kristallstruktur von PCN-521 (rechts). Nachdruck mit Genehmigung aus Lit. 100, 101, © 2016, The Royal Society of Chemistry; © 2014 Wiley-VCH Verlag GmbH & Co. KGaA, Weinheim.

Neben dem $\{Zr_6(\mu_3\text{-}O)_4(\mu_3\text{-}OH)_4(RCOO)_{12}\}$-Cluster als einem vielversprechenden Kandidaten zur gezielten Defektbildung in Zr-MOFs, kann folglich eine sehr seltene Strategie für die Defekteinführung verfolgt werden, indem gestutzte Linker (Liganden mit fehlender Carboxylat-Gruppe, *trancated ligands*) eingesetzt werden und dementsprechend potenziell eine höhere innere Oberfläche generiert, sowie die katalytische Aktivität moduliert werden.[102]

1.4. Phosphonat-basierte MOFs mit Schwerpunkt auf Zr-Verbindungen

Organophosphonate sind potente O-Liganden, die sich hervorragend als Liganden für MOF-Synthese eignen. Jedoch ist die Anzahl der Phosphonat-basierten MOFs mit hoher Oberfläche sehr begrenzt. In Schema 2 ist das Protolysegleichgewicht der Alkyl-Phosphonsäure abgebildet. Grundsätzlich kommen drei Sauerstoffatome, die an

Metallionen koordinieren in chelatisierter oder verbrückender Form vor.[103] Die ersten Arbeiten mit Metallphosphonaten gehen auf Alberti *et al.* 1978 zurück.[104] Hierbei handelt es sich um eine Synthese eines Zirconium-phosphonat-Komplexes. Seitdem wurde eine Vielzahl von Phosphonatkomplexen mit anderen Metallionen (z.B. Co^{2+}, Zn^{2+}) sowie Phosphonat-basierten MOFs veröffentlicht.

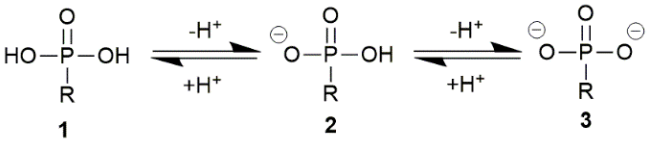

Schema 2 Darstellung drei verschiedener Formen der Alkyl-Phosphonsäure (R = Organyl-Rest z.B. Alkyl-/Aryl-Gruppe). Phosphonsäure (R =H, 1), einfach deprotonierte Form (2), Phosphonat-Gruppe (3).

Metallorganische Gerüste (MOFs) auf der Basis von Zirkoniumphosphonaten weisen eine hervorragende chemische Stabilität auf und eignen sich für Anwendungen unter harten Reaktionsbedingungen. Dines *et al.* synthetisierten eine erste Reihe von Zr-Verbindungen, die auf Biphenyl-bis(phosphonsäure) und Methylphosphonsäure basierten.[105] Seine Überlegung war, dass die Methyl-Gruppen im Raum zwischen den Schichten aus Biphenyl-Gruppen vorkommen können und dadurch Porosität erzeugen würden. Die resultierenden Materialien waren tatsächlich porös und zeigten eine ziemlich große Porengröße. Die Porosität nahm mit der Menge der eingesetzten Methylphosphonsäure zu. Clearfield stellte jedoch fest, dass selbst die Verbindung, die keine Methylphosphonat-Gruppen enthielt, war fast so porös wie die poröseste Verbindungen aus beiden Liganden.[106] Mit dieser Beobachtung als Ausgangspunkt haben Clearfield und Alberti die weitere Erforschung dieser Familien poröser Materialien vorangetrieben.

In den letzten zehn Jahren wurden zahlreiche Arbeiten zur Entwicklung und Synthese von MOFs durchgeführt, die gegenüber strukturellen Zersetzungen durch Feuchtigkeit, Säuren/Basen, Oxidations-/Reduktionsmittel sowie Strahlung beständig sind und für viele praktische Anwendungen von entscheidender Bedeutung sind.[99,107] In der Literatur beschriebenen Zr-phosphonat-basierten MOFs zeigen eine Klasse vielseitiger Materialien mit vielversprechenden Anwendungen wie Katalysator-Trägern, Schwermetall-Sorbentien sowie protonenleitenden Materialien.[108,109]

Es gibt jedoch zwei wesentliche Hindernisse bei der Entwicklung dieser Materialien. Als erstes Problem kann die schlechte Löslichkeit von Zr-phosphonaten, aufgrund der außerordentlich starken Affinität zwischen Zr^{4+} und Phosphonatliganden, genannt werden, welche häufig zu schnellen Fällungsprodukten bzw. Niederschlägen mit geringer Kristallinität oder sogar zu vollständig amorphen Feststoffen führt. Dies wurde bei den Pionierarbeiten von Clearfield und

Alberti *et al.* berichtet.[110] Obwohl Strukturen einiger dieser Materialien teilweise mithilfe von Röntgen-Pulverdiffraktogrammen gelöst wurden, ist eine Einkristallstruktur von Zr-phosphonat-MOF mit präzisen Strukturinformationen schwer zu erhalten. Zweitens basieren die meisten berichteten Zirkoniumphosphonat-MOFs auf anorganischen Zirkoniumphosphat-1D-Ketten oder 2D-Schichten, wobei die Bildung des nulldimensionalen Zr-phosphat-Cluster fehlte, der als sekundäre Baueinheit (SBU) fungieren kann. Dies führt zum Problem auf Basis rationaler topologischer Designprinzipien.[111] Im Gegensatz dazu finden sich, wie bereits erwähnt, viele Beispiele über Zr_6-Cluster für Zr-Carboxylat-basierte MOFs, wie z.B. UiO-66,[60] PCN-222,[58] MOF-525, sowie NU-1000,[112] welches einen Zr_6-Cluster als SBU enthält. Hierzu sind Zr-Phosphonate mit 3D-Gerüststrukturen sehr selten.[113]

Hierbei überwanden Zheng *et al.* diese Herausforderungen und erhielten Einkristalle aus drei Zirkoniumphosphonaten, die für die Strukturanalyse geeignet waren.[114] Um oben genannte Probleme zu lösen, wurden dabei zwei Strategien verfolgt: Erstens haben die Taddei *et al.* durch die Verwendung eines sterisch anspruchsvollen Spacermoleküls die Bildung einer 2D-Struktur verhindert.[115] Hierzu wurden zwei tetraedische Liganden bzw. tetrakis[4-(dihyroxyphosphoryl)phenyl]methan ($TppmH_8$) und 1,3,5,7-tetrakis(4-phosphonophenyl)adamantan ($TppaH_8$) ausgewählt, um die Bildung der dicht gepackten Strukturen zu verhindern. Zweitens wurde die ionothermische Synthese verwendet, um das Problem der Hydrolyse bzw. Solvatisierung von Zr^{4+}, welches bei den traditionellen hydrothermalen bzw. solvothermalen Reaktionen auftritt, zu vermeiden. Folglich ergibt sich eine Verlangsamung der Kristallisationskinetik und somit eine Förderung des Wachstums großer Einkristalle. Außerdem lieferte die ionothermische Reaktion von $ZrCl_4$ mit $TppmH_8$ oder $TppaH_8$ in der ionischen Flüssigkeit N-Butyl-N-methylpyrrolidiniumbromid ($[C_4mpyr][Br]$) und N-Ethylpyridiniumbromid ($[C_2py][Br]$) in Gegenwart von HF drei hochkristalline dreidimensionale mikroporöse Zr-phosphonat-MOFs, welche für eine Röntgenstrukturanalyse geeignete Kristallgröße zur Verfügung stellen. Solche Verbindungen bestehen aus einem nulldimensionalen Zr-phosphat-Cluster als SBU und eröffnen somit einen Weg für das retikuläre Design von Zr-Phosphonat-basierten MOFs. Darüber hinaus zeigten diese Verbindungen Ultrastabilitäten in sauren Lösungen, insbesondere in rauchenden Säuren. Ferner besitzen zwei dieser Verbindungen eine hohe permanente Porosität und ein ausgezeichnetes Uranaufnahmevermögen, während eine Verbindung das poröseste kristalline Zr-phosphonat ist, welches bisher berichtet wurde, und das einzige poröse MOF ist, welches in Königswasser stabil bleibt.

1.5. Pyrazol- und Pyrazolat-basierte MOFs

Azole sind die fünfgliedrigen aromatischen Stickstoff-Heterocyclen und stellen sehr wichtige Rolle als sekundäre Baueinheiten (SBUs) für die Synthese von zahlreichen Verbindungen dar, die in der Medizin, Landwirtschaft, Industrie und Koordinationschemie verwendet werden können.[116] Die Koordinationsverhältnisse der zweizähnigen sp^2-N-Donor-Liganden in Azolen sowie Pyridinen sind grundsätzlich identisch. Azole lassen sich meist als Basen (die protonierte Form ist Azolium-Kation) betrachten, wobei Pyridinhaltige-Liganden eine Ladungsneutralität besitzen. Als weitere N-Heterocyclen-basierten Liganden zur Synthese von MOFs können Imidazole (*H*im), Pyrazole (*H*pz), 1,2,4-Triazole (Htz), 1,2,3-Triazole (*H*vtz) und Tetrazole (*H*ttz) genannt werden, welche durch Deprotonierung die entsprechenden Azolat- (oder Azolid-) Anionen bilden können. Hierbei ist das 1*H*-Pyrazol (Hpz, Schema 3) ein Molekül aus dieser Gruppe, welches zu den am häufigsten in MOFs anzutreffenden Liganden gehört. Trofimenko *et al.* führte es erstmals 1972 als Ligand in der Koordinationschemie ein.[117, 118] Pyrazol-funktionalisierten Liganden stellen eine wichtige Gruppe von Liganden bei der Herstellung von Koordinationspolymeren dar, welche für verschiedene Anwendungen wie Katalyse,[119] Magnetismus[120] und Medizin[121] verwendet werden können. Bemerkenswert sind die Fortschritte, die in den letzten zehn Jahren bei der Synthese von Pyrazolderivaten erzielt wurden.[122] Wichtiger als das 1*H*-Pyrazol, das bei der Monohapto-Koordination über den N2-Stickstoff verknüpft wird, ist das Pyrazolat (pz^-), bei dem das 1*H*-Pyrazol am N1 deprotoniert ist. Hierbei ist die Affinität zu leichten Metallionen (z.B. Cu^{2+}, Co^{2+}, Cd^{2+}, Ni^{2+}) viel stärker als die von Carboxylaten. Aufgrund der räumlichen Nähe der beiden Stickstoffatome zählen Pyrazole zur exobidentaten Liganden, die relativ kleine Bindungswinkel aufweisen.

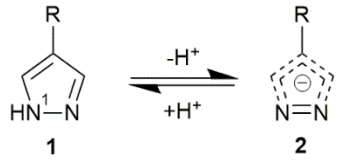

Schema 3 Das 1*H*-Pyrazol (R = H, **1**) und das Pyrazolatanion (**2**). Die R-Gruppe in 4-Position kann ein beliebiger Rest für geeignete polyfunktionelle Liganden sein.

Pyrazolat-funktionalisierten Liganden können in unterschiedlichen Koordinationsmodi vorkommen. Sie können als verbrückende Liganden über N1 und N2 sowie chelatisierende Liganden fungieren. Ferner weisen andere Azolat-basierten Liganden wie 1,2,3-Triazole sowie 1*H*-Tetrazole ähnliche Koordinationsmodi auf.[123] Pyrazolat-Liganden zeigen gleiche pK_a wie Imidazol-Liganden, jedoch eine höhere pK_a im Vergleich zu Triazol- sowie Tetrazol-basierten

Liganden, welche zur Bildung stärkerer Bindung zwischen Pyrazolat-/Imidazolat-Liganden und Metallionen führen.[124] Aufgrund der stärkeren Bindungen besitzen die Pyrazolat- sowie Imidazolat-Komplexe eine höhere thermische sowie Wasserstabilität im Vergleich zu analogen Carboxylat-basierten Komplexen. ZIF-8, [Zn(2-methylimidazolat)$_2$][125] ist ein häufig angeführter Vertreter auf dem Gebiet von Imidazolat-funktionalisierten MOFs , welches in kochendem Wasser, über einen weiten pH-Bereich sowie unter starken alkalischen Bedingungen eine Stabilität aufweist und somit MIL-101[89] übersteigt. Tranchemontagne *et al.* synthetisierten aus einem Pyrazolat-Carboxylat-basierten Liganden MOF-325, welches aus dem bekannten Schaufelrad-Cluster (paddle-wheel) {$Cu_2(O_2C)_4$} und trigonalen pyramidalen Bausteinen besteht.[126] Später konnten Heering *et al.* vier isoretikuläre MOFs, aufgebaut aus {$M_4(\mu_4\text{-}O)$}-Einheiten (M = Co, Zn) und Pyrazolat-Carboxylat-funktionalisierten Liganden, herstellen.[127]

Des Weiteren können bifunktionelle Liganden zur Synthesestrategie von MOFs eingesetzt werden, um die Vorteile verschiedener Arten von Koordinationsgruppen zu kombinieren und sie somit in einer strukturellen Untersuchung synergistisch zu nutzen. Durch die Variation der organischen Baueinheiten können die gebildeten Koordinationspolymeren (CPs) in ihren Eigenschaften und Topologie gesteuert werden. Von besonderem Interesse hierbei ist, dass sich durch den Einsatz eines bifunktionellen Pyrazolat-Phosphonat-Liganden, sowohl mono- als auch bimetallische Komplexe ergeben können. Pyrazolat-funktionalisierte Gruppen weisen nach dem HSAB-Konzept eine Affinität zu weicheren Metallionen (z.B. Cu^{2+}, Zn^{2+}) auf, während die O-Donoren von Phosphonat-Gruppen eine Affinität zu harten Metallionen (z.B. Fe^{3+}, Zr^{4+}) besitzen. Dies ermöglicht eine gezielte Einführung von einem bimetallischen System. MOFs mit bifunktionellen Pyrazolat-Phosphonat-Liganden sind in der bisherigen Literatur nicht bekannt. Bei einer genauen Betrachtung von bekannten Kooprdinationspolymeren mit Phosphonat-Liganden,[128,129] zusammen mit Pyrazolat-Liganden-basierten MOFs, lässt sich eine Realisierbarkeit dieses Konzeptes zur Synthese der Koordionationspolymere auf Basis von bifunktionellen-Liganden mit vielseitigen Architekturen[130,131] schließen. Hierbei sind für resultierenden Koordinationspolymere eine hohe chemische sowie thermische Stabilität aufgrund der bekannten MOFs beziehungsweise Koordinationspolymeren auf Basis von bifunktionellen Carboxylat-Pyrazolat-Liganden,[132,138,107] sowie Carboxylat-Phosphonat-Linkern[133] zu erwarten.

2. Zielsetzung und Motivation

In der vorliegenden Arbeit wurden zwei allgemeine Ziele verfolgt. Das erste Ziel war die Synthese von Zirkonium-Metall-organischen Gerüstverbindungen mitgemischt-Liganden-Ansätzen auf Basis von Oligophenyladamantan-carbonsäuren. Hierbei sollten gezielte Defekte in MOFs, basierend auf ((Adamantan-1,3,5,7-tetrayl)tetra(phen-4-yl))tetracarbonsäure (H_4L^4) und seinen gestutzten Analoga ((Adamantan-1,3,5-triyl)tri(phen-4-yl))tricarbonsäure (H_3L^3) sowie ((Adamantan-1,3-diyl)-diphen-4-yl)dicarbonsäure (H_2L^2) eingefügt werden. Aufgrund der schnellen Komplexbildung bei der Synthese von Zr-basierten MOFs, welche zur Herstellung der mikrokristallinen sowie teilweise amorphen Verbindungen führt, sollten hierbei diverse Modulatoren eingesetzt werden. Diese sollten die Kristallisation verlangsamen und damit die Kristallinität und in einigen Fällen die Topologie beeinflussen. Da die Modulatoren mit funktionalisierten terminalen Carbonsäuren bei der Koordination am Metallion konkurrieren, sollte somit die Deprotonierung von Linkern verlangsamt werden. Infolgedessen wird die Kristallwachstumsgeschwindigkeit herabgesetzt und es werden hochkristalline Produkte erhalten. Im Allgemeinen ist das Thema der Defektstruktur und Fehlordnung im Gebiet der MOFs bekannt. Jedoch ermöglicht der Einsatz der gestutzten Linker mit fehlenden Carboxylatgruppen (*truncated linker*) das bewusste Design von Fehlordnung in MOF-Strukturen. Die Absicht dieses Ansatzes sollte ebenfalls zur Bildung sogenannter koordinativ ungesättigter Metallzentren (*coordinatively unsaturated sites*, CUSs) führen. Des Weiteren sollten aus der Umsetzung großer Linker mit höherer Konnektivität stabilere Materialien erhalten werden. Die Strukturen der resultierenden Verbindungen sollten mittels Einkristallröntgendiffraktometrie bzw. Rietveldmethode bestimmt werden. Anschließend sollten die katalytische Aktivität sowie die Adsorptionsfähigkeit untersucht werden.

Im zweiten Teil sollten neue bifunktionelle Liganden mit der Kombination aus Pyrazolat- und Phosphonat-Gruppen eingebaut werden. Diese Liganden sollten im Anschluss zur Herstellung neuer hochstabiler metall-organischer Gerüstverbindungen eingesetzt werden. Von besonderem Interesse hierbei ist, dass sich durch den Einsatz eines bifunktionellen Pyrazolat-Phosphonat-Liganden, sowohl mono- als auch bimetallische Komplexe ergeben können. Pyrazolat-funktionalisierte Gruppen weisen nach dem HSAB-Konzept eine Affinität zu weicheren Metallionen (z.B. Cu^{2+}, Zn^{2+}) auf, während die O-Donoren von Phosphonat-Gruppen eine Affinität zu harten Metallionen (z.B. Fe^{3+}, Zr^{4+}) besitzen. Dies könnte eine gezielte Hinführung zu einem bimetallischen System (*mixed-metal* MOFs) ermöglichen.

3. Kumulativer Teil

Das folgende Kapitel beinhaltet die Ergebnisse dieser Dissertation, die in Form von Veröffentlichungen in internationalen Journalen publiziert beziehungsweise eingereicht wurden.

Für die Publikationen als Co-Autor ist jeweils nur eine kurze Zusammenfassung und Beschreibung des Beitrags zu der Veröffentlichung aufgeführt.

Zu den Erstautor-Publikationen ist jeweils eine kurze Zusammenfassung gegeben, welche die Relevanz der Arbeit im Rahmen dieser Dissertation einordnet. Darüber hinaus wurde der eigene Beitrag zur Veröffentlichung dargestellt. Die Publikationen werden so präsentiert, wie sie im jeweiligen Journal ersichtlich sind. Sie sind mit eigenen Nummerierungen, Abbildungen, Schemata, Tabellen und Literaturverzeichnis versehen, welche nicht den Reihenfolgen im restlichen Teil dieser Dissertation entsprechen.

3.1. More versatility than thought: large {Zr_{26}} oxocarboxylate cluster by corner-sharing of standard octahedral subunits

Bahareh Nateghi, Ishtvan Boldog, Konstiantyn V. Domasevitch, Christoph Janiak

CrystEngComm, **2018**, *20*, 5132–5136.

DOI: 10.1039/C8CE01064A

Zr_{26}-Oxo-Carboxylat-Cluster wurde durch solvothermale Umsetzung von $ZrOCl_2$ in DMF/HCOOH synthetisiert, welcher einen größeren Zr-Cluster aufweist, wie in der bisherigen Literatur bekannt ist. Die mittels Röntgeneinkristalldiffraktometrie aufgeklärte Struktur entspricht der idealisierten Zusammensetzung $[Zr_{26}O_{18}(OH)_{30}(HCOO)_{38}]\cdot 5(HCOOH)\cdot kH_2O$, ($k$ = 2–10). Davor wurde 2017 {Zr_{18}},[77] $[Zr_{18}O_{21}(OH)_2(RCOO)_{28}]$ als größter Zr-Oxocluster berichtet. Das Feld der M(IV)-Oxocluster ist benachbart mit dem Gebiet der klassischen Polyoxometallate, kurz POMs, mit der generellen Formel $[X_xM_aO_b]^-$.[75] Hierbei sind Atome M frühe Übergangsmetalle, wie Vanadium, Niob, Tantal, Molybdan oder Wolfram in ihren hohen bzw. höchsten Oxidationsstufen ($M^{IV, V, VI}$), damit die hohe negative Ladung der Oxo-Anionen im Cluster kompensiert werden kann. Als weitere wichtigen Beispiele im Bereich von MOF-SBUs können $M_3OX(RCOO)_6$ (M (III) = Fe, Cr, V, Al, In; X = OH, F) und $Zn_4O(RCOO)_6$ genannt werden, die sich ebenfalls in der Nachbarschaft der M(IV)-Oxocluster befinden.[12] Die bekannten Zr-Oxocluster sind typischerweise klein, auch die größten fullerenartigen {Ti_{42}} und {Ti_{52}}, die kürzlich vorgestellt wurden.[77] Zr-Oxocluster lassen sich in folgenden Haupttypen unterteilen: der dreieckige {Zr_3} ~ ({Zr_6})$_{1/2}$-,[78] der parallelogrammförmige {Zr_4}-,[79] der unvollständige oktaedrische {Zr_5} ~ {$Zr_{(6-1)}$}-,[83] der archetypische oktaedrische {Zr_6}-,[81] der kubische {Zr_8}-,[82] der {Zr_9} ~ {$Zr_{(6-1+4)}$}-,[83] der {Zr_{10}} ~ {$Zr_{(6+4)}$}-,[77] der pseudo-{Zr_{12}} ~ {Zr_6}$(COO)_4${Zr_6}-, der instabile kubische {Zr_{13}}-[84] sowie der größte {Zr_{18}}-[77] Cluster. Für die Beschreibung all dieser Cluster ist der oktaedrische {Zr_6}-Cluster mit dem invariabelen {Zr_6 (μ_3-O/OH)$_8$}-Kern von besonderer Bedeutung. Aus diesem Grund wurden auch große Aggregate mit Hilfe der archetypischen Zr_6-Cluster als Standardbaustein beschrieben, deren Ecken, Kanten oder Flächen geteilt sind. In Folgearbeiten könnte der neue {Zr_{26}}-Cluster als sekundäre Baueinheit zur Synthese von porösen Koordinationspolymeren eingesetzt werden. Dies könnte durch etablierte Methoden zum Ligandenaustausch unter milden Bedingungen eingeführt werden. Die Tatsache, dass solche Strukturen noch nicht beschrieben wurden, könnte durch ihre geringe Löslichkeit und damit Unzugänglichkeit von Einkristallen erklärt werden. Durch Einsatz des supramolekularen Clusters in organisch-anorganischen Hybridmaterialien könnte eine permanente Porosität sowohl bei frisch-synthetisierten als auch bei thermisch behandelten Proben erzeugt werden.

Anteile an der Veröffentlichung:

- Synthese des Zr_{26}-oxocarboxylat-Cluster, vollständige Charakterisierung (P-XRD, Sorptionsmessungen, IR, TGA, ESI, MALDI, CHN-Analyse) sowie Auswertung und Darstellung der Ergebnisse.
- Die Unterstützung bei der Einkristallröntgenanalyse erfolgte durch Herrn Dr. Konstiantyn V. Domasevitch
- Das Lösen der Einkristallstruktur erfolgte durch Herrn Dr. Konstiantyn V. Domasevitch und Herrn Dr. Ishtvan Boldog.
- Kommunikation und finale Abstimmung der experimentellen Ergebnisse mit den externen Kooperationspartnern Herrn Dr. Ishtvan Boldog.
- Kontinuierliche Überarbeitung des Manuskripts.
- Die Einreichung in dem inernationalen Journal **"***CrystEngComm***"** und finale Abstimmung des Manuskripts erfolgte in Zusammenarbeit mit Herrn Dr. Ishtvan Boldog.
- Korrekturen erfolgten in Zusammenarbeit mit Herrn Prof. Dr. Christoph Janiak und Herrn Dr. Ishtvan Boldog.

CrystEngComm

COMMUNICATION

View Article Online
View Journal | View Issue

Cite this: *CrystEngComm*, 2018, **20**, 5132

Received 28th June 2018,
Accepted 15th August 2018

DOI: 10.1039/c8ce01064a

rsc.li/crystengcomm

More versatility than thought: large $\{Zr_{26}\}$ oxocarboxylate cluster by corner-sharing of standard octahedral subunits†

Bahareh Nateghi, [a] Ishtvan Boldog, *[a]
Konstiantyn V. Domasevitch [b] and Christoph Janiak *[a]

The largest known zirconium cluster with an idealized formula of $[Zr_{26}O_{18}(OH)_{30}(HCOO)_{38}]$ was obtained *via* solvolysis of $ZrOCl_2$ in DMF/HCOOH. The observed $\bigcup_5\{Zr_6\}$ structural organization suggests generalization, with an outlook for even larger clusters promising in the context of organo–inorganic composites and porous materials including MOFs.

M(IV)-oxo/(hydroxo,alcoxo)-carboxylates, $M_aO_b(OH/OR)_c(RCOO)_d$ (M = Ti, Zr, Hf), together with other rarer anion analogues, *e.g.* phosphonates,[1] are a relatively small class of compounds,[2] further referred to as M(IV)-oxoclusters, which have recently attracted a surge of interest as building blocks for materials chemistry. These compounds typically form under controlled hydrolysis of $M(OR)_4$ species and hence they are traditionally associated with sol–gel chemistry. The organic moiety bearing an alkene functionality could be cross-linked during polymerization, yielding polymers with altered mechanical properties and increased chemical stability.[2,3] However, the strongest developmental impetus came recently from the area of promising Zr metal–organic frameworks (MOFs/PCPs)[4] with especial importance of the octahedral $\{Zr_6\}$ cluster as a secondary building-unit (SBU).

The field of M(IV)-oxoclusters neighbors the field of the classical polyoxometalates (POMs; $X_xM_aO_b^-$ ($m > x$, $x \geq 0$), M(V, VI) = V, Mo, W, Nb, Ta; X – another element or anion),[5] as well as $M(II, III)_aO_b(OH/OR)_c(OOCR)_d$ compounds of primarily 3d metals including some single molecular magnets, like the paradigmatic $[Mn_{12}O_{12}(OAc)_{16}(H_2O)_4]\cdot 2AcOH\cdot 4H_2O$,[6] antiferromagnetic 'ferric wheels' like $[Fe(III)(OCH_3)_2(O_2CCH_2Cl)]_{10}$,[7] and important MOF-SBUs such as $M_3OX(RCOO)_6$ (M(III) = Fe, Cr, V, Al, In; X = OH, F) and $Zn_4O(RCOO)_6$ (for similar MOF-SBUs see also ref. 8). It is also worth mentioning the loose structural analogies with halogenido-bridged clusters like $[M_6Hal_{12}]^{n+}$ of low valent (~2) Zr (ref. 9 and 10) as well as the principal closeness to polymeric metal-oxide compounds, primarily zeolites and analogies with POM chemistry, where polymeric objects like POMzites are also targeted.[11] These neighboring areas attracted surges of interest fueled by their magnetic and/or catalytic properties as well as porosity in the case of polymeric species.

The area of classical POMs is the oldest field and closest to M(IV)-oxoclusters. The larger oxygen/metal ratio allows POMs without dedicated counter-cations, while in the latter case capping ligands are mandatory to prevent further aggregation. POMs are often highly complex and the majority of large structures in inorganic structure databases are represented by them. While the complexity reaches maximum in the case of Mo with the famous gigantic $\{Mo_{368}\}$ cluster (notably, Mo-POMs obtained under non-reductive conditions are much smaller, ≤57 Mo atoms[12]), POMs consisting of more than 20 metal atoms are considered large and relatively rare for other metals.[13]

The known Zr-oxoclusters are typically small in size, even compared to the largest fullerene-like $\{Ti_{42}\}$[14] and elongated $\{Ti_{52}\} \sim \sum\{Ti_6\}$,[15] both reported recently. The main types are: the triangular $\{Zr_3\} \sim (\{Zr_6\})_{1/2}$ cluster additionally supported by cyclopentadienyl ligands,[16] the parallelogram-shaped $\{Zr_4\}$,[17] the incomplete-octahedral $\{Zr_5\} \sim \{Zr_{(6-1)}\}$,[18] the archetypal 'standard' octahedral $\{Zr_6\}$ (Fig. 1) and the alternative non-octahedral $\{Zr_6\}$,[19] the cubic $\{Zr_8\}$ known only as a part of an **ftw** MOF framework,[20] the $\{Zr_9\} \sim \{Zr_{(6-1+4)}\}$[21] and $\{Zr_{10}\} \sim \{Zr_{(6+4)}\}$[21] clusters both related to the archetypal octahedral cluster, the pseudo-$\{Zr_{12}\} \sim \{Zr_6\}(COO)_4\{Zr_6\}$, the unstable expanded cubic $\{Zr_{13}\}$[22] and the largest $\{Zr_{18}\}$ cluster also, even if not straightforwardly, interpretable as an expansion of the $\{Zr_6\}$ cluster.[23] The standard $\{Zr_6\}$ with the invariable $\{Zr_6(\mu_3\text{-}O/OH)_8\}$ core has the highest importance,

[a] *Institute of Inorganic Chemistry and Structural Chemistry, Heinrich-Heine-Universität Düsseldorf, Universitätsstr. 1, D-40225 Düsseldorf, Germany. E-mail: ishtvan.boldog@gmail.com, janiak@uni-duesseldorf.de*
[b] *Inorganic Chemistry Department, Taras Shevchenko National University of Kiev, Vladimirskaya Street 64, Kiev 01033, Ukraine*

† Electronic supplementary information (ESI) available: Additional notes concerning the synthesis, detailed description of solution and refinement of the single crystal XRD structure, PXRD pattern, TG-DTA, and IR spectra. CCDC 1852050. For ESI and crystallographic data in CIF or other electronic format see DOI: 10.1039/c8ce01064a

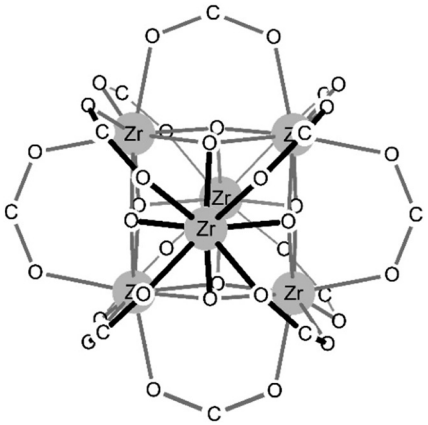

Fig. 1 The prototypal $\{Zr_6(\mu_3\text{-}O)_4(\mu_3\text{-}OH)_4(RCOO)_{12}\}$ cluster. The μ_3-O/OH ligands share the same sites.

and the other clusters could be often viewed as its derivatives, which are either incomplete forms or expansions. The octahedral $\{Zr_6\}$ (Fig. 1) is more dense compared to the well-known Lindqvist POM, $[M_6O_{19}]^{n-}$ (M = Nb(v), Ta(v), Mo(vi), W(vi)), as the former possesses no central oxygen atom and features μ_3- instead of μ_2-(O/OH) ligands as well as demands stabilizing edge-capping carboxylates, residing at the vertices of a cuboctahedron. The carboxylate-complete $\{Zr_6\}$ cluster is primarily the SBU in very numerous UiO-66 type compounds, while carboxylate-incomplete versions sustain the absolute majority of other known Zr-MOFs. The high predictability of the $\{Zr_6\}$ cluster formation in DMF-based solvent mixtures, also tolerating significant amounts of water,[24] plays an important role in the rational design of MOFs. Systematic exceptions are rare: the MOF-140 type isoreticular series[25] with 1D chain SBUs is the single most important among them. Facile ligand exchange on the surface of the clusters[26] allows deep post-synthetic modifications and functionalization of Zr-MOFs,[27] while the presence of coordinatively unsaturated Lewis acidic sites and the possibility to generate defects *via* elimination of the carboxylato ligands are interesting for catalysis.

Clusters other than $\{Zr_6\}$ are usually obtained by controlled hydrolysis in non-aqueous, primarily alcoholic, medium. This method is also used for the preparation of $\{Zr_{18}\}$,[23] $[Zr_{18}O_{21}(OH)_2(RCOO)_{28}]$, the largest known true molecular Zr-oxocluster to the best of our knowledge (the non-individual $\{Zr_{24}\}$ cluster, stabilized by capping lacunary POM germanovanadates, is also worth mentioning as the largest structurally characterized finite Zr-oxocluster[28]). However, it is conceivable, even if not straightforwardly, that the archetypal $\{Zr_6\}$ cluster might itself be a building block for larger aggregates by vertex, edge or face sharing, to some extent similar to the role of $\{Mo_8\}$ in giant polyoxomolybdates.[13] In this contribution we report the synthesis and structural characterization of the largest known individual Zr-cluster, $\{Zr_{26}\}$, built precisely on this principle.

Attempted synthesis of a $\{Zr_6\}$ cluster-based PCP using ((adamantane-1,3-diyl)-diphen-4-yl)dicarboxylic acid (Scheme S1†) in *N*,*N*-dimethylformamide at 130 °C did not yield well crystallized products, seemingly because the angular ligand was not compatible with the suitable periodic structure based on the $\{Zr_6\}$-cluster. Optimization studies were performed focusing primarily on the nature and concentration of the modulator. The use of a high concentration of formic acid led to the formation of very small needle-like single crystals of **1**,‡ and the product turned out to incorporate no significant amounts of the adamantane ligand, which was confirmed by ^{1}H NMR (Fig. S10†) of a digested sample and the IR spectrum (Fig. S9†). Repeated experiments showed that **1** could be produced also without the presence of the adamantane ligand. Even if the size of the single-crystals was slightly smaller, the phase purity according to powder XRD (Fig. S6†) was generally satisfactory. Scaling-up was successful on ~1 g quantity (see also the ESI†).

According to the single crystal X-ray diffraction studies (SCXRD) of **1**,§ the product consists of molecular $\{Zr_{26}\}$ clusters (Fig. 2a), one per unit cell situated on the inversion

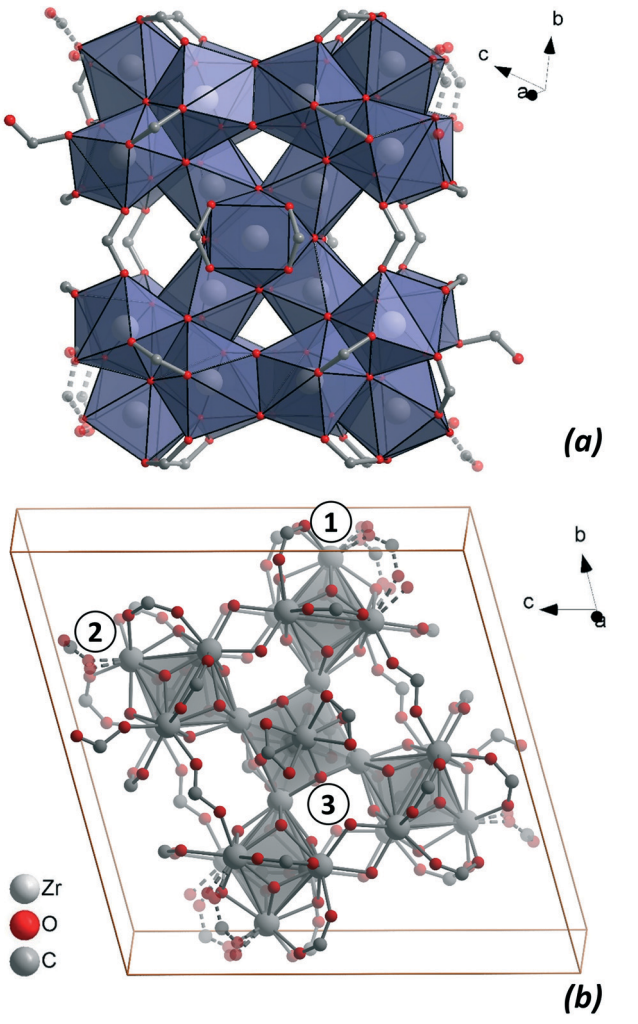

Fig. 2 The structure of **1**; the guest molecules and hydrogen atoms are not shown for clarity. (a) Classic polyhedral representation at the level of the $\{ZrO_8\}$ units with a near square-antiprismatic shape and (b) representation at the level of the $\{Zr_6\}$ subunits, shown as octahedra.

center of the $P\bar{1}$ space group (Fig. 2b). The idealized molecular formula of the cluster, with an assumed complete carboxylate environment, is $[Zr_{26}O_{18}(OH)_{30}(HCOO)_{38}]\cdot 5(HCOOH)\cdot kH_2O$, **1-id** ($k$ = 2–10, **id** stands for idealized). The experimental crystal structure evidences that some of the bridging carboxylate ligands are defected by site sharing with water molecules and the actual formula of the compound is $[Zr_{26}O_{21}(OH)_{27}(HCOO)_{35}(H_2O)_5]\cdot 5HCOOH\cdot kH_2O$, **1** (the description of those imperfections is given below; see also the ESI†).

The asymmetric unit, which effectively constitutes half of the molecule, could be viewed as composed of three parts, associated with the formal $\{Zr_6\}$-subunits (Fig. 3). The crystallographically independent 'corner' sub-units are the $\{[Zr_6(\mu_3\text{-}O)_4(\mu_3\text{-}OH)_4(\mu\text{-}HCOO)_{7-\delta}(H_2O)_{2\delta}\}$ (Fig. 3.1) and $\{Zr_6(\mu_3\text{-}O)_4(\mu_3\text{-}OH)_4(\mu\text{-}HCOO)_6(HCOO)_{2-\delta'}(H_2O)_{n+\delta'}]\}$ (Fig. 3.2) fragments (the delta values, δ = 0.6 + 0.4 and δ' = 0.5, are associated with structural disorder, as explained below). Together with the inversion symmetry equivalents, four $\{Zr_6\}$ 'corner' sub-units form a ring, the outer rim of which is reinforced by two sets of inter-subunit 4 × μ-(OH^-) and 2 × μ-($HCOO^-$) bridges. The inner four zirconium atoms are 'capped' by two symmetry related $\{Zr(O)_{1+\delta''}/(OH)_{3-\delta''}(\mu\text{-}HCOO)_2\}$ ($\delta'' = \delta + \delta' = 1.5$) fragments formally completing a fifth central $\{Zr_6\}$ sub-unit, whose four equatorial vertices are shared with the 'corner' sub-units. Hence the structure could be interpreted as a $\{4 \times \{Zr_6\} + 2Zr\} \sim \{Zr_{4\times6+2}\}$ cluster or as a $\bigcup_5\{Zr_6\}$ vertex shared union.¶ Doubling the sum of the symmetry-independent fragments yields the molecular formula, in which the ligands are distinguished also by the coordination mode, $[Zr_{26}(\mu_3\text{-}O)_{18+m+n}(\mu_3\text{-}OH)_{22-m-n}(\mu\text{-}OH)_8(\mu\text{-}HCOO\text{-}\kappa^2O{:}O')_{26-m}(HCOO\text{-}\kappa^2O{:}O')_4(HCOO\text{-}\kappa O)_{8-n}(H_2O)_{2m+n}]\cdot 5HCOOH\cdot kH_2O$, where m = 2 and n = 1 are the total number of 'defected' bridging and terminal carboxylates, respectively (*i.e.* $m = 2\delta$ and $n = 2\delta'$), site-sharing with aqua ligands, as established by SCXRD. The simplified systematic name of the idealized, carboxylate-complete composition of **1** is, accordingly, octadeca(μ_3-oxo)doicosa(μ_3-hydroxo)octa(μ-hydroxo)hexaicosa(μ-formato-$\kappa^2O{:}O'$)tetra(μ-formato-$\kappa^2O{:}O'$)-octa(formato-κO)hexaicosazirconium, solvated with formic acid and water.

The μ_3-(O^{2-}) and μ_3-(OH^-) ligands are precisely identifiable only for the corner $\{Zr_6\}$-subunits, d(Zr–O) < 2.12 Å and > 2.20 Å respectively, while for the central subunit they are evidently site-sharing, with average d(Zr–O) ~2.15 Å (Fig. 3; see also the ESI,† chapt. 2 for the detailed discussion). The actual 5 : 3 ratio is defined by electroneutrality and hence, the number of possible 'defected' sites, associated with the loss of formates, might be variable and potentially dependent on the method of crystallization. The electroneutrality could be reinstated by deprotonation of the hydroxo-ligands, which occurs in the central subunit (it is worth noting that the fine structural observations, discussed further in the ESI,† suggest a tendency to maintain the ratio of μ_3-(O^{2-}) and μ_3-(OH^-) close to unity in average also in the central subunit, which would be reached at $\delta'' = 1$ or $m + n = 2$). Whether the observed structural 'disorder' is correlated, *i.e.* some of the formates are missing in each and every molecule, or it is rather statistic and additionally dependent on the conditions of preparation is an open question. This makes the descriptive approach based on the idealized formate-complete version the most purposeful (the attempted ESI and TOF MALDI MS studies of **1** were expectedly not successful due to the instability of such heavy clusters under the measurement conditions).

The molecular packing of **1** is remarkably loose, with 31.7% solvent accessible residual space, or 1180 Å^3 per formula unit.[29] The vdW dimensions of the channels are ~8 × 3+ Å for the structure with excluded guest molecules (Fig. S5b;† the calculated[30] 'maximal free sphere' diameter, which could pass freely, is 3.8 Å). The SCXRD data establish five formic acid molecules in the areas of the structure, where the

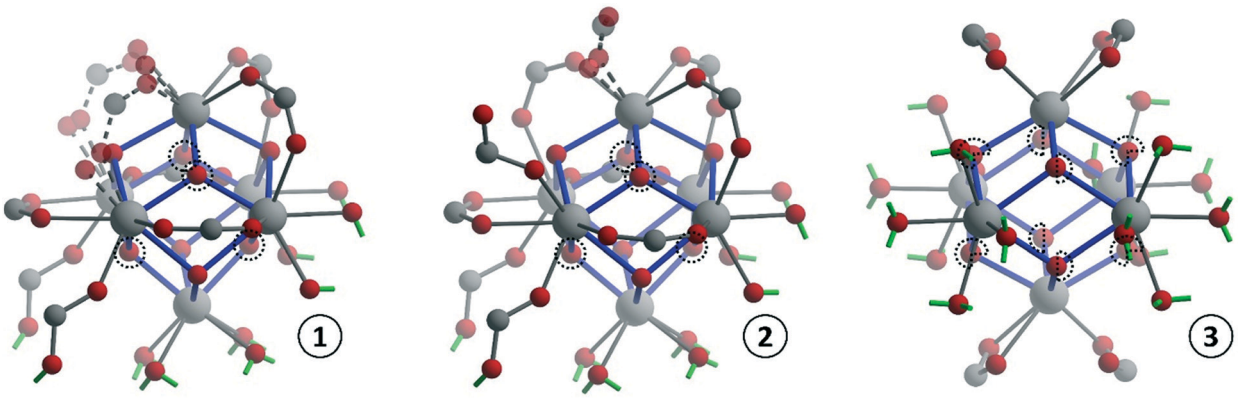

Fig. 3 The corner-sharing $\{Zr_6\}$ subunits of the Zr_{26}-cluster, **1**. The numbers correspond to the parts shown in Fig. 2b. The Zr–μ_3-O/OH bonds are given in blue and the broken-off 'dangling' bonds in green (note that redundant duplicates are shown for clarity, as the inter-subunit OH and HCOO bridges and the corner-sharing Zr atoms together with their immediate environment in subunit 3). The O^{2-} sites are outlined by dashed circles or their fragments, 0.75 or 0.5, indicating their share in mixed O^{2-}/OH^- sites. The site-sharing ligands are depicted semi-transparent, with dashed bonding. Hydrogen atoms are not shown for clarity.

clusters are near each other and the guest molecules participate in multiple H-bonded contacts (Fig. S5a†), and no molecular fragments, which could be associated with DMF, are found (the absence of the latter is confirmed by ^{1}H NMR of a digested sample). The 20.9% solvent accessible space and the analysis of the residual electronic density in the pores suggest the presence of k = ~10 additional guest water molecules.

The crystallosolvate of **1** quickly loses solvent in air and the precise solvent amount depends on the preparation of the sample. The elemental analysis on a fresh, only moderately dried sample is consistent with a content of 5 formic acid molecules, k = ~10 water and 7 DMF molecules per formula unit, with the latter evidently being surface adsorbed solvent molecules (which is also confirmed by the IR spectrum of a dried sample, Fig. S9†). The thermogravimetric analysis on a sample, dried until permanent weight, could be interpreted as consistent with k = ~2 (see Fig. S7 and 8 and the related discussion in the ESI†).

The powder XRD pattern demonstrated good coincidence of peak positions in the experimental and simulated patterns (Fig. S6†), provided that the measurement was performed on a freshly synthesized sample soaked with the mother liquor. Even short drying causes noticeable changes in the PXRD, however without complete loss of crystallinity.

The potential intrinsic porosity[31] of the {Zr_{26}} cluster-based solids is a question, which evidently posed itself upon examination of the structure. Supercritical CO_2 drying with subsequent degassing at 190 °C, which was established as close to optimal (see the ESI†), yielded a solid with S_{BET} = ~146 m^2 g^{-1}. The adsorption isotherm (Fig. S11†) features an H2-type hysteresis, which is characteristic of mesoporous solids with 'ink-bottle' pores. The activated material adsorbs 0.55 mmol g^{-1} CO_2 at 273 K and 0.25% wt H_2 at 1 bar and 77 K, which are close to the expected values for the given surface area (see the ESI†). The observed surface area is reasonably high for a material with intrinsic, *i.e.* non-framework, porosity as a significant part of the micropore openings should not be permeable to nitrogen after imminent structure collapse during activation of a molecular solid. The observation of measurable surface area suggests enhancements for derived materials, where the {Zr_{26}} molecules/moieties are kept further apart, preferably by the use of coordination bonded linkers.

Conclusions

In conclusion, the observation of **1**, arguably the largest Zr_{26} zirconium carboxylate cluster known to date, suggests the existence of even larger clusters, possibly similar aggregates of the 'standard' {Zr_6} octahedral cluster. The new 'superclusters' might serve as secondary building units in porous coordination polymers, introduced *via* established methods of ligand exchange under mild conditions. The fact that such structures are not yet reported might be explained by their low solubility and hence inaccessibility of single crystals (the success of this report also crucially relied on the use of the most modern state-of-the-art diffractometer). Despite the large clusters, which could be quite labile, being tough objects for investigation, they are definitely interesting targets. The putative poly-{Zr_6} compounds together with the derived supramolecular structures and organo–inorganic composites have potential to demonstrate permanent porosity either in the as-synthesized or in the partially condensed form as a result of thermal treatment. This includes the possibility of thorough calcination yielding porous zirconium oxides, which are valued as catalyst supports.

Conflicts of interest

There are no conflicts to declare.

Notes and references

‡ A solution of 42.5 mg (132 μmol) of $ZrOCl_2{\cdot}8H_2O$ and 12.4 mg (33 μmol) of ((adamantane-1,3-diyl)-diphen-4-yl) dicarboxylic acid (an optional additive, which slightly improves the crystallinity of the product) in a mixture of 7.28 ml DMF and 4.56 ml of formic acid was heated at 140 °C for 4 days. The formed needle-like crystals were filtered off, washed with DMF and dried in air until constant weight. Yield: 16 mg (14%).

§ Selected crystal data for **1**: $C_{43}H_{82}O_{133}Zr_{26}$, FW = 5062.8, triclinic, $P\bar{1}$, a = 11.4132(8) Å, b = 18.7392(12) Å, c = 19.1989(11) Å, α = 71.434(5)°, β = 73.347(5)°, γ = 81.818(5)°, V = 3723.3(4) Å^3, ρ = 2.258, Z = 1, $R_1[F^2 > 2\sigma(F^2)]$ = 0.0561, wR_2 (all data) = 0.1625. CCDC reference number is 1852050.

¶ U$_i$ {*unit*} designates the *union* of i units in terms of set theory, *i.e.* the joint of units with possible common fragments. The designation is efficient for description of large clusters by referring to characteristic fragments.

1 M. Czakler and U. Schubert, *Monatsh. Chem.*, 2015, **146**, 1371–1374.
2 S. Gross, *J. Mater. Chem.*, 2011, **21**, 15853.
3 M. Carraro and S. Gross, *Materials*, 2014, **7**, 3956–3989.
4 Y. Bai, Y. Dou, L.-H. Xie, W. Rutledge, J.-R. Li and H.-C. Zhou, *Chem. Soc. Rev.*, 2016, **45**, 2327–2367.
5 M. T. Pope, in *Encyclopedia of Inorganic and Bioinorganic Chemistry*, John Wiley & Sons, Ltd, Chichester, UK, 2011, pp. 1–11.
6 D. G. R. S. J. Villain, D. Gatteschi, R. Sessoli, J. Villain and K. Firm, *Molecular Nanomagnets*, OUP Oxford, 2006.
7 K. L. Taft, C. D. Delfs, G. C. Papaefthymiou, S. Foner, D. Gatteschi and S. J. Lippard, *J. Am. Chem. Soc.*, 1994, **116**, 823–832.
8 D. J. Tranchemontagne, J. L. Mendoza-Cortés, M. O'Keeffe and O. M. Yaghi, *Chem. Soc. Rev.*, 2009, **38**, 1257–1283.
9 R. P. Ziebarth and J. D. Corbett, *J. Am. Chem. Soc.*, 1985, **107**, 4571–4573.
10 C. E. Runyan and T. Hughbanks, *J. Am. Chem. Soc.*, 1994, **116**, 7909–7910.
11 L. Vilà-Nadal and L. Cronin, *Nat. Rev. Mater.*, 2017, **2**, 17054.
12 A. Müller and S. Roy, *Coord. Chem. Rev.*, 2003, **245**, 153–166.
13 A. Müller, F. Peters, M. T. Pope and D. Gatteschi, *Chem. Rev.*, 1998, **98**, 239–272.

14 M.-Y. Gao, F. Wang, Z.-G. Gu, D.-X. Zhang, L. Zhang and J. Zhang, *J. Am. Chem. Soc.*, 2016, **138**, 2556–2559.
15 W.-H. Fang, L. Zhang and J. Zhang, *J. Am. Chem. Soc.*, 2016, **138**, 7480–7483.
16 U. Thewalt, K. Döppert and W. Lasser, *J. Organomet. Chem.*, 1986, **308**, 303–309.
17 G. Kickelbick and U. Schubert, *Chem. Ber.*, 1997, **130**, 473–478.
18 G. Kickelbick, D. Holzinger, C. Brick, G. Trimmel and E. Moons, *Chem. Mater.*, 2002, **14**, 4382–4389.
19 G. Kickelbick and U. Schubert, *J. Chem. Soc., Dalton Trans.*, 1999, 1301–1306.
20 D. Feng, H.-L. Jiang, Y.-P. Chen, Z.-Y. Gu, Z. Wei and H.-C. Zhou, *Inorg. Chem.*, 2013, **52**, 12661–12667.
21 C. Artner, M. Czakler and U. Schubert, *Inorg. Chim. Acta*, 2015, **432**, 208–212.
22 B. Morosin, *Acta Crystallogr., Sect. B: Struct. Crystallogr. Cryst. Chem.*, 1977, **33**, 303–305.
23 T. Xu, X. Hou, Y. Wang, J. Zhang, J. Zhang and B. Liu, *Dalton Trans.*, 2017, **46**, 10185–10188.
24 H. Reinsch, B. Bueken, F. Vermoortele, I. Stassen, A. Lieb, K.-P. Lillerud and D. De Vos, *CrystEngComm*, 2015, **17**, 4070–4074.
25 V. Guillerm, F. Ragon, M. Dan-Hardi, T. Devic, M. Vishnuvarthan, B. Campo, A. Vimont, G. Clet, Q. Yang, G. Maurin, G. Férey, A. Vittadini, S. Gross and C. Serre, *Angew. Chem*, 2012, **124**, 9401–9405.
26 P. Walther, M. Puchberger, F. R. Kogler, K. Schwarz and U. Schubert, *Phys. Chem. Chem. Phys.*, 2009, **11**, 3640.
27 S. M. Cohen, *Chem. Rev.*, 2012, **112**, 970–1000.
28 L. Huang, S. Wang, J. Zhao, L. Cheng and G. Yang, *J. Am. Chem. Soc.*, 2014, **136**, 7637–7642.
29 A. L. Spek, *Acta Crystallogr., Sect. C: Struct. Chem.*, 2015, **71**, 9–18.
30 T. F. Willems, C. H. Rycroft, M. Kazi, J. C. Meza and M. Haranczyk, *Microporous Mesoporous Mater.*, 2012, **149**, 134–141.
31 N. B. McKeown, *ISRN Mater. Sci.*, 2012, **2012**, 1–16.

Supplementary Information

More versatility than thought: large {Zr_{26}} oxocarboxylate cluster by corner-sharing of standard octahedral subunits

Bahareh Nateghi,[a] Ishtvan Boldog,*[a] Konstantin V. Domasevitch,[b] Christoph Janiak*[a]

[a] Institute of Inorganic Chemistry and Structural Chemistry, Heinrich-Heine-Universität Düsseldorf, Universitätsstr. 1, D-40225 Düsseldorf, Germany. E-mail: ishtvan.boldog@gmail.com, janiak@uni-duesseldorf.de
[b] Inorganic Chemistry Department, Taras Shevchenko National University of Kiev, Vladimirskaya Street 64, Kiev 01033, Ukraine

E-mail: ishtvan.boldog@gmail.com, janiak@uni-duesseldorf.de

Contents

1. Synthesis

Materials. $ZrOCl_2 \cdot 8H_2O$ (99%, Sigma-Aldrich), N,N-dimethylformamide (DMF; 99.8%, Sigma-Aldrich), formic acid (99%, Sigma-Aldrich), deionized water. The ((adamantane-1,3-diyl)-diphen-4-yl) dicarboxylic acid (H_2L) was synthesized according to the literature [1].

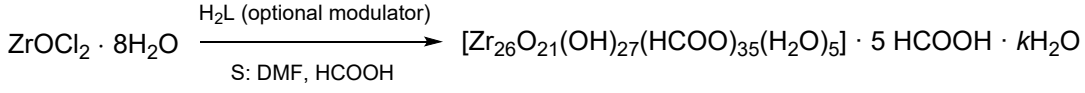

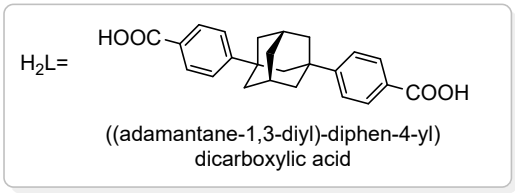

Scheme. S1.

Synthesis of **1**: 42.5 mg (132 μmol) of $ZrOCl_2 \cdot 8H_2O$ were dissolved in 7.28 ml DMF after prolonged shaking until formation of a clear solution with, possibly, a very small amount of insoluble residues (Scheme 1). Addition and dissolution of 12.4 mg (33 μmol) of H_2L was followed. Finally, 4.56 mL (121 μmol) of formic acid was added. The mixture was thoroughly mixed and sealed in a 20 ml culture tube. The sealed tube was heated for 4 days at 140 °C. The formed white deposit, composed of small needle-like crystals, was filtered off, washed with a few small portions of DMF and left drying in air on a Petri dish until constant weight. Yield of the white microcrystalline material was 16 mg (~14%). The used high dilution was seemingly necessary for sufficient purity and crystallinity of the product (including the suitability of monocrystals for SCXRD). The addition of H_2L seemed to have only one important effect: it increased the single-crystal sizes slightly, which allowed the SCXRD studies. Otherwise, there is no need for its use.

The scaled-up experiments were performed analogously, but without the addition of H_2L, using 5.8× times of the initial quantities in a 250 ml hermetic vessel (Caution! The vessel is pressurized during the synthesis due to partial decomposition of the formic acid. It is advisable to leave a significant overhead space, up to ½ of the flask's volume. Large scale experiments, typically in vessels that has comparably lower pressure resistance, pose more risk compared to the small scale ones). The results of IR, PXRD measurements and the adsorption studies are given for the samples obtained in scaled-up syntheses.

Elemental analysis for $[Zr_{26}O_{21}(OH)_{27}(HCOO)_{35}(H_2O)_5] \cdot 5\ HCOOH \cdot k H_2O \cdot l$DMF:

calcd (%) for $C_{40}H_{86}O_{135}Zr_{26}$ ($k = 2$, $l = 0$; conforms with the TGA): C 9.42, H 1.70

calcd (%) for $C_{40}H_{102}O_{143}Zr_{26}$ ($k = 10$, $l = 0$; conforms with the SCXRD): C 9.16, H 1.96

calcd (%):for $C_{61}H_{151}N_7O_{150}Zr_{26}$ ($k = 10$, $l = 7$; best conformance with the elemental analysis): C 12.73, H 2.64, N 1.70

found (%): C 12.35, H 2.63, N 1.74

Notes. the elemental analysis was performed on sample from a repeated large scale synthesis. The sample for the analysis was not dried to constant weight to avoid the loss of the solvent of crystallization. A small amount of sample was, rather, pressed between filter-papers, then dried for a short time in air, until no aggregation of the particles, characteristic for a wet sample was observed. The sample was then sealed in a hermetic vial and stored in it until the analysis.

The short time drying allowed to avoid significant loss of solvent, but it has the drawback of incomplete removal of the surface adsorbed / interparticle solvent. The result of the analysis witnesses a presence of significant amount of DMF (and, most probably, a commensurate amount of formic acid, however with low impact on elemental analysis data in the latter case). Fortunately, either the analysis of the residual peaks in the pre-SQUEEZEd SCXRD structure (see p. 2) and, especially, the ^{1}H NMR spectrum of a digested sample, which was washed by acetone, shows no significant presence of DMF inside the crystals and hence in was not added to the final formula.

In any case, the results are considered to be satisfactory, given the possible presence of other phases as admixtures (see PXRD) and the relatively low sensitivity of elemental analysis due to low content of organics.

2. Single crystal X-ray diffraction structure determination

The single crystals of **1** could be best described as thin elongated wedge-shaped blocks (Fig. S1). A thin 'blade' end of suitable optical quality was cut-off for the measurement. The diffraction data were collected on a Stoe STADIVARI diffractometer with a Dectris Pilatus 300K detector and with a Cu microfocus source (Cu-Kα, λ = 1.54186 Å) at 180(2) K using a nitrogen gas open-flow cooler Cobra from Oxford Cryosystems. Data reduction and cell refinement were processed using X-Area [2]. Face-indexed numerical absorption correction using X-RED and X-SHAPE [3] was applied. The structure was solved by direct methods and refined by full-matrix least-squares on F^2 using the programs SHELXS-97 and SHELXL-2014/7 [4]. The information regarding data collection and structure refinement is summarized in Table S1.

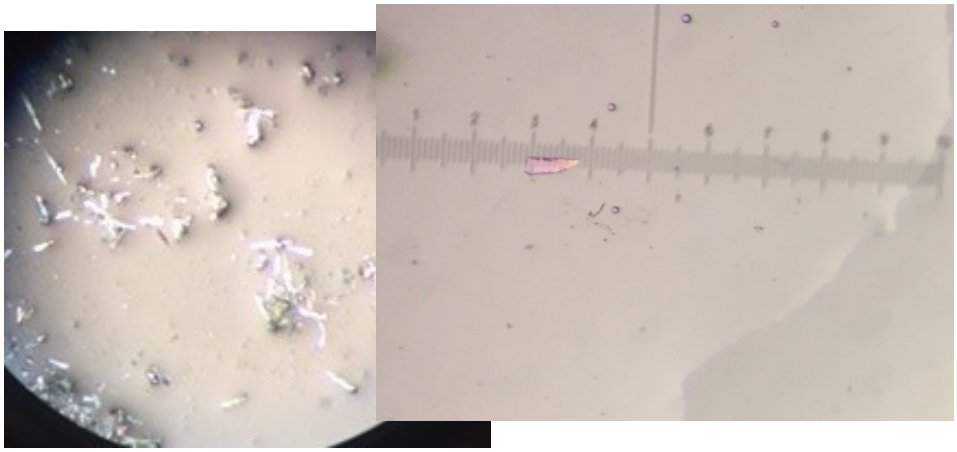

Fig. S1. Micrographs of the crystals of **1**.

Refinement details.

All non-hydrogen atoms belonging to the cluster were refined in anisotropic model, while the atoms of the solvate formic acid molecules in isotropic. The (C)**H** hydrogen atoms of the formates / formic acid molecules were placed geometrically and refined in a riding model, $U_{iso}(H) = 1.2U_{eq}(CH)$. The (O)**H** hydrogen atoms were not placed explicitly (see below).

The structure of the cluster features two major problems: a) the site-sharing of the $H_2O/HCOO^-$ ligands and b) the correct assignment of the μ_3-O^{2-}/μ_3-OH^- ligands.

The first problem becomes evident after careful examination of the atomic thermal motion parameters and residual electron densities, which shows features characteristic for disorder both on the periphery of the cluster and in the solvate regions. Large thermal displacement parameters of the formate ligands referenced further by their C6 and C7 atoms, which are bridging the Zr3, Zr5 and Zr5, Zr4 atoms respectively, and the residual peaks at 2.10-2.21 Å from the Zr ions suggests partial occupancies of the formate groups and presence of two aqua ligands as the second site-sharing components (Fig. S2). The μ-COO^- / $2H_2O$ site-sharing was resolved smoothly with partial occupancies of 0.60 / 0.40 for O35-C6-O36 / (O3w, O4w) components and 0.40 / 0.60 for O37-C7-O38 / (O1w, O2w) ones. A similar monodentate $HCOO^-$ / H_2O site-sharing with 0.5/0.5 ratio of components was observed at the Zr11 ion. Additionally, all the three monodentate formate groups exhibit

disorder of carbon atoms, which were refined with fixed partial occupancies set to make their thermal parameters approximately equal.

The possible μ_3-O^{2-}/μ_3-OH^- site-sharing is expected from the chemical composition and is confirmed by the high anisotropy of the thermal motion for some of the μ_3-O atoms (O17 to O20). Although the positions of the hydrogen atoms belonging to μ-OH were not located, the assignment of the hydroxo- and oxo-ligands within the cluster was possible in view of subtle coordination features. All four unique μ-oxygen atoms (O21 to O24) represents the bridging hydroxo ligands with Zr-O bond length in the range of 2.140(2)-2.199(5) Å and Zr-O-Zr bond angle in the range of 108.4(2)-111.5(2)°. These values perfectly match the corresponding parameters for the similar moieties in the known crystal structure of $[Zr_6(\mu_3\text{-}O)_4(\mu_3\text{-}OH)_4](\mu\text{-}OH)_4[Zr_6(\mu_3\text{-}O)_4(\mu_3\text{-}OH)_4]$, Zr-O 2.159 Å and Zr-O-Zr 111.5°, where the dodecanuclear units are integrated further by dicarboxylate ligands in a polymer [5].

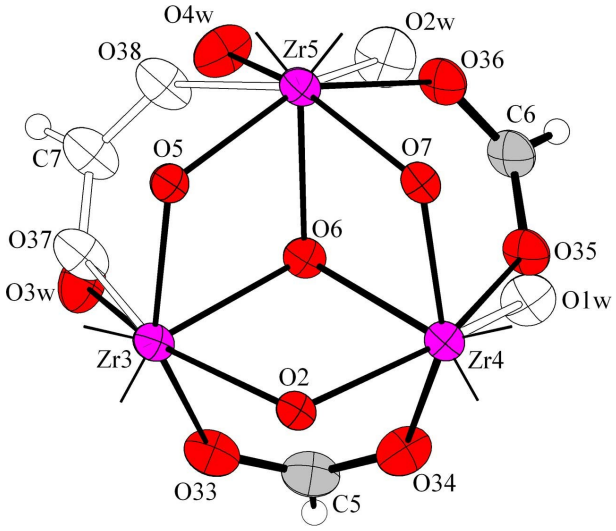

Fig. S2. The site-sharing scheme for the formate and aqua ligands coordinated to the Zr3, Zr4 and Zr5 atoms. The O35-C6-O35 carboxylate in one case and the water molecules represented by the O3w, O4w atoms are the mayor components (0.6 share in both cases). The minor components (O1w, O3w and O37-C7-O38 respectively) are given in white. Thermal ellipsoids are at 35% probability level.

Table S1. Selected geometry parameters involving μ_3-O/OH bridges [a)]

O atom	d(Zr-O)/ Å		∠Zr-O-Zr /°	d(O···plane)/ Å	Assignment
	range	mean	mean		
O2	2.092-2.130	2.106	114.4	0.505(5)	
O4	2.062-2.120	2.086	117.3	0.347(5)	
O5	2.051-2.087	2.069	115.9	0.423(5)	
O7	2.046-2.083	2.062	116.3	0.400(5)	μ_3-O
O10	2.086-2.129	2.103	114.6	0.495(5)	
O12	2.062-2.116	2.084	117.2	0.351(5)	
O13	2.030-2.084	2.053	117.0	0.361(5)	
O15	2.074-2.081	2.076	115.6	0.441(5)	
O1	2.256-2.342	2.292	101.8	1.014(5)	μ_3-OH
O3	2.246-2.347	2.283	102.4	0.996(5)	

O6	2.240-2.269	2.256	101.3	1.016(6)	
O8	2.254-2.304	2.274	101.1	1.028(6)	
O9	2.257-2.351	2.293	101.9	1.013(5)	
O11	2.249-2.314	2.276	102.5	0.988(5)	
O14	2.235-2.316	2.269	100.7	1.036(5)	
O16	2.241-2.284	2.265	101.5	1.014(5)	
O17 × 2	2.034-2.207	2.146	111.0	0.658(7)	μ_3-$O_{0.75}$/$(OH)_{0.25}$
O18 × 2	2.035-2.212	2.147	110.3	0.685(6)	
O19 × 2	2.196-2.236	2.219	106.6	0.838(8)	μ_3-$O_{0.5}$/$(OH)_{0.5}$
O20 × 2	2.176-2.245	2.210	107.3	0.810(7)	

[a] The e.s.d. values for Zr-O bond lengths and Zr-O-Z bond angles are 0.005-0.006 Å and 0.2-0.3°, respectively. The μ_3-O···plane separation is the distance of the O-atom from the plane defined by the three coordinating Zr ions.

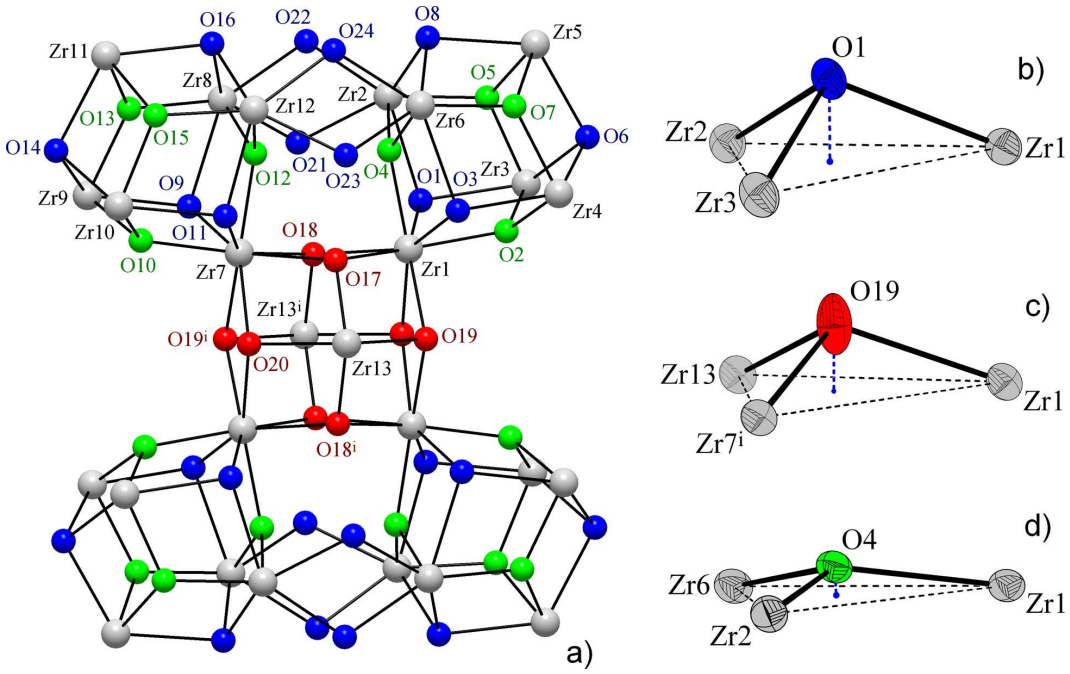

Fig. S3. a) Cluster-scheme featuring only the hydroxo- and oxo- ligands, with O-atoms of μ-OH and μ_3-OH ligands marked in blue, μ_3-O-atoms marked in green, and the averaged oxygen atom positions of the site sharing μ_3-OH / μ_3-O ligands marked in red. b-d) Typical geometries of the {μ_3-O(H)Zr_3} fragments with the same color notations of ligands as in the previous point. The fragments show decrease in the distance between the O-atom to the plane defined by the three coordinating metal ions. Note the high anisotropy of thermal motion of O-atom in the case of μ_3-(OH/O) site sharing [Symmetry code: (i) 1-*x*, 1-*y*, 1-*z*].

For the other twenty unique μ_3-oxygen atoms (O1 to O20), the ranges of median Zr-O bond lengths (i.e. the averages of the three formed bonds), 2.034(5)-2.351(5) Å, and the median Zr-O-Zr bond angles, 99.2(2)-118.0(2)°, are much broader. However, three distinct types of the μ_3-bridges are clearly distinguishable, featuring characteristic bond lengths and angles (Table S1).

Thus, for the group of eight μ_3-O atoms, namely O2, O4, O5, O7, O10, O12, O13, O15, the Zr-O coordination bonds are the shortest (the range of the mean values are 2.030(5)-2.130(5) Å) and the Zr-O-Zr angles exceed 112° (114.4(2)-117.3(3)°), with the distance between the O atom to the plane of the three coordinating Zr ions being as low as 0.347(5)-0.505(5) Å.

Contrarily, the eight μ_3-O atoms, namely O1, O3, O6, O8, O9, O11, O14, O16, adopt longer coordination bonds with average values in the range of 2.235(5)-2.351(5) Å and average bond angles below 105° (100.7(2)-102.5(2)°), while the $\{Zr_3O\}$ fragment deviate further from planar with separation between the O-atoms and the Zr_3 plane being in the range of 0.988(5)-1.036(5) Å.

The differences in average bond length and bonding angles allow the unambiguous assignment of the listed cases to μ_3-O and μ_3-OH ligands respectively. Exactly the same distribution of bond length and angles was reported, e.g. for $[Zr_{12}O_8(OH)_8(CH_3COO)_{24}] \cdot 4CH_3COOH \cdot 2HCOOH \cdot 0.5H_2O$ complex [6]. In the latter, the average Zr-O distances for μ_3-O^{2-} are in the range of 2.047-2.091 Å, the average ∠Zr-O-Zr angles are in 114.4-119.6°, and the O···plane distance is 0.400 Å. The same parameters for μ_3-OH are: the average Zr-O is 2.219-2.374 Å, average ∠Zr-O-Zr is 99.5-105.9°, and O···plane separation is 1.019 Å. Thus, each of the two crystallographically unique $[Zr_6(\mu_3\text{-}O/OH)_8]$ 'corner' fragments of the Zr_{26}-cluster shows an already observed distribution of four μ_3-O and four μ_3-OH bridges, with alternation of the associated Zr_3 faces (Fig. S3).

For the central $[Zr_6(\mu_3\text{-}O/OH)_8]$ fragment the situation is slightly more complicated. This fragment reside on a center of inversion and for all four unique μ_3-O atoms, namely O17, O18, O19, O20, the bonding parameters (Zr-O, ∠Zr-O-Zr, O···plane, See Table S1) are intermediate between the values for the two above cases. This implies site-sharing of μ_3-O and μ_3-OH ligands. Such assignment agrees with the observed anisotropy of the oxygen atoms's ADPs in the direction perpendicular to the respective Zr3 plane of the $\{\mu_3\text{-}OZr_3\}$ fragment (Fig. S3, c). Very similar situation, involving either the apparent average geometry or features of thermal motion, was observed for many examples of $\{Zr_6(\mu_3\text{-}O/OH)_8\}$ carboxylates [7]. In the present case, contributions of μ_3-O and μ_3-OH groups are similarly unequal. Thus, for two symmetry related pairs of O17 and O18 atoms, deviation from the Zr_3 plane (0.658(7) and 0.685(6) Å) is appreciably smaller than for pairs of O19 and O20 atoms (0.838(8) and 0.810(7) Å). The latter pair exhibit also significantly narrower ∠Zr-O-Zr angles and longer Zr-O bond lengths (Table S1). This suggests higher contribution of the μ_3-O component to the site-sharing μ_3-O/OH ligands represented by O17 and O18 atoms. It worth noting that O17 and O18 atoms are involved in very short O17···O23 and O18···O21 intracluster contacts with 2.657(8) Å and 2.651(8) Å length respectively, where the second atom in the pair belongs to the μ-OH ligand (Fig. S3), suggesting strong and highly directional [*i.e.*, ∠ZR8-O21···O18 = 102.0(5)°] intra-cluster hydrogen bonding. The above geometries allows to assign the O19 and O20 atoms to site-sharing μ_3-O/OH ligands with 0.5/0.5 ratio, while for O17, O18 with 0.75/0.25 ratio, together constituting the central $\{Zr_6(\mu_3\text{-}O)_5(\mu_3\text{-}OH)_3(COO)_4\}$ hexanuclear sub-cluster.

This scheme, incorporating 21 oxo and 27 hydroxo bridges in total, describe a neutral Zr_{26} cluster with a formula of $[Zr_{26}(\mu_3\text{-}O)_{21}(\mu_3\text{-}OH)_{19}(\mu\text{-}OH)_8(HCOO)_{35}(H_2O)_5]$ and a structure, which has clear analogues on the level of $\{Zr_6\}$ sub-clusters with known compounds featuring the same fragment.

The highest residual electronic density peaks in the space between the loosely packed Zr_{26} cluster molecules were identified as solvate formic acid molecules. A set of geometry restraints and similarity restraints in the anisotropic thermal motion parameters (ADPs) were employed to improve the refinement stability. Three solvate formic acid molecules were treated

as disordered and refined with partial occupancy factors 0.60/0.40, 0.70/0.30 and 0.50 with fixed molecular geometry. Atoms of these groups were refined isotropically. The remaining electron density peaks in the V = 780 Å^3 per unit cell or 20.9% of the crystal volume were excluded from the refinement by the SQUEEZE/PLATON routine (132 e per unit cell; cf. with the ~31.7% of solvent accessible space calculated for the structure with all the solvent molecules removed from the inter-cluster space) [8, 9].

The final molecular composition is ascribed as a compromise with the TGA study (see below). The ~31.7% solvent accessible volume corresponds to 1180 Å^3 pro unit cell, *i.e.* pro one Zr_{26}-cluster unit. Such volume could host up a few tens of water and formic acid molecules pro formula unit, however a part of it belongs to very narrow pores, not well suited for dense packing of even such a small molecule as water (the molecular volumes of H_2O and HCOOH estimated from the density in the liquid phase are 29.9 and 62.7 Å^3 / molecule respectively). Such high solvent contents were not confirmed, most probably due to partial solvent loss during drying.

The molecular graphics was computed using Diamond 3.2i [10].

Table S2 Crystal data and structure refinement for $[Zr_{26}O_{18}(OH)_{30}(HCOO)_{38}] \cdot 5(HCOOH) \cdot 2H_2O$, **1**.

	1
Empirical formula	$C_{40}H_{82}O_{133}Zr_{26}$
M_r /g mol^{-1}	5062.77
T /K	180(2)
Wavelength / Å	1.54186
Crystal system	Triclinic
Space group	$P\bar{1}$
a /Å	11.4132(8)
b /Å	18.7392(12)
c /Å	19.1989(11)
α /°	71.434(5)
β /°	73.347(5)
γ /°	81.818(5)
V /Å^3	3723.3(4)
Z	1
Calc. density /g cm^{-3}	2.258
μ / mm^{-1}	15.360
F(000)	2426

Crystal size /mm^3	0.04 × 0.02 × 0.02
θ range /°	4.025 to 70.953
Index ranges /*hkl*	[-13, 6]; [-21, 22]; [-23, 23]
Reflections collected (R_{int})	36620 (0.0451)
Independent reflections	14209
Completeness /% to θ /°	99.2 % to 67.69
Data / restraints / parameters	14209 / 168 / 979
Goodness-of-fit	0.981
R[F^2>2σ(F^2)], *wR*2 [a)]	0.0561, 0.1533
*R*1, *wR*2 (all data)	0.0719, 0.1625
Largest diff. peak and hole, eÅ^{-3}	1.416 and -1.537
Solvent accessible volume []	20.9%
Electron count in the voids per formula unit	132

[a)] Full-matrix least-square refinement on F^2 as implemented in SHELX-2014 [3]. $R1 = \Sigma||F_o| - |F_c||/\Sigma|F_o|$; $wR2 = \{\Sigma[w(F_o^2-F_c^2)]^2/\Sigma[w(F_o^2)^2]\}^{1/2}$ where $w^{-1} = [\sigma^2(F_o^2) + (aP)^2 + bP]$, $P = [2F_c^2 + \mathrm{Max}(F_o^2, 0)] / 3$, *a* and *b* are refined parameters; $\mathrm{GooF} = \{\Sigma[w(F_o^2-F_c^2)^2] / (n-p)\}^{1/2}$.

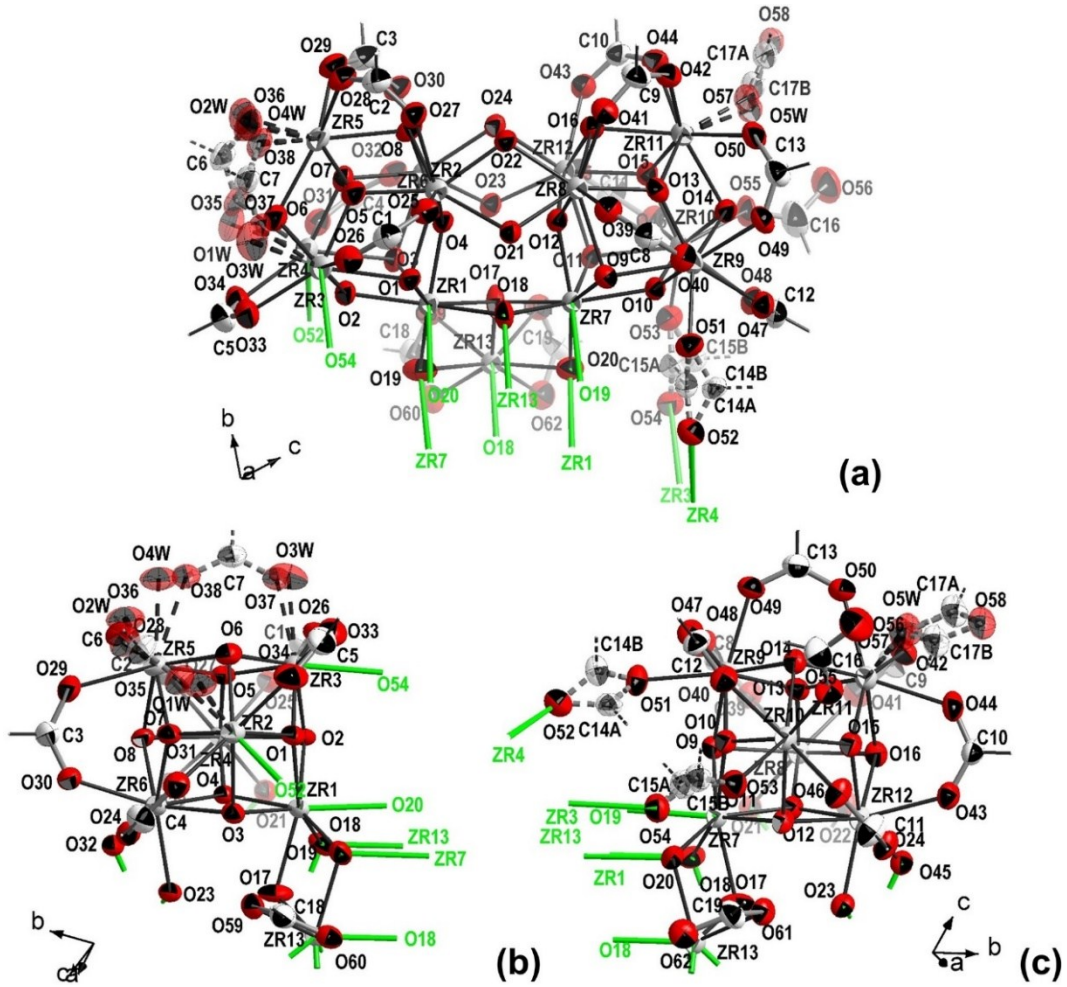

Fig. S4. ORTEP-style drawing of **1**; broken-off bonds are shown by green
(a) The asymmetric unit.
(b, c) The Zr_6-subunits depicted separately for better visibility of the connectivity.

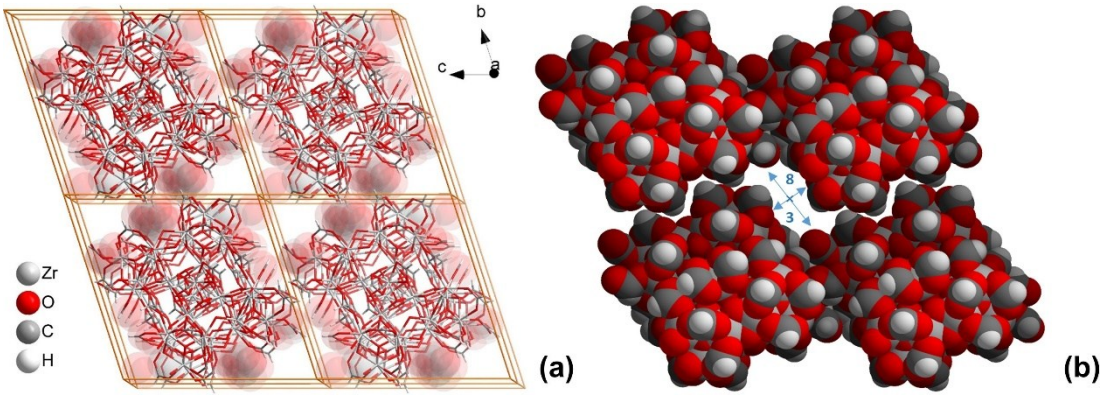

Fig. S5. The packing of the Zr_{26}-clusters in **1** (the unit cells are shown in orange).
(a) The cluster molecules are shown in wireframe representation, while the refined solvent molecules in semitransparent space-filling representation.
(b) The cluster molecules are shown only; space-filling representation is used. The thorough-pore vdW dimension is ~8×3 Å (centerline runs through the cell-

origin along *c*-axis).

3. PXRD

The diffractogram (Fig. S6) was recorded using a Bruker D2 Phaser diffractometer in reflective mode, equipped with a Bragg-Brentano goniometer, graphite monochromator (Cu Kα, λ = 1.5418 Å; 30 kV, 10 mA source) and Lynxeye 1D detector. The measurement was performed at room temperature with 0.05° steps on a freshly prepared sample, amply wetted with mother solution and placed on a zero-background Si single crystal plate sampleholder. Drying of the sample leads quickly to partial deterioration of the sample's quality. While application of cover foil decreased the quality of the sample substantially, a short and fast measurement with a relatively small sampling rate was performed, ensuring that the sample remains wet (wetting the sample also mostly eliminates the possible problem of preferred orientation). Despite of the relatively low number of data points collected, the near perfect correspondence of the experimental and simulated patterns (generated by Mercury 3.3.1. software, CCDC) is evident.

It is worth noting the importance of performing the measurement on a freshly synthesized sample. The PXRD patterns change noticeably after a few days of storage of the sample in the mother-solution at room temperature (even if the ensuing patters were all quite close, precise overlapping was not possible anymore). It was also observed that similar variation of quality might occur in repeated syntheses. We interpreted those variations rather as change in quality of the material than as significant presence of phase impurities (the main arguments are the closeness of the patterns and the observance of near perfect overlap in one case).

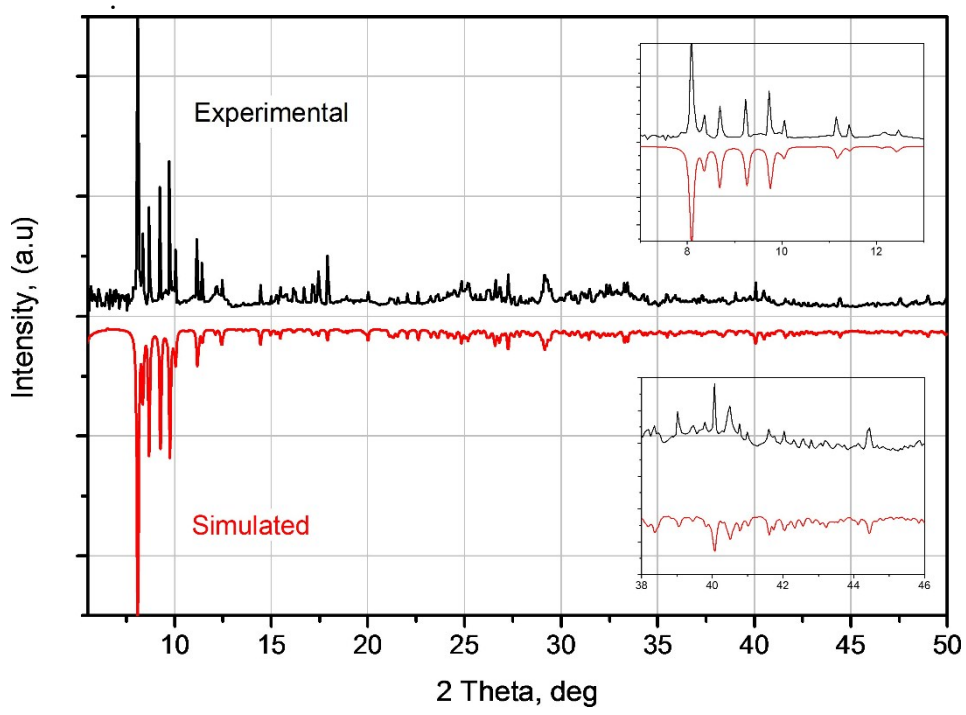

Fig. S6. Comparison of the experimental PXRD pattern of as-synthesized **1** with the simulated pattern calculated from SCXRD data.

4. TGA

Thermogravimetric analysis data was collected on a Netzsch TG 209F3 instrument using corundum sampleholder under N_2 gas stream (10 ml min^{-1}) at 10 °C min^{-1} heating rate.

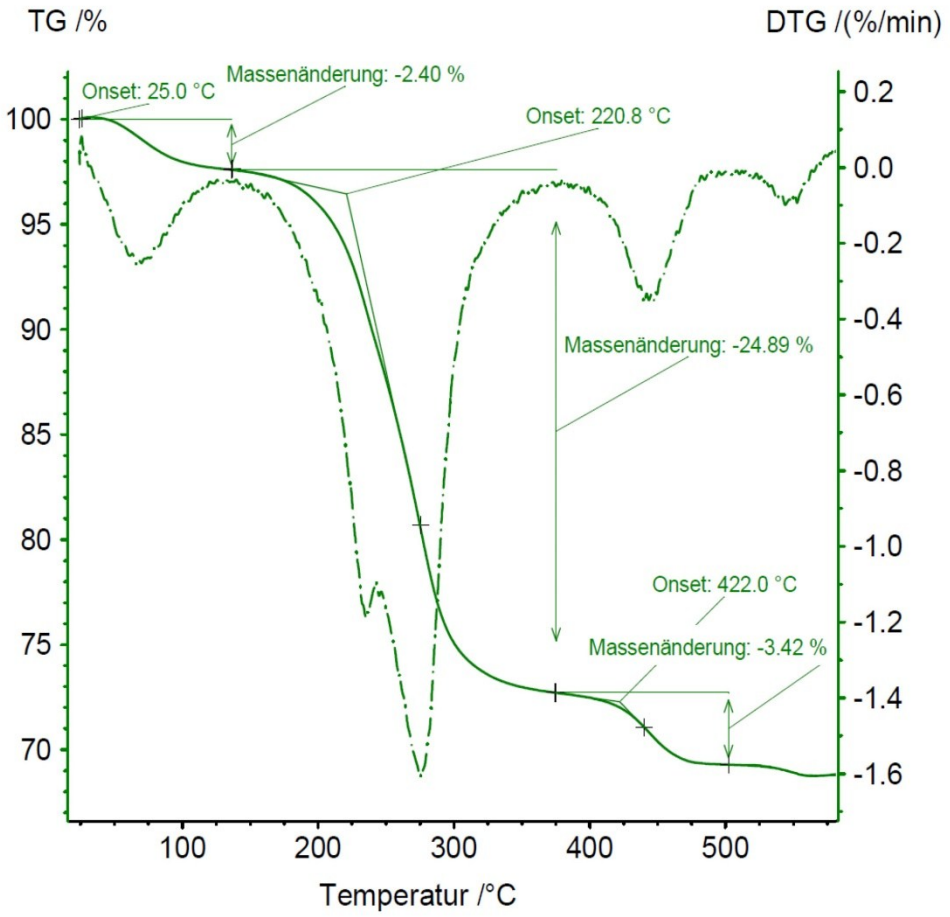

Fig. S7 Thermogravimetric analysis (TGA) of 1. The m(T) dependence is given by a solid line, while the differential dm/dT(T) dependence in a dot-and-dash line.

There are three weight-loss steps: 2.4% at r.t. - ~150 °C, 24.9% at ~150 – 380 °C and ~4.0% at 380 – 550 °C, in total accounting for 31.3% (Fig S7).

$$[Zr_{26}O_{18}(OH)_{30}(HCOO)_{38}] \cdot 5(HCOOH) \cdot 2H_2O$$

r.t - ~150 °C ↓ - 5 HCOOH, -2 H_2O

$$[Zr_{26}O_{18}(OH)_{30}(HCOO)_{38}]$$

> ~150 °C ↓ - 30 HCOOH

$$[Zr_{26}O_{48}(HCOO)_8]$$

> ~ 300 °C ↓ - 8 CO, 4 H_2O

$$[Zr_{26}O_{52}] \equiv 26\ ZrO_2$$

Fig. S8 Plausible decomposition steps for 1 under the TGA conditions.

The proposed decomposition scheme is given in Fig. S8 with the anticipated temperatures. Complete release of water and e.g. formic acid with comparable boiling point from moderately hydrophilic microporous compound should mostly take place at temperatures typically below 150 °C (strongly bound water could be to some small extent retained even at that temperature). Regarding the second step, it is known as a method of defect generation in UiO-66 type compounds that trifluoroacetate could be released in a form of trifluoroacetic acid at temperatures around 250 °C using the -OH groups as the source of proton [11]. Further increase of temperature necessarily leads to decomposition of the remaining formates to carbon monoxide, water and oxo-anions, resulting in formation of zirconium oxide. It is worth to stress that the steps, especially the second and the third one are surmised as not being rigorously separated.

The calculated weight of the residues after the proposed steps are 94.8%, 68.0% and 62.2%. The observed weight of the residue after the third step is 68.7%, which is somewhat more than the predicted value. It points out on the impurity of the isolated phase and probably on a significant presence of hydrated zirconium oxides, which do not contain formates / formic acid.

5. FT-IR spectroscopy

The FT-IR spectra (Fig. S9) were collected by a Bruker Tensor 37 system equipped with an ATR unit (Platinum ATR-QL, diamond) in the 4000-550 cm^{-1} range with a 2 cm^{-1} resolution (32 scans per measurement). Peak intensities were designated as: s – strong, m – medium, w – weak, br – broad, sh – shoulder, v- 'very' prefix:

FT-IR (ATR), $\tilde{\nu}$, cm^{-1} : 3398 (vw, b), 2866 (vw), 1567 (vs), 1467 (w), 1389 (w), 1361 (vs), 1019 (w), 916 (w), 805 (w), 760 (m), 704 (w), 644 (vs), 566 (w) (the data is given for a scaled-up synthesis of **1** after its drying until constant weight).

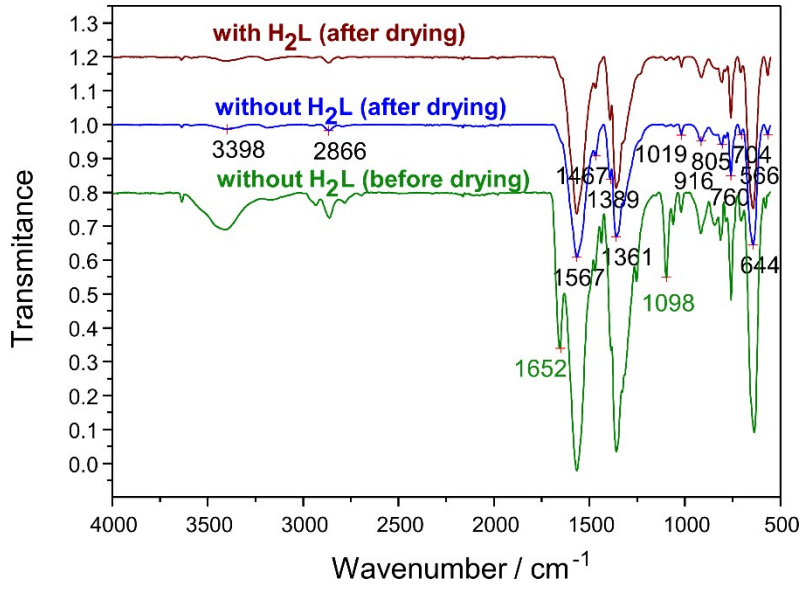

Fig. S9. IR(ATR) spectrum of **1**. The IR spectra of the compounds synthesized in the presence of 1,3-di(4-carboxyphenyl)adamantane, H2L, or without it are nearly identical. Note the disappearance of the peaks characteristic to DMF, ~1650 and 1100 cm^{-1}, upon drying.

6. ^{1}H NMR spectrum of **1** after digestion

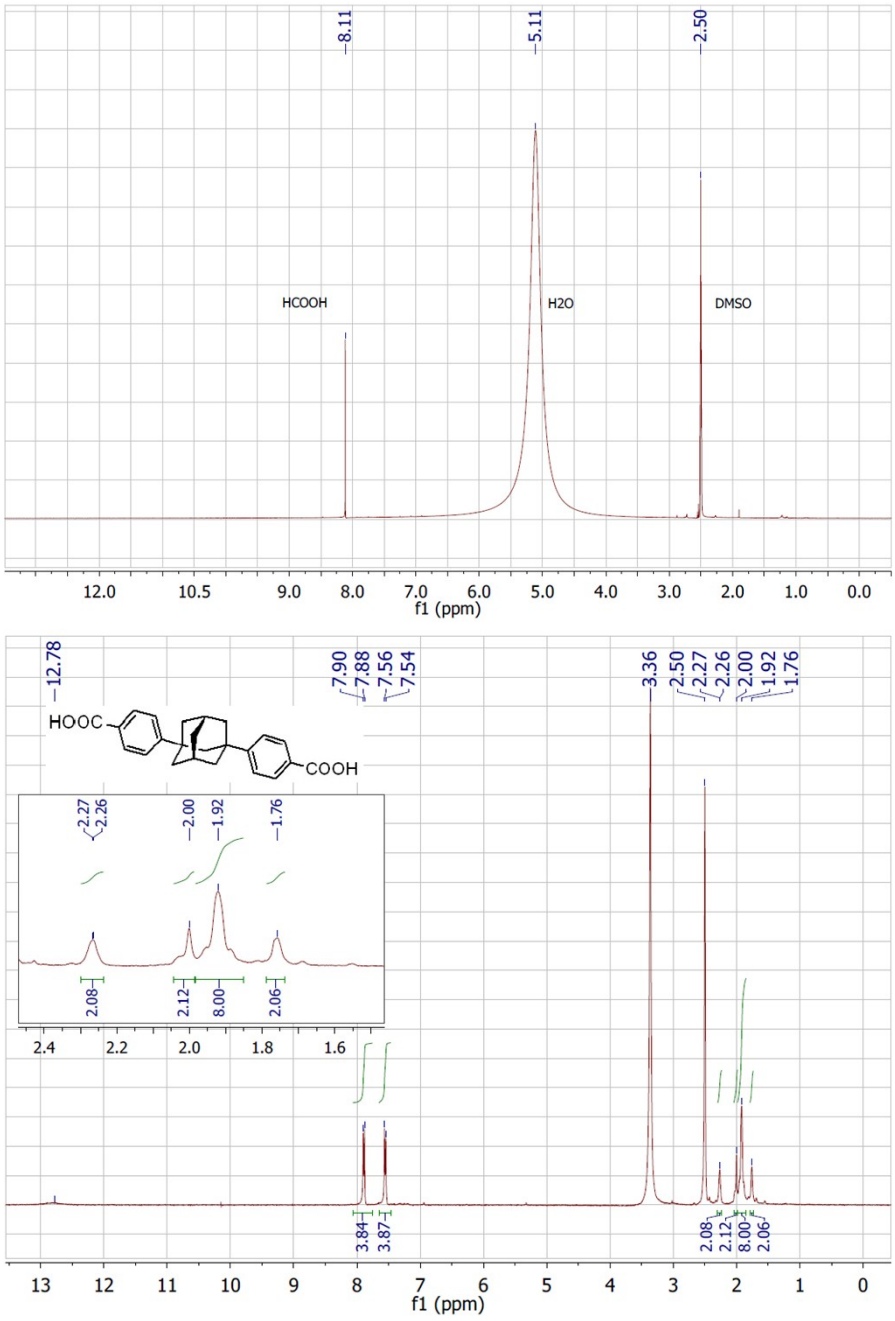

Fig. S10. a) ^{1}H NMR spectrum of **1** synthesized in the presence of H_2L after digestion b) ^{1}H NMR of H_2L for comparison.

A sample of **1** prepared in presence of 1,3-di-(4-carboxyphenyl)-adamantane, H_2L was thoroughly washed with DMF in order to remove the non-bound H_2L, and after drying in air until permanent weight, was digested in a mixture of 30 µL HF (40% solution in H_2O) and 570 µL of DMSO-d_6 (Fig. S10a; 300 MHz). The ^{1}H NMR spectrum of the digested sample (Fig. S10a) clearly indicates that no ligand incorporation occurred (see Fig. S10b for the spectrum of the pure ligand; DMSO-d_6, 200 MHz).

7. Gas adsorption studies

The preliminary N_2 adsorption isotherms were collected using a Quantachrome Nova-, while the final adsorption data for N_2, CO_2 and H_2 by Micromeritics ASAP 2020 automatic gas sorption analyzers. The control equilibration time, i.e. the time between subsequent data points, used for checking whether the equilibration is complete, was set to 30 s for the high quality measurements on the ASAP 2020 (this value is ~2-3 times more than it is used for typical measurements on a material with large or medium pores. In this way it was ensured that the hysteresis loop is not an artifact of the measurement). The minimum absolute surface area measurable with reasonable precision on the ASAP 2020 is approx. 5 m^2, which was accounted for adjustment of the used sample weights.

The N_2 data was measured repeatedly, with one pair of cross-check measurements using both instruments. The used gases (He, N_2, CO_2, H_2) were of ultra-high purity (UHP, grade 5.0, 99.999% or better) and the STP volumes are given according to the NIST standards (293.15 K, 101.325 kPa). Helium gas was used for the determination of the cold and warm free space of the sample tubes. The N_2 and H_2 adsorption isotherms were measured at 77 K (liq.-N_2 bath), while the CO_2 adsorption isotherm at 273.15 K using an ice-water isothermal bath.

A freshly prepared sample was filtered-off from the mother solution, washed 3 times with DMF and then soaked for a short time in acetone (<30 min. The short soaking time was a most probably unnecessary precaution against the deterioration of the sample's quality. Longer times might gave better results, but most probably by a small margin only). The soaking in acetone was repeated once and the collected sample was thereafter transferred in LEICA EM CPD300 supercritical CO_2 drier. 99 standard cycles were performed. ~100-110 mg of the dried and degassed material was used for the subsequent degassing and adsorption measurements.

A cursory optimization of the degassing temperature was done by performing comparative measurement after degassing at 100, 150, 190, 240 °C (The same sample was used and the degassing was sequentially done at higher temperature after each measurement). Degassing at 150 °C or below yielded materials with surface areas not exceeding 32 $m^2\ g^{-1}$, while the degassing at 240 °C afforded a material with negligible porosity. Thus, the optimum was found to be around 190 °C). The samples (~110-120 mg) were activated via heating under ~10^{-3} mbar vacuum in the case of Quantachrome Nova or ~10^{-5} mbar in the case of ASAP 2020 at 190 °C during 16-24 h.

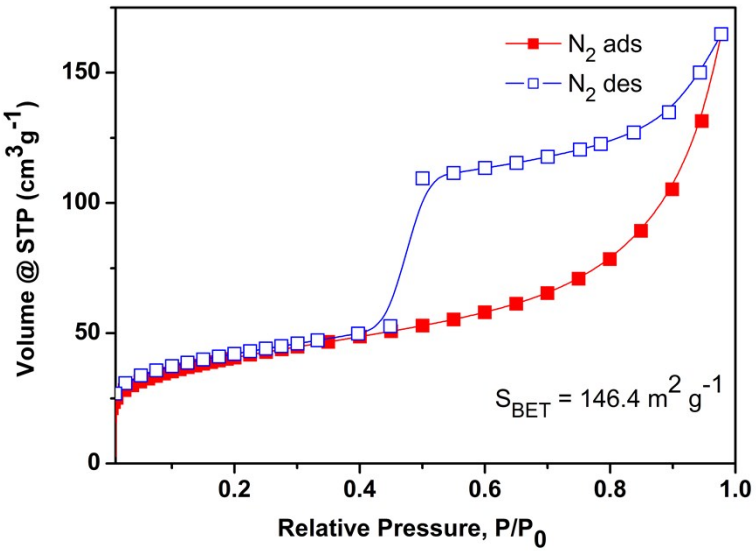

Fig. S11. N_2 adsorption isotherm for $\mathbf{1'}_{463}$ measured on 77K on the sample

obtained by degassing of **1** at 463 K.

An S_{BET} = 146 m^2 g^{-1} Brunauer–Emmett–Teller (BET) surface area was found (repeated N_2-only measurements on the same batch, but dried and degassed separately, gave 153 and 156 m^2 g^{-1}). The adsorption isotherm (Fig. S11) demonstrates a strong hysteresis (H2-type) with a distinct shape, having an abrupt desorption branch contrasting with the steady adsorption branch. The shape of the hysteresis is characteristic for capillary condensation of gases in mesoporous materials, particularly in the presence of 'ink-bottle' pores.[12] The latter term is standard and denotes 'bottle-necked' pores, with effective entrance diameter of the pore significantly smaller than the effective inner-diameter. Simulations of the adsorption isotherm shapes see for example in ref. [13].

The adsorption isotherms of CO_2 at 273K and H_2 at 77K are shown on Fig. 12 and Fig. 13 respectively. Both isotherms demonstrate narrow hysteresis loops over the whole measurement range, most probably reflecting the kinetic hindrances of desorption from the narrowest pores (the molecules of both gases have smaller equivalent kinetic diameters than N_2 and could reach areas associated with especially narrow pores with increased heats of adsorption). The observed values are in the standard range, if one takes in account the surface area. Thus, the so called 'Chahine's rule' [14] establishes an excess adsorption of 0.021 mg m^{-2} at 1 bar and 77 K, while **1**′$_{463}$ demonstrates a value of 0.017 mg m^{-2} (at 1 bar and the observed adsorption the difference between the total and excess adsorption is only a few percent).

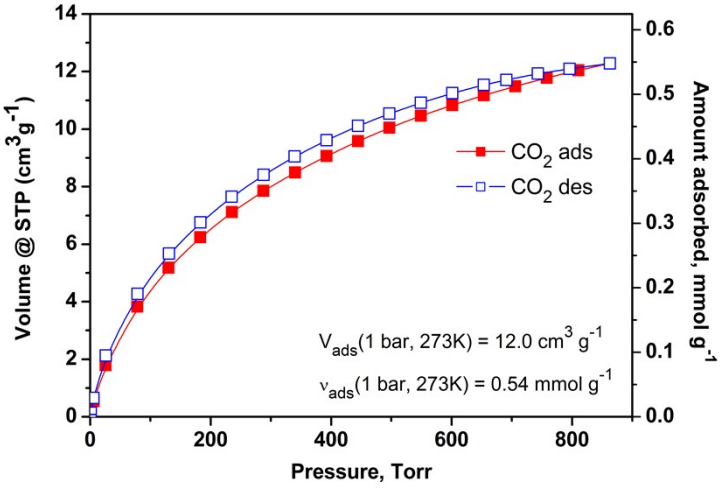

Fig. S12. CO_2 adsorption isotherm for **1**′$_{463}$, measured at 273 K.

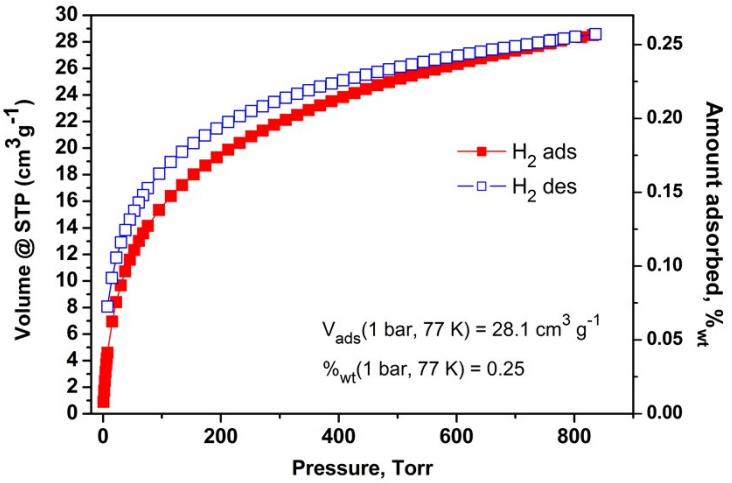

Fig. S13. H_2 adsorption isotherm for $\mathbf{1'}_{463}$, measured at 77 K.

References

1 T. Zhao, C. Heering, I. Boldog, K. V. Domasevitch, and C. Janiak, *CrystEngComm*, 2017, **19**, 776–780.

2 STOE & Cie GmbH (2016). X-Area 1.76, software package for collecting single-crystal data on STOE area-detector diffractometers, for image processing, scaling reflection intensities and for outlier rejection; Darmstadt, Germany.

3 STOE & Cie. *X-SHAPE*. Revision 1.06. Stoe & Cie GmbH, Darmstadt, Germany, 1999; Stoe & Cie. *X-RED*. Version 1.22. Stoe & Cie GmbH, Darmstadt, Germany, 2001.

4 G. M. Sheldrick, *Acta Crystallogr.* **2008**, *A64*, 112-122. G. M. Sheldrick, *Acta Crystallogr*. **2015**, *C71*, 3-8.

5 P. Ji, K. Manna, Z. Lin, X. Feng, A. Urban, Y. Song, and W. Lin, *J. Am. Chem. Soc*. **2017**, *139*, 7004−7011.

6 A.A. Bezrukov, K.W. Törnroos, E. Le Roux and P. D. C. Dietzel, *Chem. Commun.*, **2018**, *54*, 2735-2738.

7 P. Piszczek A. Radtke, A. Grodzicki, A. Wojtczak, J. Chojnacki, *Polyhedron*, **2007**, *26*, 679–685.

8 A. L. Spek, *Acta Crystallogr. Sect. C Struct. Chem.*, 2015, **71**, 9–18.

9 A. L. Spek, *Acta Crystallogr. Sect. D Biol. Crystallogr.*, 2009, **65**, 148–155.

10 H. Putz and K. Brandenburg, *Diam. 3.2, Cryst. Impact; Kreuzherrenstr. 102, 53227 Bonn, Ger.*, 2012.

11 F. Vermoortele, B. Bueken, G. Le Bars, B. Van De Voorde, M. Vandichel, K. Houthoofd, A. Vimont, M. Daturi, M. Waroquier, V. Van Speybroeck, C. Kirschhock, and D. E. De Vos, *J. Am. Chem. Soc.*, 2013, **135**, 11465–11468.

12 S. J. Gregg and K. S. W. Sing, Adsorption, Surface Area, and Porosity, Academic, New York, 2-nd ed, 1982, pp. 303.

13 Y. Zeng, C. Fan, D. D. Do, and D. Nicholson, *Ind. Eng. Chem. Res.*, 2014, **53**, 15467–15474.

14 B. Panella, M. Hirscher, and S. Roth, *Carbon N. Y.*, 2005, **43**, 2209–2214.

3.2. Ligand Excess "Inverse-Defected" Zr_6 Tetrahedral Tetracarboxylate Framework and Its Thermal Transformation

Bahareh Nateghi, Kostiantyn V. Domasevitch, Roman Bulánek, Christoph Janiak*, Ishtvan Boldog*

Inorg. Chem. **2019**, *58*, 19, 12786–12797.

DOI: 10.1021/acs.inorgchem.9b01721

Ausgehend von ((Adamantan-1,3,5,7-tetrayl)tetra(phen-4-yl))tetracarbonsäure (H_4L^4) über die klassische MOF-Synthese im DMF durch Einsatz von Ameisensäure oder Essigsäure wurde ein neues MOF **ZRTE-10** hergestellt. Das MOF mit der Zusammensetzung $[Zr_6(\mu_3\text{-}O)_4(\mu_3\text{-}OH)_4(L^4)(HL^4)_2(OH)_2(H_2O)_2]$ stellt eine niedrige Symmetrie (C_2/c) dar und basiert auf einem seltenen zehn Metallknoten. Zwei Drittel der Liganden tragen hierbei eine nicht-deprotonierte Carboxylgruppe. Das Gerüst weist ein komplexes trinodales $\{4^{14}.6^{24}.8^7\}\{4^3\}_2\{4^5.6\}$-Netz auf. Eine überkritische Trocknung mit CO_2 und eine milde Entgasung bei 120 °C ergab ein poröses Material mit einer BET-Oberfläche von 1190 m^2g^{-1}. Beim Erhitzen auf ~ 200 °C wandelte sich **ZRTE-10** in ein anderes kristallines Gerüst **ZRTE-11** um. Es wurde festgestellt, dass die Topologie von **ZRTE-11** mit der erwarteten Fluorit-Topologie übereinstimmt, die zuvor für andere literaturbekannten MOFs, basiert auf tetraedrischen Liganden, beobachtet wurde. **ZRTE-11** mit einer hohen Symmetrie (*I*4/m) basiert auf acht Metallknoten und hat die Formel $[Zr_6(\mu_3\text{-}O)_4(\mu_3\text{-}OH)_4(OH)_4(L^4)_2]$. Die thermisch induzierte Umwandlung von **ZRTE-10** verläuft durch Entfernung eines Liganden pro Zr_6-Knoten in den Poren des Gerüsts, was zu einer relativ niedrigen BET-Oberfläche von 585 m^2g^{-1} für das aktivierte **ZRTE-11** führt. Ein *mixed*-Ligand-Ansatz für **ZRTE-10,11** wurde folglich unter Verwendung von ((Adamantan-1,3,5-triyl)tri(phen-4-yl))tricarbonsäure (H_3L^3) versucht, welches ein gestutztes Analogon (*trancated analogou*) zum H_4L^4 ist. Hierbei wurde eine monokristalline Probe von **ZRTE-10** mit einer geringen Ausbeute erhalten. Dies zeigt jedoch nur einen geringen Einsatz von H_3L^3. Der Einsatz von HCl als Modulator ermöglicht ferner eine höhere Ausbeute (~80%). Röntgenpulverdiffraktogramme der erhaltenen Materialien zeigen die Bildung semiamorpher Materialien. Die thermische Behandlung dieser Materialien erhöht ihre Kristallinität. Jedoch liegen die BET-Oberflächen für die Ansätze mit H_4L^4 im Bereich von 400 bis 550 m^2g^{-1}.

Anteile an der Veröffentlichung:

- Synthese des **ZRTE-10** MOFs sowie alle *Mixed-Linker*-Ansätze, vollständige Charakterisierung (^{1}H-NMR, P-XRD, Sorptionsmessungen, IR, TGA, ESI, CHN-Analyse, SC-XRD für die vorläufige Kristallstruktur von **ZRTE-10**) sowie Auswertung und Darstellung der Ergebnisse.
- Synthese von Liganden H_4L^4, H_3L^3, H_2L^2 erfolgte von Herrn Dr. Ishtvan Boldog.
- Die Unterstützung bei der Einkristallröntgenanalyse erfolgte über Herrn Dr. Konstiantyn V. Domasevitch.
- Das Lösen der Einkristallstruktur erfolgte über Herrn Dr. Konstiantyn V. Domasevitch und Dr. Herrn Ishtvan Boldog.
- Die Unterstützung der Kapillarmessungen von Herrn Prof. Dr. Roman Bulánek.
- Kommunikation und finale Abstimmung der experimentellen Ergebnisse mit den externen Kooperationspartnern Herrn Dr. Ishtvan Boldog.
- Kontinuierliche Überarbeitung des Manuskripts.
- Die Einreichung in dem internationalen Journal "*Inorg. Chem.*" und finale Abstimmung des Manuskripts erfolgte in Zusammenarbeit mit Herrn Dr. Ishtvan Boldog.
- Korrekturen erfolgten in Zusammenarbeit mit Herrn Prof. Dr. Christoph Janiak und Herrn Dr. Ishtvan Boldog.

Inorganic Chemistry
Cite This: Inorg. Chem. 2019, 58, 12786−12797
Article
pubs.acs.org/IC

Ligand Excess "Inverse-Defected" Zr_6 Tetrahedral Tetracarboxylate Framework and Its Thermal Transformation

Bahareh Nateghi,[†] Kostiantyn V. Domasevitch,[‡] Roman Bulánek,[§] Christoph Janiak,*[,†] and Ishtvan Boldog*[,§]

[†]Institute of Inorganic Chemistry and Structural Chemistry, Heinrich-Heine-Universität Düsseldorf, Universitätsstr. 1, D-40225 Düsseldorf, Germany

[‡]Inorganic Chemistry Department, Taras Shevchenko National University of Kyiv, Volodymyrska Str. 64/13, Kyiv 01601, Ukraine

[§]University of Pardubice, Faculty of Chemical Technology, Department of Physical Chemistry, Studentská 573, 532 10 Pardubice, Czech Republic

Supporting Information

ABSTRACT: A new porous coordination polymer (PCP/MOF), **ZRTE-10**, based on a tetrahedral 1,3,5,7-tetra(carboxyphenyl)-benzene ligand (H_4L^4) was synthesized using formic or acetic acids as modulators. The low symmetry (*C*2/*c*) framework, $[Zr_6(\mu_3\text{-}O)_4(\mu_3\text{-}OH)_4(L^4)(HL^4)_2(OH)_2(H_2O)_2]$, is built upon a rare 10-connected Zr_6 cluster. Two-thirds of the ligands bear one nondeprotonated carboxy group, and the framework has a complex trinodal 3,4,10-c, $\{4^{14}.6^{24}.8^7\}\{4^3\}_2\{4^5.6\}$, underlying net. Supercritical CO_2 drying and mild degassing at 120 °C yielded a porous material with S_{BET} = 1190 $m^2\ g^{-1}$. When heated up to ∼200 °C, **ZRTE-10** converts to another crystalline framework, **ZRTE-11**. The latter was identified to be identical to the expected fluorite (**flu**) observed previously for other tetrahedral ligands. The high symmetry (*I*4/*m*) framework is built upon 8-connected Zr_6 clusters and has a formula of $[Zr_6(\mu_3\text{-}O)_4(\mu_3\text{-}OH)_4(OH)_4(L^4)_2]$. The complicated trinodal network of **ZRTE-10** and the simple **flu** net in **ZRTE-11** are topologically interrelated via the operation of the merging of two neighbor three-connected nodes to one four-connected one. The thermally induced conversion of **ZRTE-10** proceeds with expulsion of one ligand per Zr_6 node in the pores of the framework, resulting in a relatively low S_{BET} = 585 $m^2\ g^{-1}$ for the activated H_4L^4@**ZRTE-11**. A mixed ligand approach for **ZRTE-10,11** was attempted using 1,3,5-tetra(carboxyphenyl)benzene (H_3L^3), which is a truncated analog of H_4L^4 with one missing branch. The monocrystalline sample of **ZRTE-10** obtained in small yields demonstrated only minor inclusion of H_3L^3. However, the high-yielding (∼80%) procedure with HCl as a modulator allows near proportional incorporation of the ligands. The formed materials are semiamorphous with powder XRDs intermediary between pure **ZRTE-10** and **-11**. Thermal treatment of the semiamorphous materials increases their crystallinity and allows S_{BET} = 400−550 $m^2\ g^{-1}$ surface areas to be reached for pure H_4L^4 and H_3L^3 or their mixture alike. The approach proposes a viewpoint on the H_3L^3 trifunctional ligand as a model of a ligand platform, suitable for bearing a large functionality on the fourth "truncated" branch. The significance of **ZRTE-10** as a material for postsynthetic introduction of metal-based cluster functionality and as a model of functionality encapsulation, an alternative to the ship-in-the-bottle method, is discussed.

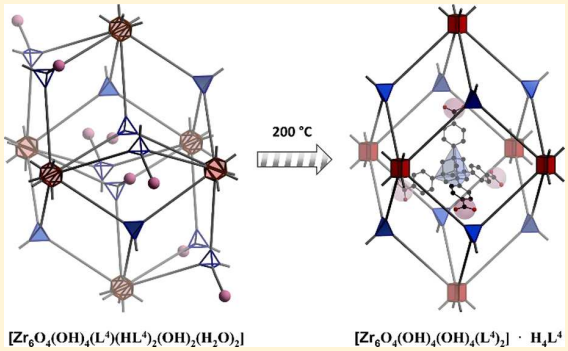

INTRODUCTION

Porous coordination polymers (PCP), also known as metal−organic frameworks (MOFs), are porous crystalline compounds consisting of metal ions or clusters interconnected by organic ligands. Zirconium carboxylates[1] are an important subclass of PCPs possessing an infrequent combination of high porosity, considerable thermal and hydrolytic/chemical stability, low toxicity, optical transparency and diamagnetism (important for use as matrixes for hosting active species), and a price that is not prohibitive. Indeed, most of the potential applications for PCPs typically consider zirconium carboxylates among the most promising candidates. Typical applications are small molecule storage,[2,3] separation,[4−6] and delivery[7] as well as catalysis[8−12] and sensorics.[13,14]

The structural predictability of zirconium carboxylates is a feature that is highly valued in PCP research. It is associated with the high stability of the $\{Zr_6(\mu_3\text{-}O)_4(\mu_3OH)_4(RCOO)_{12}\}$ cuboctahedral cluster (Figure 1) and its carboxylate-incomplete variants. The reticular chemistry approach is highly suitable for this class of compounds, comparable to the much less stable zinc carboxylates. The prototypal structural types are

Received: June 10, 2019
Published: September 18, 2019

DOI: 10.1021/acs.inorgchem.9b01721
Inorg. Chem. 2019, 58, 12786−12797

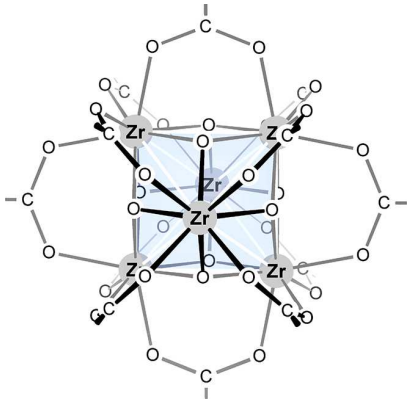

Figure 1. $\{Zr_6(OH)_4(O)_4(COOH)_{12}\}$ cluster.

reproduced after functionalization of the ligands by a broad range of groups, including potential ligating moieties like amino,[15] hydroxy,[16] sulfonic acid,[17] carboxylic acid,[18] bipyridyl,[19] etc., as well as very bulky fragments such as an *n*-membered macrocycle.[20] The geometric scalability of the ligands is also one of the best for the known isoreticular series (the classical $\{Zn(O)(RCOO)_6\}$-based MOF-5 type IRMOF series[21] is the classical competitor with properties often plagued by interpenetration; the $\{[Mg(R'O)(RCOO)]_\infty\}$ based IRMOF-74-*n* series[22] is unique regarding the extent of possible ligand elongation; some $\{M_3(O)(X)(RCOO)_6\}$-based series, particularly of the MIL-88 type, have an apparent potential,[23,24] which is yet to be fully disclosed). The availability of an isoreticular series with a large number of representatives makes it possible to focus on the functional side of a material's design and invest less time in fundamental structural aspects.

The three most important isoreticular series are based on (a) linear ligands, yielding mostly compounds with an **fcu** underlying net or its subnets (UiO-66 type[15]), (b) square-shaped ligands[25] yielding the **ftw** net, and (c) regular-tetrahedral ligands[26] producing the **flu** net.[1] In these cases, the ligands are perfectly compatible with the $\{Zr_6(\mu_3\text{-}O)_4(\mu_3\text{-}OH)_4(RCOO)_{12-n}(OH)_n(H_2O)_n\}$ cluster, ensuring connectivity ranging from 12 (cuboctahedral unit) to 8 (typically a cubic unit) to be combined in periodic nets close to their most symmetric representations. It is important to note that, despite the excellent matching of prerequisites for the formation of highly symmetric compounds, there are alternatives, primarily because of easy geometric deformations on either the side of the ligand or the cluster. The realization of alternative types is typical for square ligands, e.g., in the cases of PCN-222[27] (**csq**), PCN-224 (**she**),[28] and PCN-225(**sqc**),[29] and "exceptions" are dominant for regular triangular-shaped ligands like MOF-808 (**spn**),[30] PCN-777[31] (β-crystobalite), and UMCM-309[32] (**kgd**). All the listed cases are based on the Zr_6 cluster; PCPs based on other secondary building units are of lesser importance (even if some highly symmetric alternatives are known, like the Zr_8 cubic cluster[33]).[1] A notable exception is the MIL-140 series.[34]

The variability in the number of carboxylate groups in the $\{Zr_6(\mu_3\text{-}O)_4(\mu_3\text{-}OH)_4(RCOO)_{12-n}(OH)_n(H_2O)_n\}$, where n = 0−4 are the number of "defects," allows the adjustment of connectivity of the Zr_6 cluster ("capping" terminal carboxylates are an alternative to pairs of OH and H_2O terminal ligands). In high-connectivity Zr-PCPs, a part of the linker ligands could be missing to form defects,[35] which in the case of UiO-66 could be so numerous that the two limiting cases featuring four missing carboxylates are practically different compounds, as in the case of defect-poor (with **fcu** topology) and defect-rich UiO-66 (e.g., with **reo** topology).[36,37] The eliminated carboxylic acids leave coordinatively unsaturated sites (CUS-es),[10] which are "dockable" not only by carboxylic acids but by a variety of other species (for example, vanadium acetylacetonate was docked for gas-phase catalysis of the oxidative dehydrogenation of cyclohexane[38]). The Lewis acidity of the CUS-es,[39] which could be tuned even to form species resembling the active sites in the well-known sulfated-zirconia,[40] as well as possibilities for introduction of ligand based basicity,[41] explains the interest in Zr-MOFs as potential catalysts,[9] especially for the synthesis of organic compounds performed under mild conditions.[42−44]

The introduction of defects in PCPs is more feasible when the network is more highly connected, due to lowering the impact of a single linker on network stability. Coordination bonded clusters could easily ensure much higher connectivities than the organic connectors and are easily accessible. The $\{Zr_6(\mu_3\text{-}O)_4(\mu_3OH)_4(RCOO)_{12}\}$ cluster is an example of a secondary building block (SBU) of highest connectedness, and its prominence in "defect-engineered" PCPs is not surprising. However, the level of control on the cluster-based defects is relatively low as they are self-assembling during the synthesis.

An inverse strategy for defect introduction is the truncation of the ligand.[45−47] The truncated site could potentially be functionalized, while ultimate control could be exercised as the synthesis of the ligand precedes the last step of the PCP's self-assembly. Provided that the connectedness of the cluster is high, the ligand-candidate for truncation might have relatively low branching (potentially, it could be a pair consisting of a bifunctional linker and its monofunctional "half," however high lability and lowered incorporation control makes such an approach *a priori* disadvantaged). However, high connectedness of the ligand is favorable for overall mechanical stability and preservation of maximal similarity between the prototypal and truncated ligands. The connectivity of at least four as well as the nonplanar geometry seems to be sufficient, and the obvious choice in the case of Zr-MOFs is the truncation of tetrahedral ligands. Recently, we have explored the crystallization outcomes for complete and "truncated" adamantane-based tetrahedral ligands and have found that the self-assembly is strongly symmetry driven (see refs and also the discussion herein).[46] To explore potential defect-creation strategies, a compound class with strictly defined cluster-type should be chosen (i.e., a "cluster-driven" self-assembly approach), and Zr-MOFs meet this demand very well.

The first two Zr-PCPs with tetrahedral ligands were first reported almost simultaneously by Furukawa et al.[30] and Zhang et al.[26] in 2014. A small ((methanetetrayl)tetrakis-(phen-1,4-ylene)) tetracarboxylic acid (H_4MTB) and its larger homologue, ((methanetetrayl)tetrakis(biphen-4,4′-diyl)) tetracarboxylic acid (H_4MTBC), were used, respectively. We have chosen 1,3,5,7-tetraphenyladamantane as a tetrahedral platform, which has a size between tetraphenylmethane and its phenyl-expanded tetrakis(biphenyl)methane homologue used in this role before. The primary reason for using a yet unreported platform was the synthetic accessibility of all the bridgehead substituted oligophenyladamantanes by the same "Newman's route"[48] and the assuredness that the respective isoreticular compound with a **flu** net topology based on the

DOI: 10.1021/acs.inorgchem.9b01721
Inorg. Chem. 2019, 58, 12786−12797

tetrahedral ligand should exist. Accordingly, we aimed the investigation of the ((adamantane-1,3,5,7-tetrayl)tetra(phen-4-yl))tetracarboxylic acid, H_4L^4, and its "truncated" analogue, the ((adamantane-1,3,5-triyl)tri(phen-4-yl))tricarboxylic acid, H_3L^3, as a building block pair for the special ligand-based introduction of defects (Figure 2). The results were only partially expected, and the curious implications are reported in this contribution.

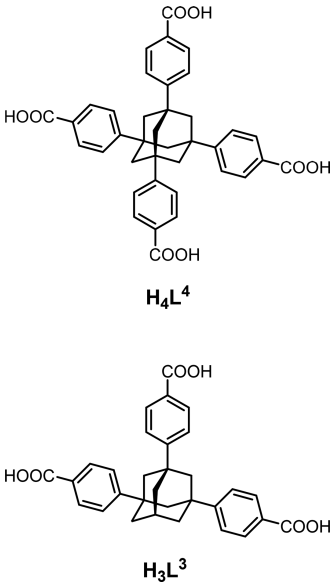

Figure 2. H_4L^4 and H_3L^3 ligands.

EXPERIMENTAL SECTION

Concise description of the synthesis and the crystal data for selected compounds are given below (see Supporting Information for complete description). **1**: A solution of 42 mg of $ZrOCl_2{\cdot}8H_2O$ and 22 mg of H_4L^4 in 4.60 mL of DMF and 2.64 mL of HCOOH was heated at 130 °C for 96 h in a sealed culture tube (note, 3% of H_3L^3 as an additive to H_4L^4 was used in repeated syntheses, see SI.1). The product, consisting of small single-crystals was filtered off, washed with DMF and with acetone, and dried in air until a permanent weight was reached. Yield: 9 mg (18%). When acetic acid was used, the yield of 1-AcOH-as was 20.2 mg (~40%). **1′**: **1**, after sc-CO_2 drying (see SI.7), was heated in a vacuum (10^{-3} mbar) at 120 °C, for 3 h. **2′**: **1** was heated in a vacuum (10^{-3} mbar) at 220 °C for 3 h. I/II-HCl-as: 19 mg of $ZrCl_4$ and 20 mg of H_4L^4 in 2.5 mL of DMF and 0.17 mL of HCl were heated at 120 °C for 24 h in a sealed culture tube. The white gel-like product was washed by DMF and acetone followed by drying in air until a permanent weight was reached. The yield of the white solid was 31 mg (74% approx.).

Selected crystal data for **1**: $C_{114}H_{96}O_{36}Zr_6$ (framework only), FW = 2589.34, monoclinic, *C*2/*c*. *a* = 24.261(5) Å, *b* = 30.967(6) Å, *c* = 25.454(5) Å, *β* = 101.91(3), *V* = 18712(7) Å^3, *Z* = 4, R1[$F^2 > 2\sigma(F^2)$] = 0.0341. The CCDC reference number is 1921424. The crystallographic data in CIF format can be downloaded free of charge at https://www.ccdc.cam.ac.uk/structures/. **2-Guest** (**2**·H_4L^4): $C_{80}H_{64}O_{32}Zr_{12.8}$ (note: the H_4L^4 guest molecule was modeled by a few Zr atoms), FW = 1352.5, tetragonal, *I*4/*m*, *a* = 17.9142, *c* = 31.5291, *V* = 10118.3 Å^3, *Z* = 2, wR_p = 0.155. The Supporting Information contains also the data on I-AcOH-as, isostructural to **1**.

Notes on the naming system. The code names **ZRTE-10** for **1′** and **ZRTE-11** for **2′** materials are used for the convenience of external referencing only (the code is generic; ZR stands for zirconium and TE for the tetrahedral ligand). The internal naming system is two-fold. The primary compounds are named **1**, **1′**, **2**, and **2′** (the prime (′) suffix designates the experimental degassed forms containing no volatile guests; **2** is the idealized framework, **2′** ≡ **2**·H_4L^4). The secondary materials are referred using a general sample code, *Phase[d][-mix]-Modulator-Condition*, where *Phase* = {I, II, I/II}, the actual phase-type; *[d]* is an optional suffix designating the use of H_3L^3 (otherwise H_4L^4 is implied); *[-mix]* is an optional suffix, for the use of H_3L^3 + H_4L^4; *Modulator* = {HCOOH, AcOH, PhCOOH, HCl, TFA, no-modul}; *Condition* = {as, temperature}, where "as" stands for as-synthesized and "temperature" is the temperature in Celsius, e.g., "120C". For example, I-HCOOH-as (which is equivalent to **1**) means the as-synthesized sample of the phase I type, synthesized using HCOOH as a modulator.

RESULTS AND DISCUSSION

$[Zr_6(\mu_3\text{-}O)_4(\mu_3\text{-}OH)_4(L^4)(HL^4)_2(OH)_2(H_2O)_2]{\cdot}4DMF{\cdot}2HCOOH{\cdot}4H_2O$, 1 (Phase I). Attempts to synthesize Zr-PCPs by reacting $ZrOCl_2{\cdot}8H_2O$ or $ZrCl_4$ and the H_4L^4 or H_3L^3 ligands in DMF at 80−150 °C did not lead to products consisting of single crystals.[46] The syntheses were modified by the addition of typical modulators,[1,26] including formic, acetic, and benzoic acids and HCl (SI.1, i.e., chapter 1 of the Supporting Information). Pure phases, consisting of very small, but well-formed single crystals were obtained only in the case of the H_4L^4 ligand, when formic or acetic acid was used; the large quantities of the modulators used were essential (Figure 3). The obtained I-HCOOH-as and I-AcOH-as materials were proven to be nearly identical. Interestingly, the crystallinity of the samples significantly improved upon the use of a mixture of H_4L^4 with a small additive of H_3L^3, as low as 3%$_{mol}$. A significant increase of H_3L^3's share eventually led to a decrease of crystallinity and the already low yield (10−20%; Tables S1, S2). While the use of acetic acid led to higher yields (~40%), formic acid ensured slightly better crystallinity, particularly evident during the single crystal XRD determination, and was used for scaled-up syntheses of material **1** (= I-HCOOH-as, synthesis with 3% of H_3L^3; **ZRTE-10** is the given framework code for external referencing; see Figure 3 and the Experimental Section for explanations of the used naming system).

A single crystal X-ray diffraction study (SCXRD) of the crystals of **1** (Figure S1) established a framework structure with a composition of $[Zr_6(\mu_3\text{-}O)_4(\mu_3\text{-}OH)_4(L^4)(HL^4)_2(OH)_2(H_2O)_2]$ (the solvent content of the air-dried compound—4 DMF, 2 HCOOH, and 4 H_2O per formula unit—was derived via TGA, see SI.6). The framework features the characteristic Zr_6 cluster (Figure 4) with a connectivity of 10 (which is equal to the number of coordinated carboxylates). This value is unusual, compared to the typical value of 8 or 12, and to the best of our knowledge,[1] there are only two well-documented Zr_6-based MOF structures with such connectivity: MOF-802[30] and DUT-69.[49] These two structures are based on slightly bent "pseudolinear" ligands and overall are essentially different from **1**. Unlike the "complete" octahedral cluster with 12 carboxylates, **1** does not feature one pair of

DOI: 10.1021/acs.inorgchem.9b01721
Inorg. Chem. 2019, 58, 12786−12797

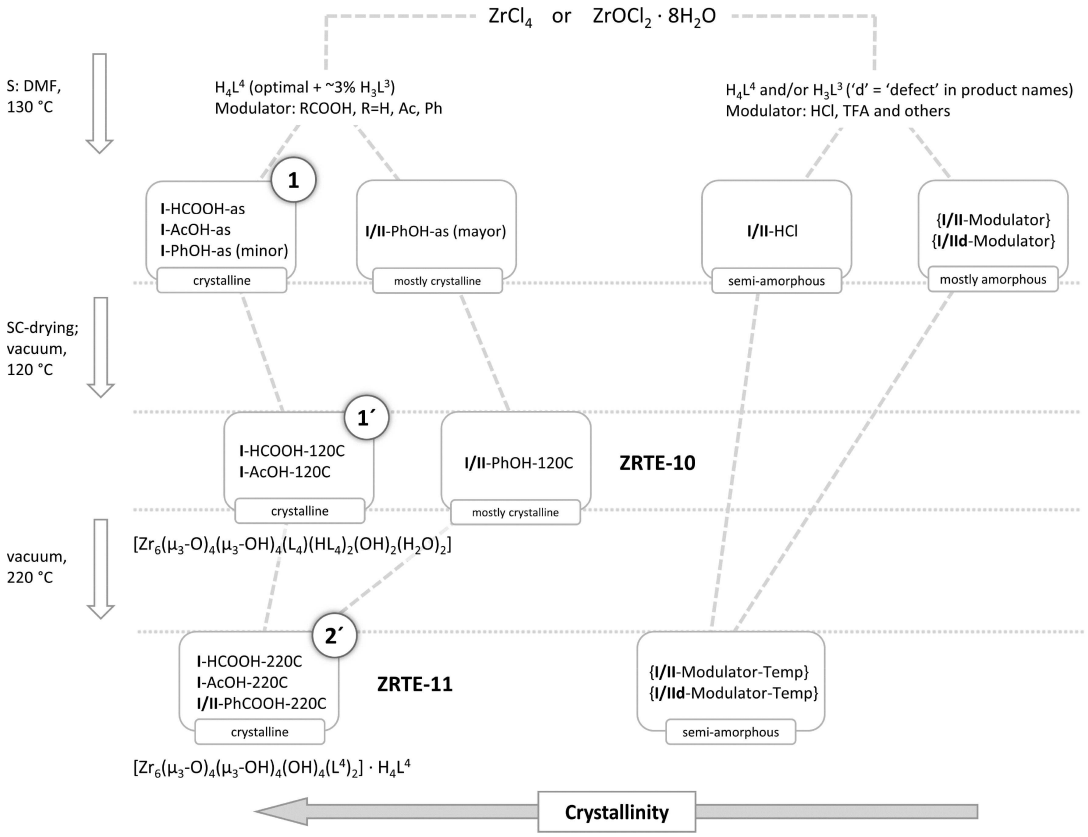

Figure 3. Scheme of the synthesis and the transformations of the products at elevated temperatures. The prime (′) modifier stands for "degassed;" the framework formulas are given with a minimal level of dehydration.

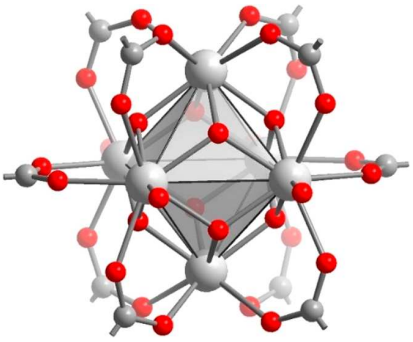

Figure 4. Zr_6 cluster in **1**, serving the role of a 10-c node of the framework. H atoms are not shown for clarity; the positions of the oxygen atoms belonging to the O/OH ligands are averaged.

bridging carboxylates, disposed in the equatorial plane and opposing each other. The respective coordination positions are filled with terminal *O* ligands (Figures 4, 5, S4). The analysis of the residual densities in the high-quality single crystal structure indicates that the coordinated oxygen atoms are isolated (in other words, the presence of site-sharing formate or DMF molecules is minimal). As the Zr−O bond lengths involving the terminal *O* ligands are of relevant difference, 2.1796(16) and 2.2146(6) Å, they were interpreted as belonging to hydroxido and aqua ligands, respectively (SI.2). In this case, the Zr_6 cluster has an equal number of μ_3-O and μ_3-OH ligands (4/4). This symmetric realization is the most typical for Zr_6 clusters, even if further deprotonation of the μ_3-OH ligands is possible. While bridging formate might be viewed as a more beneficial "capping" ligand compared to a pair of hydroxido and aqua ligands, both situations are common. Terminal formates are observed for example in the case of MOF-841, while hydroxido ligands are found in PCN-521,[26] or in a number of compounds featuring less than 12 carboxylates per cluster.[50]

Evidently, the framework structure of **1**, based on the 10-c node (-c stands for connectedness), is not equivalent topologically to the potentially expected **flu** net (which allows attaining $Fm\bar{3}m$ symmetry for a combination of a regular cubic and a regular tetrahedral building block). The 8-c node embodied by the most incomplete version of the Zr_6 cluster (four missing carboxylate "defects"), on one hand, and the 4-c node represented by a CR_4 or adamantane platform, on the other, possesses the necessary symmetry. The structures of the known MOF-841[30] and PCN-521[26] follow that scenario; however, they demonstrate lower symmetry ($I4/m$) than maximally possible. The distortions of the structure are obligatory for the realization of the **flu** net (it is enough to tell here that the reason is that the carboxylate group is not a geometric point; its bonding requirements are in conflict with the highest symmetry realization). The PCN-521 was the first structure of this type, and the authors were eager to recognize the importance of the distortions. Due to the evidently strong bent of the long biphenyl "branches" of the ligand (D_{2d} symmetry, instead of T_d; *cf.* D_{2h} max *vs* O_h symmetry for the Zr_6 cluster in **1** and in UiO-66 type structure), they even concluded that a structure with a **flu** underlying net cannot be

DOI: 10.1021/acs.inorgchem.9b01721
Inorg. Chem. 2019, 58, 12786−12797

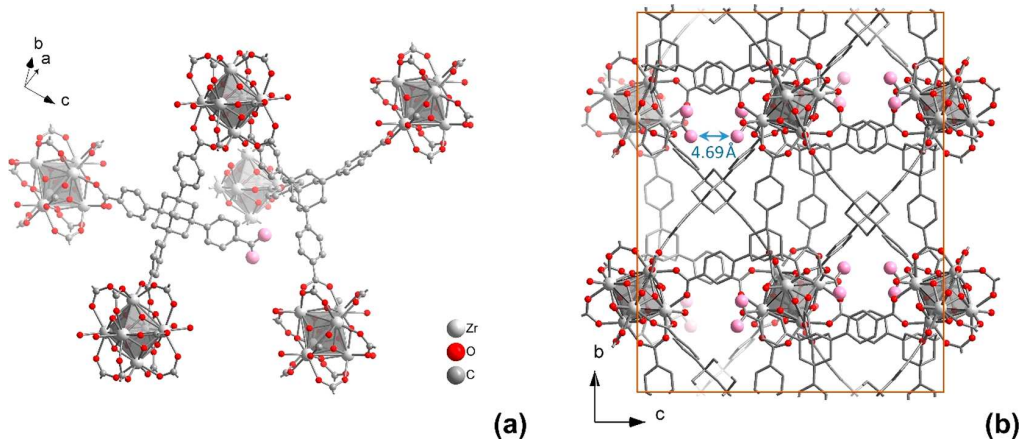

Figure 5. (a) A representative fragment of the structure of **1**, demonstrating the μ_8-$(L^4)^{4-}$ and μ_6-$(HL^4)^{3-}$ ligands. The oxygen atoms of the noncoordinated carboxylic acid functionality of μ_6-$(HL^4)^{3-}$ are shown in pink. (b) The unit cell of the structure of **1**. Note the close disposition of the noncoordinated carboxylic acid functionalities (indicated by an arrow). The hydrogen atoms are not shown for clarity; the oxygen atoms of μ_3-O and μ_3-OH are averaged.

Table 1. Summary on the Topology and Porosity Related Data for 1 and 2[a]

compd.	framework composition; space group; {point symbol}; RCSR code[b]	surface area, experimental (calculated)[c]/ $m^2\ g^{-1}$	void volume part, experimental (calculated)[d]/ $cm^3\ cm^{-3}$	max. included/max. free probe diameter[e]/ Å	density of the desolvated framework, calculated/ $g\ cm^{-3}$
1	$[Zr_6(\mu_3\text{-}O)_4(\mu_3\text{-}OH)_4(L^4)(HL^4)_2(OH)_2(H_2O)_2]$; *C*2/*c*; 3,4,10-c net; $\{4^{14}.6^{24}.8^7\}\{4^3\}_2\{4^5.6\}$; –	1190 for **1′**, (1886)	0.463 (0.576)	8.9, 5.3	0.906
2	*I*4/*m*; 8-c $[Zr_6(\mu_3\text{-}O)_4(\mu_3\text{-}OH)_4(OH)_4(L^4)_2(H_2O)_4]$; $\{4^{12}.6^{12}.8^4\}\{4^6\}_2$; **flu**	[585 for **2′**][f] (3197)	[0.261][f](0.718)	15.8, 6.6	[0.860][f] ~0.63
MOF-841 lit.[30]	$[Zr_6(\mu_3\text{-}O)_4(\mu_3\text{-}OH)_4(MTB)_2(HCOO)_4(H_2O)_4]$, $\{4^{12}.6^{12}.8^4\}\{4^6\}_2$, **flu**	1390 (2078.11)	(0.631)	11.2, 5.9	0.914
PCN-521, lit.[26]	$[Zr_6(\mu_3\text{-}OH)_8(OH)_8(MTBC)_2]$, $\{4^{12}.6^{12}.8^4\}\{4^6\}_2$; **flu**	3411 (4167)	(0.795)	19.4, 8.6	0.449

[a]The respective data for the known MOF-841 and PCN-521 are listed for comparison. [b]The RCSR (Reticular Chemistry Structure Resource) code is a unique net identifier.[54] [c]Connoly surface area calculated by Monte Carlo method employing a probe with 3.681 Å diameter.[55] The SCXRD structural data were used for experimental structures with removed solvent molecules, including the terminally coordinated ones. The disordered parts of the molecules were "collapsed." [d]Experimental Gurvich pore volume at P/P0 = 0.95; calculated pore volume by SOLV/PLATON (probe diameter of 2.4 Å).[56] [e]Maximal diameter of a spherical probe, which could be included in the framework (i.e., hosted in it) and the maximal diameter of the spherical probe, which could pass along a thorough channel.[57] [f]The formally assigned experimental data for **2′** (1-HCOOH-190C sample), which is interpreted as $[Zr_6(\mu_3\text{-}O)_4(\mu_3\text{-}OH)_4(OH)_4(L^4)_2]\cdot H_4L^4$.

obtained for a smaller ligand.[26] This conjecture was proven wrong with the report of MOF-841[30] based on a minimal tetraphenylmethane core. Indeed, the distortions should not be necessarily associated with the bending of the ligand branches.

The necessary symmetry lowering in the real structures with a **flu** underlying net is a subtle indication that alternative structures might not be rare. At least, they might be more expected than the deviation from the maximum symmetry in the UiO-66 type (**fcu**), where the maximal symmetry ($Fm\bar{3}m$) is very compatible with the linear dicarboxylates. Notably, even in the latter case, such deviation occurs, and other topologies with 12-c Zr_6 clusters exist, as in the case of MOF-812 (**ith**, *C*2/*c* actualization).[30] It seems that up to now the only well-known observed alternative to **fcu** is the highly porous NPF-200[51] (β-UH_3-like topology, high symmetry $Pm\bar{3}n$ actualization), which is an alternative product to PCN-521 (it is worth noting, however, that this trinodal network features also Zr_8 along with the Zr_6 cluster).

Thus, **1**, instead of **flu**, adopts a topology of a complex three-nodal underlying net with a stoichiometry of {HL^4-node: 3-c}{L^4-node: 4-c}$_2${Zr_6-node: 10-c} and, respectively, a point symbol of $\{4^{14}.6^{24}.8^7\}\{4^3\}_2\{4^5.6\}$ (see Table 1). Unlike in NPF-200, the deviation from the simplest binodal **flu** topology proceeded to two different ligand nodes instead of two metal cluster nodes. The 10-c Zr_6 cluster coordinates 2 × 3 carboxylates of the triply deprotonated ligand and 4 carboxylates of the fully deprotonated ligand (Figure 5; see also Figure 6b, left).

The formal topological descriptors do not disclose the curious fact that the underlying net in **1** is related to the actually expected **flu** net via a simple transformation: pairs of metrically close 3-c nodes are merged to 4-c nodes via overlapping two out of the three edges (Figure 6). Notably, **1** is not interpenetrated. High symmetry realizations of the **flu** net, on its own, are known to be "not-prone" to interpenetrating with its copies. It is a typical property of highly connected non-self-dual nets (the net, dual to **flu**, is **fcu**) in contrast to realizations of self-dual nets, like **srs**, **dia**, and **pcu**.[52,53] This feature of the **flu** net makes it a desirable target for reaching optimal porosity characteristics,[26] and the related **1** does not fail in this regard as well.

DOI: 10.1021/acs.inorgchem.9b01721
Inorg. Chem. 2019, 58, 12786−12797

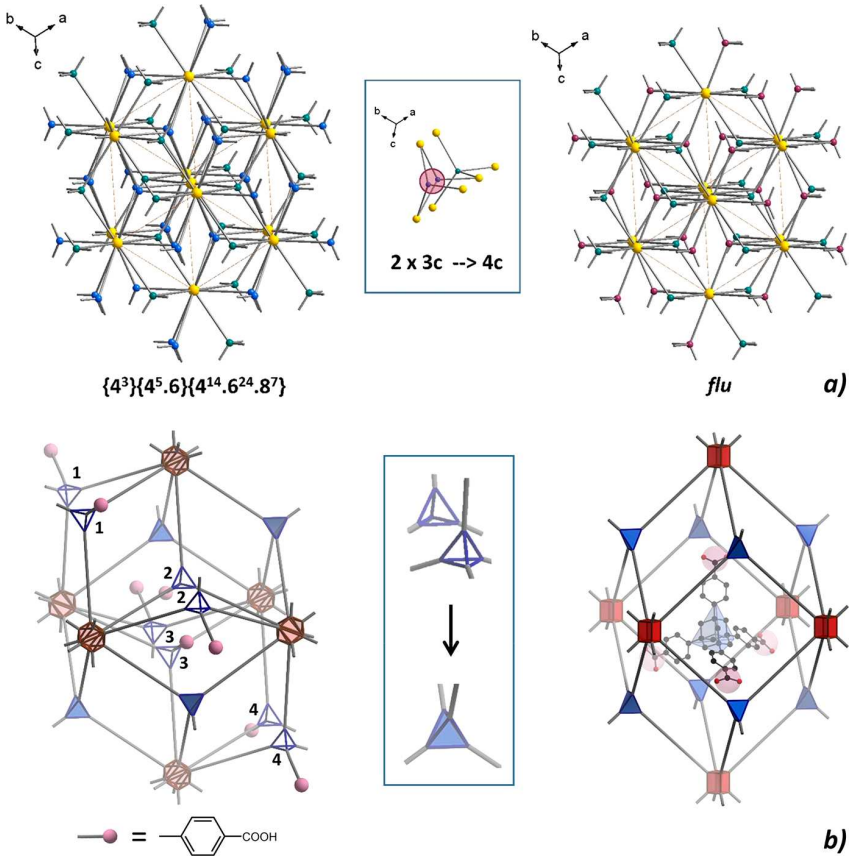

Figure 6. Relation between the underlying net of **1** and the **flu** net: the topological equivalence by merging two three-connected nodes to one four-connected one. (a) Network representation. (b) Related cages. The wireframe tetrahedron stands for the HL^{3-} and the filled tetrahedron for the L^{4-} ligand. The pink spheres designate the noncoordinated carboxy groups. The representation of the encapsulated H_4L^4 guest in a cage of the **flu** net is illustrative, without suggested localization.

Probably the most interesting structural feature of **1** on the framework level is associated with the noncoordinated carboxyphenyl groups. The smallest distance between the *O* atoms of the close pairs is only 4.69 Å from each other (Figure 5b). The method of preparation of **1** included a large amount of formic acid as a modulator, ensuring nondeprotonation. The region between the close carboxy functions contains only weak residual electron density peaks, precluding the presence of zirconium, but suggesting partial occupancy of the area by H-bonded species (see SI.2). The structure of **1** should favor the postsynthetic introduction of a coordination-bonded cluster with tailorable catalytic functions, using the carboxy functions as anchors.

$[Zr_6(\mu_3\text{-}O)_4(\mu_3\text{-}OH)_4(OH)_4(L^4)_2]\cdot H_4L^4$; 2′ (phase II). The degassing of compound **1** in a vacuum under heating (Figure 3), which aimed at a preparation for a routine sorption measurement, caused a phase transition, resulting in **2′** (**ZRTE-11**). The transformation takes place between 120 and 190 °C, and the process was evidently concomitant with the complete removal of the guest solvent molecules. The product of the transition possesses a peculiar PXRD pattern with only two remarkably sharp peaks and nearly no other details (Figure 7). The absence of fine detail is not surprising, taking into account the inevitable decrease of crystallinity: the low-temperature solid state transition does not allow efficient defect healing. The low number of strong peaks suggested that the formed crystalline compound has a structure of high symmetry. The evident candidate for phase II is the expected structure with the **flu** underlying net. In this case, the phase transition of I to II under heating could be interpreted as a conversion of an intermediary product, stable at a lower temperature, to a more symmetric final product.

The interpretation of the phase transition is complicated by the fact that the stoichiometries of the nets are different: Zr/H_nL^4 is 1:3 for **1** and 1:2 for the expected compound with the **flu** underlying net. During such conversion, 1/3 of the ligands should be expelled from the framework into the pores. While the formed ligand could be hosted in the formed highly porous structure with large inner cavities (~16 Å diameter max. cavity; the relative size of the ligand is given faithfully in Figure 6b), the process of the framework's reassembly did not proceed smoothly, which is evident from the somewhat decreased crystallinity (absence of weak peaks in the PXRD pattern).

Note, the patterns marked by [*] are measured using a flat sample-holder reflectance mode, compared to the much more precise measurement in capillaries for other cases. A part of the broadening for the marked patterns could be attributed to the method of measurement.

The decrease of crystallinity of **2′** under phase transition poses a critical problem for structural determination. Either a single crystal XRD determination or a Rietveld refinement based on two peaks is not realistic. However, the high-quality PXRD data allowed us at least to verify the hypothesis regarding the structure of **2**·H_4L^4. For that, a structural model

DOI: 10.1021/acs.inorgchem.9b01721
Inorg. Chem. 2019, 58, 12786−12797

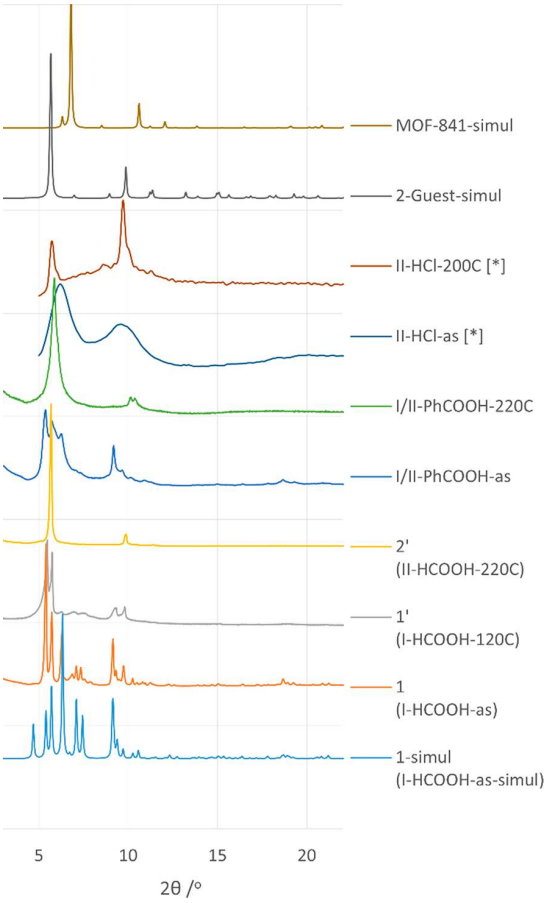

Figure 7. PXRD patterns of **1** and **2**, both experimental and simulated, and their comparison with the simulated pattern of MOF-841.

of **2** ($I4/m$) was created, using the structure of MOF-841 as a prototype (Figure 8; the atomic coordinates are given in SI.4; note that the variant of the framework formula of **2** is given with maximal number of hydroxido ligands, which could convert to oxo ligands upon strong degassing). The refinement strategy, taking into account the featurelessness of the pattern, was to refine the two independent cell parameters and two profile parameters. The LeBail fit gave a satisfactory correspondence (wR_p = 0.052) with a <2% change of the cell parameters compared to the initial model, constructed geometrically. The subsequent Rietveld fitting revealed that the calculated pattern contained three strong peaks, with one of them having no correspondence in the experimental pattern (Figure S11). In this case, preferred orientation is of low probability; however the presence of the guest might have an influence on the relative intensities of the peaks. The placement of a model guest in the vicinity of the (1/2, 0, 0) coordinate, which is in the middle of a void, strongly diminished the "redundant" peak. Finally, the H_4L^4 guest molecule was modeled with three heavy atoms, arbitrarily chosen to be Zr atoms. The crude modeling approach for **2-Guest** still allowed to reach wR_p = 0.15 (Figure S12 for profile fitting and Figure 7, Figure S11 for comparison of the simulated PXRDs with the experimental ones; for further details, see SI.5; the cif files for the refined structure are available from the CCDC). That result should be viewed as a verification of the structural hypothesis regarding **2**, rather than full-fledged refinement. The latter is impossible due to inherent limitations in the quality of the PXRD data.

The Use of Other Modulators (phase I/II). The use of modulators other than formic or acetic acids yielded mostly products of medium to poor crystallinity, even if the yields tend to be higher, up to ∼80−90% in the case of HCl (Table 1). The PXRD patterns of these, typically semiamorphous, materials contained two very broad peaks (Figure 7, for the example of I/II-HCl-as). The broad peaks are mostly but not entirely overlapped with the PXRD pattern of **1** (phase I) and entirely overlap with **2′** (phase II), being slightly closer to the latter. All these materials are classified as representing semiamorphous mixed I/II phases (Figure 3).

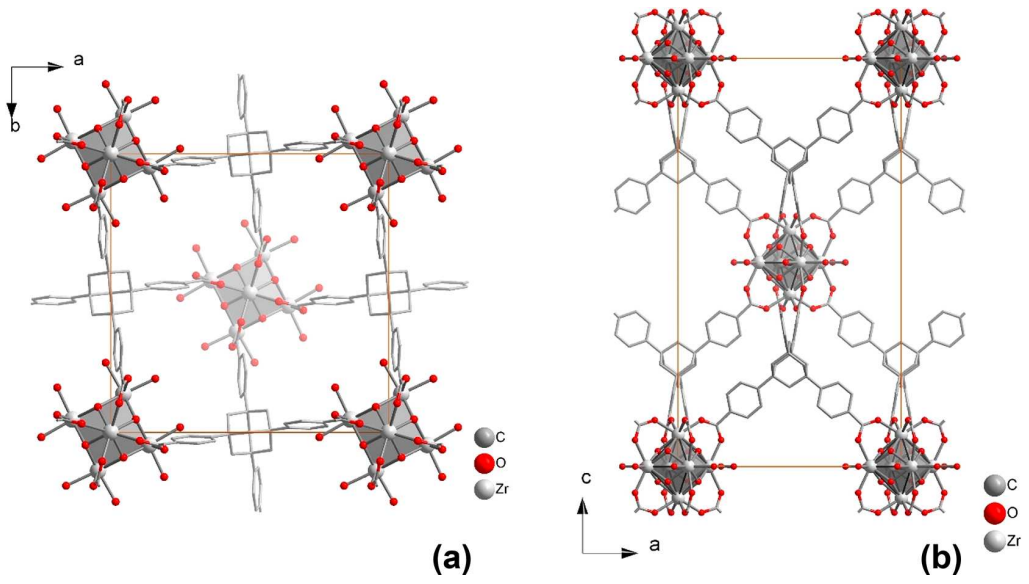

Figure 8. Structural model of $[Zr_6(\mu_3\text{-}O)_4(\mu_3\text{-}OH)_4(OH)_4(L^4)_2]$, **2**, with a **flu** underlying net. (a) View along c axis. (b) View along b axis.

DOI: 10.1021/acs.inorgchem.9b01721
Inorg. Chem. 2019, 58, 12786−12797

An interesting intermediary case and a partial exception is the I/II-PhCOOH-as, synthesized with benzoic acid as a modulator. While the sample was primarily represented by very small monocrystals, they diffracted very poorly. The maximal achievement in that regard was the indexing of a few particularly small crystals among dozens of attempted ones. The exception crystals turned out to belong to phase I (*i.e.*, isostructural with **1**, Table S3). The PXRD pattern for the sample, isolated immediately after the synthesis, demonstrated significantly better crystallinity, compared to the very poor diffraction witnessed by the single crystal studies. We came to the conclusion that, under the temperature of synthesis (130 °C), another phase forms, but upon cooling, it transforms to phase I in the mother liquor (rapid isolation decreases the speed of conversion significantly and allows a "mixed-phase" PXRD with a significant crystallinity to be measured). Unfortunately, we were not able to prove that the initially formed phase is identical to phase II. In any case, I/II-PhCOOH-as transforms to **2′** (Figure S11) with quite good crystallinity upon heating, demonstrating an identical behavior to **1** in this respect.

All the I/II phases, except I/II-PhCOOH-as, are nearly amorphous in the as-synthesized form but improve their crystallinity upon heating at ∼200 °C (the process could be viewed as a partial crystallization/aging). The strongest improvement was found for I/II-HCl-as (Figure 7). The use of hydrochloric acid as a modulator ensures also high yield, which made the method interesting for the mixed ligand approach.

Semiamorphous Mixed Ligand Materials. The structure of **1**, with two out of three ligands acting as three-functional, endows the potential H_4L^4/H_3L^3 mixed ligand approach with a clear context. Indeed, **1** contains an $(HL^4)^{3-}$ ligand, which is functionally equivalent to the $(L^3)^{3-}$ ligand. Hence, an individual compound with a framework composition of $[Zr_6(\mu_3\text{-}O)_4(\mu_3\text{-}OH)_4(L^4)(L^3)_2(OH)_2(H_2O)_2]$ is structurally feasible. The analysis of the single crystal structure of **1** is encouraging in this regard; the noncoordinated branches of the $(HL^4)^{3-}$ ligand have large equivalent thermal displacement parameters. The disorder of the branches (see SI.2) only partially explains the effect. It is reasonable to assume that a part of the $(HL^4)^{3-}$ is substituted to $(L^3)^{3-}$, which is present as an additive. The independent refinement of the two disordered components gives an aggregate occupancy of ∼0.96. In other words, around 4% of the $(HL^4)^{3-}$ to $(L^3)^{3-}$ substitution rate is estimated from the structural data. This value is very approximative, but the high-quality of the SCXRD data gives them certain weight. Nevertheless, the NMR spectra of the HF-digested sample (SI.8) did not show an appreciable presence of H_3L^3 in a bulk sample.

A number of experiments with different initial H_3L^3/H_4L^4 ratios aiming at mixed-ligand Zr-PCPs were performed. With HCOOH and AcOH used as modulators, the yield and crystallinity dropped, when the content of H_3L^3 increased to amounts comparable to H_4L^4. At a ∼1:1 ratio, the products were already noncrystalline. The NMR spectra of crystalline samples confirmed that the inclusion of H_3L^3 is minimal at best. It could be, hence, concluded that the role of H_3L^3 at low concentrations is limited to induction of the crystallization (it is worth noting that even the "pure" H_4L^4 might contain trace amounts of H_3L^3 due to the method of preparation; the "Newman's" protocol of benzene alkylation[48] yields a mixture of all the possible bridge-head functionalized adamantanes, starting from mono- to 1,3,5,7-tetraphenyladamantanes that are functionalized further). Under slow, controlled crystal growth, the much less soluble H_4L^4 is included in the product preferentially. The low yields for these modulators were equivalent to a recrystallization, with harvesting the most pure, single-ligand product.

The inclusion of $(L^3)^{3-}$ is achievable for semiarmorphous samples. When a 1:2 ratio of H_4L^4/H_3L^3 is used, the NMR of the digested sample indicates a 1:0.64 ratio of the ligands in the product (Figure S20; see Figure S7 for the PXRD). The low yielding synthesis still causes enrichment of the product with H_4L^4.

The high yielding (up to ∼80%) HCl-modulated synthesis turned out to be the best suited for "forcing" the incorporation of the H_3L^3. An amorphous model compound I/IId-mix-HCl-as was prepared by using an H_4L^4/H_3L^3 1:1 ratio; the incorporation of the ligand was confirmed by NMR (1:1.09 ratio in the product; Figure S20) and comparative IR spectroscopy (Figure S22). The primary motivation in making this model material, which crystallinity increases upon activation (Figure S10), was the assessment of ligand substitution on the porosity characteristics, discussed below.

N_2 Gas Adsorption Studies. The results on the adsorption studies and the found BET areas are summarized in Table 2. The preparation for low temperature degassing (120 °C) involved an acetone exchange with short exposition, followed by thorough supercritical CO_2 drying (sc-CO_2). The procedure allowed the removal of nearly all the DMF, which was confirmed by IR spectroscopy (Figure S21). **1′**, obtained by the degassing of **1** (or its analogue, prepared using acetic acid), is mostly retained in the framework structure under low temperature degassing (Figure 7, first signs of conversion to **2′** after 24 h of degassing in a capillary; Figure S8, typical 3 h degassing, less precise flat sample-holder measurement). The maximal surface area of 1190 $m^2\ g^{-1}$ was registered, with little difference between materials synthesized using formic or acetic acid (Table 2, Figures 9, S14). The simulated value for the solvent-free framework of **1′** is 1886 $m^2\ g^{-1}$ (Table 1); the discrepancy might be explained by the decrease of crystallinity due to start of conversion to **2′** and the presence of minor amounts of residual solvent. The converted structure of **2′** has a maximum observed porosity of 576 $m^2\ g^{-1}$. It is only a fifth of the simulated value of the idealized **2** with a fluorite structure (**2′** ≡ **2**·H_4L^4). Evidently, the encapsulated ligand, which is expelled to the pores during conversion, takes its toll. The ligand is larger than the vdW opening of the **flu** net cage; the openings have a lozenge shape with sides equal to the ligand's

Table 2. Degassing Conditions and Observed Surface Areas

sample name	degassing temp, °C	sample pretreatment	S_{BET}, $m^2\ g^{-1}$
I-HCOOH-120C or **1′**	120	sc-CO_2	1190
I-HCOOH-190C or **2′**	120	sc-CO_2	576
I-AcOH-120C	120	sc-CO_2	1126
I/II-PhCOOH-120C	120	sc-CO_2	763
I/II-HCl-200C	200	sc-CO_2	546
I/IId-mix-HCl-200C	200		452
I/IId-HCl-200C	200		396
I/II-TFA-120C	120	sc-CO_2	253
I/II-no-modul-200C	200		233

DOI: 10.1021/acs.inorgchem.9b01721
Inorg. Chem. 2019, 58, 12786−12797

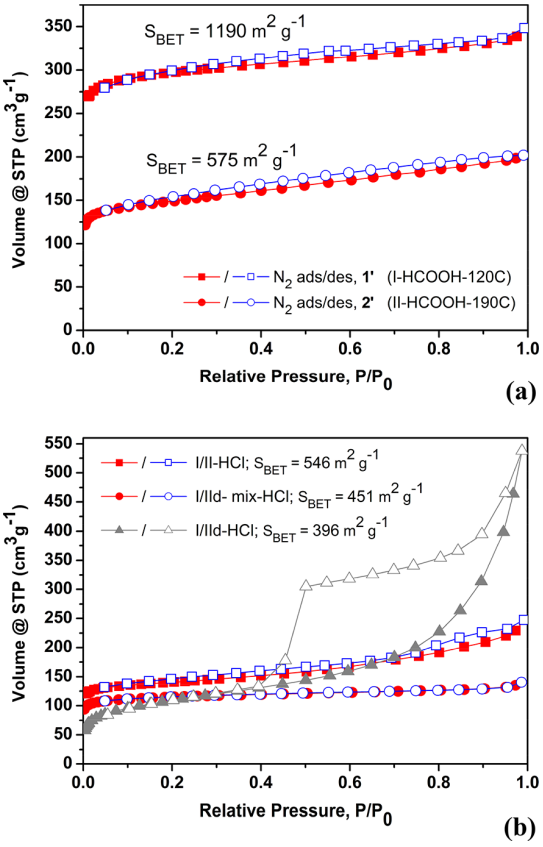

Figure 9. N_2 gas adsorption isotherms. (a) **1**-HCOOH after sc-CO_2 drying followed by activation at 120 °C and the same sample after activation at 190 °C, causing conversion to phase **2**. (b) Semi-amorphous samples obtained for H_4L^4 only (top legend line), mixture of H_4L^4/H_3L^3 1:1 (middle), and with H_3L^3 only (bottom).

branch, Figure 6. Hence, no ligand's mobility was expected, especially because of the generally low solubility of the H_4L^4 ligand. The hypothesis was checked experimentally, but no increase of surface area was registered for **2**·H_4L^4 after soaking in DMF for 2 days and subsequent activation.

The semiamorphous phases degassed at a low temperature (120 °C) demonstrated low surface areas, with the remarkable exception of the I/II-PhCOOH sample (763 $m^2\ g^{-1}$). Composed of crystalline phase I at least partially, and demonstrating conversion to pure **2′**, I/II-PhCOOH is much closer to **1**, compared to the rest of the I/II materials. However, the latter demonstrates a strong increase in crystallinity, when degassed at 200 °C. The best result is obtained for I/II-HCl-200C with a 546 $m^2\ g^{-1}$ surface area. This value is surprisingly close to the surface area of the much more crystalline **2′**. The thermal treatment at ∼200 °C evidently "equilibrates" the structures with a tendency toward being near the phase II-type structurally. The considerable surface area of the semiamorphous I/II-HCl-200C might be explained by a lesser amount of the expulsed H_4L^4 ligand in the pores (indeed, the PXRD pattern of parent I/II-HCl-as corresponds slightly better to phase II than to I according to PXRD). The material prepared without a modulator, I/II-no-modul-200C, demonstrated the lowest surface area, indicating that the use of modulators has a beneficial effect in partial "crystallization" at elevated temperatures.

The mixed-ligand material, I/IId-mix-HCl-200C, had a surface area of 452 $m^2\ g^{-1}$, which is right in-between the values for I/II-HCl-200C and I/IId-HCl-200C materials, based on pure H_4L^4 and H_3L^3, respectively (400−550 $m^2\ g^{-1}$). Even if the increase of the H_3L^3 share expectedly decreased the surface area, the moderate influence confirms that H_3L^3 functions similarly to H_4L^4. However, there is an interesting distinction from the H_3L^3-only based material. Unlike the H_4L^4- or mixed-ligand-based materials with adsorption isotherms characteristic for microporous solids (type I isotherm, IUPAC classification), the H_3L^3-only based material demonstrates a strong and distinctive mesoporosity with a very pronounced, large hysteresis (type IV; Figure 9b). It could be interpreted the next way: the "truncation" of one "branch" of the H_4L^4 decreases the local order (crystallinity), which is associated with high microporosity. However, the "truncation" creates more defects, which translates to larger mesoporosity. The result bears an interesting similarity to mostly amorphous covalent organic framework materials, based on tris- and tetrakis-adamantanes,[58] where no dramatic difference exists between the two (even if larger values could be predicted for the tetrahedral building blocks due to possible realization of highly symmetric periodic structures).

Water Stability. **1′** and **2′** were subjected to water stability tests. The degassed samples were left in contact with water for 1 day at room temperature and for 1 h at 100 °C. The treatment at room temperature showed some deterioration of the crystallinity of **1′** with a clear tendency to commence the transition to phase II (equiv to **2′**) and no changes in crystallinity of **2′** (Figure S23). The treatment in boiling water caused complete transition of **1′** to phase II with a crystallinity not visibly different from the initial sample of **2′**, or **2′** treated with boiling water. As for the actual surface areas (Table S4), the treatment in water even at room temperature causes a drop approximately four times, with a further decrease after the treatment in boiling water. Thus, the water stability of the synthesized materials is low. The most remarkable observation is that water stimulates the conversion of **1′** to **2′** at significantly lower temperatures than observed in the solid state.

CONCLUSIONS

The Zr-PCP/MOF structure of **1** features a highly symmetric tetrahedral ligand and yet, unexpectedly, it is of low symmetry ($C2/c$). The structure, based on an unusual 10 connected Zr_6 cluster, has a significant proven porosity (up to 1190 $m^2\ g^{-1}$) and is in a number of ways remarkable. The monodeprotonated HL^4 ligand in the $[Zr_6(\mu_3\text{-}O)_4(\mu_3\text{-}OH)_4(L^4)\text{-}(HL^4)_2(OH)_2(H_2O)_2]$ framework is equivalent to a trifunctionalized "truncated" tetrahedral ligand. Such structural organization allows the introduction of a bulky functionality instead of the noninvolved carboxyphenyl moiety. Alternatively, the noninvolved carboxy groups, protruding inside the cavities and nearly meeting with each other, are suitable for postsynthetic anchoring of functional entities, particularly for building up coordination-bonded clusters.

The conversion of **1** to the expected **flu** structure of **2′** with higher symmetry ($I4/m$) takes place at a relatively low temperature (<190 °C) in a vacuum. It is a relatively rare phase transition for PCPs, as it undergoes it in the solid state (no solvent assistance) and is accompanied with expulsion of a ligand (notably, the conversion also takes place in the presence of water, very slowly, at near room temperature and fast at 100

DOI: 10.1021/acs.inorgchem.9b01721
Inorg. Chem. 2019, 58, 12786−12797

°C). The latter is hosted in the pores of the structure, and **2′** is an inclusion compound with a $[Zr_6(\mu_3\text{-}O)_4(\mu_3\text{-}OH)_4(OH)_4(L^4)_2]\cdot H_4L^4$ formula (the ligand is geometrically larger than the vdW size of the pore openings). The solid-state network rearrangement with ligand expulsion in the pores is a potential method for encapsulation of functional entities, superior to the simpler "ship-in-the-bottle" synthesis.

Interestingly, the complex three-nodal topology of **1** and the **flu** topology of **2′** are related. The imaginary transformation that makes them equivalent is the merge of certain three-connected node pairs in a single four-connected node by making two pairs of edges common (the node pairs are close in the structure, which might explain the facility of the transformation). The structure of **1** could be viewed as a "defect" structure, but in an unusual, inversed way: it contains an excess of ligands, and the thermally induced phase transition "heals" the structure (the "standard" PCP/MOFs defects are associated with lack of ligands).

The attempt to synthesize a pure crystalline analog of **1** with a trifunctional L^3 "truncated" ligand equivalent to HL^4 was not successful. The best quality crystals were enriched by H_4L^4 compared to H_3L^3, seemingly due to a high solubility difference (it might be a lesser issue in the case of potential functionalized H_3RL^3 ligands). However, the mixed ligand approach was successful for semiamorphous products, which could be obtained in high yields using HCl as a modulator. The semiamorphous PCP gels increase their crystallinity upon thermal treatment and demonstrate close porosities of 400–550 $m^2\ g^{-1}$ when synthesized using pure ligands or their mixtures alike. The structures of the partially crystallized gels (phase I/II) could be regarded as composed of domains corresponding to frameworks of **1** and **2** according to the intermediary nature of the respective PXRD patterns.

■ ASSOCIATED CONTENT

Supporting Information

The Supporting Information is available free of charge on the ACS Publications website at DOI: 10.1021/acs.inorgchem.9b01721.

Detailed synthetic descriptions, SCXRD crystal data and refinement for **1** as well as for its variants, topological description of **1**, PXRD based model of **2** and refinement details, TGA, gas adsorption data, ^{1}H NMR spectra, and FT-IR spectra (PDF)

Crystallography_extended.cif containing all relevant structural data, including the isostructural compound obtained with acetic acid as a modulator and a refinement variant with retained solvent molecules (CIF)

Accession Codes

CCDC 1921424 and 1955286 contains the supplementary crystallographic data for this paper. These data can be obtained free of charge via www.ccdc.cam.ac.uk/data_request/cif, or by emailing data_request@ccdc.cam.ac.uk, or by contacting The Cambridge Crystallographic Data Centre, 12 Union Road, Cambridge CB2 1EZ, UK; fax: +44 1223 336033.

■ AUTHOR INFORMATION

Corresponding Authors

*E-mail: ishtvan.boldog@gmail.com.
*E-mail: janiak@uni-duesseldorf.de.

ORCID

Roman Bulánek: 0000-0002-9926-6823
Christoph Janiak: 0000-0002-6288-9605
Ishtvan Boldog: 0000-0001-6077-4524

Notes

The authors declare no competing financial interest.

■ ACKNOWLEDGMENTS

R.B. acknowledges the funding by "Intelligent Design of Nanoporous Adsorbents and Catalysts" no. P106/12/G015 from the Czech Science Foundation, and C.J. expresses his gratitude for the support by Optimat 03SF0492C grant from the Federal German Ministry of Education and Research (BMBF). The authors are grateful to Dr. Michal Dusek and Dr. Pavel Macek from the Academy of Sciences of the Czech Republic for respectively organizing and carrying out the high-quality PXRD capillary measurements. Dr. Tobias Stürzer and Dr. Holger Ott from Bruker AXS GmbH are acknowledged for their effort in testing the identity of the I/II-PhCOOH-as sample with the newest state-of-art single crystal diffractometer.

■ REFERENCES

(1) Bai, Y.; Dou, Y.; Xie, L.-H.; Rutledge, W.; Li, J.-R.; Zhou, H.-C. Zr-Based Metal-Organic Frameworks: Design, Synthesis, Structure, and Applications. *Chem. Soc. Rev.* **2016**, *45*, 2327–2367.

(2) Lu, W.; Yuan, D.; Makal, T. A.; Wei, Z.; Li, J.-R.; Zhou, H.-C. Highly Porous Metal-Organic Framework Sustained with 12-Connected Nanoscopic Octahedra. *Dalton Trans* **2013**, *42*, 1708–1714.

(3) Li, B.; Wen, H.-M.; Zhou, W.; Chen, B. Porous Metal-Organic Frameworks for Gas Storage and Separation: What, How, and Why? *J. Phys. Chem. Lett.* **2014**, *5*, 3468–3479.

(4) Wang, Y.; Zhao, D. Beyond Equilibrium: Metal-Organic Frameworks for Molecular Sieving and Kinetic Gas Separation. *Cryst. Growth Des.* **2017**, *17*, 2291–2308.

(5) Wang, B.; Lv, X.-L.; Feng, D.; Xie, L.-H.; Zhang, J.; Li, M.; Xie, Y.; Li, J.-R.; Zhou, H.-C. Highly Stable Zr(IV)-Based Metal-Organic Frameworks for the Detection and Removal of Antibiotics and Organic Explosives in Water. *J. Am. Chem. Soc.* **2016**, *138*, 6204–6216.

(6) Xie, L.-H.; Liu, X.-M.; He, T.; Li, J.-R. Metal-Organic Frameworks for the Capture of Trace Aromatic Volatile Organic Compounds. *Chem.* **2018**, *4*, 1911–1927.

(7) Wu, M.-X.; Yang, Y.-W. Metal-Organic Framework (MOF)-Based Drug/Cargo Delivery and Cancer Therapy. *Adv. Mater.* **2017**, *29*, 1606134.

(8) Lee, J.; Farha, O. K.; Roberts, J.; Scheidt, K. A.; Nguyen, S. T.; Hupp, J. T. Metal-Organic Framework Materials as Catalysts. *Chem. Soc. Rev.* **2009**, *38*, 1450–1459.

(9) Huang, Y.-B.; Liang, J.; Wang, X.-S.; Cao, R. Multifunctional Metal-Organic Framework Catalysts: Synergistic Catalysis and Tandem Reactions. *Chem. Soc. Rev.* **2017**, *46*, 126–157.

(10) Liu, J.; Chen, L.; Cui, H.; Zhang, J.; Zhang, L.; Su, C.-Y. Applications of Metal-Organic Frameworks in Heterogeneous Supramolecular Catalysis. *Chem. Soc. Rev.* **2014**, *43*, 6011–6061.

(11) Zhang, T.; Lin, W. Metal-Organic Frameworks for Artificial Photosynthesis and Photocatalysis. *Chem. Soc. Rev.* **2014**, *43*, 5982–5993.

(12) Sun, D.; Li, Z. Robust Ti- and Zr-Based Metal-Organic Frameworks for Photocatalysis. *Chin. J. Chem.* **2017**, *35*, 135–147.

(13) Lustig, W. P.; Mukherjee, S.; Rudd, N. D.; Desai, A. V.; Li, J.; Ghosh, S. K. Metal-Organic Frameworks: Functional Luminescent and Photonic Materials for Sensing Applications. *Chem. Soc. Rev.* **2017**, *46*, 3242–3285.

DOI: 10.1021/acs.inorgchem.9b01721
Inorg. Chem. 2019, 58, 12786–12797

(14) Stavila, V.; Talin, A. A.; Allendorf, M. D. MOF-Based Electronic and Opto-Electronic Devices. *Chem. Soc. Rev.* **2014**, *43*, 5994−6010.
(15) Garibay, S. J.; Cohen, S. M. Isoreticular Synthesis and Modification of Frameworks with the UiO-66 Topology. *Chem. Commun.* **2010**, *46*, 7700−7702.
(16) Cmarik, G. E.; Kim, M.; Cohen, S. M.; Walton, K. S. Tuning the Adsorption Properties of UiO-66 via Ligand Functionalization. *Langmuir* **2012**, *28*, 15606−15613.
(17) Biswas, S.; Van Der Voort, P. A General Strategy for the Synthesis of Functionalised UiO-66 Frameworks: Characterisation, Stability and CO 2 Adsorption Properties. *Eur. J. Inorg. Chem.* **2013**, *2013*, 2154−2160.
(18) Ragon, F.; Campo, B.; Yang, Q.; Martineau, C.; Wiersum, A. D.; Lago, A.; Guillerm, V.; Hemsley, C.; Eubank, J. F.; Vishnuvarthan, M.; Taulelle, F.; Horcajada, P.; Vimont, A.; Llewellyn, P. L.; Daturi, M.; Devautour-Vinot, S.; Maurin, G.; Serre, C.; Devic, T.; Clet, G. Acid-Functionalized UiO-66(Zr) MOFs and Their Evolution after Intra-Framework Cross-Linking: Structural Features and Sorption Properties. *J. Mater. Chem. A* **2015**, *3*, 3294−3309.
(19) Manna, K.; Zhang, T.; Greene, F. X.; Lin, W. Bipyridine- and Phenanthroline-Based Metal-Organic Frameworks for Highly Efficient and Tandem Catalytic Organic Transformations via Directed C-H Activation. *J. Am. Chem. Soc.* **2015**, *137*, 2665−2673.
(20) Chen, T.-H.; Popov, I.; Miljanić, O. Š. A Zirconium Macrocyclic Metal-Organic Framework with Predesigned Shape-Persistent Apertures. *Chem. - Eur. J.* **2017**, *23*, 286−290.
(21) Eddaoudi, M.; Kim, J.; Rosi, N.; Vodak, D.; Wachter, J.; O'Keeffe, M.; Yaghi, O. M. Systematic Design of Pore Size and Functionality in Isoreticular MOFs and Their Application in Methane Storage. *Science* **2002**, *295*, 469−472.
(22) Deng, H.; Grunder, S.; Cordova, K. E.; Valente, C.; Furukawa, H.; Hmadeh, M.; Gándara, F.; Whalley, A. C.; Liu, Z.; Asahina, S.; Kazumori, H.; O'Keeffe, M.; Terasaki, O.; Stoddart, J. F.; Yaghi, O. M. Large-Pore Apertures in a Series of Metal-Organic Frameworks. *Science* **2012**, *336*, 1018−1023.
(23) Feng, D.; Wang, K.; Wei, Z.; Chen, Y.-P.; Simon, C. M.; Arvapally, R. K.; Martin, R. L.; Bosch, M.; Liu, T.-F.; Fordham, S.; Yuan, D.; Omary, M. A.; Haranczyk, M.; Smit, B.; Zhou, H.-C. Kinetically Tuned Dimensional Augmentation as a Versatile Synthetic Route towards Robust Metal-Organic Frameworks. *Nat. Commun.* **2014**, *5*, 5723.
(24) Zhai, Q.-G.; Bu, X.; Mao, C.; Zhao, X.; Daemen, L.; Cheng, Y.; Ramirez-Cuesta, A. J.; Feng, P. An Ultra-Tunable Platform for Molecular Engineering of High-Performance Crystalline Porous Materials. *Nat. Commun.* **2016**, *7*, 13645.
(25) Liu, T.-F.; Feng, D.; Chen, Y.-P.; Zou, L.; Bosch, M.; Yuan, S.; Wei, Z.; Fordham, S.; Wang, K.; Zhou, H.-C. Topology-Guided Design and Syntheses of Highly Stable Mesoporous Porphyrinic Zirconium Metal-Organic Frameworks with High Surface Area. *J. Am. Chem. Soc.* **2015**, *137*, 413−419.
(26) Zhang, M.; Chen, Y.-P.; Bosch, M.; Gentle, T.; Wang, K.; Feng, D.; Wang, Z. U.; Zhou, H.-C. Symmetry-Guided Synthesis of Highly Porous Metal-Organic Frameworks with Fluorite Topology. *Angew. Chem., Int. Ed.* **2014**, *53*, 815−818.
(27) Feng, D.; Gu, Z.-Y.; Li, J.-R.; Jiang, H.-L.; Wei, Z.; Zhou, H.-C. Zirconium-Metalloporphyrin PCN-222: Mesoporous Metal-Organic Frameworks with Ultrahigh Stability as Biomimetic Catalysts. *Angew. Chem., Int. Ed.* **2012**, *51*, 10307−10310.
(28) Feng, D.; Chung, W.-C.; Wei, Z.; Gu, Z.-Y.; Jiang, H.-L.; Chen, Y.-P.; Darensbourg, D. J.; Zhou, H.-C. Construction of Ultrastable Porphyrin Zr Metal-Organic Frameworks through Linker Elimination. *J. Am. Chem. Soc.* **2013**, *135*, 17105−17110.
(29) Jiang, H.-L.; Feng, D.; Wang, K.; Gu, Z.-Y.; Wei, Z.; Chen, Y.-P.; Zhou, H.-C. An Exceptionally Stable, Porphyrinic Zr Metal-Organic Framework Exhibiting PH-Dependent Fluorescence. *J. Am. Chem. Soc.* **2013**, *135*, 13934−13938.
(30) Queen, W. L.; Hudson, M. R.; Jiang, J.; Yaghi, O. M.; Gándara, F.; Furukawa, H.; Zhang, Y. Water Adsorption in Porous Metal-Organic Frameworks and Related Materials. *J. Am. Chem. Soc.* **2014**, *136*, 4369−4381.
(31) Feng, D.; Wang, K.; Su, J.; Liu, T.-F.; Park, J.; Wei, Z.; Bosch, M.; Yakovenko, A.; Zou, X.; Zhou, H.-C. A Highly Stable Zeotype Mesoporous Zirconium Metal-Organic Framework with Ultralarge Pores. *Angew. Chem., Int. Ed.* **2015**, *54*, 149−154.
(32) Ma, J.; Wong-Foy, A. G.; Matzger, A. J. The Role of Modulators in Controlling Layer Spacings in a Tritopic Linker Based Zirconium 2D Microporous Coordination Polymer. *Inorg. Chem.* **2015**, *54*, 4591−4593.
(33) Feng, D.; Jiang, H.-L.; Chen, Y.-P.; Gu, Z.-Y.; Wei, Z.; Zhou, H.-C. Metal-Organic Frameworks Based on Previously Unknown Zr 8 /Hf 8 Cubic Clusters. *Inorg. Chem.* **2013**, *52*, 12661−12667.
(34) Guillerm, V.; Ragon, F.; Dan-Hardi, M.; Devic, T.; Vishnuvarthan, M.; Campo, B.; Vimont, A.; Clet, G.; Yang, Q.; Maurin, G.; Férey, G.; Vittadini, A.; Gross, S.; Serre, C. A Series of Isoreticular, Highly Stable, Porous Zirconium Oxide Based Metal-Organic Frameworks. *Angew. Chem., Int. Ed.* **2012**, *124*, 9401−9405.
(35) Taddei, M. When Defects Turn into Virtues: The Curious Case of Zirconium-Based Metal-Organic Frameworks. *Coord. Chem. Rev.* **2017**, *343*, 1−24.
(36) Shearer, G. C.; Chavan, S.; Bordiga, S.; Svelle, S.; Olsbye, U.; Lillerud, K. P. Defect Engineering: Tuning the Porosity and Composition of the Metal-Organic Framework UiO-66 via Modulated Synthesis. *Chem. Mater.* **2016**, *28*, 3749−3761.
(37) Katz, M. J.; Brown, Z. J.; Colón, Y. J.; Siu, P. W.; Scheidt, K. A.; Snurr, R. Q.; Hupp, J. T.; Farha, O. K. A Facile Synthesis of UiO-66, UiO-67 and Their Derivatives. *Chem. Commun. (Cambridge, U. K.)* **2013**, *49*, 9449−9451.
(38) Nguyen, H. G. T.; Schweitzer, N. M.; Chang, C.-Y.; Drake, T. L.; So, M. C.; Stair, P. C.; Farha, O. K.; Hupp, J. T.; Nguyen, S. T. Vanadium-Node-Functionalized UiO-66: A Thermally Stable MOF-Supported Catalyst for the Gas-Phase Oxidative Dehydrogenation of Cyclohexene. *ACS Catal.* **2014**, *4*, 2496−2500.
(39) Hu, Z.; Zhao, D. Metal-Organic Frameworks with Lewis Acidity: Synthesis, Characterization, and Catalytic Applications. *CrystEngComm* **2017**, *19*, 4066−4081.
(40) Jiang, J.; Gándara, F.; Zhang, Y.-B.; Na, K.; Yaghi, O. M.; Klemperer, W. G. Superacidity in Sulfated Metal-Organic Framework-808. *J. Am. Chem. Soc.* **2014**, *136*, 12844−12847.
(41) Zhu, L.; Liu, X.-Q.; Jiang, H.-L.; Sun, L.-B. Metal-Organic Frameworks for Heterogeneous Basic Catalysis. *Chem. Rev.* **2017**, *117*, 8129−8176.
(42) Dhakshinamoorthy, A.; Asiri, A. M.; Garcia, H. Metal-Organic Frameworks Catalyzed C-C and C-Heteroatom Coupling Reactions. *Chem. Soc. Rev.* **2015**, *44*, 1922−1947.
(43) Dhakshinamoorthy, A.; Garcia, H. Metal-Organic Frameworks as Solid Catalysts for the Synthesis of Nitrogen-Containing Heterocycles. *Chem. Soc. Rev.* **2014**, *43*, 5750−5765.
(44) Dhakshinamoorthy, A.; Opanasenko, M.; Čejka, J.; Garcia, H. Metal Organic Frameworks as Heterogeneous Catalysts for the Production of Fine Chemicals. *Catal. Sci. Technol.* **2013**, *3*, 2509−2540.
(45) Xu, T.; Hou, X.; Wang, Y.; Zhang, J.; Zhang, J.; Liu, B. A Gigantic Polyoxozirconate with Visible Photoactivity. *Dalt. Trans.* **2017**, *46*, 10185−10188.
(46) Zhao, T.; Heering, C.; Boldog, I.; Domasevitch, K. V.; Janiak, C. A View on Systematic Truncation of Tetrahedral Ligands for Coordination Polymers. *CrystEngComm* **2017**, *19*, 776−780.
(47) Liu, J.; Wang, W.; Luo, Z.; Li, B.; Yuan, D. Microporous Metal-Organic Framework Based on Ligand-Truncation Strategy with High Performance for Gas Adsorption and Separation. *Inorg. Chem.* **2017**, *56*, 10215−10219.
(48) Newman, H. Facile Syntheses of 1,3-Diphenyl-, 1,3,5-Triphenyl-, and 1,3,5,7-Tetraphenyladamantane from 1-Bromoadamantane. *Synthesis* **1972**, *1972*, 692−693.
(49) Bon, V.; Senkovska, I.; Baburin, I. A.; Kaskel, S. Zr- and Hf-Based Metal-Organic Frameworks: Tracking Down the Polymorphism. *Cryst. Growth Des.* **2013**, *13*, 1231−1237.

DOI: 10.1021/acs.inorgchem.9b01721
Inorg. Chem. 2019, 58, 12786−12797

(50) Ma, J.; Tran, L. D.; Matzger, A. J. Toward Topology Prediction in Zr-Based Microporous Coordination Polymers: The Role of Linker Geometry and Flexibility. *Cryst. Growth Des.* **2016**, *16*, 4148−4153.
(51) Zhang, X.; Zhang, X.; Johnson, J. A.; Chen, Y.-S.; Zhang, J. Highly Porous Zirconium Metal-Organic Frameworks with β-UH 3 -like Topology Based on Elongated Tetrahedral Linkers. *J. Am. Chem. Soc.* **2016**, *138*, 8380−8383.
(52) Bonneau, C.; O'Keeffe, M. High-Symmetry Embeddings of Interpenetrating Periodic Nets. Essential Rings and Patterns of Catenation. *Acta Crystallogr., Sect. A: Found. Adv.* **2015**, *71*, 82−91.
(53) Delgado Friedrichs, O.; O'Keeffe, M.; Yaghi, O. M. The CdSO4, Rutile, Cooperite and Quartz Dual Nets: Interpenetration and Catenation. *Solid State Sci.* **2003**, *5*, 73−78.
(54) O'Keeffe, M.; Peskov, M. A.; Ramsden, S. J.; Yaghi, O. M. The Reticular Chemistry Structure Resource (RCSR) Database of, and Symbols for, Crystal Nets. *Acc. Chem. Res.* **2008**, *41*, 1782−1789.
(55) Düren, T.; Millange, F.; Férey, G.; Walton, K. S.; Snurr, R. Q. Calculating Geometric Surface Areas as a Characterization Tool for Metal-Organic Frameworks. *J. Phys. Chem. C* **2007**, *111*, 15350−15356.
(56) Spek, A. L. PLATON SQUEEZE: A Tool for the Calculation of the Disordered Solvent Contribution to the Calculated Structure Factors. *Acta Crystallogr., Sect. C: Struct. Chem.* **2015**, *71*, 9−18.
(57) Willems, T. F.; Rycroft, C. H.; Kazi, M.; Meza, J. C.; Haranczyk, M. Algorithms and Tools for High-Throughput Geometry-Based Analysis of Crystalline Porous Materials. *Microporous Mesoporous Mater.* **2012**, *149*, 134−141.
(58) Bhunia, A.; Boldog, I.; Möller, A.; Janiak, C. Highly Stable Nanoporous Covalent Triazine-Based Frameworks with an Adamantane Core for Carbon Dioxide Sorption and Separation. *J. Mater. Chem. A* **2013**, *1*, 14990−14999.

NOTE ADDED AFTER ASAP PUBLICATION

This paper was published on the Web on September 18, 2019. A CIF file was added to the paper, and the corrected version was reposted on September 24, 2019.

DOI: 10.1021/acs.inorgchem.9b01721
Inorg. Chem. 2019, 58, 12786−12797

Supplementary Information

Ligand excess 'inverse-defected' Zr_6 tetrahedral tetracarboxylate framework, and its thermal transformation

Bahareh Nateghi,[a] Kostiantyn V. Domasevitch,[b] Roman Bulánek,[c] Christoph Janiak*[a], Ishtvan Boldog*[c]

[a] Institute of Inorganic Chemistry and Structural Chemistry, Heinrich-Heine-Universität Düsseldorf, Universitätsstr. 1, D-40225 Düsseldorf, Germany.
[b] Inorganic Chemistry Department, Taras Shevchenko National University of Kyiv, Volodymyrska Str. 64/13, Kyiv 01601, Ukraine
[c] University of Pardubice, Faculty of Chemical Technology, Department of Physical Chemistry, Studentská 573,532 10 Pardubice, Czech Republic.

E-mails: ishtvan.boldog@gmail.com, janiak@uni-duesseldorf.de

Contents

1. Synthesis

Materials. $ZrCl_4$ (99%, Sigma-Aldrich), $ZrOCl_2 \cdot 8H_2O$ (99%, Sigma-Aldrich), N,N-dimethylformamide (DMF; 99.8%, Sigma-Aldrich), formic acid (99%, Sigma-Aldrich) were used as delivered. Benzoic acid, trifluoroacetic acid, conc. aqueous hydrochloric acid (35-37%, $\rho \sim 1.19$ g cm^{-3}) were *p.a.* grade (*pro analysis*, puriss) or equivalent. The ((adamantane-1,3,5,7-tetrayl)tetra(phen-4-yl))tetracarboxylic acid (H_4L^4), ((adamantane-1,3,5-triyl)tri(phen-4-

yl))tricarboxylic acid (H_3L^3) and ((adamantane-1,3-diyl)-diphen-4-yl) dicarboxylic acid (H_2L^2) were synthesized according to the literature [1].

The results on synthetic screening and synthesis of the final compounds are summarized in Tables S1, 2.

General method of synthesis: In a typical experiment, 0.1 mmol of $ZrCl_4$ or $ZrOCl_2 \cdot 8H_2O$ were thoroughly dissolved in 1-4 ml DMF. The specified amount of modulator(s) (2-100 mmol) was subsequently added. After complete dissolution and homogenization, 0.033 mmol of H_4L^4 and/or H_3L^3 were added in 1-2 ml of DMF (according to our experience the addition of the ligand in solid form is acceptable, but might necessitate prolonged shaking). The mixture was homogenized until formation of a clear solution (minor turbidity was admissible). The solution was hermetically sealed in a threaded culture tube of a suitable size (6-12 ml) with a PTFE-lined screw cap. The sealed tube was heated for 24 h at 130 °C. If no precipitate was formed, or its quantity was not significant, the heating was continued at 130 °C for three more days (Caution! Pressure build up in the vessels are possible, particularly when formic acid is used. While not posing significant risk, the cracking of typical commercial plastic caps for culture tubes might happen). After cooling, the precipitate was centrifuged out and washed once by DMF, once by acetone and dried in air to permanent weight (the lengthy drying, which could have taken up too one week, was rigorously followed for the samples intended for all analytics except PXRD and adsorption studies. In the latter case, the batches were dried for approx. one day, aiming shorter contact time with air). For preparation of larger quantities parallel syntheses were used (i.e. the volumes were not scaled up).

The description for the principal materials, with IR and elemental analysis included, are given below (the quantities for other syntheses are given in Table S2).

Synthesis of **1** (I-HCOOH-as): To 42 mg (0.13 mmol) of $ZrOCl_2 \cdot 8H_2O$ dissolved in a mixture of 2.60 ml of DMF and 2.64 ml of HCOOH, a solution of 22 mg (0.036 mmol) of H_4L^4 in 2 ml of DMF was added and thoroughly homogenized (note: in all standard syntheses H_4L^4 containing ~3%$_{mol}$ of H_3L^3 was used. The only role of the minor component is to slightly improve the crystallinity. The synthesis could be performed using pure H_4L^4 with similar results). The solution was sealed in a culture tube and heated at 130 °C for 96 h. The formed microcrystalline precipitate, consisting of small single-crystals suitable for SCXRD studies was filtered off, washed once with DMF, once with acetone and dried in air. Yield: 9 mg (18%). When acetic acid is used, the yield of 1-AcOH-as was 20.2 mg (~40%).
Elemental analysis for $[Zr_6(\mu_3\text{-}O)_4(\mu_3\text{-}OH)_4(L^4)(HL^4)_2(OH)_2(H_2O)_2] \cdot 4$ DMF $\cdot$ 2 HCOOH $\cdot$ 4 H_2O, $C_{128}H_{136}O_{48}N_4Zr_6$; calcd (%): C 50.48, H 4.50, N 1.84; found (%): C 47.44, H 5.16, N 2.58.
FT-IR ATR (neat) ν / cm^{-1}: 3489 w vbr, 2930 w br, 2846 w, br, 1653 vs 1597 m, 1550 w, 1499 w, 1387 w, 1255 w, 1187 w, 1094 s, 1016 w, 862 w, 764 m, 712 w, 658 s.

Synthesis of **1´** (I-HCOOH-120C): **1**, after sc-CO_2 drying (see the procedure on p. 16), was heated in vacuum (10^{-3} mbar) at 120 °C, for 3 h.
Elemental analysis for $[Zr_6(\mu_3\text{-}O)_4(\mu_3\text{-}OH)_4(L^4)(HL^4)_2(OH)_2]$, $C_{114}H_{92}O_{34}Zr_6$; calcd (%): C 53.63, H 3.63, N 0.00; found (%): C 53.59, H 4.26, N 0.41.
FT-IR ATR (neat) ν / cm^{-1}: 2925 w br, 2842 w, 1698 w, 1605 s, 1536 m, 1409 vs, 1353 s, 1189 m, 1111 w, 1015 w, 947 w, 854 m , 761 s, 709 w, 651 m.

Synthesis of **2´** (sample I-HCOOH-220C): **1** was heated in vacuum (10^{-3} mbar) at 220 °C for at least 3 h (in a few cases, 190 °C was used with similar outcome).
Elemental analysis for $[Zr_6(\mu_3\text{-}O)_4(\mu_3\text{-}OH)_4(OH)_4(L^4)_2]$ · H_4L^4, $C_{114}H_{96}O_{36}Zr_6$; calcd (%): C 52.88, H 3.74, N 0.00; found (%): C 50.96, H 3.80, N 0.51.
FT-IR ATR (neat) ν / cm^{-1}: 2918 w br, 1698 w, 1605 s, 1536 m , 1408 vs , 1346 s, 1189 m, 1111 w, 1015 m, 945 w, 854 w, 761 s, 703 m, 651 s.

Synthesis of I/II-HCl-as: To a solution of 19 mg (0.08 mmol) of $ZrCl_4$ in 1.5 ml of DMF and 0.17 ml of HCl (~2.0 mmol) a solution of 20 mg of H_4L^4 (0.033 mmol) in 1 ml of DMF was added. The mixture was thoroughly homogenized, sealed in a culture tube and heated at 130°C for 24 h. The formed white gel-like product was washed once by DMF and once by acetone followed by drying in air. Yield of the white solid was 31 mg (74%-approx.).
FT-IR ATR (neat) ν / cm^{-1}: 3474 vbr, 2930 w, 2850 w, 1655 vs, 1594 m, 1500 w, 1386 vs, 1255 m, 1189 w, 1092 s, 1015 w, 864 w, 764 m, 658 s.

Synthesis of I/II-HCl-220C: I/II-HCl-as was heated in vacuum (10^{-3} mbar) at 220 °C for at least 3 h.
Elemental analysis for $[Zr_6(\mu_3\text{-}O)_4(\mu_3\text{-}OH)_4(OH)_4(L^4)_2]$ (equivalent to phase II type), $C_{76}H_{64}O_{28}Zr_6$; calcd (%): C 46.27, H 3.74, N 0.00; found (%): C 44.04, H 3.06, N 0.41.
FT-IR ATR (neat) ν / cm^{-1}: 2920 vw, 2851 vw, 1655 m, 1607 s, 1527 s, 1414 vs, 1190 w, 1111 w, 1016 w, 856 w, 765 s, 705 m, 656 m

Table S1. Preliminary screening of the synthetic conditions screening, aiming crystalline Zr-PCP products for H_4L^4, H_3L^3 ligands or their mixtures (the most relevant experiments are listed).

N	$ZrCl_4$		$ZrOCl_2 \cdot 8H_2O$		H_4L^4		H_3L^3		Modulator (Solvent)	Amount of modulator		Amount of solvent		Temp. (time)	Yield [a]		Comment	Exp. code
	mg	mmol	mg	mmol	mg	mmol	mg	mmol		mg	mmol	ml	mmol	°C (h)	mg	%		
1	23	0.10			20	0.032	-	-	- (DMF)	-	-	3.4	46.5	120 (24)	11	27	White solid	
2	23	0.10			20	0.032	-	-	PhCOOH (DMF)	926	7.6	2.4	32.8	120 (96)	9	22	White microcrystalline solid	
3	23	0.10			20	0.032	-	-	HCl conc. aq. (DMF)	205	2.1	2.5	34.2	120 (24)	30	75	White solid (precipitates as a gel)	
4	23	0.10			20	0.032	-	-	HCl conc. aq. (DMF)	205	2.1	2.5	34.2	120 (24)	39	96	White solid (precipitates as a gel)	
5	23	0.10			20	0.032	-	-	HCl/TFA (DMF)	1.3 / 3.7	0.013 / 0.033	5	68.4	120 (24)	28	69	White precipitate	
6	23	0.10			20	0.032	-	-	HCl/Proline (DMF)	35 / 19	0.36 / 0.17	2	27.4	120 (24)	29	74	White precipitate	
7			21	0.07	22	0.036	-	-	HCOOH (DMF)	3355	72.9	4.5	61.6	130 (96)	9	17	Crystalline	
8	42	0.18			-		32	0.064	HCl (DMF)	371	3.8	4.6	62.9	120 (24)	28	37	White solid (precipitates as a gel)	
9	35	0.15					32	0.064	HCl (DMF)	371	3.8	4.6	62.9	120 (24)	23	30	White solid (precipitates as a gel)	
10			42	0.13			17	0.034	HCOOH (DMF)	5563	120.9	4.5	61.6	130 (96)	15	37	White solid (precipitates as a gel, non crystalline)	
11			42	0.13	22	0.036	0.5	0.001	HCOOH (DMF)	5563	120.9	8.1	110.8	130 (96)	9	16	White solid (precipitates as a gel)	

[a] The percentual yields are indicative, the molecular weights were approximated in most cases. See also the footnote for Table 2.

Table S2. Synthetic summary on primary materials (the materials obtained via further degassing are not listed).

N	$ZrCl_4$		$ZrOCl_2 \cdot 8H_2O$		H_4L^4		H_3L^3		Modulator (Solvent)	Amount of modulator			Amount of solvent		Temp. (time)	Yield		Comment
	mg	mmol	mg	mmol	mg	mmol	mg	mmol		µL	mg	mmol	ml	mmol	°C (h)	mg	%	
1-HCOOH-as [a]			32.2	0.10	20.4	0.033	-	-	HCOOH (DMF)	2641	3222	70.0	4.4	60.0	130 °C (96)	9.0	18 [b]	White, crystalline
1-AcOH-as [a]	23.3	0.10			20.4	0.033			AcOH (DMF)	2862	3003	50.0	4.4	60.0	130 °C (96)	20.2	40 [b]	White, crystalline
12-PhCOOH-as	23.3	0.10			20.4	0.033	-	-	PhCOOH (DMF)		916	7.5	4.4	60.0	130 °C (96)	10.2	24 [c]	White, mostly crystalline
12-HCl-as	23.3	0.10			20.4	0.033	-	-	HCl conc. aq. (DMF)	166	197	2.0	2.9	40.0	130 °C (24)	31.0	74 [c]	White gel
12d-mix-HCl-as	23.3	0.10			10.3	0.017	8.3	0.017	HCl conc. aq. (DMF)	166	197	2.0	2.9	40.0	130 °C (24)	31.3	77 [d]	White gel
12d-HCl-as	23.3	0.10					16.4	0.033	HCl conc. aq. (DMF)	166	197	2.0	2.9	40.0	130 °C (24)	28.0	71 [e]	White gel
12-TFA-as			32.2	0.10	20.4	0.033	16.4	0.033	TFA (DMF)	15.3	23	0.2	4.4	60.0	130 °C (96)	12.9	10 [c]	White solid
12-no-modul-as	23.3	0.10			20.4	0.033	-	-	- (DMF)	-	-	-	4.4	60.0	130 °C (96)	13.1	31 [c]	White solid

[a] The H_4L^4 ligand, used for preparation, contained app. ~3mol% of H_3L^3 for slight increase of crystallinity of the product. The synthesis could be performed with similar outcome without the use of the additive.

[b,c,d,e] The procentual yields are approximated for most cases and is intended for comparative evaluation. The used molecular weights for calculation of the yields were: b) 3046, based on fully established $[Zr_6(\mu_3\text{-}O)_4(\mu_3\text{-}OH)_4(L^4)(HL^4)_2(OH)_2(H_2O)_2] \cdot 4\,DMF \cdot 2\,HCOOH \cdot 4\,H_2O$ formula of **1**-HCOOH-as c) 2501.3 for $[Zr_6(O)_4(OH)_4(L^4)_2(OH)_4(H_2O)_4] \cdot 4\,DMF \cdot 2\,HCOOH \cdot 4\,H2O$ as a postulated dominant contributor in the semi-amorphous solids d) averaged value of cases '*c*' and '*e*' and e) 2359.18 value for hypothetic $[Zr_6(OH)_6(OH)_6(HCOO)_2(HL^3)_2]$ 4DMF 2HCOOH $4H_2O$ compound based on the H_3L^3.

2. Single crystal X-ray diffraction structures of **1** (I-HCOOH-as) and I-AcOH-as

Suitable single crystals were mounted on glass fiber and transferred to the diffractometer, a Stoe imaging plate diffraction system Stadivari with Dectris Pilatus detector and a pinhole collimator. The diffraction data were collected using a Cu X-ray source at 180(2) K under protective dinitrogen gas stream. The information regarding data collection and structure refinement is summarized in Table S3. The structures were solved by SIR-2002 [2] and refined by SHELX [3] using WinGX shell [4].

The elongated block-shaped single crystals of 1-HCOOH and 1-AcOH were similar in appearance (Fig. S1). The crystals in 1/2-PhCOOH were also elongated blocks, but practically all of them demonstrated very poor diffraction; it was only possible to index the unit cell of a very small specimen after many attempts (Table S3).

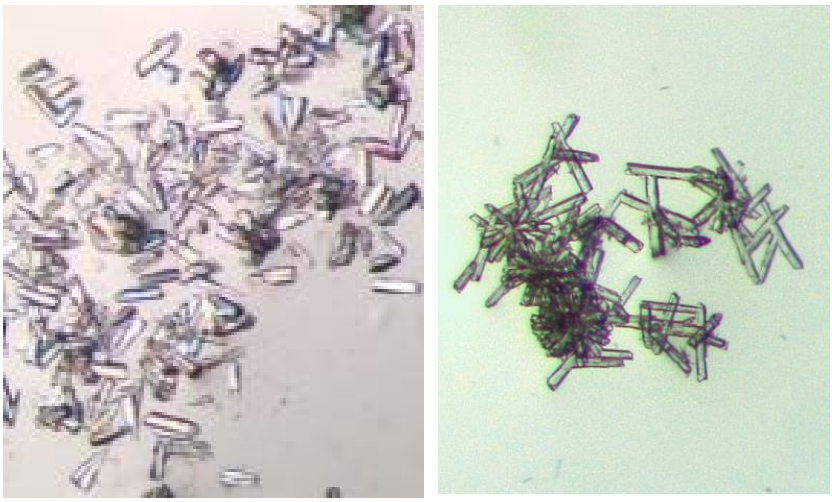

Fig. S1. Single crystals of I-HCOOH (left) and I-AcOH (right)

Refinement details. The isostructural I-HCOOH-as and I-AcOH-as were refined both with modelled guest solvent molecules and without them, using PLATON/SQUEEZE [5, 6] procedure for accounting their contribution. The two pairs of *cif* files are included as supplementary files (**nonSq** suffix in the file name indicates the SQUEEZEd structures). The results are summarized in Table 2. The quality of the **1**-HCOOH structure is significantly higher compared to **1**-AcOH and hence only the first structure with the applied SQUEEZE procedure was deposited in the Cambridge Structural Database.

Table S3 Crystal data and structure refinement for $[Zr_6(\mu_3\text{-}O)_4(\mu_3\text{-}OH)_4(L^4)(HL^4)_2(OH)_2(H_2O)_2] \cdot 4$ DMF $\cdot$ 2 HCOOH $\cdot$ 4 H_2O, **1**; $[Zr_6(\mu_3\text{-}O)_4(\mu_3\text{-}OH)_4(L^4)(HL^4)_2(OH)_2(H_2O)_2] \cdot$ *n Guest[AcOH]*, I-AcOH-as; $[Zr_6(\mu_3\text{-}O)_4(\mu_3\text{-}OH)_4(L^4)(HL^4)_2(OH)_2(H_2O)_2] \cdot$ *n Guest[PhCOOH]*, I-PhCOOH-as.

	1 (I-HCOOH-as)	**I-AcOH-as**	**I-PhCOOH-as**
Empirical formula	$C_{114}H_{96}O_{36}Zr_6$ [a]	$C_{114}H_{96}O_{36}Zr_6$ [a]	$C_{114}H_{96}O_{36}Zr_6$ [a]
M_r /g mol^{-1}	2589.34	2589.34	2589.34
T /K	180(2)	180(2) K	180(2)
Wavelength / Å [b]	1.54186	1.54186 Å	1.54186
Crystal system	Monoclinic	Monoclinic	Monoclinic
Space group	*C*2/*c*	*C*2/*c*	*C*2/*c*
a /Å	24.2611(2)	24.5829(6)	25.0642(-)
b /Å	30.9669(4)	30.8205(5)Å	29.8487(-)
c /Å	25.4544(3)	25.6723(5)	26.4363(-)
β /°	101.9120(10)	100.624(3)	97.476(-)
V /Å^3	18711.8(4)	19117.4(7)	19609.77
Z	4	4	
Calc. density /g cm^{-3}	0.919	0.900	
μ / mm^{-1}	3.058	2.993	
F(000)	5232	5232	
Crystal size /mm^3	0.10×0.08×0.06	0.08×0.05×0.04	
θ range /°	3.17 to 68.93	3.50 to 71.07	
Index ranges /*hkl*	[-29, 21]; [-34, 37]; [-21, 30]	[-24, 30]; [-30, 37]; [-31, 22]	
Reflections collected (R_{int})	96140 (0.0268)	56519 (0.1131)	
Independent reflections	17064	17877	
Completeness /% to θ /°	99.1 %	98.8 %	
Max. and min. transmission	0.6705 and 0.4922	0.876 and 0.855	
Data / restraints / parameters	17057 / 201 / 822 {17064 / 227 / 938}[d]	17877 / 277 / 823 {17881 / 299 / 871}[d]	
Goodness-of-fit	1.040 {1.074}[d]	0.930 {1.032}[d]	
$R[F^2>2\sigma(F^2)]$, *wR*2 [c]	0.0339, 0.1055 {0.0627, 0.2100}[d]	0.0592, 0.1464 {0.0931, 0.2707}[d]	
*R*1, *wR*2 (all data)	0.0389, 0.1082 {0.0698, 0.2182}[d]	0.0856, 0.1569 {0.1315, 0.2990}[d]	
Largest diff. peak and hole, eÅ^{-3}	0.691 , -0.590 {1.173, -1.158}[d]	1.060, -0.891 {1.587 and -1.221}[d]	
Solvent accessible volume per formula unit (SQUEEZE) [5]	2591	2599	
Electron count in the voids per formula unit (SQUEEZE)	668.5	735	

[a] The framework only formula

[b] Stoe Stadivari four circle diffractometer, Dectris Pilatus detector.

[c] Full-matrix least-square refinement on F^2 as implemented in SHELX-2014 [3]. $8R1 = \Sigma||F_o| - |F_c||/\Sigma|F_o|$; $wR2 = \{\Sigma[w(F_o^2\text{-}F_c^2)]^2/\Sigma[w(F_o^2)^2]\}^{1/2}$ where $w^{-1} = [\sigma^2(F_o^2) + (aP)^2 + bP]$, $P = [2F_c^2 + \mathrm{Max}(F_o^2, 0)] / 3$, *a* and *b* are refined parameters; $\mathrm{GooF} = \{\Sigma[w(F_o^2\text{-}F_c^2)^2] / (n\text{-}p)\}^{1/2}$.

[d] The R-factor values in the curly brackets refers to structure without SQUEEZE applied. Only the **1** with SQUEEZE applied is deposited in the Cambridge Structural Database). The versions without SQUEEZE for **1** and without SQUEEZE for I-AcOH-as are given as supplementary information.

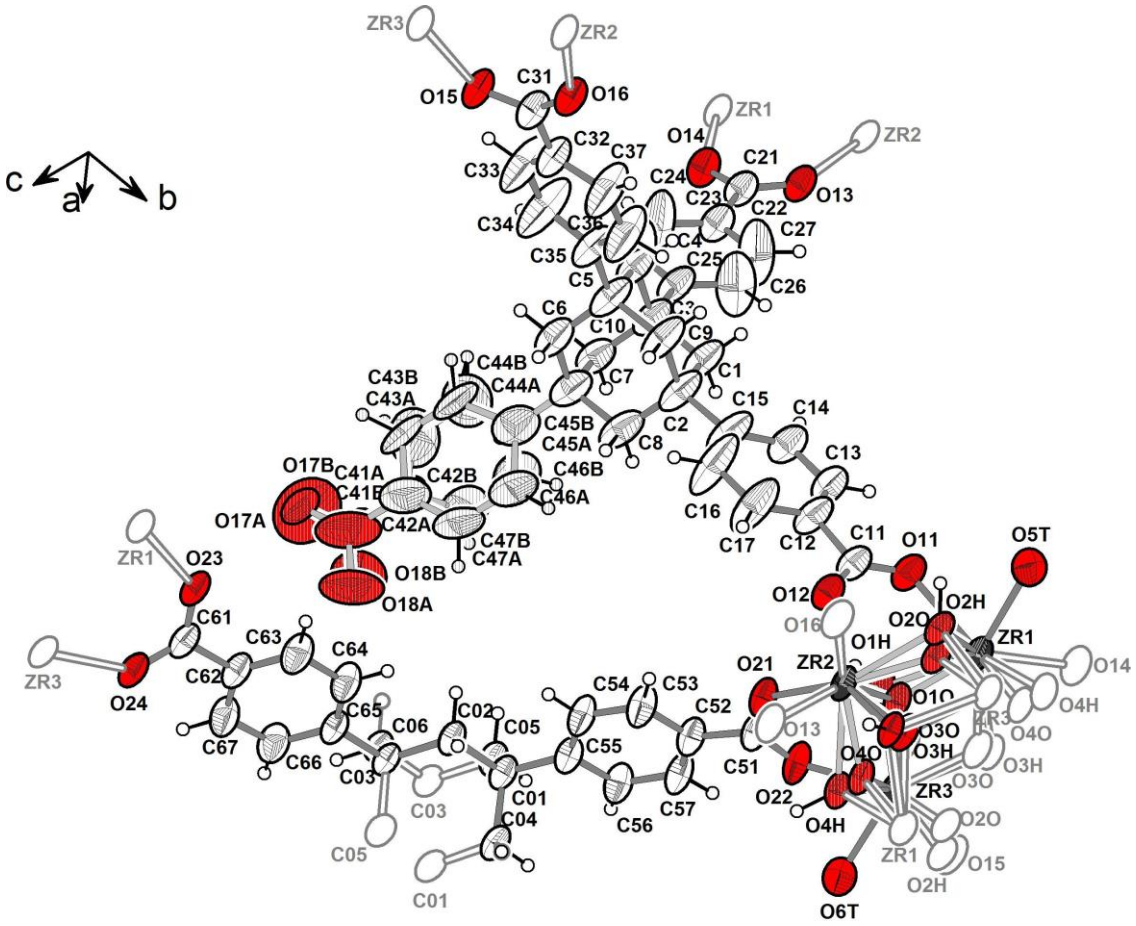

Fig. S2. ORTEP-style drawing of **1** with atom numbering. The symmetry equivalent non-hydrogen atoms are shown in light gray, with no hatching. There disordered non-coordinated carboxyphenyl group (C41-C47, O17, O18) and the site-sharing O*n*H/O*n*O, *n*=1-4 are marked with additional very fine hatching.

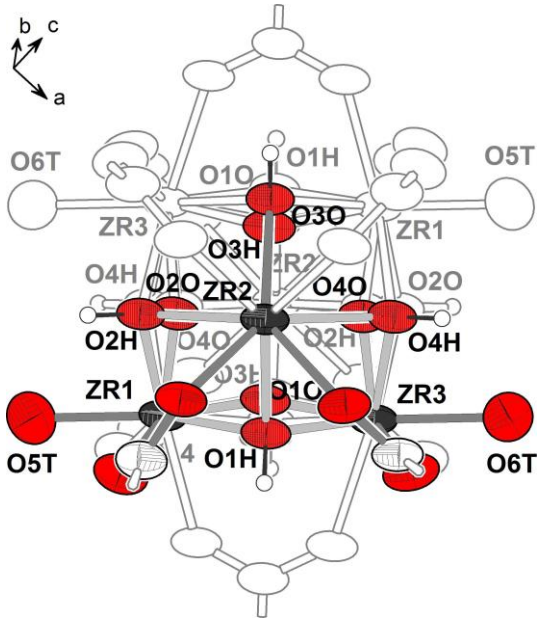

Fig. S3. ORTEP-style drawing of the {Zr_6} cluster in **1**-HCOOH. The symmetry equivalent non-hydrogen atoms are shown in light gray, with no hatching.

All non-hydrogen atoms were refined anisotropically. The atom numbering scheme is given in Fig. S2. The site-sharing oxygen atoms belonging to the μ_3-O^{2-} / μ_3-OH^- ligands were explicitly refined (the H-atoms were placed geometrically and refined in a riding model. The two-component rotational disorder of the carboxyphenyl moiety of the non-coordinated branch of the $(HL^4)^{3-}$ ligand (C41-C47, O17, O18 atoms) was refined (0.54 : 0.46 ratio).

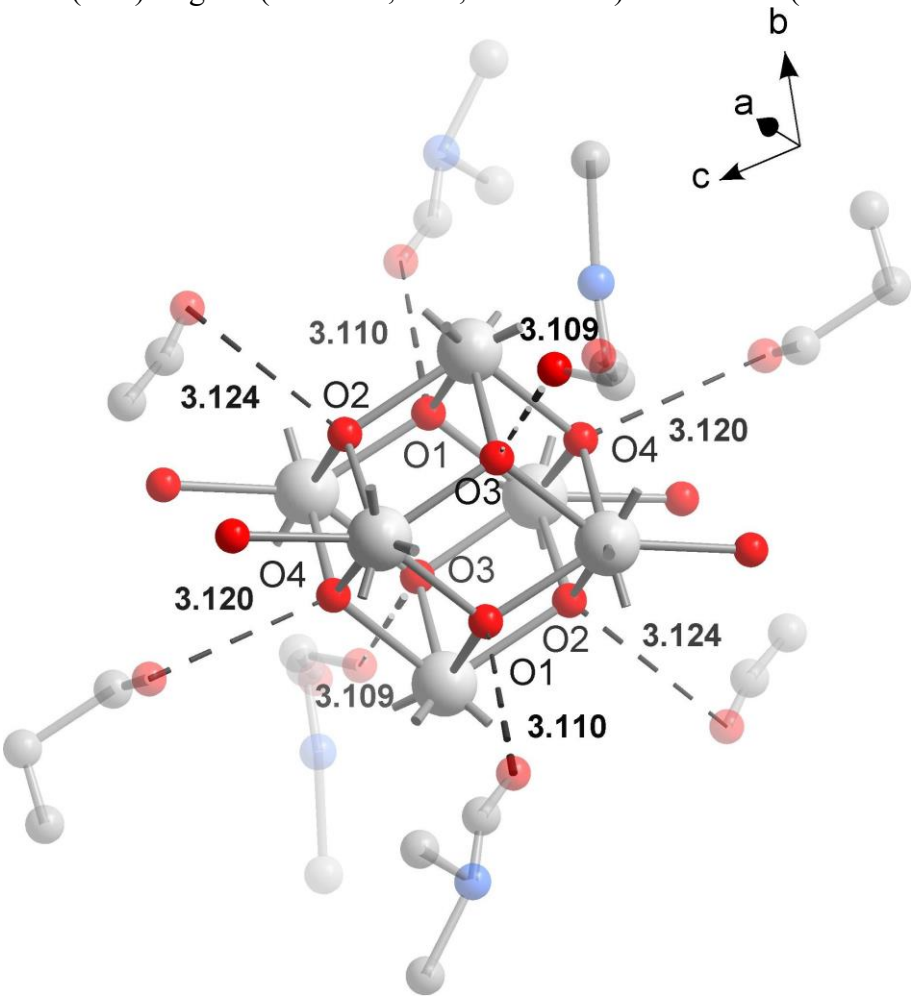

Fig. S4. The H-bonds between the μ_3-O(H) ligands and the modelled quests in the non-SQUEEZEd version of **1**-HCOOH. The poorly defined parts of the guest molecules (typically DMF, but HCOOH is also possible) are modelled by carbon atoms. The distances are given for the averaged positions of the site-sharing oxigen atoms.

The O5T and O6T atoms were identified as belonging to hydroxide- and aqua ligands with respective Zr-O distances of 2.17 and 2.23 Å. There were no residual electron densities found in the covalent bonding vicinity of those oxygen atoms, and their belonging to formate anion or DMF is practically excluded (the same conclusion was made upon analysis of the structure of I-AcOH-as). Such assignment of the O5T and O6T atoms as well as the electroneutrality principle demands cluster formula of $\{Zr_6(\mu_3\text{-}O)_4(\mu_3\text{-}OH)_4(COOH)_{10}(OH)_2(H_2O)_2\}$. The equal number of the μ_3-O and μ_3-OH ligands seems plausible, being the most typical symmetric case of the Zr_6-clusters. As for the preference of aqua ligand over DMF it is not particularly surprising due to 'hard acidic' nature of Zr^{4+}. The distribution of the O^{2-} / OH^- / H_2O ligands is important for the elucidation of the possible chemical properties, but from the point of view of structural description and characterization of a new PCP-material they are secondary.

In the given derivation of the most plausible $[Zr_6(\mu_3\text{-}O)_4(\mu_3\text{-}OH)_4(L^4)(HL^4)_2(OH)_2(H_2O)_2]$ framework formula, the state of the non-coordinated carboxyphenyl group of the HL^4 ligand-molecule deserves additional discussion. Under modulator-free conditions deprotonation of all carboxylic acid groups are plausible. However, in the presence of acidic modulators the non-involved carboxy-functionalities of the ligand might remain non-deprotonated. Notably, the hydrolysis of the DMF by residual water, yielding dimethylamine and formic acid would not change the acidity significantly. The non-SQUEEZEd dataset of the **1** contains no identifiable counter anions in the neighborhood of the carboxy group. There is strictly no coordinated metal ion, as the residual electronic density peaks are weak. The presence of dimetylammonium cation with partial occupancy should not be excluded, however no molecular fragments could be found, which would support the existence of $COO^{-}\cdots NH_2Me_2^{+}$ stronger than average hydrogen bond. Careful analysis of the space between the carboxylic acid groups demonstrated that there are poorly defined molecular fragments with closest contacts at > 3.0 Å, which should rather be interpreted as representing neutral molecules like DMF or, possibly, HCOOH (Fig. 5)

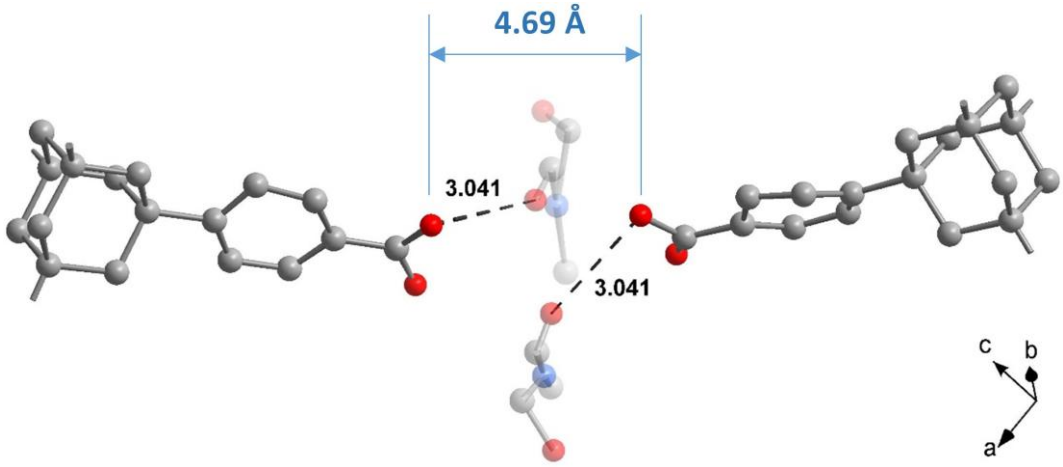

Fig. S5. The interpreted residual densities in the area between- and near the non-coordinated carboxylic acid functionalities of the HL^4 ligand (the occupation factors of these fragments are lower than unity). The distances are given for oxygen atoms, refined without accounting the disorder of the carboxyphenyl group.

The solvent accessible space in **1**, with the guest solvent molecules removed and the disorder 'collapsed' was found to be 71.8% by the PLATON/SQUEEZE routine [6] (For the non-SQUEEZEd dataset of **1** the refinement the major part of the guest molecules were located, mostly with occupancies of 0.5. The final molecular composition is ascribed according to the TGA for the product after drying. The analysis of the number of electrons in the voids and the possible composition for the non-dried compound is given below:

- The total volume of the solvent accessible voids is 2591 Å and the electron count is 668.5 e per formula unit. The molecular volume of DMF, H_2O and formic acid calculated using the density in liquid phase is 129, 29.9 and 62.7 $Å^3$ and the combined number of the larger DMF and HCOOH molecules could be estimated to be < 20, with some smaller water molecules present. The number of electrons per molecule is 40, 10 and 24 respectively, which suggest approximately the same number. Note, that this estimation is the maximum theoretical value for a crystal freshly extracted from mother liquor.

- The partial guest refinement for the non-SQUEEZEd data suggest 4 molecules of DMF (2 molecules could be interpreted either as HCOOH or DMF) and 2 molecules of water (0.5 occupancy for the guest molecules is assumed. These values are surprisingly well matches the TGA data (see the respective section) and may represent the solvent molecules, which are bound in the cavities most strongly by intermolecular interactions.

The final ascribed molecular formula with 4 DMF, 2 HCOOH and 4 H_2O is based on the TGA (see the respective section), and corresponds to a sample dried in air. Additional minor solvent loss might have occurred in the TGA chamber, just prior to the measurement.

The molecular graphics was computed using Diamond 3.2i [7].

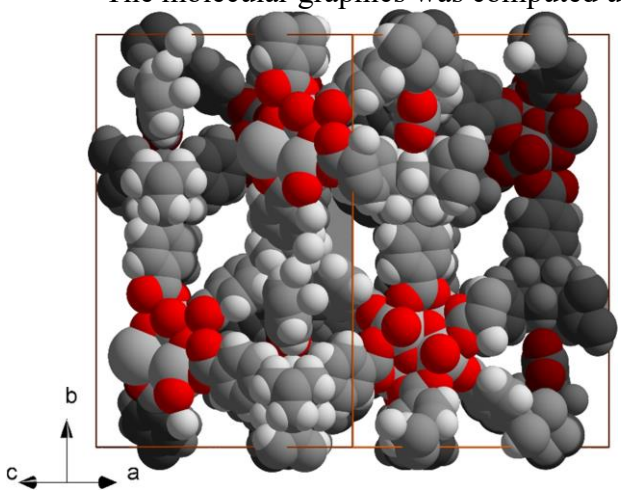

Fig. S6. A cross-section of the framework in space-filling representation with strong depth cueing to illustrate the porosity of the structure of **1**.

2.1. Topological description

The structure of $[Zr_6(\mu_3\text{-}O)_4(\mu_3\text{-}OH)_4(L^4)(HL^4)_2(OH)_2(H_2O)_2]$, **1**, has a 3,4,10-c underlying net with a stoichiometry of $(3\text{-}c)_2(4\text{-}c)(10\text{-}c)$ and full point symbol of $\{4^{14}.6^{24}.8^7\}\{4^3\}2\{4^5.6\}$ (the topological analysis was performed by Topos program package [8]. The notations are preserved):

(HL^4) node, 3-c:
Point symbol: $\{4^3\}$
Extended point symbol: [4.4.4(2)]

(L^4) node, 4-c:
Point symbol: $\{4^5.6\}$
Extended point symbol: [4.4.4.4.4(2).6(10)]

Zr_6-cluster node:
Point symbol: $\{4^{14}.6^{24}.8^7\}$
Extended point symbol:
[4.4.4.4.4.4.4.4.4.4.4.4.4.4.6(2).6(2).6(2).6(2).6(2).6(2).6(2).6(2).6(2).6(2).6(3).-6(3).6(3).6(3).6(3).6(3).6(3).6(3).6(3).6(4).6(4).6(4).6(4).6(4).6(4).8(8).8(12).8(12).-8(16).8(16).8(16).8(32)].

3. PXRD

The diffractograms were recorded using two techniques. The samples demanding lesser precision the faster and simpler technique using a Bruker D2 Phaser diffractometer in reflective mode using a flat low-background silicon sampleholder (the respective 'express' measurements are marked by [*] on the figures). The samples demanding high precision were measured in capillary using a Malvern Panalytical Empyrean diffractometer.

The Bruker D2 Phaser diffractometer (0.02° formal angular resolution) was equipped with a Bragg-Brentano goniometer, graphite monochromator (Cu Kα, λ = 1.5418 Å) and Lynxeye 1D detector. The measurement was performed at room temperature with 0.02-0.05° steps. Note, that the optimal angular resolution of the small benchtop Bruker D2 could be reached only under quite controllable conditions (minimal Soller slit opening); the resolution is our non-demanding experiments were much lower than that. The flat sample-holder does not in general ensure high angular resolution. The $2\theta < 6°$ area were not recorded on the Bruker D2 due to strong influence from the beam-stop attenuator. The degassed samples were measured without protection from air.

The measurements on the Empyrean diffractometer (0.026° angular resolution) were performed in dedicated thin-walled capillaries with 0.3 or 0.5 mm diameter (0.3 mm capillaries is used, when the filling was easy). The samples were degassed already in capillaries, which were placed in the sample-holders of the Micromeritics ASAP 2020, with both vacuum onset and temperature ramping controlled in order to avoid ejection of the sample from the capillary. The degassing of the materials was performed at the specified temperature (120 - 220°C for ~12h; the sample names contain a suffix, designating the precise value). The sampleholder with the capillaries were refilled with nitrogen after cooling down. The capillaries were sealed immediately after extraction from the sampleholder-tubes; only a short contact with air was allowed prior to sealing.

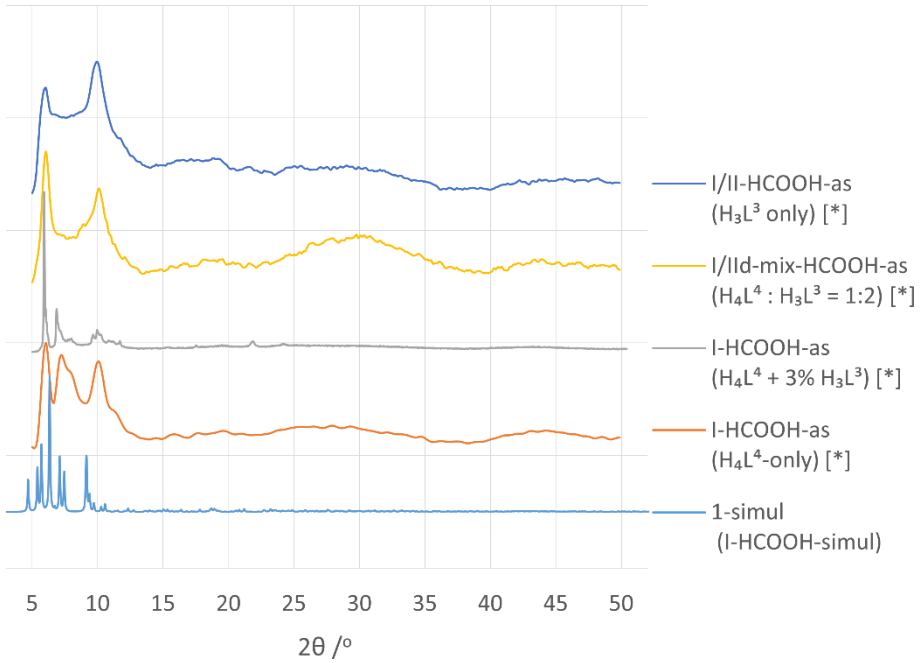

Fig. S7. Influence of the ratio of H_4L^4 and H_3L^3 on the crystallization outcome of **1**.
[*] denotes measurements with lower resolution.

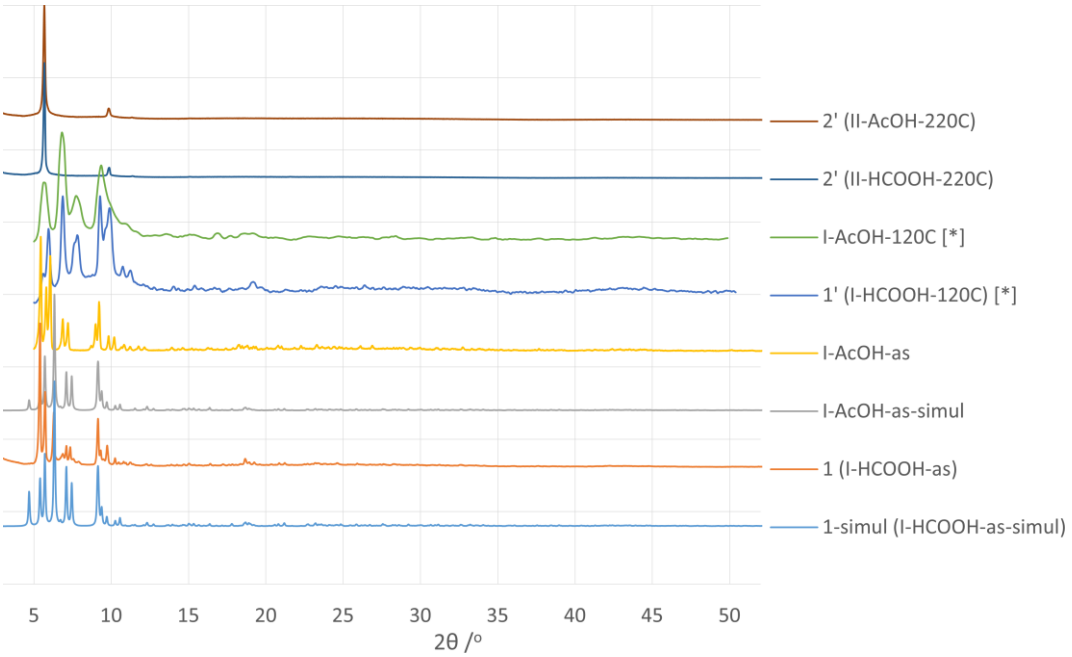

Fig. S8. The temperature induced changes registered by PXRD for the **1** prepared using HCOOH and AcOH as modulators.
[*] denotes measurements with lower resolution.

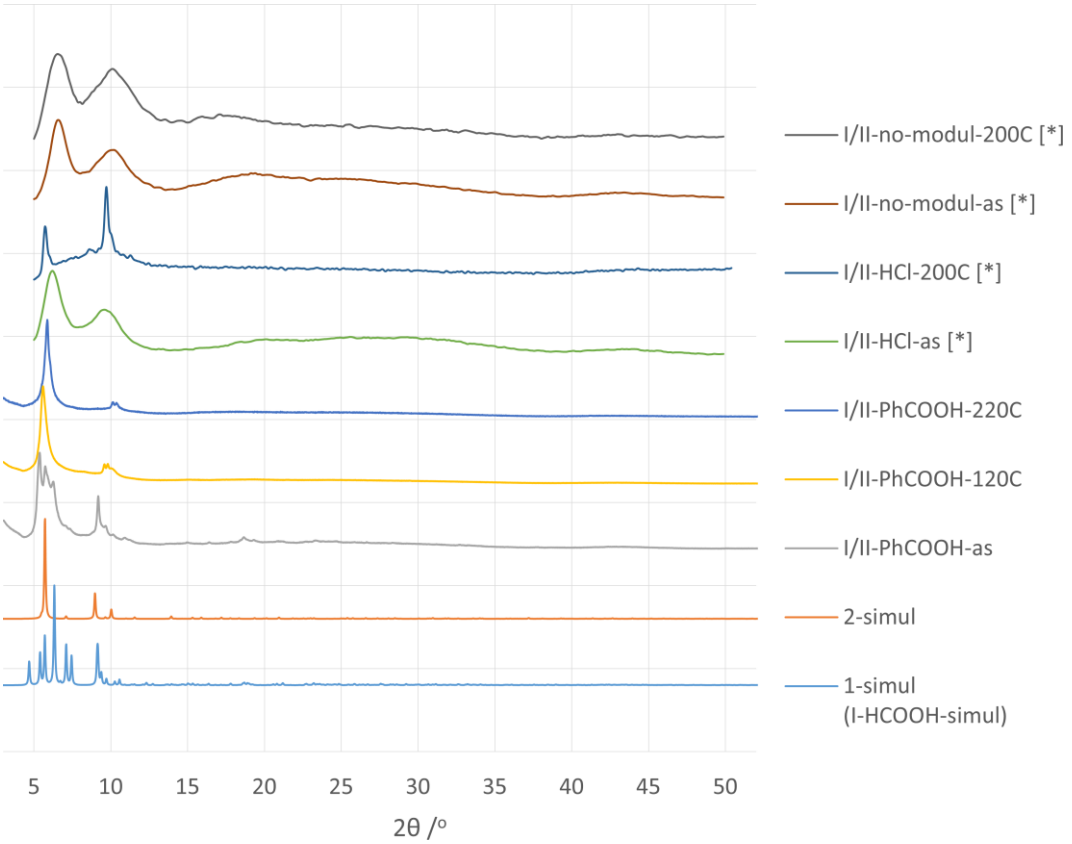

Fig. S9. Comparison of the still largely crystalline I/II-PhCOOH with other semi-amorphous I/II phases. Except the former, which is more crystalline and closer to phase I, the others represent a continuum of intermediary phases, generally closer to phase II (particularly after thermal processing at ~200 °C).
[*] denotes measurements with lower resolution.

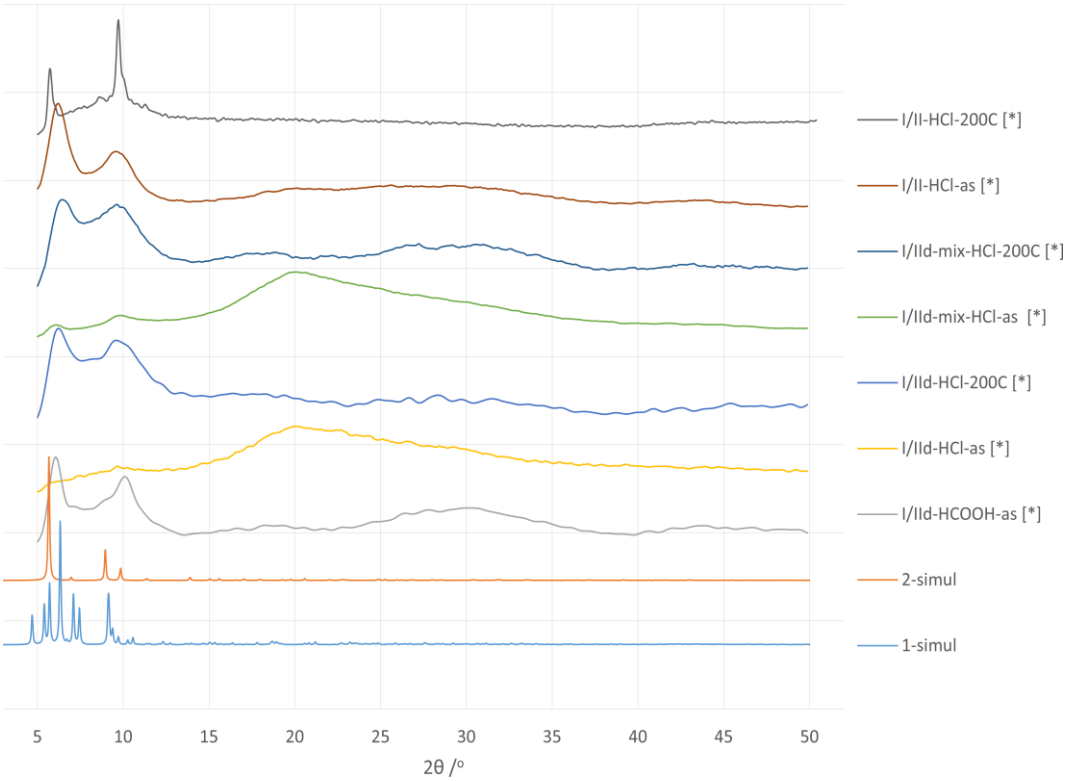

Fig. S10. The comparison of materials synthesized with the use of H_4L^4 and H_3L^3 ligands with the simulated **1** and **2** (the codes with with the 'd' suffix denotes the presence of H_3L^3. Themixed ligad approach, 1:1 ratio, is denoted by the 'mix' suffix).
[*] denotes measurements with lower resolution.

4. Structural model of $[Zr_6(\mu_3\text{-}O)_4(\mu_3\text{-}OH)_4(OH)_4(L^4)_2]$, **2** (flu)

The structural model was created using the published experimental SCXRD structure of MOF-841 as a prototype [9].The central carbon atom of the 4,4',4",4"'-(methanetetrayl)tetraphenylcarboxylate was 'decorated' to form the adamantane moiety with C-C bond length of 1.55 Å. The initial rotation angle of the adamantane moiety, situated on the 4-fold rotation axis, and the phenyl branches were adjusted to minimize the strain. The given cell dimensions (see the SHELX *res* file below) refers to the non-optimized model. Note that on all figures the O1A and O1B atoms belonging to the μ_3-oxo and μ_3-hydroxido ligands are represented as one averaged atom.

```
###############CODE###############
TITL Zr-Ad(PhCOO)4 flu
CELL 0.71073 17.626597 17.626597 32.175232 90 90 90
ZERR 2 0.0006 0.0006 0.001 0 0 0
LATT 2
SYMM -X,-Y,+Z
SYMM -Y,+X,+Z
SYMM +Y,-X,+Z
SFAC C H O Zr
UNIT 152 112 64 12
C1    1     0.17270  0.04560  0.10140  1.00000  0.05000
C2    1     0.23560  0.03579  0.13476  1.00000  0.05000
C3    1     0.22071  0.02265  0.17742  1.00000  0.05000
H3    2     0.16865  0.01989  0.18723  1.00000  0.06000
C4    1     0.28174  0.01339  0.20559  1.00000  0.05000
H4    2     0.27156  0.00428  0.23482  1.00000  0.06000
C5    1     0.35789  0.01735  0.19118  1.00000  0.05000
C6    1     0.37293  0.03062  0.14860  1.00000  0.05000
H6    2     0.42497  0.03332  0.13869  1.00000  0.06000
C7    1     0.31178  0.03985  0.12033  1.00000  0.05000
H7    2     0.32203  0.04883  0.09113  1.00000  0.06000
C8    1     0.42570  0.00733  0.22168  1.00000  0.05000
C9    1     0.42197 -0.06342  0.25053  1.00000  0.05000
H9A   2     0.37795 -0.05834  0.26840  1.00000  0.06000
H9B   2     0.41635 -0.10814  0.23323  1.00000  0.06000
C10   1     0.50000  0.00000  0.19520  0.50000  0.05000
H10A  2     0.49559 -0.04472  0.17779  0.50000  0.06000
H10B  2     0.50441  0.04472  0.17779  0.50000  0.06000
O1A   3    -0.07600  0.03870  0.03280  0.50000  0.05000
O1B   3    -0.10560  0.05360  0.04200  0.50000  0.05000
O2    3     0.10460  0.03070  0.11340  1.00000  0.05000
O3    3     0.19290  0.06220  0.06470  1.00000  0.05000
O4    3     0.19220  0.16050  0.00000  0.50000  0.05000
O5    3     0.24960 -0.01790  0.00000  0.50000  0.05000
Zr1   4     0.00000  0.00000  0.07770  0.25000  0.05000
Zr2   4     0.13800  0.04560  0.00000  0.50000  0.05000
###############ENDofCODE###############
```

4.1. Topological description

The underlying net in **2** is the well-known **flu** (fluorite) net. It is a two-nodal net with (4-c)$_2$(8-c) stoichiometry with $\{4^{12}.6^{12}.8^4\}\{4^6\}_2$ full point symbol (notations according to).

(L) node, 4-c:

Point symbol: $\{4^6\}$

Extended point symbol: [4.4.4.4.4.4]

Zr_6-cluster node:

Point symbol: $\{4^{12}.6^{12}.8^4\}$

Extended point symbol:

[4.4.4.4.4.4.4.4.4.4.4.4.6(4).6(4).6(4).6(4).6(4).6(4).6(4).6(4).6(4).6(4).6(4).6(4).6(4).8(24).8(24).8(24).8(24)]

5. PXRD-based refinement of $[Zr_6(\mu_3\text{-}O)_4(\mu_3\text{-}OH)_4(OH)_4(L^4)_2]$, **2** and **2 · Guest**

The samples of **1** (**I**-HCOOH-as), I-AcOH-as and I/II-PhCOOH-as upon degassing at 220°C are all yielded **2´**. The high-resolution PXRD data was measured as described in Chapter 3. Importantly, the samples sealed in capillaries were protected from ambient air (only a short contact was allowed during the sealing of the capillary with the degassed sample).

The experimental patterns of **2´** and their comparison with the simulated models after Rietveld refinement on the range of 3-80° are shown in Fig. S11. The experimental patterns consist of two strong peaks and notably devoid of practically any other details. The very low amount of information, which could be extracted from those two peaks excluded the possibility to do true refinement of the created structural model of **2** (p. 10**)**, but it allowed to verify its credibility. In all cases practically only the two independent cell-dimensions for the assumed *I*4/*m* symmetry) and the two profile-defining parameters. The refinements were performed using the program package Jana [10] (Fig. S12), using the dataset for the 1-HCOOH-220C sample (the full as-measured pattern is included as a supplementary file). The refinement on the full span (2θ = 3-80°) was unstable and demonstrated too high influence of the somewhat noisy background on the wRp and GOF statistical figures of merit. It was necessary to use only the relevant range of 2θ <3- 20 and downsample the data (the latter is not a good practice [11]; the only excuse in this case that the goal was to confirm the structural type and not to refine it on the level of atomic coordinates). The peak shapes were approximated by a two parameter Lorenzian function (Lx and Ly parameters in Jana).

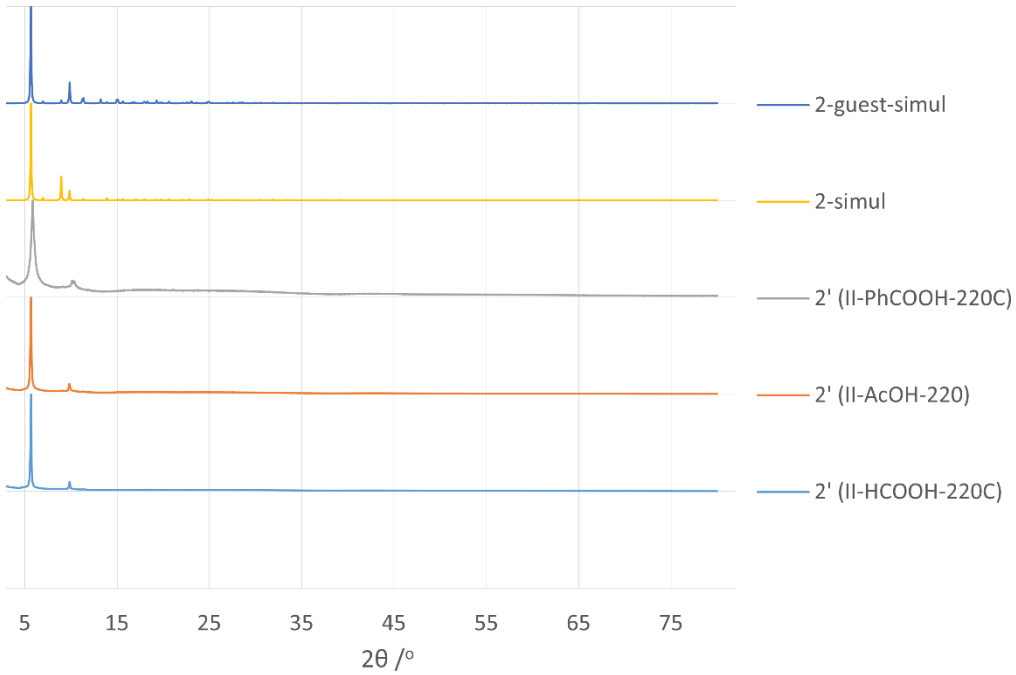

Fig. S11. The comparison of phase II exprimental PXRD patterns with the simulated models, without and with modelled guest molecules.

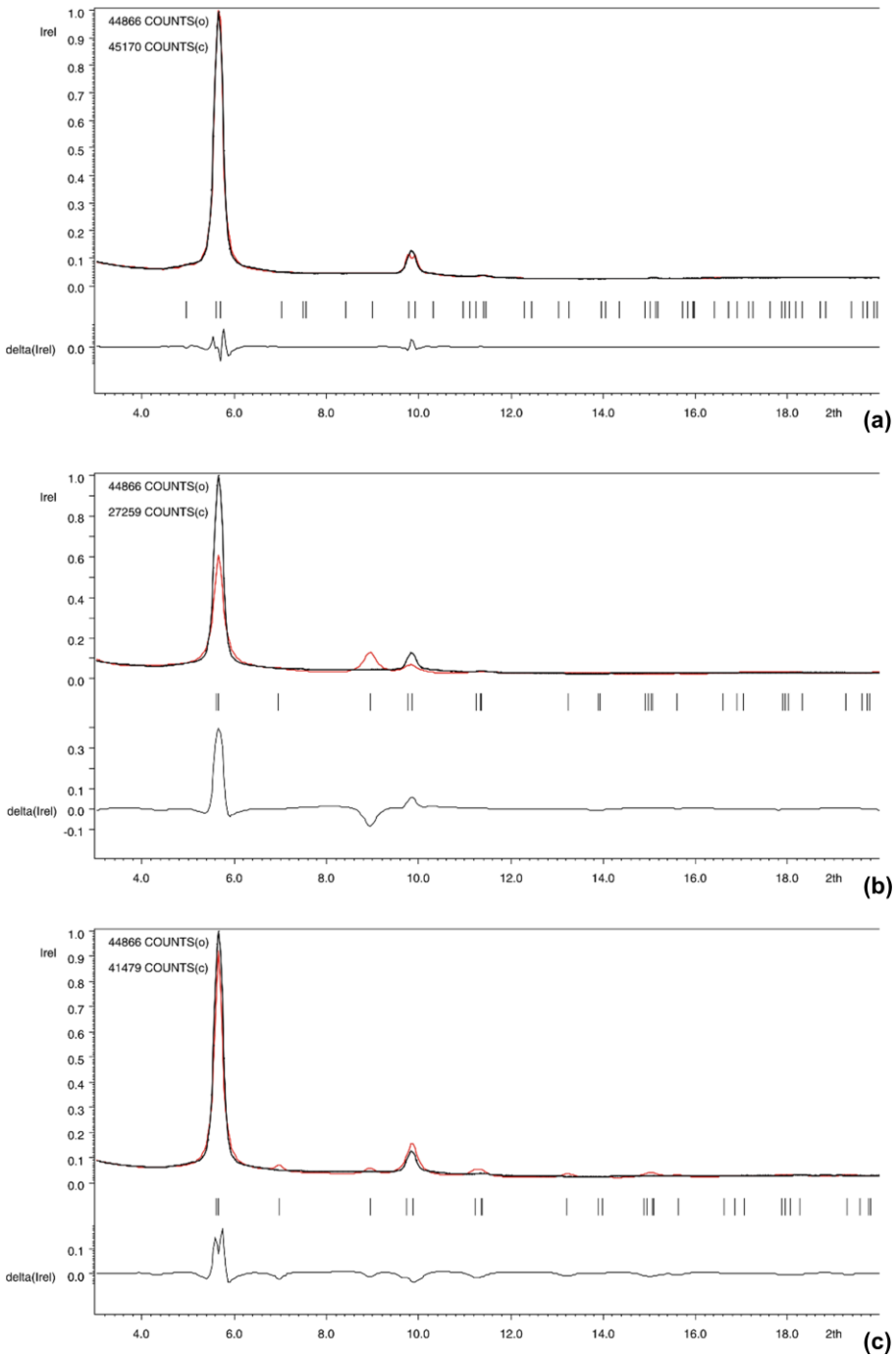

Fig. S12. Refinement of the structural model of **2**:
a) LeBail (i.e. the type of fitting, which is independent of the unit-cell content);
b) Rietveld, without the account of guest molecules;
c) Rietveld, with guest molecules modelled.

The Le Bail fitting of the as-constructed model of **2** demonstrated a reasonably good fit (Fig. S12a; a = 17.8007 c = 31.4662 Å cell dimensions; wR_p = 0.052; GOF = 2.67). Note the peak at 2θ ~ 10°, which is fitted as corresponding to two reflexes (h k l: 1 0 3 and 2 0 3) could indeed be observed as a pair of non-completely merged peaks in the data for 1-PhCOOH-220C (see also Fig. 7 in the main text for the expansion). This observation is an important support of the model's correctness in the current case of feature-poor spectrum.

The Rietveld refinement for the as-constructed **2** would result in a reasonably good correspondence, had the 1 1 0 reflection been observed at app. 2θ ~7° (Fig. S12b; a = 17.9522

c = 31.4332 Å cell dimensions). The analysis of the structure indicated, that the intensity of the peak is strongly dependent on the electronic density in the vicinity of (1/2, 0, 0) coordinate. This area belongs to a cavity and it could be assumed that it is occupied by a guest (the structural rearrangement of **1´** to **2´** undergoes with an expulsion of one ligand molecule per each $\{Zr_6\}$ cluster. Hence the pores of the compound are no empty, even if the solvent molecules are removed). The guest molecule was formally modelled by three Zr atoms (heavy atoms were used in order to keep the model simple, but account for the electronic density). Even such a crude approach allowed to reach $wR_p = 0.15$, which generally would be regarded as poor, but could be deemed satisfactory in the current case (note, that the major fitting discrepancy comes from a number of weak peaks, which are supposedly broadened to near disappearance in the experimental structure of compromised crystallinity.).

The Rietveld refinement of the **2-Guest** with the accounted guest molecules gives a satisfactory fit (Fig. S12b; a = 17.914, c = 31.529 Å). It is not reasonable to expect an excellent Rietveld fitting for this case. The II-Modulator-220C, Modulator = HCOOH, AcOH, PhCOOH, materials are porous compounds formed through a solid-state rearrangement (and hence relatively defect-rich) and containing non-removable guest molecules, expectedly without precise but rather preferential placement in the pores.

Recapitulating, the Rietveld refinement in the case of scarce information from the PXRD pattern could only be used for supporting the identity of **2´**, but not for true refinement of its structural features on the level of atoms. The main supporting observations are:

- Confirmed high symmetry of the structure due to simplicity of the PXRD pattern;
- Excellent Le Bail fit for the structure of **2** constructed in analogy with the structure of MOF-841;
- The observation the two constituting sub-peaks for the compound peak at $2\theta \sim 10°$ for at least one material, in accordance with the expectations;
- Sufficiently good Rietveld fit of **2-Guest**, as a model of **2´**, when the expected ligand-guest is modelled by a few heavy atoms.

6. TGA

Thermogravimetric analysis data was collected on a Netzsch TG 209F3 instrument using corundum sampleholder under N_2 gas stream (10 ml min^{-1}) at 10 °C min^{-1} heating rate. The sample of **1**-HCOOH-as was dried until constant weight in air (up to 1 week).

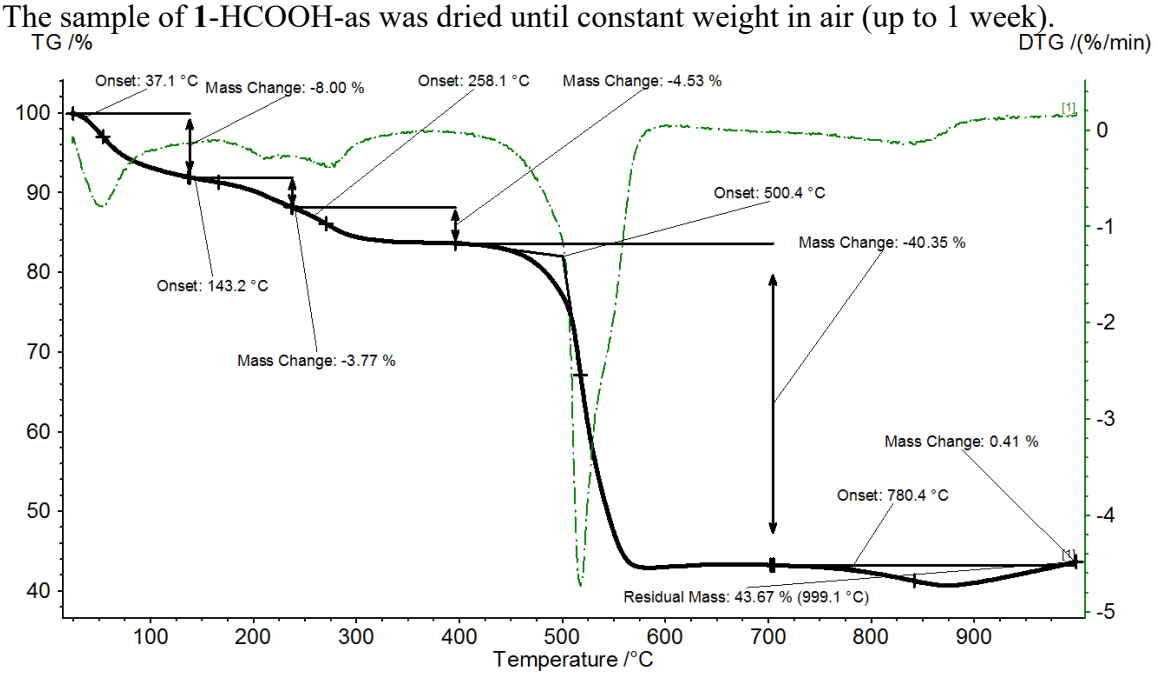

Fig. S13 TGA of **1**.

There are four weight-loss steps: 8.00% at r.t. - ~120 °C, 3.77% at ~120 – 230 °C, 4.53% at 230-400 °C and 40.35% at 400-580 °C. The first three steps, particularly the second and the third, are poorly separated. However, it is plausible that the steps correspond to the loss of: 1) water 2) a mixture of formic acid, water and DMF with the mayor part being the formic acid 3) DMF with remnants of strongly bound water, primarily originating from μ_3-OH groups and, probably, traces of formic acid or equivalent CO/H_2O mixture.

The fourth step corresponds to a deep disintegration of the ligand and it is significantly larger than the expected if only decarboxylation would occur. (we hypothesize that some amount of air might have been present in the blanketing gas due to improper isolation of the chamber; in any case we did not use the weight loss value for the fourth step for estimation of the composition).

A compromise with the structural data (see also the discussion in the respective section) resulted in assignment of the composition to 4 DMF, 2 HCOOH and 4 H_2O molecules. (total weight loss on steps 1-3 is 16.3%, calculated weight loss is 16.2%).

7. Gas adsorption studies

The adsorption isotherms were collected using a Quantachrome Nova automatic gas sorption analyzer at 77 K. The used gases (He, N_2) were of ultra-high purity (UHP, grade 5.0, 99.999% or better) and the STP volumes are given according to the NIST standards (293.15 K, 101.325 kPa). Helium gas was used for the determination of the cold and warm free space of the sample tubes.

Most of the samples were subjected to supercritical CO_2 drying (further sc-CO_2 drying) prior to degassing (see also Table 2 in the main text. The sc-CO_2 drying was essential for removal of DMF, which persist in the pores at 120 °C under direct degassing). The sample was immersed in acetone for 20 minutes, centrifuged out and dried for 99 drier cycles (approximately 7 h of total time) using a Leica CPD300 Auto automatic supercritical CO_2 drier. The short exchange time with acetone was intentional, due to observed signs of crystallinity deterioration during hours long acetone exposure (the goal of the pre-drying exchange is not complete but partial solvent exchange, which makes the sc-CO_2 drying more efficient). The contact of the sample with air during the transfers of the sample were minimized.

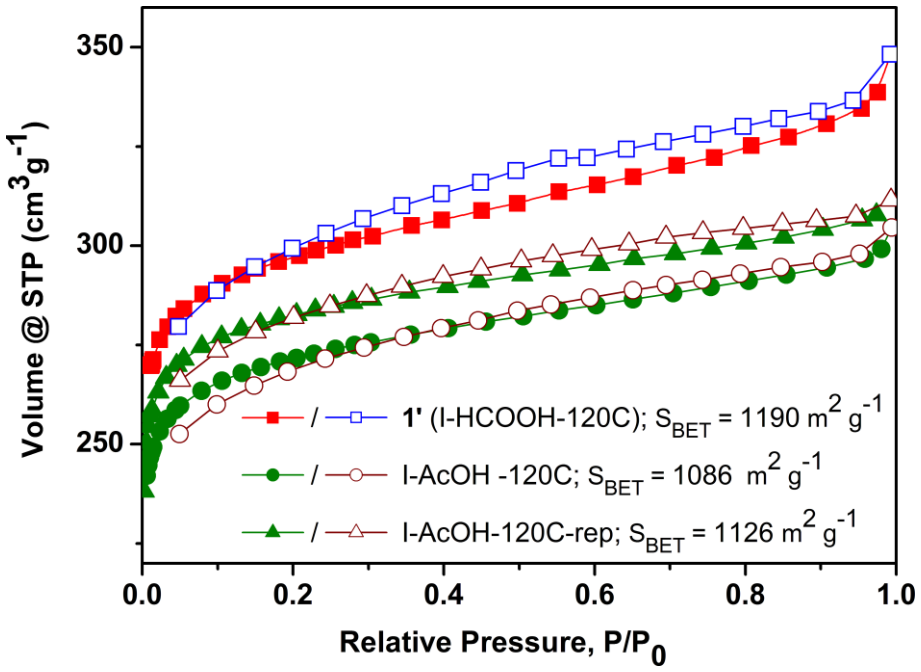

Fig. S14. N_2 adsorption isotherms for the highest surface area samples, I-HCOOH-120C and I-AcOH-120C ('rep' stands for repeated synthesis and measurement).

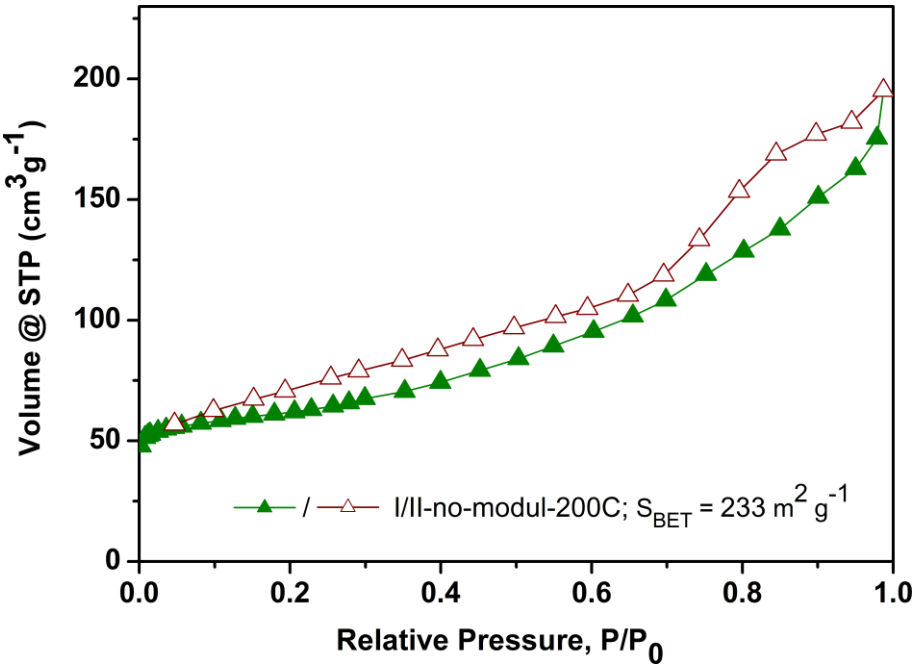

Fig. S15. N_2 adsorption isotherm for I/II-no-modul-200C sample (synthesis without modulator).

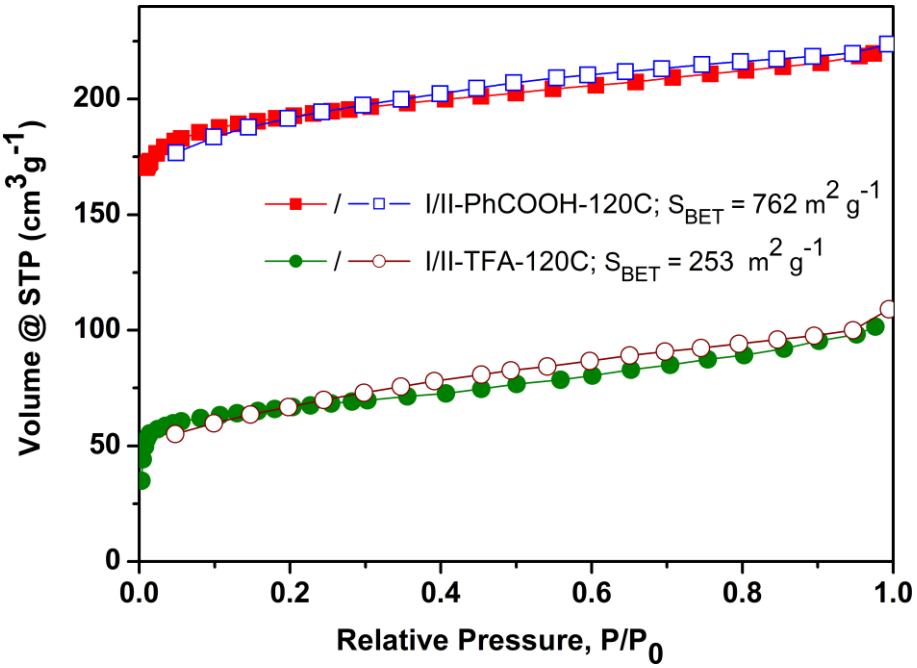

Fig. S16. N_2 adsorption isotherms for the mixed- or semi-amorphous phases obtained by use of PhCOOH (above) and TFA (below) as modulators (both were activated after sc-CO_2 drying).

8. ^{1}H NMR spectra of the ligands and the digested samples

The NMR spectra of the neat ligands were measured using a Varian Mercury (400 MHz) and the other samples on Bruker BioSpin (300 MHz) instruments.

The dissolution of the Zr-MOF sample ('digestion') was performed as follows: approx. 10 mg of the sample was weighted in an NMR tube, and mixture of 570 µL of DMSO-d_6 and ~20 µL of HF was added. The mixture was sonicated until complete dissolution of the material.

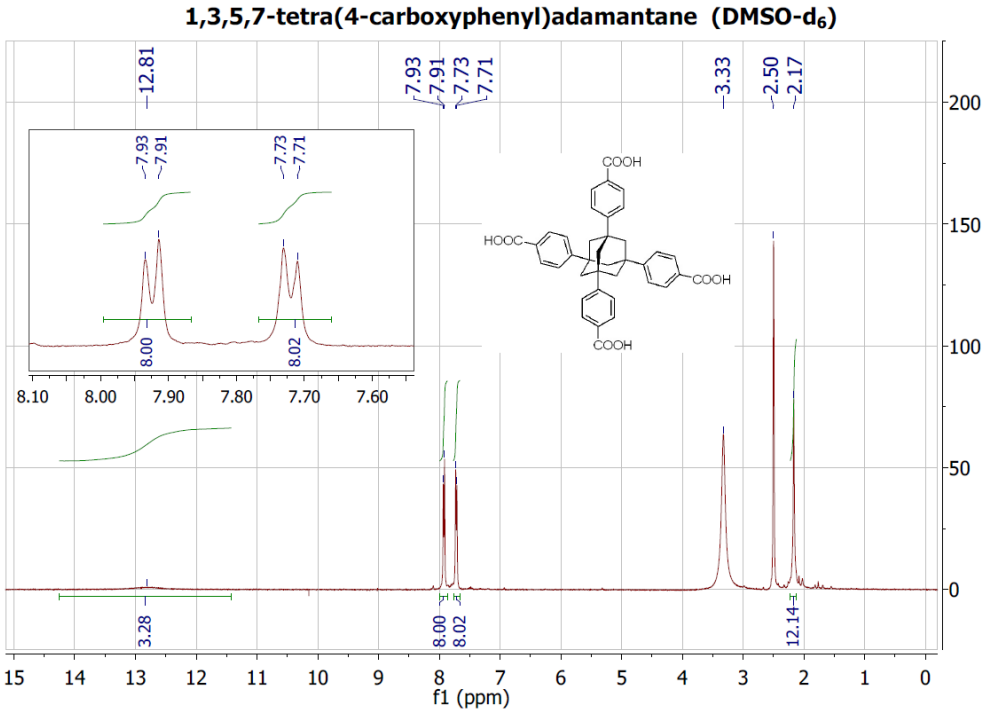

Fig. S17. ^{1}H NMR spectrum of H_4L^4.

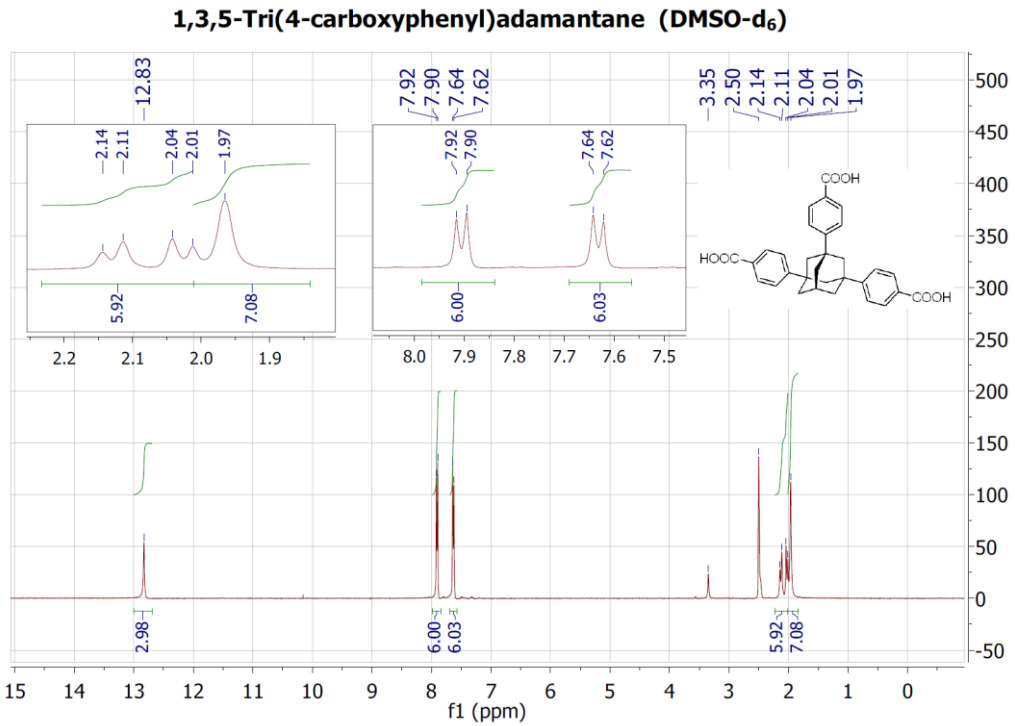

Fig. S18. ^{1}H NMR spectrum of H_3L3.

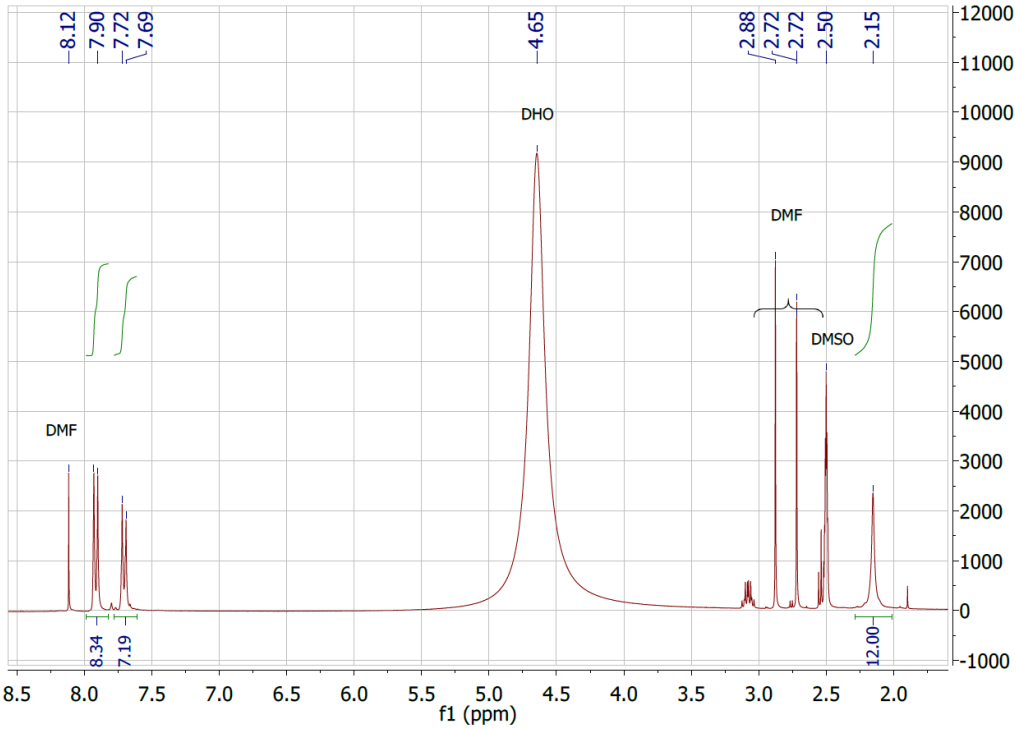

Fig. S19. ^{1}H NMR spectrum of the HF-digested sample of **1** ('standard' synthesis, H_4L4 contained an admixture of ~3%$_{mol}$ admixture of H_3L3).

The integral value for CH3-protons of DMF in this spectrum is 12.8, which gives a DMF : ligand ratio of ~2 : 1, i.e. 6 molecules of DMF per formula unit. It is a sufficiently good confirmation of the TGA-based value of 4 molecules, taking in account that the NMR based determination is of low precision and the samples originated from different batches.

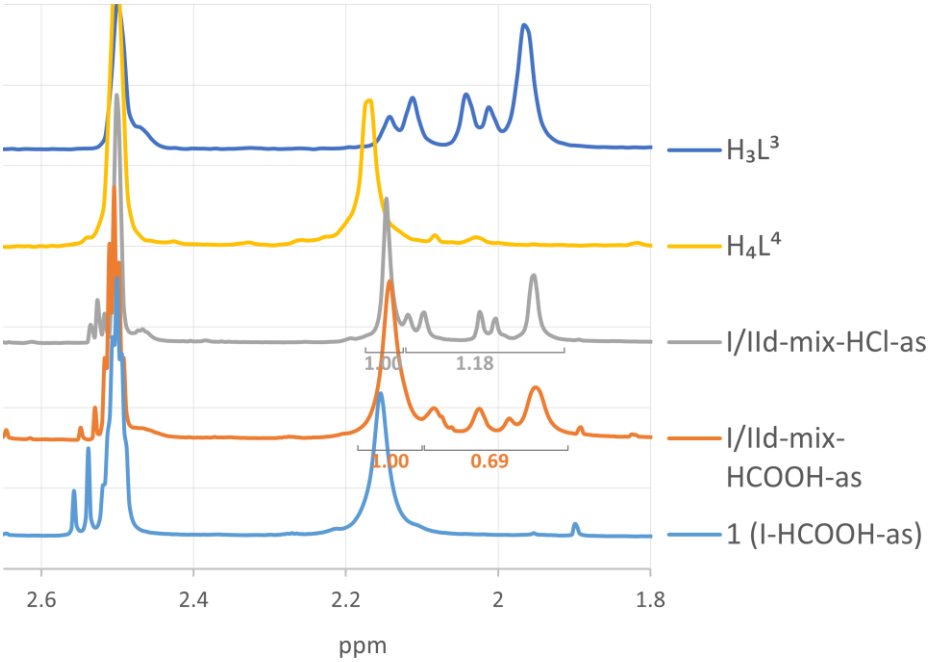

Fig. S20. ^{1}H NMR spectra overlay of selected HF-digested samples and the spectra of the ligands.

The crystalline variants of I-HCOOH-as prepared using H_4L^4 + H_3L^3 ligand mixtures with low share of the second component demonstrated very low incorporation of the latter. The increase of the H_4L^4 : H_3L^3 ratio to 1 : 2 during the synthesis of the sample I/IId-mix-HCOOH-as, does couse incorporation, but at a cost of turning the sample semi-amorphous. The sample is enriched with H_4L^4 compared to the ratio of the ligands used during synthesis (1 : 0.64 molar ratio, calculated from the ratio of the peak integrals).

The spectrum of the digested I/IId-mix-HCl-as demonstrate successful incorporation of H_3L^3 (the H_4L^4 : H_3L^3 molar ratio used for synthesis is 1 : 1, and the molar ratio in the product is 1 : 1.09).

9. FT-IR spectroscopy

The FT-IR measurements were collected using a Bruker Tensor 37 system equipped with an ATR unit (Platinum ATR-QL, diamond) in the 4000-560 cm^{-1} range with a 2 cm^{-1} resolution.

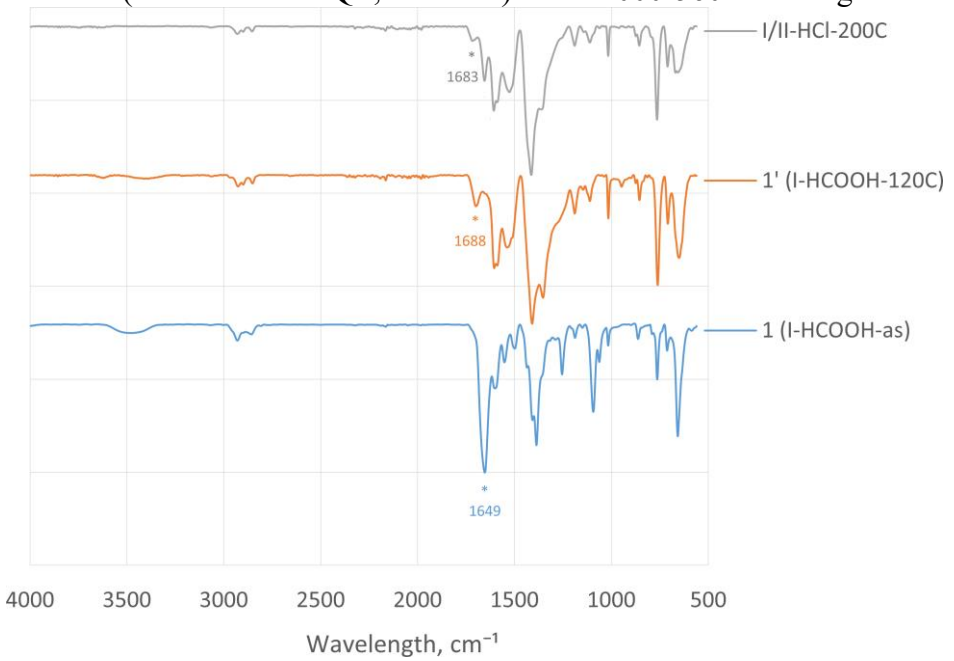

Fig. S21. Comparison of the IR (ATR) spectra of the 1-HCOOH samples: as synthesized, degassed at 120 °C and 200 °C. Note the disappearance of the strong DMF peak at 1649 cm^{-1} (ν(C=O)). The band at 1680-1690 cm^{-1} belongs to ν(C=O) of the phenylcarboxylic acid moiety.

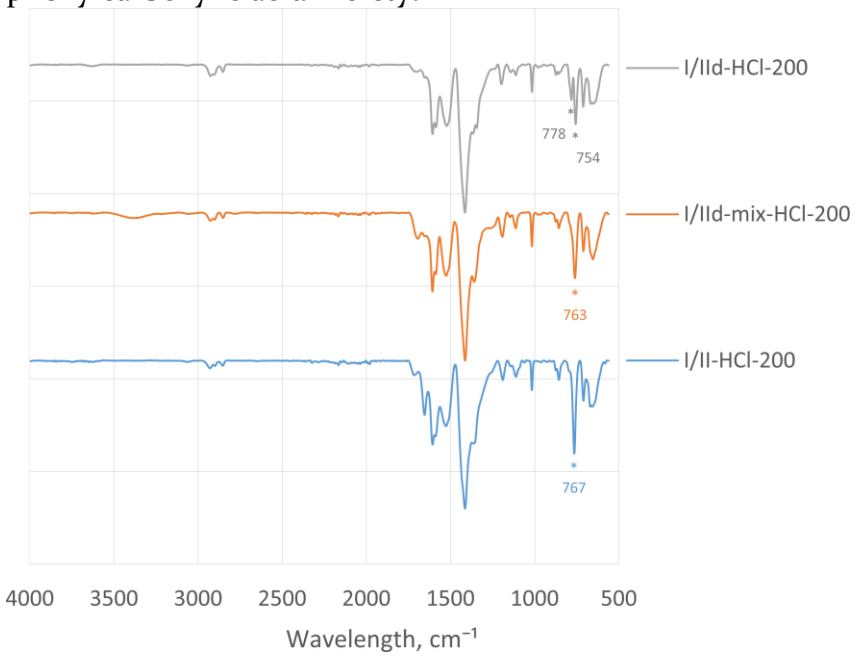

Fig. S22. Comparison of the IR (ATR) spectra of the semi-amorphous I/II phases obtained by using HCl as a modulator. I/II-HCl-200 refers to H_4L^4 used only, 1/2d-mix-HCl-200C to 1:1 mixture of H_4L^4 / H_3L^3 during synthesis and 1/2d-HCl-200C to the use of H_3L^3 only.

The region of 750-780 cm^{-1} is characteristic for differences. The sharp strong peak at 767 for the H_4L^4-based material decreases in intensity and broadens, finally splitting in two smaller peaks at 754 and 778 cm^{-1} for the H_3L^3-based material only.

10. Water stability tests

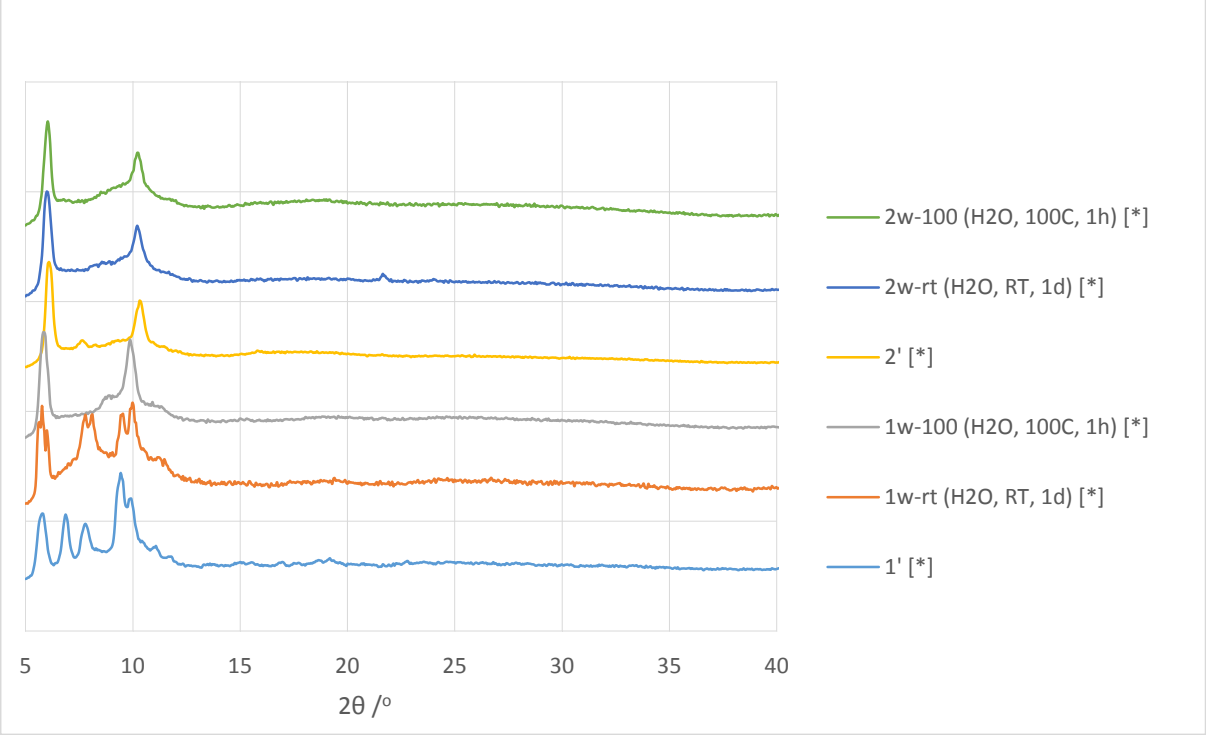

Fig. S23. PXRD patterns of the samples before and after the water stability test. the patterns marked by [*] are measured in the less precise reflectance mode.

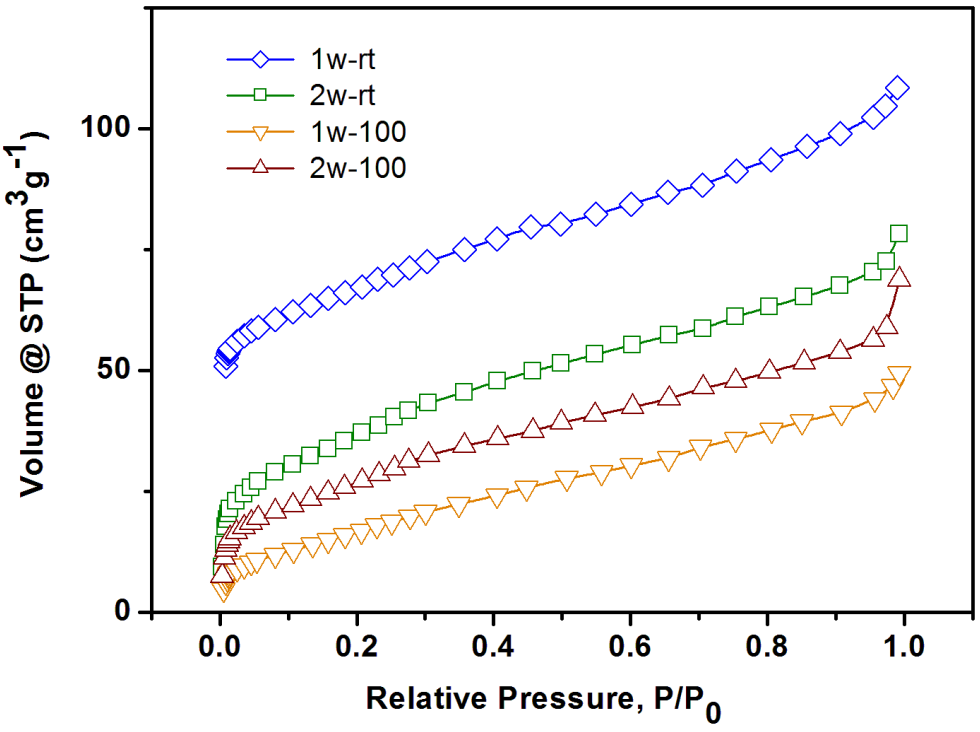

Fig. S24. N_2 gas adsorption isotherms for the samples subjected to water stability tests.

Table S4 Surface areas for materials, subjected to water stability tests.

	S_{BET}, m^2g^{-1}
1w-rt	245
2w-rt	134
1w-100	73
2w-100	109

1w-rt and **2w-rt**: ~ 20 mg of the activated samples of 1′ and 2′ were mixed with ~0.5 ml of water in small open vials. In ~1 day the water evaporated and the samples were degassed at 100 °C in 10^{-3} Torr vacuum.

1w-100 and **2w-100**: **1w-rt** and **2w-rt** after measurements were boiled in 3 ml of water for 1h. The residue was centrifuged off, dried in air and degassed at 100 °C in 10^{-3} Torr vacuum.

The PXRD patterns N_2 adsorption measurement data are shown in Fig. S23 and Fig S24 respectively. According to the data **1′** start to convert to **2′** in water already at room temperature (the heating during the degassing might additionally stimulate the process, even if the amount of residual water is small under vacuum). The conversion of **1′** to **2′** is complete after boiling in water for 1h. In the same time the crystallinity of **2′** is not visibly affected. The surface areas, nevertheless drop dramatically in all cases (Tab. S4)

11. References

[1] T. Zhao, C. Heering, I. Boldog, K. V. Domasevitch, and C. Janiak, *CrystEngComm*, 2017, **19**, 776–780.
[2] M. C. Burla, M. Camalli, B. Carrozzini, G. L. Cascarano, C. Giacovazzo, G. Polidori, and R. Spagna, *J. Appl. Crystallogr.*, 2003, **36**, 1103–1103.
[3] G. M. Sheldrick, *Acta Cryst. Sect. C*, 2015, **71**, 3–8.
[4] L. J. Farrugia, *J. Appl. Crystallogr.*, 2012, **45**, 849–854.
[5] A. L. Spek, *Acta Crystallogr. Sect. C Struct. Chem.*, 2015, **71**, 9–18.
[6] A. L. Spek, *Acta Crystallogr. Sect. D Biol. Crystallogr.*, 2009, **65**, 148–155.
[7] H. Putz and K. Brandenburg, *Diam. 3.2, Cryst. Impact; Kreuzherrenstr. 102, 53227 Bonn, Ger.*, 2012.
[8] V. A. Blatov, A. P. Shevchenko, and D. M. Proserpio, *Cryst. Growth Des.*, 2014, **14**, 3576–3586.
[9] H. Furukawa, F. Gándara, Y. Zhang, J. Jiang, W. L. Queen, M. R. Hudson, and O. M. Yaghi, *J. Am. Chem. Soc.*, 2014, **136**, 4369–4381.
[10] V. Petříček, M. Dušek, and L. Palatinus, *Zeitschrift für Krist. - Cryst. Mater.*, 2014, **229**, 345–352.
[11] B. H. Toby, *Powder Diffr.*, 2006, **21**, 67–70.

3.3. Synthesis and characterization of two bifunctional pyrazole-phosphonic acid ligands

Bahareh Nateghi, Christoph Janiak

Z. Naturforsch. B, **2019**, accepted.

DOI: 10.1515/znb-2019-0170

Zwei neuen bifunktionellen Pyrazolat-Phosphonat-Liganden zur Herstellung von metall-organischen Netzwerken wurden synthetisiert. Hierbei wurden 3,5-dimethyl-4-(4-phosphonophenyl)-1*H*-pyrazol and 4-(4-phosphonophenyl)-1*H*-pyrazol mittels einer Suzuki-Miyaura Kreuzkupplung, ausgehend von einem Boc-geschützten Pyrazolyl-boronsäureester und Iodo-arylphosphonat hergestellt, deren Strukturen mittels Röntgeneinkristalldiffraktometrie aufgeklärt wurden. Beide Verbindungen kristallisieren jeweils mit einem HCl-Molekül in Salzform und weisen Wasserstoffbrücken-Netzwerke auf. Es gibt in der Literatur wenige Berichte über die Phosphonat-basierten MOFs mit einer Porosität. Dies könnte durch die Neigung der Phosphonat-Verbindungen zur Bildung von Schichtstrukturen erklärt werden. Zudem sollte Polymorphie dieser Verbindungen, die für Komplexe mit mehrzähnigen Liganden bekannt ist, genannt werden. Außerdem liegen die rasch gebildeten Verbindungen in unlöslicher Form vor, wobei sich keine reversible Reaktion durchführen lässt. Aufgrund dieser Schwierigkeiten war im Rahmen dieser Arbeit nicht möglich, Einkristalle einer Güte zu erhalten, welche mittels Einkristalldiffraktometrie untersucht werden könnten. In Folgearbeiten sollten weitere Ansätze in unterschiedlichen Verhältnissen von Liganden zu Metallsatzen in diversen Lösungsmitteln gemacht werden, um Kristalle besserer Qualität zu synthetisieren. Außerdem könnten durch den Einsatz des bifunktionellen Pyrazolat-Phosphonat-Liganden bimetallische Komplexe synthetiesiert werden, da nach dem HSAB-Konzept Pyrazolat-Gruppe eine Affinität zu weicheren Metallionen (wie z.B. Cu^{2+}, Zn^{2+}) und Phosphonat-Gruppe eine Affinität zu harten Metallionen (wie z.B. Fe^{3+}, Zr^{4+}) aufweisen.

Anteile an der Veröffentlichung:

- Synthese von 3,5-dimethyl-4-(4-phosphonophenyl)-1*H*-pyrazol und 4-(4-phosphonophenyl)-1*H*-pyrazol und vollständige Charakterisierung (^{1}H-, ^{13}C-, ^{31}P-NMR, IR, TGA, ESI, CHN-Analyse sowie SC-XRD) sowie Auswertung und Darstellung der Ergebnisse.

- Eigenständiges Lösen der Kristallstrukturen.
- Erstellen des Manuskripts in erster Fassung mit Abbildungen und Tabellen und Einarbeitung von Korrekturen.
- Korrekturen erfolgten durch Herrn Prof. Dr. Christoph Janiak und Herrn Dr. Ishtvan Boldog.

Bahareh Nateghi, Christoph Janiak*

Synthesis and characterization of two bifunctional pyrazole-phosphonic acid ligands

DOI: 10.1515/znb-2019-0170

Received October 24, 2019; accepted October 4, 2019

***Corresponding author: Professor Dr. Christoph Janiak,** Institut für Anorganische Chemie und Strukturchemie, Heinrich-Heine-Universität Düsseldorf, Universitätsstraße 1, D-40225 Düsseldorf, Germany, Tel.:+49-211-81-12286, E-mail: janiak@uni-duesseldorf.de
Bahareh Nateghi: Institut für Anorganische Chemie und Strukturchemie, Heinrich-Heine-Universität Düsseldorf, Universitätsstraße 1, D-40225 Düsseldorf, Germany, e-mail: bahareh.nateghi@uni-duesseldorf.de

Abstract: The bifunctional compounds 3,5-dimethyl-4-(4-phosphonophenyl)-1*H*-pyrazole **1** and 4-(4-phosphonophenyl)-1*H*-pyrazole **2** were synthesized via Suzuki-Miyaura coupling, starting from a Boc-protected pyrazolylboronic acid ester and the iodoarylphosphonate. The target compounds were isolated after acidic hydrolysis in the form of the hydrochloride salts **1**·HCl and **2**·HCl·H_2O with a yield of 81% and 86%, respectively. $Pd(dppf)Cl_2$ was found to be superior to $Pd(PPh_3)_4$ as a catalyst; dry 1,4-dioxane as a solvent, Cs_2CO_3 as a base, and no co-ligands were the best found conditions. The alternative routes through iodoarylphosphonate of iodoarylpyrazole, with the crucial steps based on the copper-catalyzed coupling with acetylacetone or the Arbuzov reaction were proven inefficient. The structures of the isolated hydrochloride salts **1**·HCl and **2**·HCl·H_2O feature hydrogen-bonded networks involving the chloride anions.

Keywords: bifunctional ligands; pyrazolate; phosphonate; hydrogen bond; Suzuki-Miyaura

1 Introduction

The development of new ligand classes is crucial for the progress of the field of coordination polymers (CPs) and, in particular, its most important sub-field of metal-organic frameworks (MOFs). The increase of the stability and the tuning of structural characteristics of CPs/MOFs are important for various potential applications, including catalysis, gas storage and separation, sensing and heat transformation [1]–[4]. In recent years, many types of polytopic organic ligands with different donor groups, such as carboxylate, pyridyl, sulfonate, amine, etc., have been used for the synthesis of MOFs, with the most important and numerous class being the carboxylate compounds [5]. The far less numerous, but very promising azolate, especially pyrazolate, as well as phosphonate MOFs are the main competitors in terms of thermal and chemical, particularly hydrolytic stability [6], [7]. ZIF-8 [Zn(2-methylimidazolate)$_2$] [8]–[10] is one of the most hydrolytically stable azolate-based MOFs, and has been demonstrated to be extremely stable in boiling water over a broad pH range. Pyrazolate-based metal units often possess unsaturated metal centres and feature heterogeneous catalytic properties, like MFU-1 [Co_4O(3,5-dimethylpyrazolate)$_6$], and MFU-2 [Co_4O(bdpb)$_3$] (H_2-

bdpb = 1,4-bis[3,5-dimethyl)-pyrazol-4-yl]benzene) [11] both of which contain redox-active Co^{2+} centres. Moreover, coordination polymers and MOFs based on pyrazolate are interesting for potential applications such as heat transformation, magnetism, gas separation, etc. [12]–[16]. Phosphonate MOFs with proven porosity are still an emerging area with a relatively limited results, which are, though, very important, due to their typically high stability. The scarcity of the results might be explained by the propensity of the phosphonates to form layered structures. The polymorphism, typical for multidentate ligands, and low-reversibility of metal-ligand bond formation, which hinders the isolation of good-quality single-crystals, further complicate the synthesis and investigation of porous metal-phosphonate networks [17], [18]. Clearfield *et al.* have done extensive work to prepare a series of mesoporous metal phosphonate frameworks with 1,4-phenylenediphosphonate and biphenyldiphosphonate as ligands and zirconium as the metal atom [19]. Wharmby *et al.* reported a series of isoreticular compounds based on the linkers *N*,*N*′-piperazinediphosphonate and *N*,*N*′-bispiperidinediphosphonate with Ni and Co as metal atoms, which are porous to N_2 with a pore volume of up to 0.68 $cm^3\ g^{-1}$ [20]. More recently, the sorption properties of M-CAU-29 (M = Ni, Mn, Co and Cd), having a porphyrin-based tetraphosphonate linker, were studied [21]. Ni-CAU-29 shows no uptake of N_2 at T = 77 K, but a water uptake of 181 mg g^{-1} at 298 K. Mn-, Co- and Cd-CAU-29 show N_2 uptakes of 90, 145 and 180 $m^2\ g^{-1}$ and H_2O uptakes of 140, 166 and 116 mg g^{-1}, respectively. Further, Ni-metallated porphyrin-based tetraphosphonates with Zr and Hf atoms as metal nodes (Zr- and Hf-CAU-30) demonstrated high specific surface areas of 1070 and 1030 $m^2\ g^{-1}$, respectively [22].

The use of the mixed-functional ligands is an approach to combine the advantages of different types of coordination groups and to use them synergistically in the structural context [23], [24]. The pyrazolate and phosphonate pair is especially interesting, allowing to target both single- and bimetal species. Indeed, both the pyrazolate and phosphonate ligands are effectively coordinated by divalent transition metal ions. However, the pyrazolate anion is more affine to 'softer' metal ions (e. g. Cu^{2+}, Zn^{2+}), while the oxygen-donating phosphonate group prefers 'hard' metal ions (e. g. Fe^{3+}, Zr^{4+}) in the HSAB [25] concept, which would allow for the targeted bimetal approach. Mixed pyrazolate/phosphonate MOFs are yet practically unknown. However, existing mixed-ligand CPs with versatile architectures [26], [27], with a combination of (organo)phosphonate groups [28],[29] together with separate pyrazolate ligands, prove the viability of the concept. Besides, high chemical and thermal stabilities could also be expected as in the already more advanced CPs with mixed-functional carboxylate-pyrazolate [30],[31] or carboxylate-phosphonate linkers [32].

In this work, we have developed the synthesis of bi- or mixed-functional pyrazole-phosphonic acid molecules based on a *p*-phenylene core, which should be primary targets as MOF ligands. To the best of our knowledge, 3,5-dimethyl-4-(4-phosphonophenyl)-1*H*-pyrazole and 4-(4-phosphonophenyl)-1*H*-pyrazole Scheme 1 and Scheme 2) are unknown so far, possibly because their low-cost large-scale preparation is problematic, as is shown below.

2 Results and discussion

Our strategy was to use the 1,4-diiodobenzene as a starting compound and to substitute the iodine atoms sequentially by pentane-2,4-dion-3-yl (i.e. acetylacetonyl, as a 3,5-dimethylpyrazole synthon) and diethylphosphonyl groups in either order. This route should potentially allow the preparation of the target compounds on a large scale at low cost.

In the first attempted sequence, 3-(4-iodophenyl)-2,4-pentadione was prepared according to a method of Liu and Zeng [33], starting from 1,4-diiodobenzene and acetylacetone in the presence of CuI/L-proline as catalyst (Scheme 1a). This intermediate and hydrazine monohydrate were dissolved in deionized water to afford the respective 3,5-dimethylpyrazole, following a known procedure by Spassow [34]. However, the next step to synthesize the

phosphonate ester through the nickel(II) catalyzed conversion was not successful. The NH-pyrazole is evidently not inert under the conditions of the Michaelis-Arbuzov reaction, which proceeds at high temperature (note, that under these conditions the acetylacetonyl precursor is expected to be even less inert).

In the reverse sequence (Scheme 1b), the diethyl 4-iodophenylphosphonate was synthesized in the first step, followed by a conversion attempt to diethyl-4-(pentane-2,4-dion-3-yl)phenylphosphonate. A mixture of products was obtained and the purification trials, including column chromatography, were not successful.

The failure of stepwise introduction of functionalities prompted us to turn to the Suzuki-Miyaura cross-coupling reaction between components already containing the necessary functionalization (Scheme 2). Commercially available pinacol esters of the 1-Boc-3,5-dimethylpyrazole-4-boronic acid or 1-Boc-pyrazol-4-boronic acids (Boc stands for *N*-*tert*-butyloxycarbonyl) were used as the pyrazole containing reactants, and the synthesized diethyl 4-iodophenylphosphonate as the phosphonate containing one. Our analysis of the literature indicated that while 1*H*-pyrazoles could participate in the Suzuki-Miyaura coupling, both the number of steps and the yields are lower compared to the cases when N-protected pyrazoles are used. $Pd(dppf)Cl_2$ as a catalyst demonstrated higher efficiency compared to $Pd(PPh_3)_4$, and performed well in dry 1,4-dioxane at T = 100 °C for 6 h, in the presence of Cs_2CO_3 as a base [35]. The bifunctional pyrazole-phosphonic acid was obtained through the hydrolysis of the obtained esters, thus liberating the phosphonic acid and the 1*H*-pyrazole groups.

Thus, 3,5-dimethyl-4-(4-phosphonophenyl)-1*H*-pyrazole, **1**, and 4-(4-phosphonophenyl)-1*H*-pyrazole, **2**, were synthesized via coupling and subsequent hydrolysis. The products were isolated in the form of the hydrochlorides **1**·HCl and **2**·HCl·H_2O in overall yields of 32% and 33%, respectively (Scheme 2).

Colorless needle-like crystals of **1**·HCl and **2**·HCl·H_2O were obtained by slow evaporation of hydrochloric acid solutions of **1** and **2**. The phase purities of the bulk samples were verified by comparison of the powder X-ray diffraction patterns with the simulations from the obtained single crystal X-ray data sets (Fig. S8 and Fig. S17; Supporting information available online).

Compound **1**·HCl crystallizes in the monoclinic space group $P2_1/c$ the co-crystallizing molecule hydrochloric acid protonating the pyrazole group to a pyrazolium cation (Fig. 1a). The structure of **1**·HCl can be dissected into hydrogen-bonded chains of centrosymmetric $(\cdots{}^{+}HAB\cdots BAH^{+}\cdots 2Cl^{-})_n$ aggregates of the bifunctional pyrazolium-phosphonic acid or ^{+}HAB molecules (Fig. 1b). Two pyrazolium moieties and two chloride ions are associated in a ten-membered $\{\text{-}pzH^{+}\cdots Cl^{-}\}_2$ hydrogen-bonded ring motif, sustained by two strong charge-assisted $NH^{+}\cdots Cl^{-}$ hydrogen bonds. The two NH···Cl distances are slightly different with 3.060(2) and 3.169(2) Å, but are within the expected range of 3.05–3.2 Å for comparable $NH^{+}\cdots Cl^{-}$ cases [36]. The observed ring motif has a graph set descriptor of $R_4^2(10)$ [37], which is typically seen in structures of pyrazolium salts with halide anions [38]. The phosphonic acid groups are also associated pairwise, forming simple $\{RPO(OH)_2\}_2$ rings with a $R_2^2(8)$ graph set notation. This simple and symmetric association mode, well-known for carboxylic acids, is common for compounds containing a similar 1:1 donor/acceptor XO(OH) fragment (X = C, P, S) [39]. The $\{RPO(OH)_2\}_2$ ring is planar and built by strong O–H···O bonds, with a typical O···O distance of 2.546(2) Å [40]. The additional P–OH donor of the phosphonic acid group, which is not involved in the formation of the ring pattern, forms a strong hydrogen bond with the chloride anion of a neighboring hydrogen-bonded chain, d(O···Cl) = 2.976(2) Å (Fig. 1c). The $(\cdots{}^{+}HAB\cdots BAH^{+}\cdots 2Cl^{-})_n$ chains are, thereby, associated into sheets, which in turn are held together by weaker interactions, among which very weak methyl-CH···O and methyl-CH···Cl^{-} contacts are discernible.

The chains within the stacks are not planar and hence are not packed tightly to have a possible additional stabilization from π···π interactions. The latter would be typical for planar chains in bipyrazolium salts [38]. Two factors lead to the non-planarity: the $\{RPO(OH)_2\}_2$ ring pattern is not co-planar to that of the phenyl group due to the

tetrahedral environment of the phosphorus atom and the phenyl ring is not coplanar with the pyrazole ring. The latter deviation is due to repulsion of the methyl groups of the pyrazole ring and the hydrogen atoms on the phenyl group. The dihedral pyrazole-phenyl angle is ~37.5°.

Compound **2**·HCl·H_2O crystallizes in the monoclinic space group $P2_1/c$. The structure incorporates also a water molecule of crystallization (Fig. 2a) to give the crystallographic formula **2**·HCl·H_2O. Again, the hydrochloric acid molecule protonates the pyrazole group to a pyrazolium cation. The water molecule perturbs the expected simple chain association which was seen in the structure of **1**·HCl (Fig. 2b). The water molecule is held by hydrogen bonding from an N–H donor and to a Cl^- and O(3)=P acceptor. Each Cl^- anion interacts with three H atoms (Fig. 2b), one from pzH^+, one from an H atom of {$(RPO(OH)_2)$} and one from an H atom of the water molecule. The crystal structure shows a hydrogen bonded network with head-to-tail linked pyrazolium-phosphonic acid or $^+$HAB molecules via the N–H···Cl^- hydrogen bonds between the -$N_2H_2^+$ and -PO_3H_2 moieties. Compound **2**·HCl·H2O displays an overall three-dimensional supramolecular structure, which consists of strong charge-assisted OH···Cl^-, NH^+···Cl^-, plus OH···O and weak CH···Cl^- hydrogen bonds (Fig. 2b). The phenyl and pyrazolium rings are not coplanar but form a dihedral angle of 11.37(7)°.

The thermogravimetric behavior of **1**·HCl shows a weight loss of 11.3% between T = 150 and 250 °C, which corresponds to the one molecule of hydrogen chloride (12.5% theoretically) (Fig. 3). The mass loss of ~5% in the range of 250 and 350 °C is assigned to the dehydration (–1 H_2O, 7% theoretically) through the condensation of phosphoric acid groups to give anhydrides [41].

The themogravimetric behavior of **2**·HCl·H_2O in Fig. 4 shows a weight loss of 5.3% between T = 60 and 150 °C corresponding to the one molecule of water (6.1% theoretically). The second step of 8.4% in the temperature range of 150–320 °C is assigned to the one molecule of hydrogen chloride (14.2% theoretically).

3 Experimental section

3.1 Materials and measurements

All reagents and starting materials were commercially available and used without further purification. Elemental analyses were performed on a Perkin Elmer CHN 2400 (Perkin Elmer, Waltham, MA, USA). ^{1}H, ^{13}C, ^{31}P NMR spectra were collected with a Bruker Avance DRX-300 or Bruker Avance DRX-600 instrument. FT-IR spectra were recorded in ATR mode on a Bruker TENSOR 37 IR spectrometer (Bruker Optics, Ettlingen, Germany). The absorbance bands are presented by using of the following abbreviations: strong (s), medium (m), weak (w), broad (br) and shoulder (sh). The powder X-ray diffraction patterns (PXRD) were recorded using a Bruker AXS D2 Phaser with a flat silicon low background sample holder, using Cu$K\alpha$ radiation with λ = 1.5418 Å at 30 kV, 10 mA and a Lynxeye 1D detector. The measurement was performed at room temperature with 2θ angles in the range 5–50° and a step size of 0.02° (in 2θ). Thermogravimetric analysis data (TGA) was collected on a Netzsch TG 209 F3 Tarsus instrument (Netzsch, Selb, Germany) equipped with an aluminum crucible and using a heating rate of 5 K min^{-1} in air.

3.2 Synthesis of 3,5-dimethyl-4-(4-phosphonophenyl)-1*H*-pyrazole, 1·HCl

3.2.1 Synthesis of diethyl 4-iodophenylphosphonate

In a two necked 50 mL flask 3.0 g (0.009 mol) of 1,4-diiodobenzene and 0.059 g (0.0004 mol) of anhydrous $NiCl_2$ were suspended in 10 mL of mesitylene. The suspension was placed under nitrogen and heated to 160 °C with refluxing. After one hour 1.74 g (0.01 mol) of triethyl phosphite was added dropwise over 2 hours. After refluxing for another two hours for completion of the reaction, the yellow suspension was allowed to cool to the room temperature. The yellow mixture was filtered to remove the rest of nickel salt, washed with hexane and heated to 130 °C to remove mesitylene. The excess of solvent was removed under reduce pressure. The yellow residue was subjected to column chromatography (silica gel, 1:1 ethyl acetate:hexane). The resulting liquid was dried under reduce pressure to afford 1.83 g (61%) of pure product. – ^{1}H NMR (300 MHz, $CDCl_3$): δ (ppm) = 1.31 (t, 6H), 4.11 (q, 4 H), 7.51 (d, 2H), 7.82 (d, 2H) (Fig. S1). – ^{13}C NMR (300 MHz, DMSO-d_6): δ (ppm) = 16.94 (CH_3), 62.88 (CH_2), 127.38 (O–CH_3), 129.9 (O–CH_3), 133.80–138.39 (aromatic C atoms) (Fig. S2). – ^{31}P{H} NMR (300 MHz, DMSO-d_6): δ (ppm) = 18.05 (Fig. S3).

3.2.2 Synthesis of 3,5-dimethyl-4-(4-phosphonophenyl)-1-*tert*-butoxycarbonyl-pyrazole

According to the Suzuki-Miyaura cross-coupling reaction [42], 1.0 g (0.003 mol) of diethyl 4-iodophenylphosphonate, 1.1 g (0.004 mol) of 3,5-dimethylpyrazole-4-boronic acid pinacol ester, and 3.9 g (0.012 mol) of $Cs_2(CO_3)$ were placed in a two necked 250 mL flask under nitrogen and suspended in 100 mL of 1,4-dioxane. Finally, 0.122 mg (0.15 mmol) of $PdCl_2$(dppt) was added under constant stirring. The suspension was heated to 100 °C for 6 h. After the reaction was completed as monitored by TLC, the cooled dark beige suspension was filtered and subjected to column chromatography (silica gel, 97 : 3% ethyl acetate-methanol) to yield 0.76 g (76%) of pure oily product. – ^{1}H NMR (600 MHz, $CDCl_3$): δ (ppm) = 1.35 (t, 6H), 1.66 (m, 9H), 2.26 (s, 3H), 2.46 (s, 3H), 4.19 (q, 4H), 7.32 (d, 2H), 7.84 (d, 2H) (Fig. S4). – ^{13}C NMR (600 MHz, $CDCl_3$): δ (ppm) = 16.75 (CH_3), 28.42 (CH_3), 62.59 (CH_3), 85.74 (CH_2) 136.83 (s, C–N), 140.70 (C–O), 148.89–150.69 (aromatic C atoms) (Fig. S5). – ^{31}P{H} NMR (600 MHz, $CDCl_3$): δ (ppm) = 18.61 (Fig. S6).

3.2.3 Synthesis of 3,5-dimethyl-4-(4-phosphonophenyl)-1*H*-pyrazole, 1·HCl

In a 15 mL Pyrex tube 0.76 g (0.002 mol) of 3,5-dimethyl-4-(4-phosphonophenyl)-1-*tert*-butoxycarbonyl-pyrazole was dissolved in 3.0 mL of concentrated HCl and heated to 100 °C for 24 h. A colourless crystalline product was obtained, which was dried in air (Fig. S7). Yield 0.61 g (81%). m.p. > 350 °C, decomp. > 400°C. Elemental analysis calcd. (%) for $C_{11}H_{14}N_2O_3PCl$: C 45.77, N 9.70, H 4.89; found C 44.25, N 9.75, H 3.43. – FT-IR ATR (neat): ν_{max} (cm^{-1}) = 2708 (br), 1595 (w), 1203 (s), 1139 (s), 981 (s), 914 (s), 835 (s), 603 (s) (Fig. S9). – ^{1}H NMR (300 MHz, NaOD, DMSO-d_6): δ (ppm) = 2.24 (s, 6H), 7.23 (m, 2H), 7.68 (m, 2H) (Fig. S10).– ^{13}C NMR (300 MHz, NaOD, DMSO-d_6): δ (ppm) = 12.91 (CH_3), 115.45 (C–N), 127–144.60 (aromatic C atoms) (Fig. S11). – ^{31}P{H} NMR (300 MHz, NaOD, DMSO-d_6): δ (ppm) = 12.48 (Fig. S12).

3.3 Synthesis of 4-(4-phosphonophenyl)-1*H*-pyrazole, 2·HCl·H_2O

3.3.1 Synthesis of 4-(4-phosphonophenyl)-1-*tert*-butoxycarbonyl-pyrazole

In a two necked 250 mL flask 1.0 g (0.003 mol) of diethyl 4-iodophenylphosphonate, 1.04 g (0.004 mol) of 1-Boc-pyrazol-4-boronic acid pinacol ester and 3.8 g (0.012 mol) of $Cs_2(CO_3)$ were placed under nitrogen and suspended in 100 mL of 1,4-dioxane. Finally, 0.12 mg (0.15 mmol) of $PdCl_2$(dppt) was added under constant stirring. The suspension was heated to 100 °C for 6 h. After the reaction was completed as monitored by TLC, the cooled dark beige suspension was filtered and subjected to column chromatography (silica gel, 97 : 3% ethyl acetate-methanol) to yield 0.79 g (79%) of pure oily product. – ^{1}H NMR (300 MHz, $CDCl_3$): δ (ppm) = 1.33 (t, 3H), 1.68 (s, 9H), 4.15 (m, 4H), 7.61 (m, 2H), 7.80 (m, 2H), 8.03 (s, 1H), 8.38 (s, 1H) (Fig. S. 13). – ^{13}C NMR (300 MHz, $CDCl_3$): δ (ppm) = 16.34 (CH_3), 24.54 (CH_3), 62.27 (CH_3), 86.0 (CH_2), 125.75 (s, C–N), 127.21 (C–O), 141.65 (aromatic C atoms) (Fig. S14). – ^{31}P{H} NMR (300 MHz, $CDCl_3$): δ (ppm) = 13.03 (Fig. S15).

3.3.2 Synthesis of 4-(4-phosphonophenyl)-1*H*-pyrazole, 2·HCl·H_2O

In a 15 mL Pyrex tube 0.79 g (0.002 mol) of 4-(4-phosphonophenyl)-1-*tert*-butoxycarbonyl-pyrazole was dissolved in 3.0 mL of concentrated HCl and heated to 100 °C for 24 h. A colourless crystalline product was obtained, which was dried in air (Fig. S16). Yield 0.68 g (86%). m.p. > 300°C, decomp. > 350°C. – Elemental analysis calcd. (%) for $C_9H_{12}N_2O_4PCl$: C 38.80, N 10.05, H 4.34; found C 38.88, N 10.96, H 4.10. – FT-IR ATR (neat): ν_{max} (cm^{-1}): 3120 (v), 1682 (w), 1607 (w), 1139 (s), 1050 (s), 992 (s), 926 (s), 827 (s), 741 (s), 572 (s) (Fig. S18). – ^{1}H NMR (600 MHz, NaOD, DMSO-d_6): δ (ppm) = 7.65 (m, 2H), 7.70 (m, 2H), 8.17 (s, 1H) (Fig. S19). – ^{13}C NMR (600 MHz, NaOD, DMSO-d_6): δ (ppm) = 123.76 (C–N), 130–136 (aromatic C atoms) (Fig. S20). – ^{31}P{H} NMR (600 MHz, NaOD, DMSO–d_6): δ (ppm) = 12.96 (Fig. S21).

3.4 Single crystal X-ray diffraction

Selected needle-like single crystals of suitable optical quality of **1**·HCl and **2**·HCl·H_2O selected under a polarizing microscope and coated in perfluorinated oil were mounted on a 0.2 mm cryo loop and transferred to the diffractometer, a Bruker Kappa APEX2 CCD X-ray diffractometer system (Bruker AXS Inc., Madison, WI, USA) with microfocus tube, Cu$K\alpha$ radiation (λ = 1.54178 Å), 100±2 K; multilayer mirror system, ω scans; data collection with APEX2 [43], cell refinement with SMART and data reduction with SAINT [44], experimental absorption correction with SADABS [45]. The information regarding data collection and structure refinement is summarized in Table 1. The structures were solved by Direct Methods using SHELXL2016 [46, 47] and refined by full-matrix least-squares on F^2 using SHELX-97. Graphics were drawn with DIAMOND [48].

CCDC 1961142 and 1961143 contain the supplementary crystallographic data for **1**·HCl and **2**·HCl·H_2O, respectively. These data can be obtained free of charge from The Cambridge Crystallographic Data Centre via www.ccdc.cam.ac.uk/data_request/cif.

4 Conclusions

In summary, two novel bifunctional pyrazolate-phosphonate ligands 3,5-dimethyl-4-(4-phosphonophenyl)-1*H*-pyrazole, **1** and 4-(4-phosphonophenyl)-1*H*-pyrazole, **2** have been prepared via a Suzuki-Miyaura cross-coupling and their crystal structures determined. These multidentate ligands with five potential coordination sites offer the use as suitable organic spacers to provide new coordination polymers or metal-organic frameworks (MOFs). The high thermal stability of the synthesized compounds aids in the hydrothermal synthesis of coordination polymers or MOFs. We are confident that in continuation of this work a large number of interesting supramolecular complexes for a variety of applications will be reported in the future.

5 Supporting information

PXRD patterns, ^{1}H, ^{13}C, ^{31}P NMR and IR spectra are given as supplementary material available online (DOI: 10.1515/znb-2019-0170).

Acknowledgements: The authors thank Dr. Ishtvan Boldog for his kind support during this project.

Figures

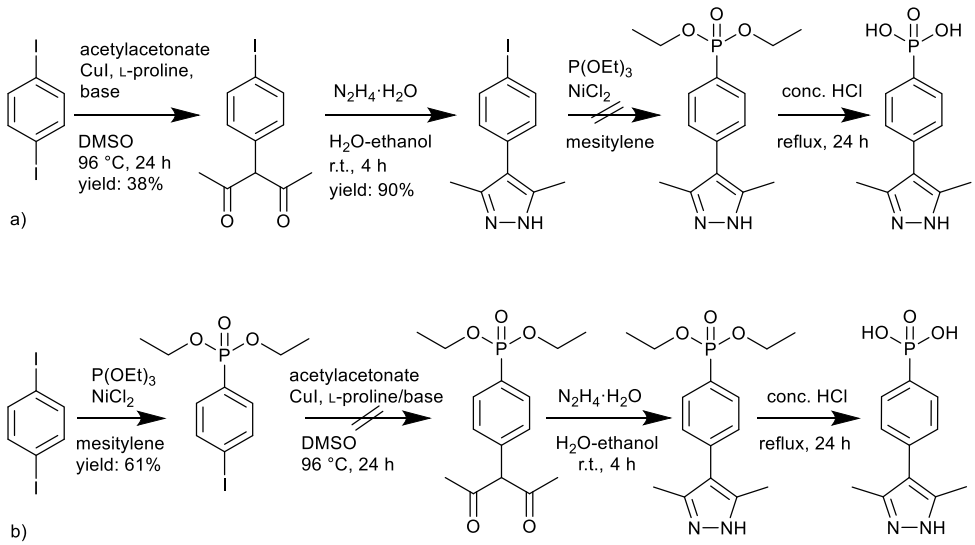

Scheme 1 Potential, but unsuccessful routes towards 3,5-dimethyl-4-(4-phosphonophenyl)-1*H*-pyrazole, **1** starting from 1,4-diiodobenzene.

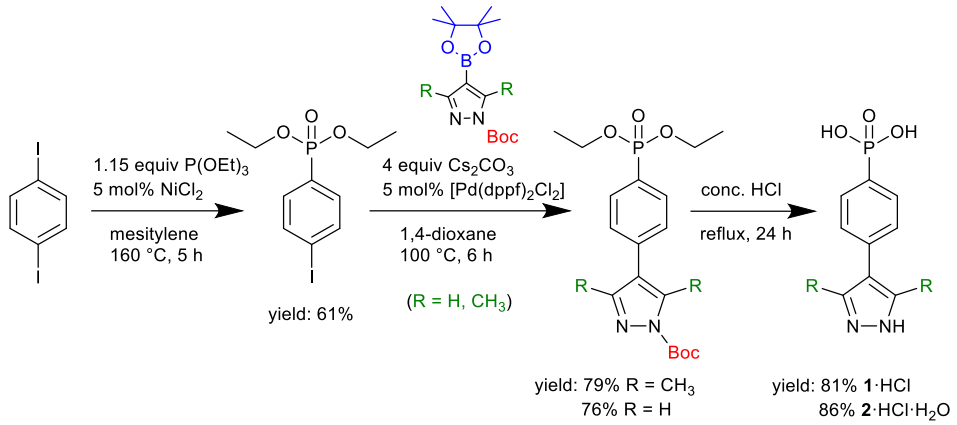

Scheme 2 Reaction sequence for the successful synthesis of **1**·HCl and **2**·HCl·H_2O starting from 1,4-diiodobenzene.

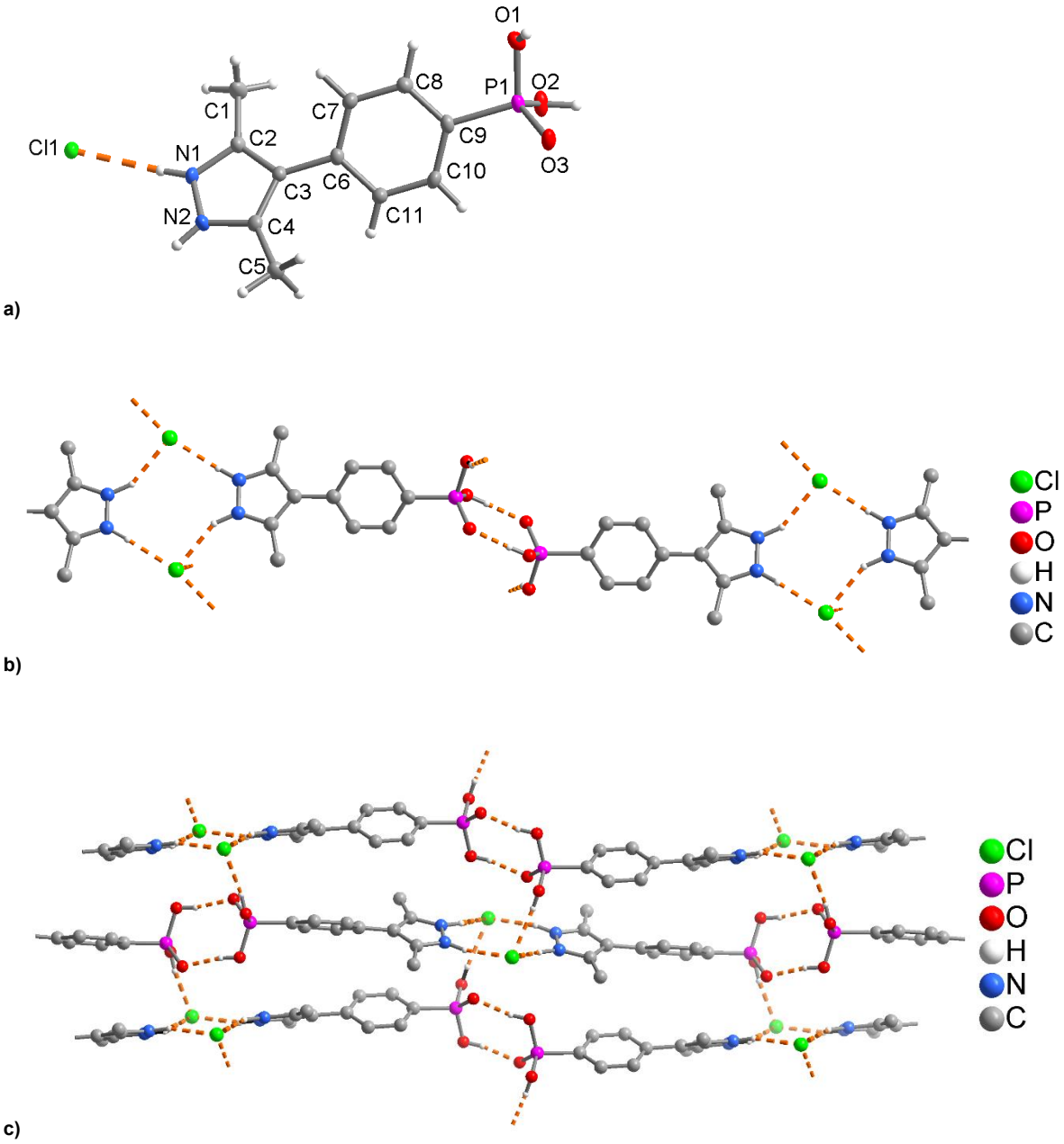

Fig. 1: (a) Asymmetric unit (50% displacement ellipsoids), (b) chain sub-structure and (c) two-dimensional hydrogen-bonded network of **1**·HCl. Details of the hydrogen bonding interactions (orange dashed lines) are given in Table 2.

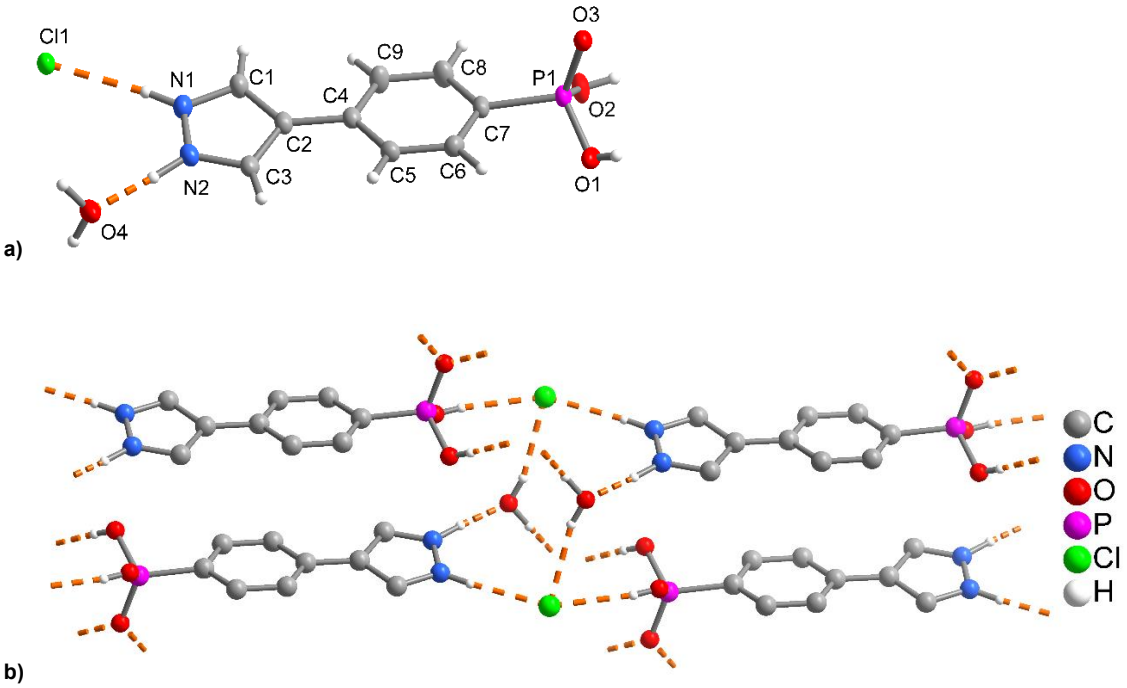

Fig. 2: (a) Asymmetric unit (50% displacement ellipsoids) and (b) section of the three-dimensional hydrogen-bonded network of **2**·HCl·H_2O. Details of the hydrogen bonding interactions (orange dashed lines) are given in Table 3.

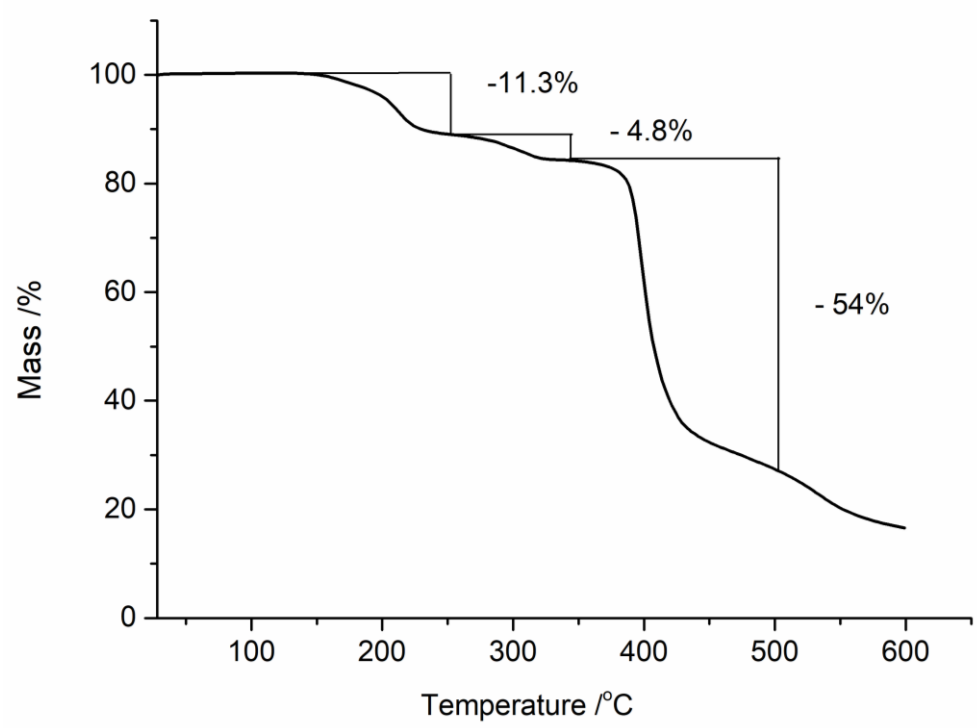

Fig. 3: TGA diagram of **1**·HCl in the temperature range 27–600°C with a heating rate of 5 K min^{-1} under N_2 atmosphere.

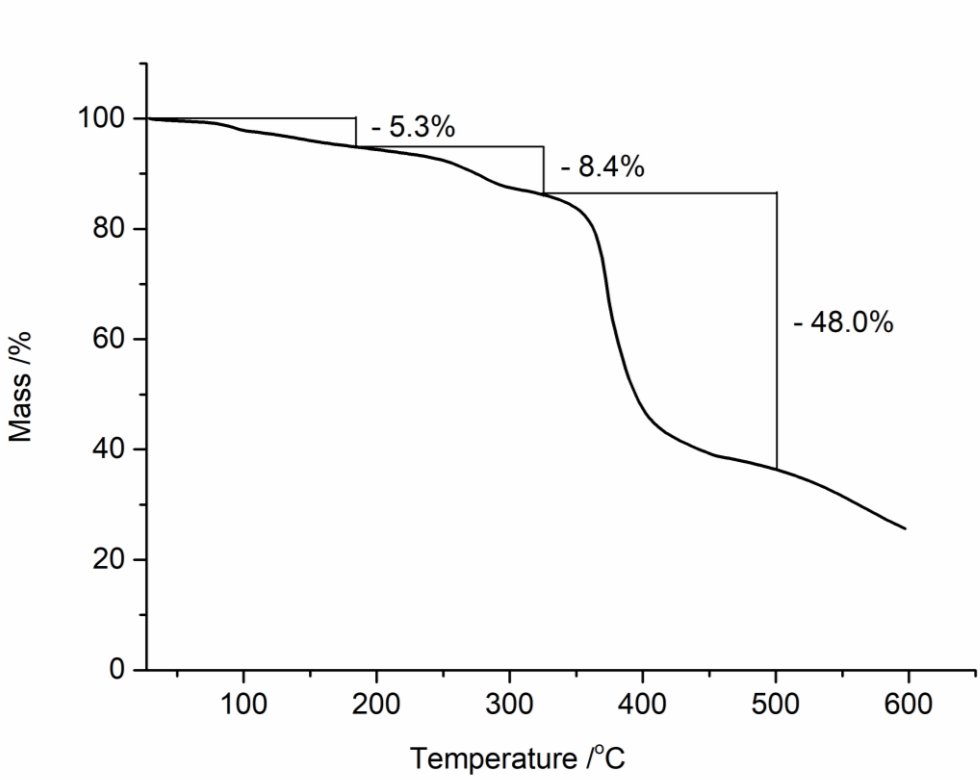

Fig. 4: TGA diagram of **2**·HCl·H_2O in the temperature range 27–600°C with a heating rate of 5 K min^{-1} under N_2 atmosphere.

Tables

Table 1: Crystal data and structure refinement for **1**·HCl and **2**·HCl·H_2O.

	1·HCl	**2·HCl·H_2O**
Empirical formula	$C_{11}H_{14}N_2O_3PCl$	$C_9H_{12}N_2O_4PCl$
M_r /g mol^{-1}	288.66	278.63
T /K	100(2)	100(2)
Wavelength /Å	1.54178	1.54178
Crystal system	monoclinic	monoclinic
Space group	$P2_1/c$	$P2_1/c$
a /Å	9.5963(19)	7.8070(5)
b /Å	7.7811(16)	12.6042(8)
c /Å	17.424(4)	12.3523(8)
β /deg	95.52(3)	90.595(2)
V /$Å^3$	1295.0(5)	1215.41(13)
Z	4	4
Calcd. density /g cm^{-3}	1.48	1.52

μ /mm^{-1}	3.8	4.1
F(000) /e	600	576
Crystal size /mm^3	0.4 × 0.2 × 0.1	0.4 × 0.1 × 0.05
θ range /deg	4.629–68.021	5.013–66.653
Reflections collected	14605	16599
Independent reflections; R_{int}	2327; 0.0477	1241; 0.0371
Completeness to θ_{max} /%	99.0	99.7
Data; ref. parameters	2327; 219	2141; 202
Goodness-of-fit	1.003	1.059
$R1$; $wR2$ (all data)	0.0379; 0.1075	0.0310; 0.0869
$\Delta\rho_{fin}$ (max; min), e Å^{-3}	0.595; -0.537	0.536; -312

Table 2: Details of the hydrogen bonding interactions in **1**·HCl.

***D*–H···*A*[a]**	***D*–H /Å**	**H···*A* /Å**	***D*···*A* /Å**	***D*–H···*A* /deg**	**Symmetry Transformations**
N1–H1···Cl1	0.83(3)	2.24(3)	3.060(2)	170(2)	
O1–H1···Cl1^{i}	0.85(4)	2.13(4)	2.9761(17)	170(3)	i = x–1, –y+1/2, z–1/2
N2–H2···Cl1^{ii}	0.82(3)	2.40(3)	3.169(2)	157(3)	ii = –x+2, –y+1, –z+2
O2–H2···O3^{iii}	0.81(3)	1.74(3)	2.546(2)	172(3)	iii = –x, –y+1, –z+1
C1–H1B···O1^{iv}	0.95(3)	2.60(3)	3.388(3)	140(2)	iv = –x+1, –y+1, –z+1
C5–H5A···Cl1^{v}	1.01(3)	2.86(3)	3.692(2)	141(2)	v = x–1, y, z

[a] D = donor, A = acceptor

Table 3: Details of the hydrogen bonding interactions in **2**·HCl·H_2O.

***D*–H···*A*[a]**	***D*–H /Å**	**H···*A* /Å**	***D*···*A* /Å**	***D*–H···*A* /deg**	**Symmetry Transformations**
N1–H1···Cl1	0.89(3)	2.23(3)	3.1092(16)	169(2)	
N2–H2···O4	0.98(2)	1.61(2)	2.5871(18)	176(2)	
O1–H1···O3^{i}	0.65(3)	1.88(3)	2.5324(17)	176(3)	i = –x+1, –y+1, –z
O2–H2···Cl1^{ii}	0.75(3)	2.31(3)	3.0491(14)	171(2)	ii = x–1, y, z–1
O4–H4···Cl1^{iii}	0.81(3)	2.31(3)	3.0881(13)	163(2)	iii = –x+2, –y+1, –z+2
O4–H3···O3^{iv}	0.89(3)	1.82(3)	2.6786(16)	161(3)	iv = –x+2, –y+1, –z+1

[a] D= donor, A= acceptor

References

[1] C. Janiak, *Dalton Trans.* **2003**, 2781–2804.

[2] S. Kitagawa, R. Kitaura, S. I. Noro, *Angew. Chem. Int. Ed.* **2004**, *43*, 2334–2375.

[3] A. H. Chughtai, N. Ahmad, H. A. Younus, A. Laypkovc, F. Verpoort, *Chem. Soc. Rev.* **2015**, *44*, 6804–6849.

[4] J. R. Li, R. J. Kuppler, H. C. Zhou, *Chem. Soc. Rev.* **2009**, *38*, 1477–1504.

[5] S. Natarajan, P. Mahata, *Curr. Opin. Solid State Mater. Sci.* **2009**, *13*, 46–53.

[6] G. Alberti, M. Casciola, U. Costantino, R. Vivani, *Adv. Mater.* **1996**, *8*, 291–303.
[7] A. Clearfield, *Dalton Trans.* **2008**, 6089–6102.
[8] X. C. Huang, Y. Y. Lin, J. P. Zhang, X. M. Chen, *Angew. Chem. Int. Ed.* **2006**, *45*, 1557–1559.
[9] K. S. Park, Z. Ni, A. P. Cote, J. Y. Choi, R. Huang, F. J. Uribe-Romo, H. K. Chae, M. O'Keeffe, O. M. Yaghi, *Proc. Natl. Acad. Sci. USA* **2006**, *103*, 10186–10191.
[10] J. J. Low, A. I. Benin, P. Jakubczak, J. F. Abrahamian, S. A. Faheem, R. R. Willis, *J. Am. Chem. Soc.* **2009**, *131*, 15834–15842.
[11] M. Tonigold, Y. Lu, A. Mavrandonakis, A. Puls, R. Staudt, J. Möllmer. J. Sauer, D. Volkmer, *Chem. Eur. J.* **2011**, *17*, 8671–8695.
[12] J. Y. Lee, O. K. Farha, J. Roberts, K. A. Scheidt, S. T. Nguyen, J. T. Hupp, *Chem. Soc. Rev.* **2009**, *38*, 1450–1459.
[13] C. Heering, I. Boldog, V. Vasylyeva, J. Sanchiz, C. Janiak, *CrystEngComm* **2013**, *15*, 9757–9768.
[14] B. J. Burnett, P. M. Barron, W. Choe, *CrystEngComm* **2012**, *14*, 3839–3846.
[15] M. Viciano-Chumillas, S. Tanase, L. J. de Jongh, J. Reedijk, *Eur. J. Inorg. Chem.* **2010**, *22*, 3403–3418.
[16] C. W. Lu, Y. Wang, Y. Chi, *Chem. Eur. J.* **2016**, *22*, 17892–17908.
[17] K. J. Gagnon, H. P. Perry,A. Clearfield, *Chem. Rev.* **2012**, *112*, 1034–1054.
[18] S. J. I. Shearan, N. Stock, F, Emmerling, J. Demel, P. A. Wright, K. D. Demadis, M. Vassaki, F. Costantino, R. Vivani, S. Sallard, I. R. Salcedo, A. Cabeza, M. Taddei, *Crystals* **2019**, *9*, 270.
[19] R. Silbernagel, C. H. Martin, A. Clearfield, *Inorg. Chem.* **2016**, *55*, 1651–1656.
[20] M. T. Wharmby, J. P. S. Mowat, S. P. Thompson and P. A. Wright, *J. Am. Chem. Soc.* **2011**, *133*, 1266–1269.
[21] T. Rhauderwiek, K. Wolkersdörfer, S. Øien-Ødegaard, K. P. Lillerud, M. Wark, N. Stock, *Chem. Commun.* **2018**, *54*, 389–392.
[22] T. Rhauderwiek, H. Zhao, P. Hirschle, M. Doeblinger, B. Bueken, H. Reinsch, D. D. Vos, S. Wuttke, U. Kolb, N. Stock, *Chem. Sci.* **2018**, *9*, 5467–5478.
[23] J. Jia, X. Lin, C. Wilson, A. J. Blake, N. R. Champness, P. Hubberstey, G. Walker, E. J. Cussen, M. Schroeder, *Chem. Commun.* **2007**, 840–842.
[24] X. J. Gu, Z. H. Lu, Q. Xu, *Chem. Commun.* **2010**, *46*, 7400–7402.
[25] T.–L. Ho, *Chem. Rev.* **1975**, *75*, 1, 1–20.
[26] M. O'Keeffe, *Chem. Soc. Rev.* **2009**, *38*, 1215–1217.
[27] M. O'Keeffe, O. M. Yaghi, *Chem. Rev.* **2012**, *112*, 675–702.
[28] P. O. Adelani, L. J. Jouffret, J. E. S. Szymanowski, P. C. Burns, *Inorg. Chem.* **2012**, *51*, 12032–12040.
[29] P. O. Adelani, G. E. Sigmon, P. C. Burns, *Inorg. Chem.* **2013**, *52*, 6245–6247.
[30] C. Heering, I. Boldog, V. Vasylyeva, J Sanchiz, C. Janiak, *CrystEngComm* **2013**, *15*, 9757–9768.
[31] J. Dechnik, A. Nuhnen, C. Janiak, *Cryst. Growth Des.* **2017**, *17*, 4090–4099.
[32] C. Heering, B. Francis, B. Nateghi, G. Makhloufi, S. Luedeke, C. Janiak, *CrystEngComm* **2016**, *18*, 5209–5223.
[33] J. Liu, R. Zeng, C. Zhou, J. Zou, *Chin. J. Chem.* **2011**, *29*, 309–313.
[34] A. Spassow, *Organic Syntheses* **1955**, *3*, 390.
[35] A. Sarkar, S. R. Roy, N. Parikh, A. K. Chakraborti, *J. Org. Chem.* **2011**, *76*, 7132–7140.
[36] T. Steiner, *Acta Crystallogr. B* **1998**, *54*, 456–463.
[37] J. Grell, J. Bernstein, G. Tinhofer *Crystallogr. Rev*. **2002**, *8*, 1–56.
[38] I. Boldog, J. C. Daran, A. N. Chernega, E. B. Rusanov, H. Krautscheid, K. V. Domasevitch, *Cryst. Growth Des.* **2009**, *9*, 2895–2905.
[39] F. H. Allen, W. D. Samuel Motherwell, P. R. Raithby, G. P. Shields, R. Taylor, *New J. Chem.* **1999**, *23*, 25–34.
[40] T. Steiner, *Angew. Chem. Int. Ed.* **2002**, *41*, 48–76.
[41] S. Vairam, S. Govindarajan, *Thermochim. Acta* **2004**, *414*, 263–270.
[42] N. Miyaura, A. Suzuki, *Chem. Rev.* **1995**, *95*, 2457–2483.
[43] APEX2, Data Reduction and Frame Integration Program for the CCD Area-Detector System, Bruker AXS Inc., Madison, WI (USA) **1997**–**2006**.
[44] SMART, SAINT, Area Detector Control and Integration Software, Bruker AXS Inc., Madison, Wisconsin (USA) **2003**.
[45] G. M. Sheldrick, SADABS, Area-Detector Absorption Correction; University of Göttingen: Göttingen (Germany) **1996**.
[46] G. M. Sheldrick, *Acta Crystallogr*. **2015**, *A71*, 3–8.
[47] G. M. Sheldrick, *Acta Crystallogr*. **2008**, *A64*, 112–122.

[48] K. Brandenburg, DIAMOND (version 4.4), Crystal and Molecular Structure Visualization, Crystal Impact - K. Brandenburg & H. Putz Gbr, Bonn (Germany) **2009**–**2017**.

Supporting Information

Bahareh Nateghi, Christoph Janiak*

Synthesis and characterization of two bifunctional pyrazole-phosphonic acid ligands

DOI: 10.1515/znb-2019-0170. Received October 24, 2019; accepted October 4, 2019

***Corresponding author: Professor Dr. Christoph Janiak,** Institut für Anorganische Chemie und Strukturchemie, Heinrich-Heine-Universität Düsseldorf, Universitätsstraße 1, D-40225 Düsseldorf, Germany, Tel.:+49-211-81-12286, e-mail: janiak@uni-duesseldorf.de

Bahareh Nateghi: Institut für Anorganische Chemie und Strukturchemie, Heinrich-Heine-Universität Düsseldorf, Universitätsstraße 1, D-40225 Düsseldorf, Germany, e-mail: bahareh.nateghi @uni-duesseldorf.de

Contents

Synthesis

Materials: 1,4-diiodobenzene (99%, Sigma-Aldrich), CuI (99.5%, Sigma-Aldrich), $Cs_2(CO_3)$ (99%, Sigma-Aldrich), Triethylphosphite (98%, Sigma-Aldrich), $NiCl_2$ (anhydrous, 98%, Alfa Aesar), Cs_2CO_3 (anhydrous, 99%, Sigma-Aldrich), Pd(dppf)Cl_2 (98%, Carbolution), 3,5-dimethylpyrazole-4-boronic acid pinacol ester (97%, Sigma-Aldrich), 1-Boc-pyrazol-4-boronic acid pinacol ester (97%, Maybridge), mesitylene (99.8%, Sigma-Aldrich), 1,4-dioxane (99%, Fisher scientific), hydrochloric acid concentrated (37%, VWR).

Synthesis of 3,5-dimethyl-4-(4-phosphonophenyl)-1*H*-pyrazole, 1·HCl

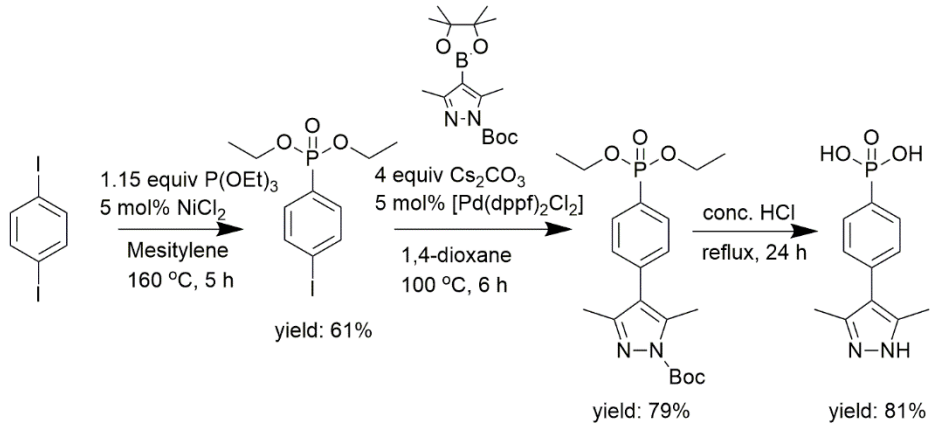

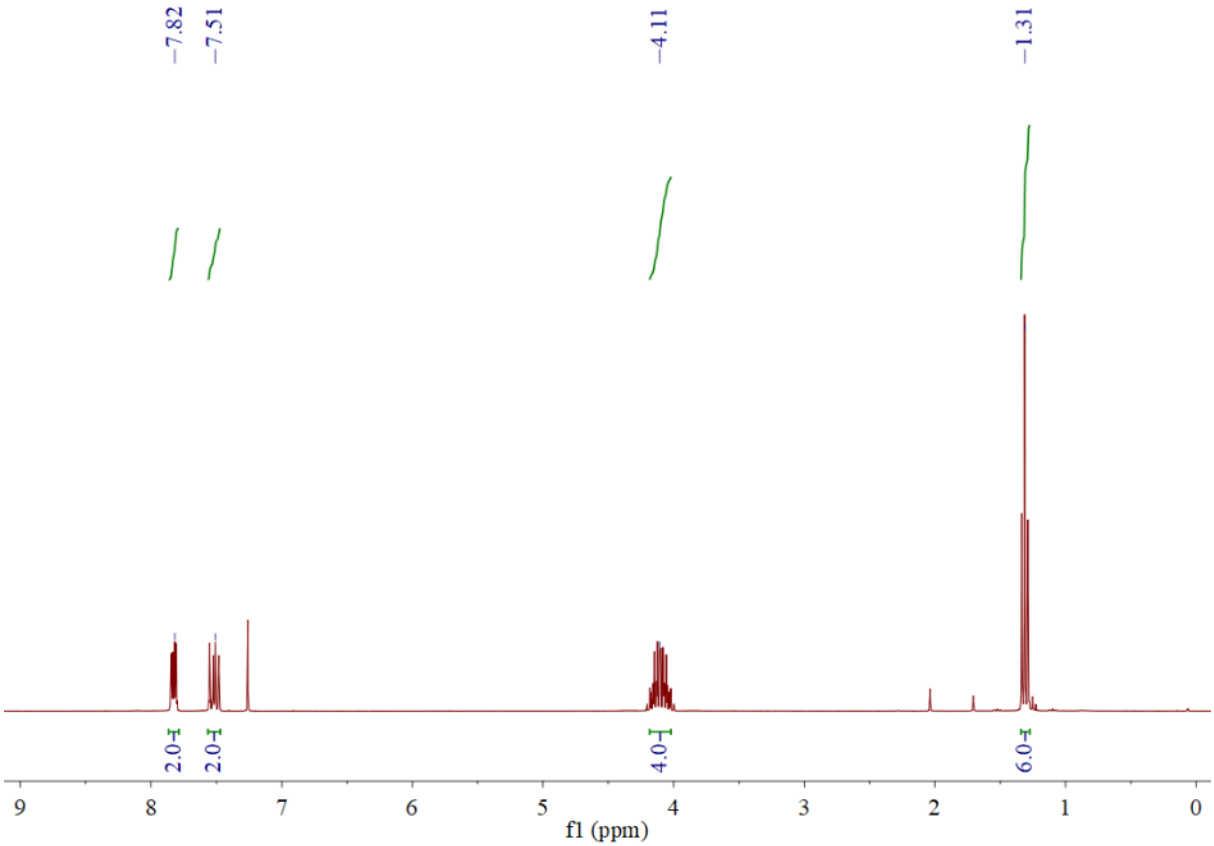

Fig. S1 ^{1}H NMR spectrum (in $CDCl_3$) of diethyl 4-iodophenylphosphonate.

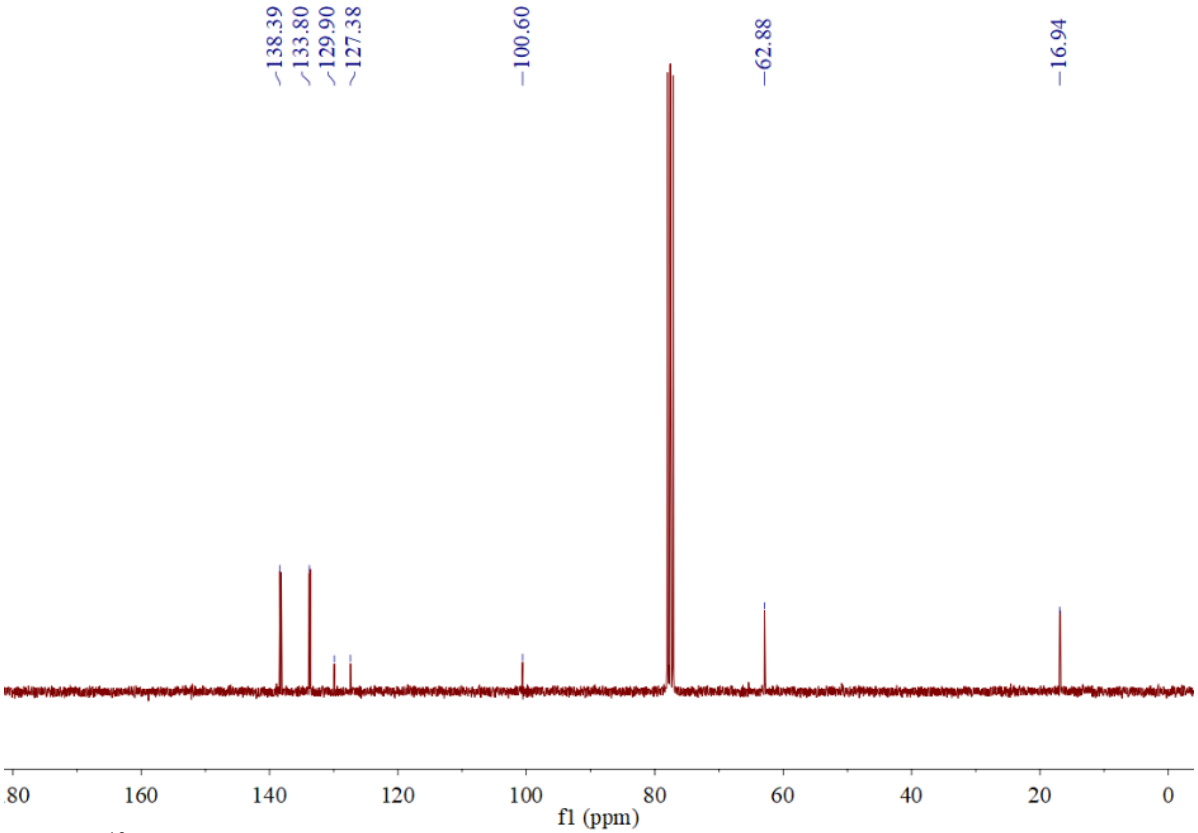

Fig. S2 ^{13}C NMR spectrum (in $CDCl_3$) of diethyl 4-iodophenylphosphonate.

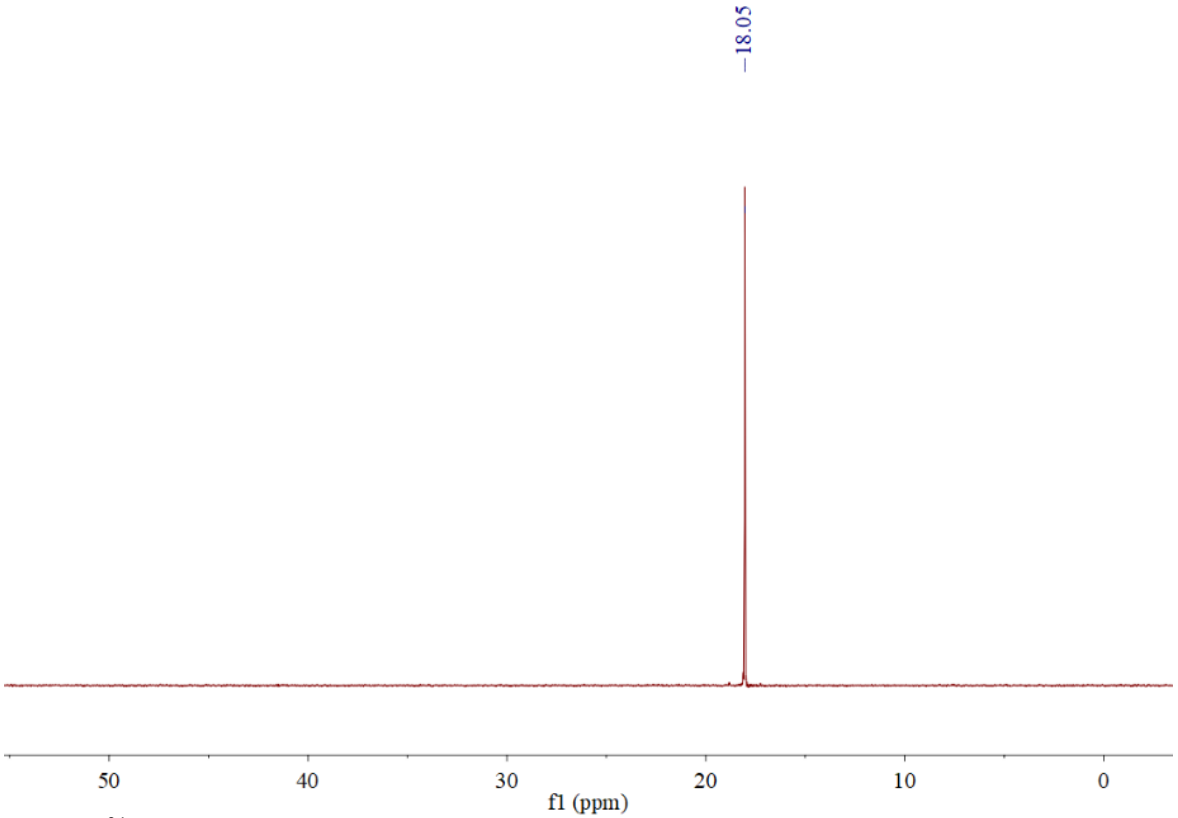

Fig. S3 $^{31}P\{H\}$ NMR spectrum (in $CDCl_3$) of diethyl 4-iodophenylphosphonate.

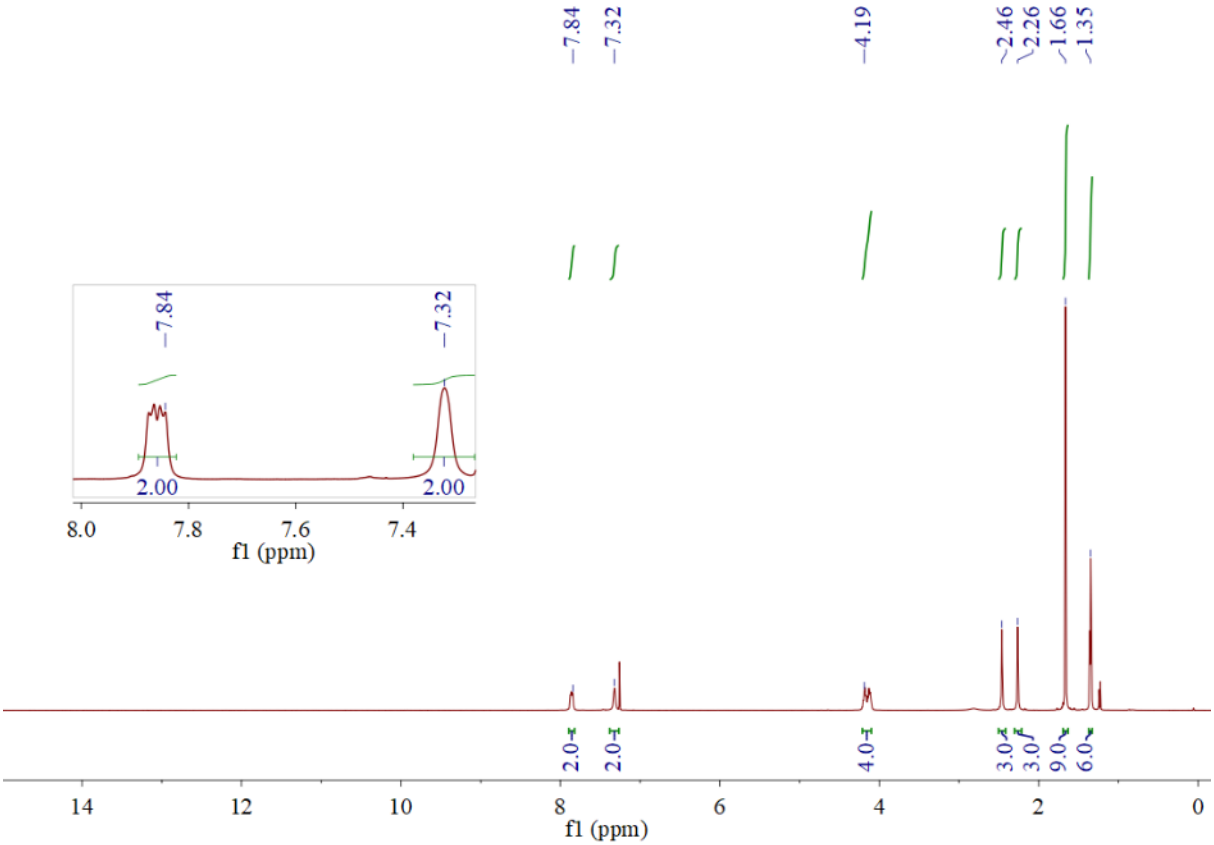

Fig. S4 ^{1}H NMR spectrum (in $CDCl_3$) of 3,5-dimethyl-4-(4-phosphonophenyl)-1-*tert*-butoxycarbonyl-pyrazole.

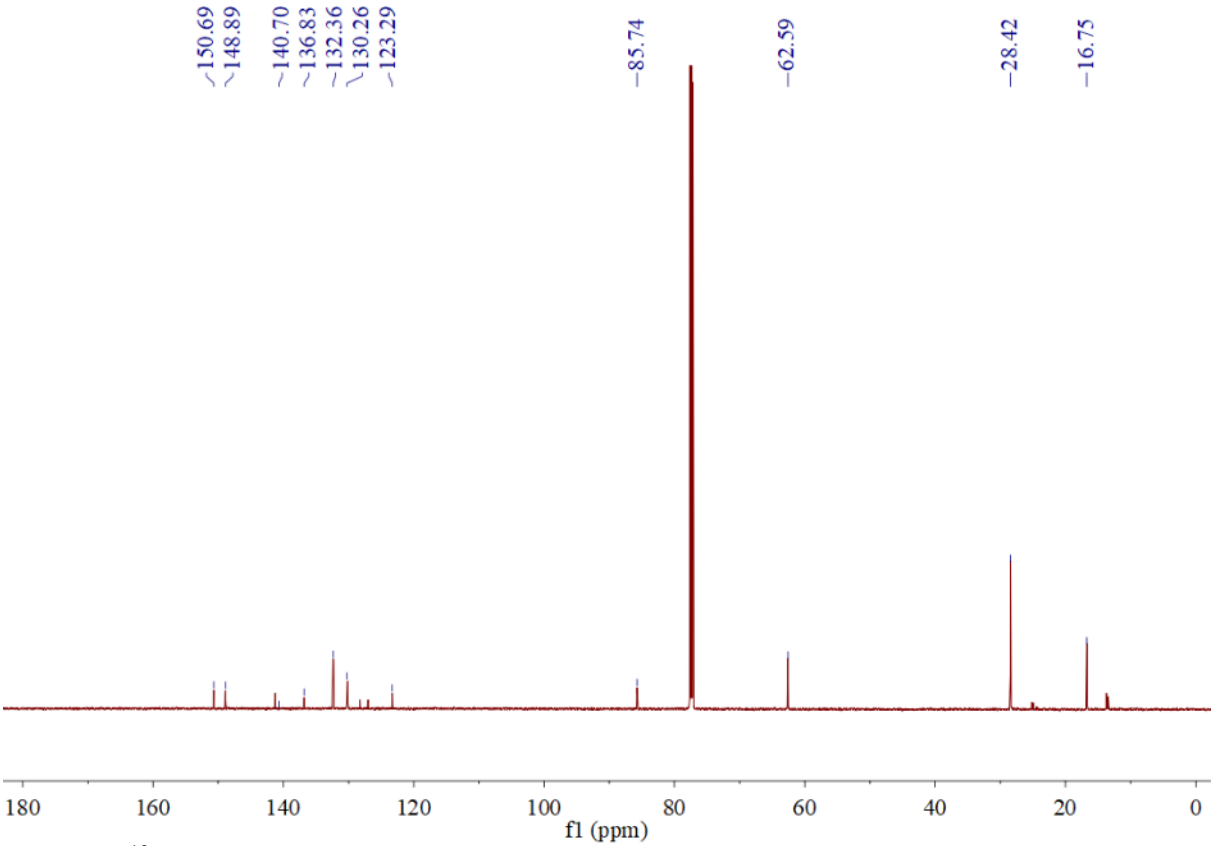

Fig. S5 ^{13}C NMR spectrum (in $CDCl_3$) of 3,5-dimethyl-4-(4-phosphonophenyl)-1-*tert*-butoxycarbonyl-pyrazole.

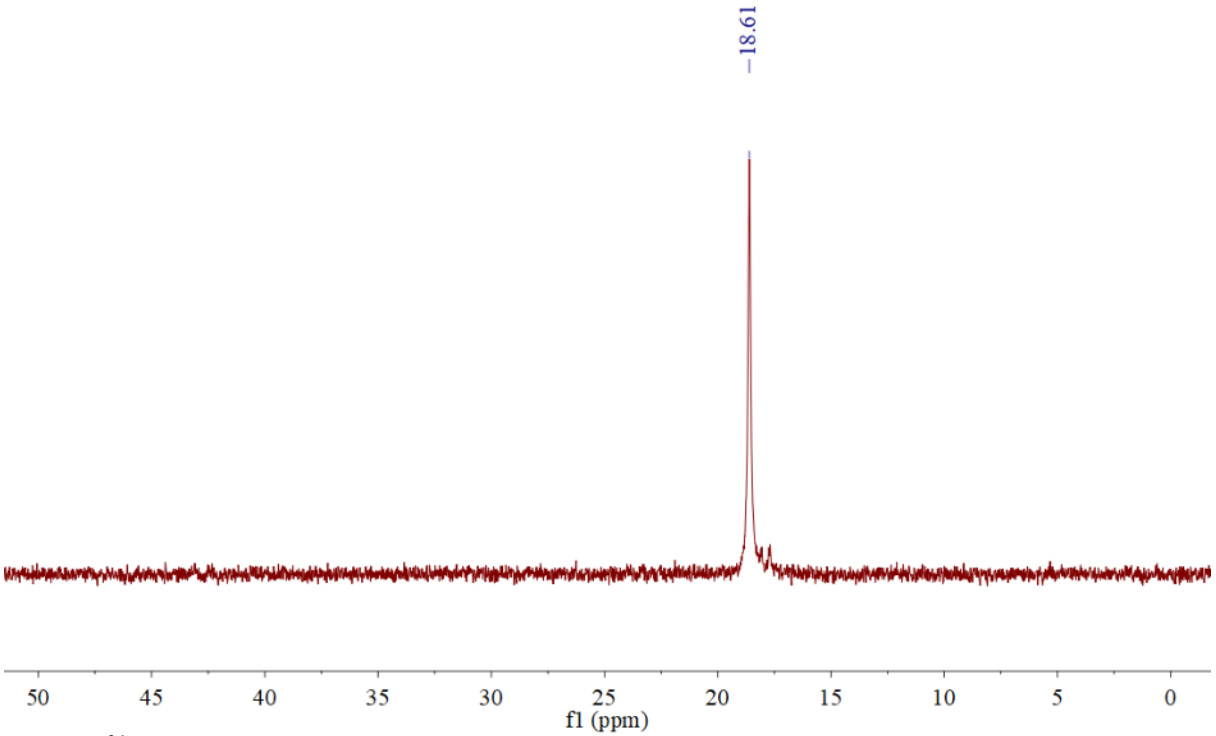

Fig. S6 $^{31}P\{H\}$ NMR spectrum (in $CDCl_3$) of 3,5-dimethyl-4-(4-phosphonophenyl)-1-*tert*-butoxycarbonyl-pyrazole.

Fig. S7 Micrograph of the crystals of **1**·HCl.

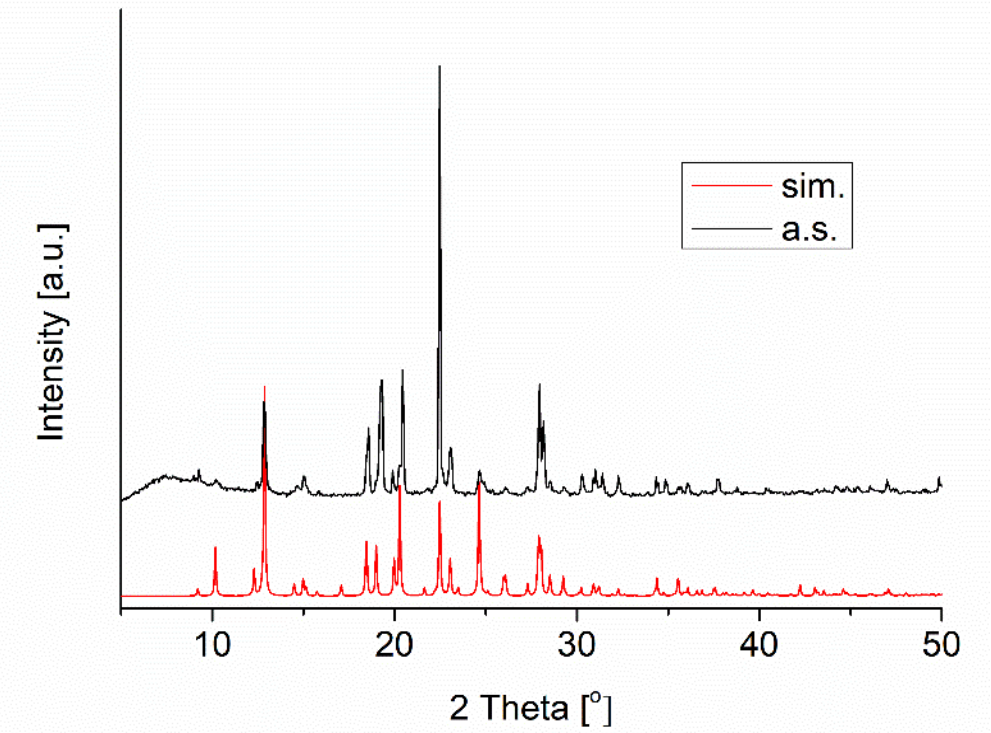

Fig. S8 Comparison of the experimental PXRD pattern of as-synthesized **1**·HCl with the simulated pattern calculated from SCXRD data.

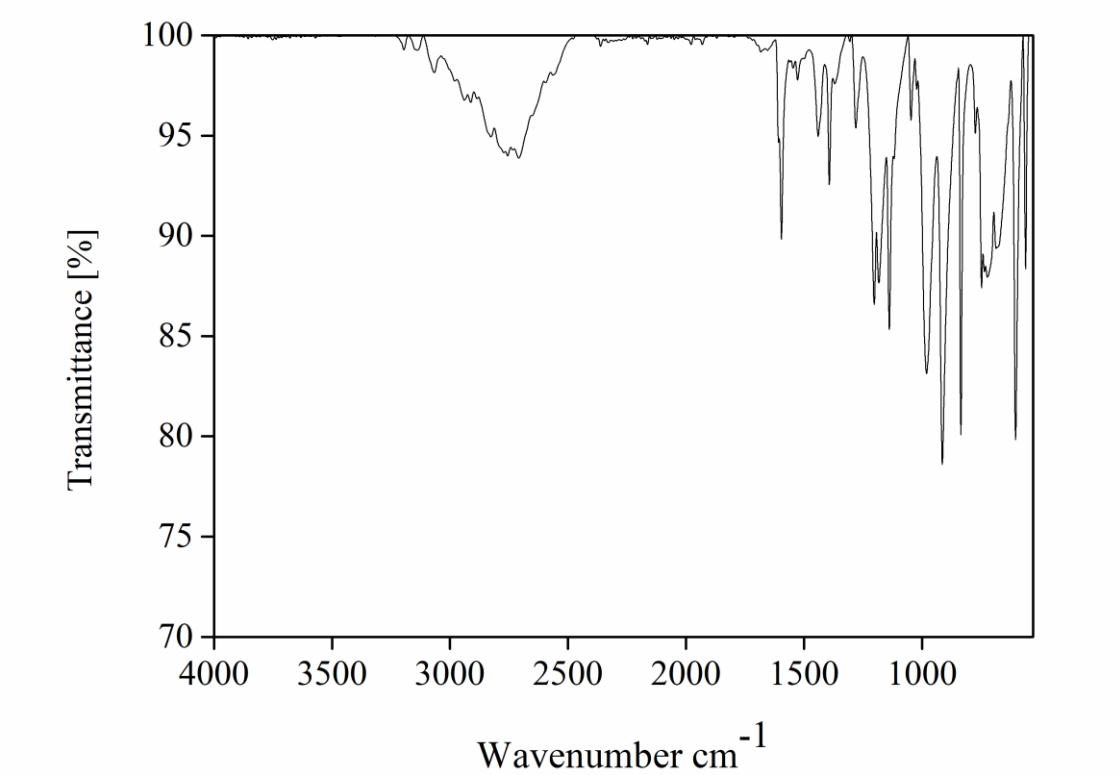

Fig. S9 FT-IR spectrum (ATR) of **1**·HCl.

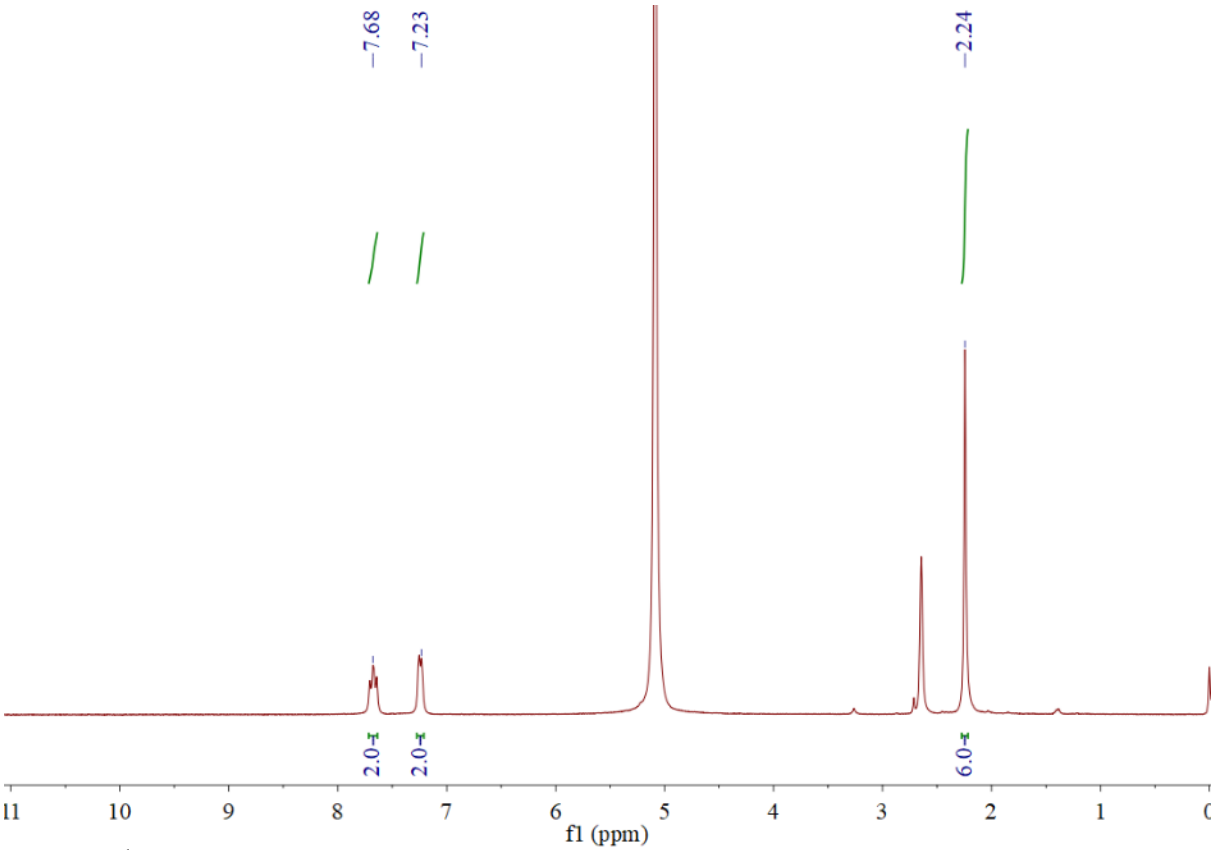

Fig. S10 ^{1}H NMR spectrum (in NaOD, DMSO-d_6) of **1**·HCl.

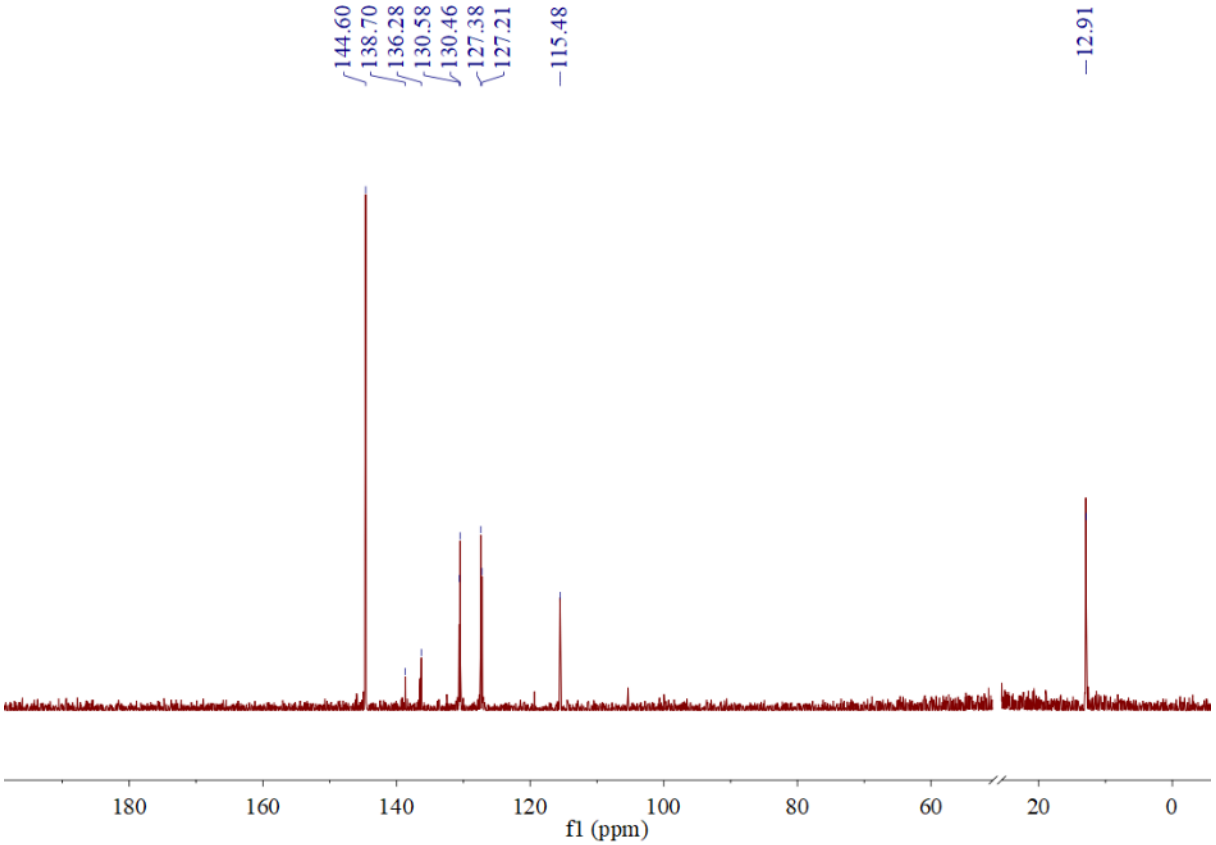

Fig. S11 ^{13}C NMR spectrum (in NaOD, DMSO-d_6) of **1**·HCl.

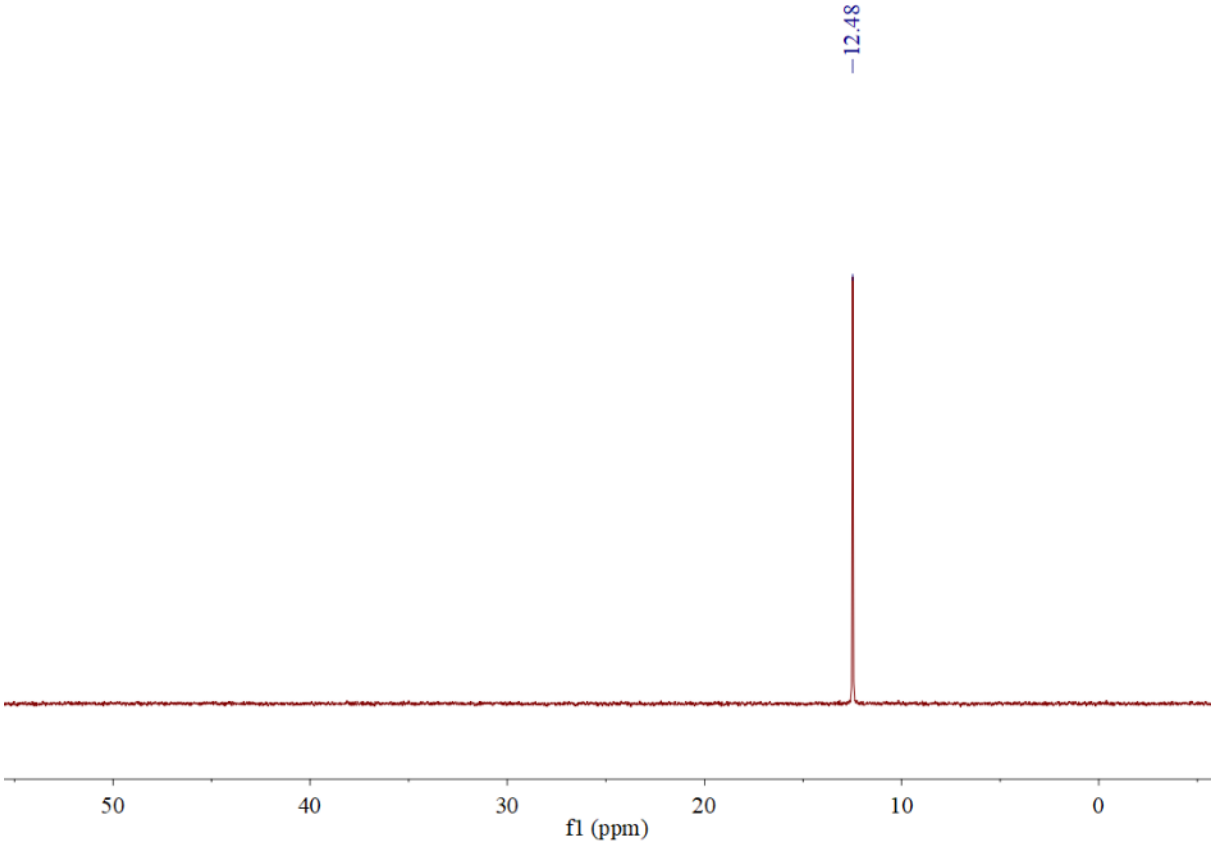

Fig. S12 $^{31}P\{H\}$ NMR spectrum (in NaOD, DMSO-d_6) of **1**·HCl.

Synthesis of 4-(4-phosphonophenyl)-1*H*-pyrazole, 2·HCl·H$_2$O:

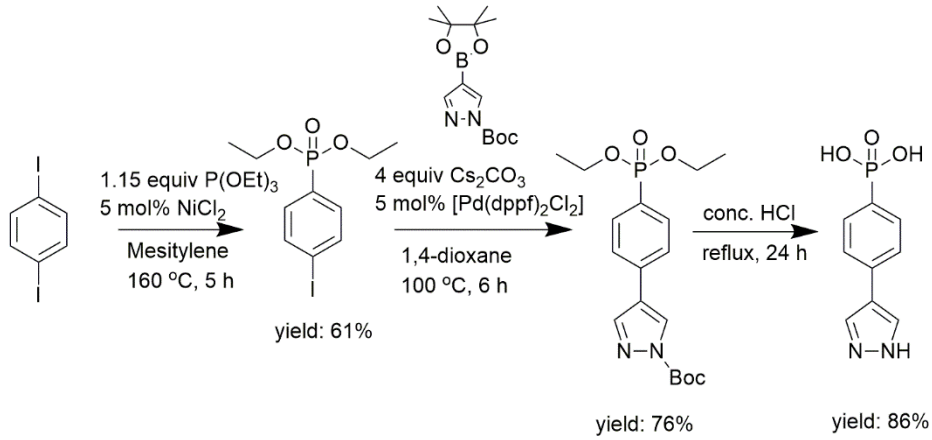

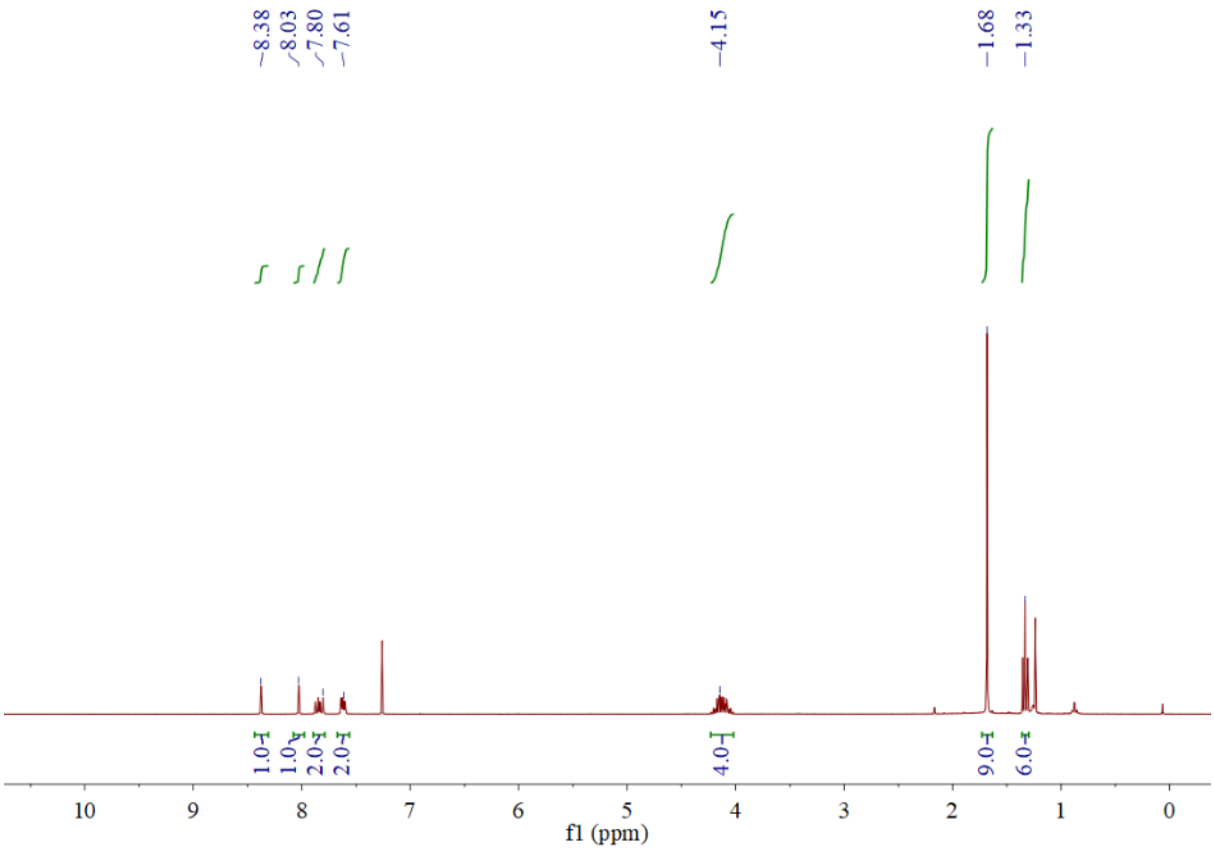

Fig. S13 ^{1}H NMR spectrum (in $CDCl_3$) of 4-(4-phosphonophenyl)-1-*tert*-butoxycarbonyl-pyrazole.

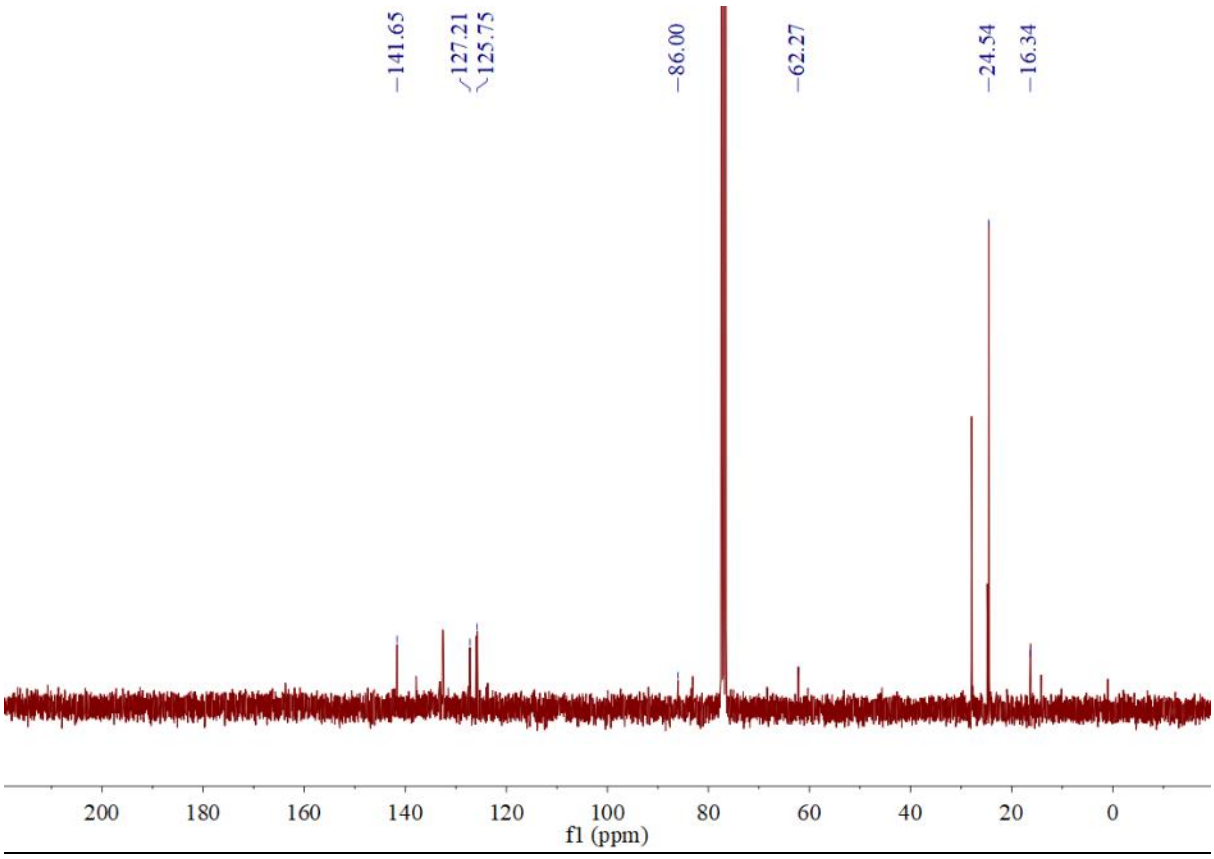

Fig. S14 ^{13}C NMR spectrum (in $CDCl_3$) of 4-(4-phosphonophenyl)-1-*tert*-butoxycarbonyl-pyrazole.

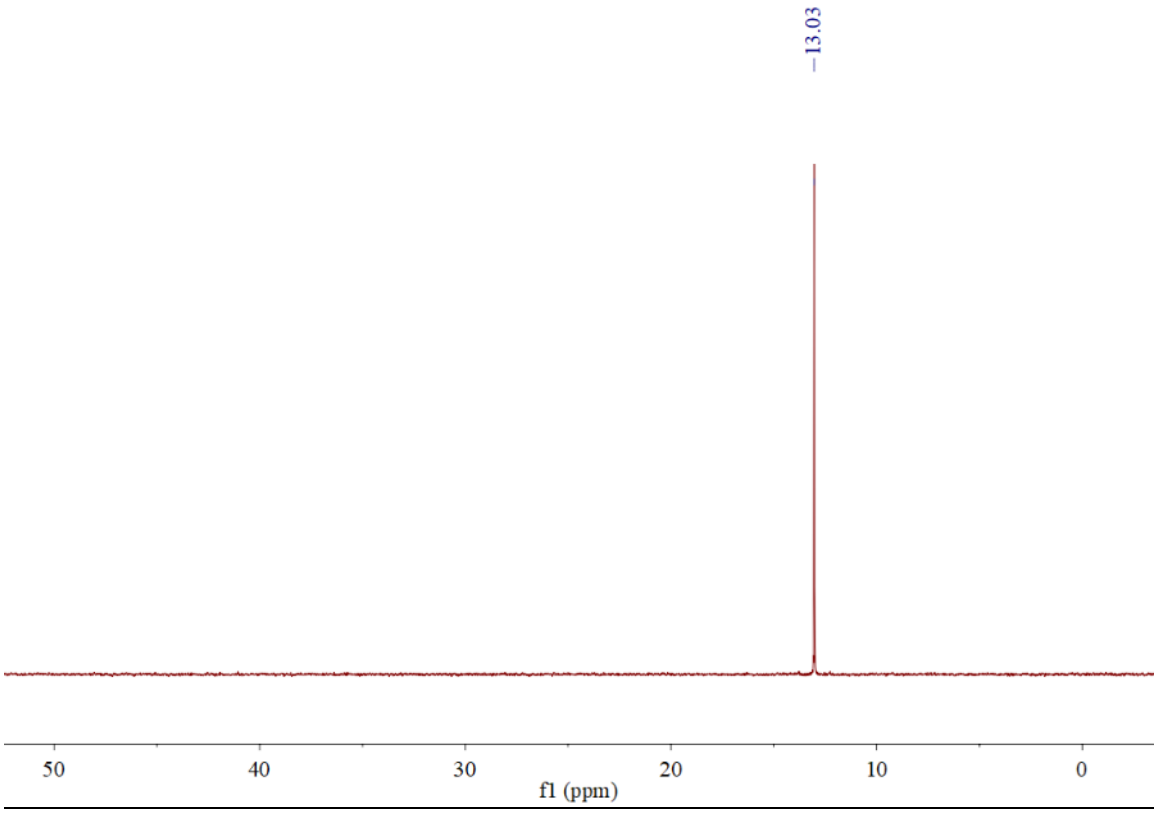

Fig. S15 $^{31}P\{H\}$ NMR spectrum (in $CDCl_3$) of 4-(4-phosphonophenyl)-1-*tert*-butoxycarbonyl-pyrazole.

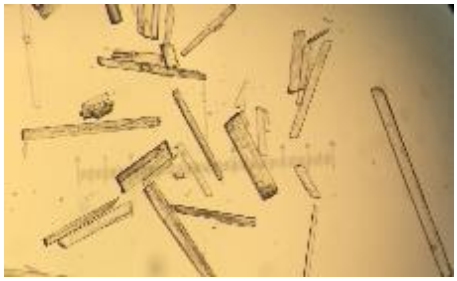

Fig. S16 Micrograph of the crystals of **2**·HCl·H_2O.

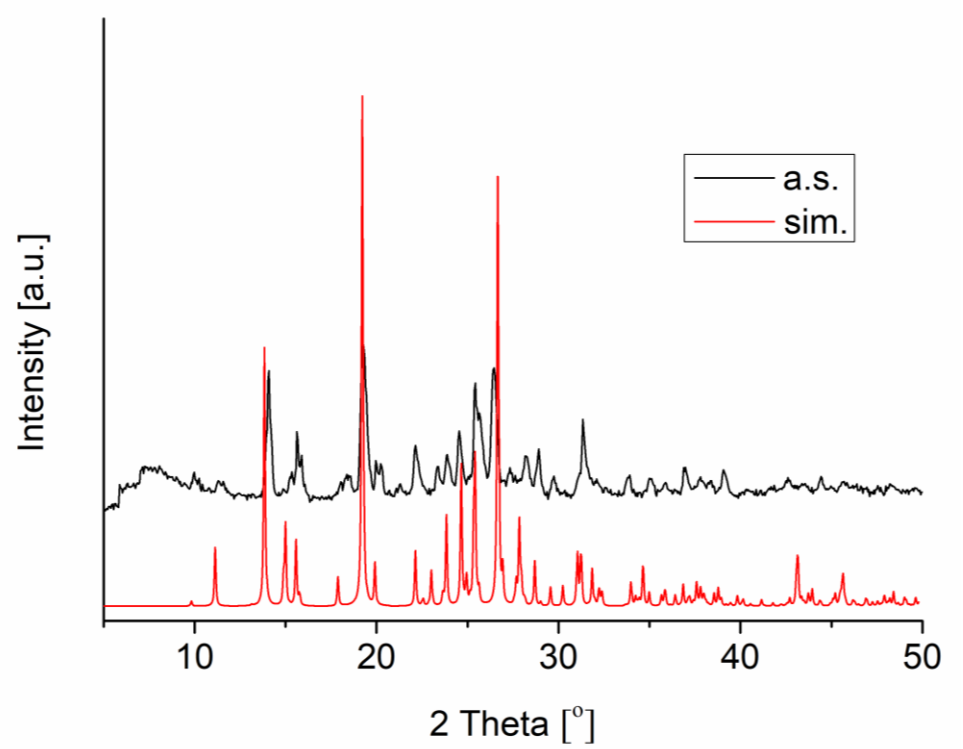

Fig. S17 Comparison of the experimental PXRD pattern of as-synthesized **2**·HCl·H_2O with the simulated pattern calculated from SCXRD data. The broadening and offset of the reflections in the experimental PXRD is probably due to a slight loss in crystal water during the sample handling (drying) and measurement. The loss in crystal water could not be avoided and will induce structural changes and amorphization.

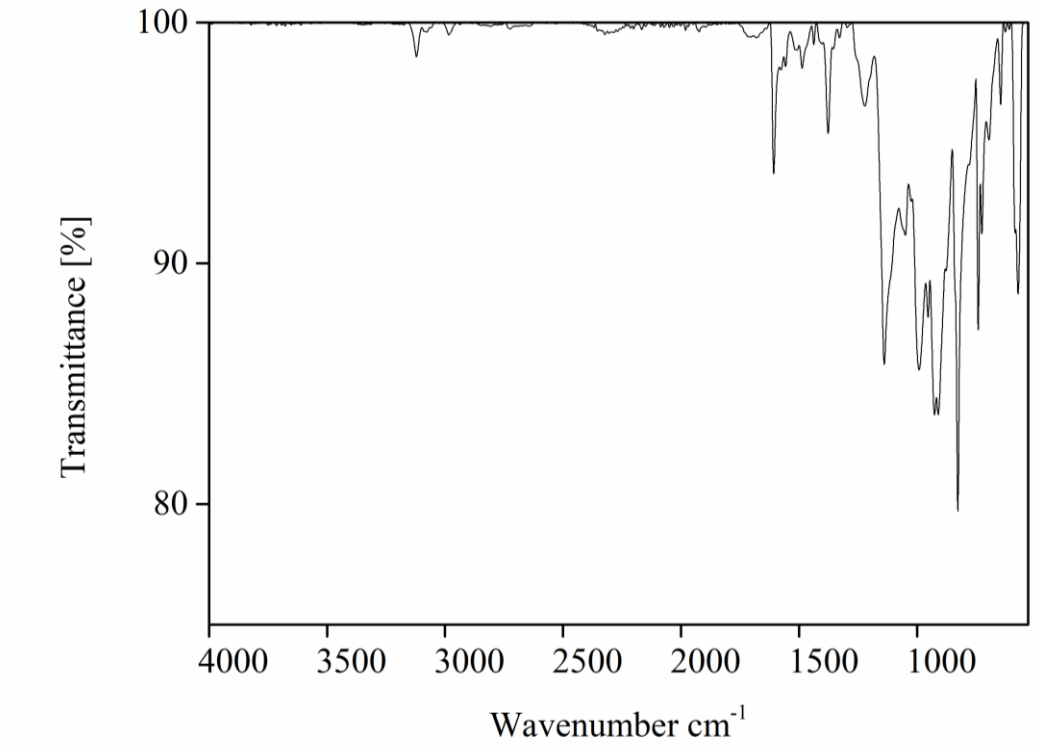

Fig. S18 FT-IR spectrum (ATR) of **2**·HCl·H_2O.

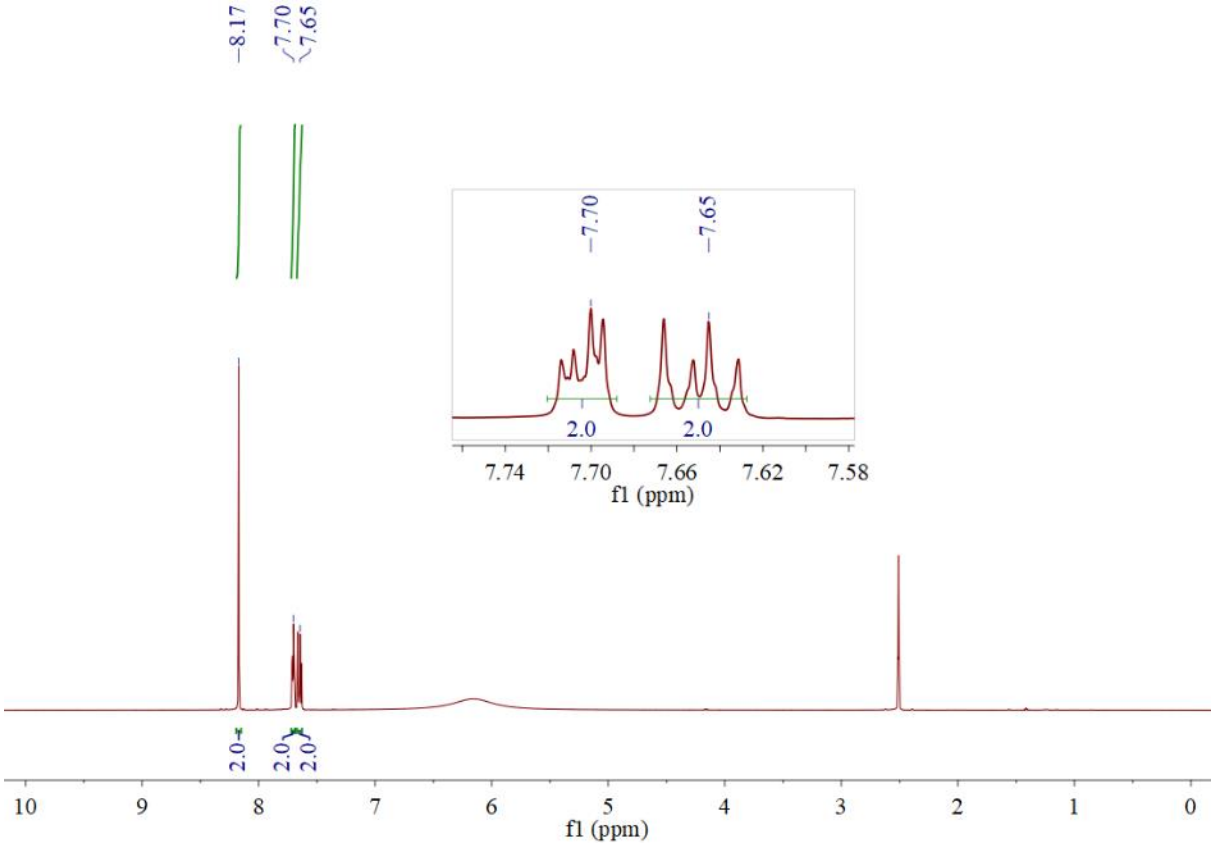

Fig. S19 ^{1}H NMR spectrum (in NaOD, DMSO-d_6) of **2**·HCl·H_2O.

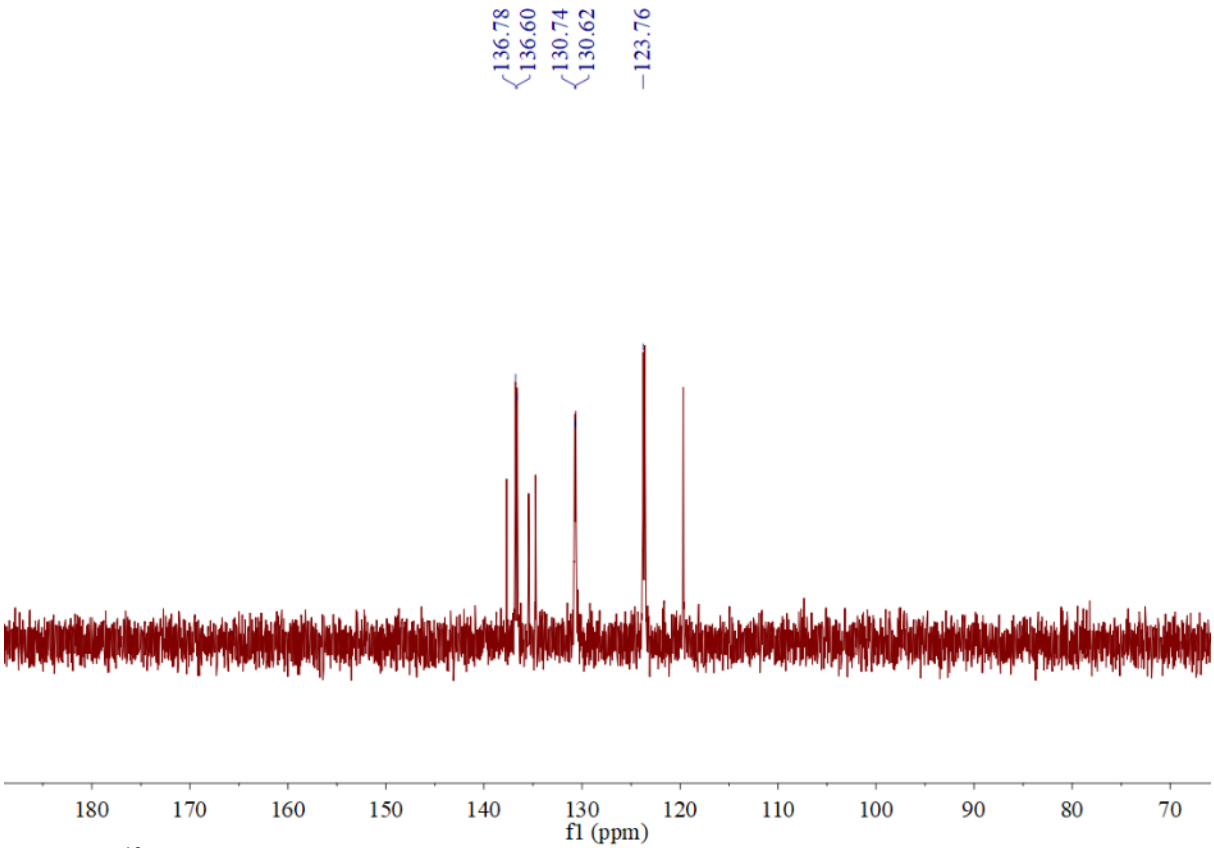

Fig. S20 ^{13}C NMR spectrum (in NaOD, DMSO-d_6) of **2**·HCl·H_2O.

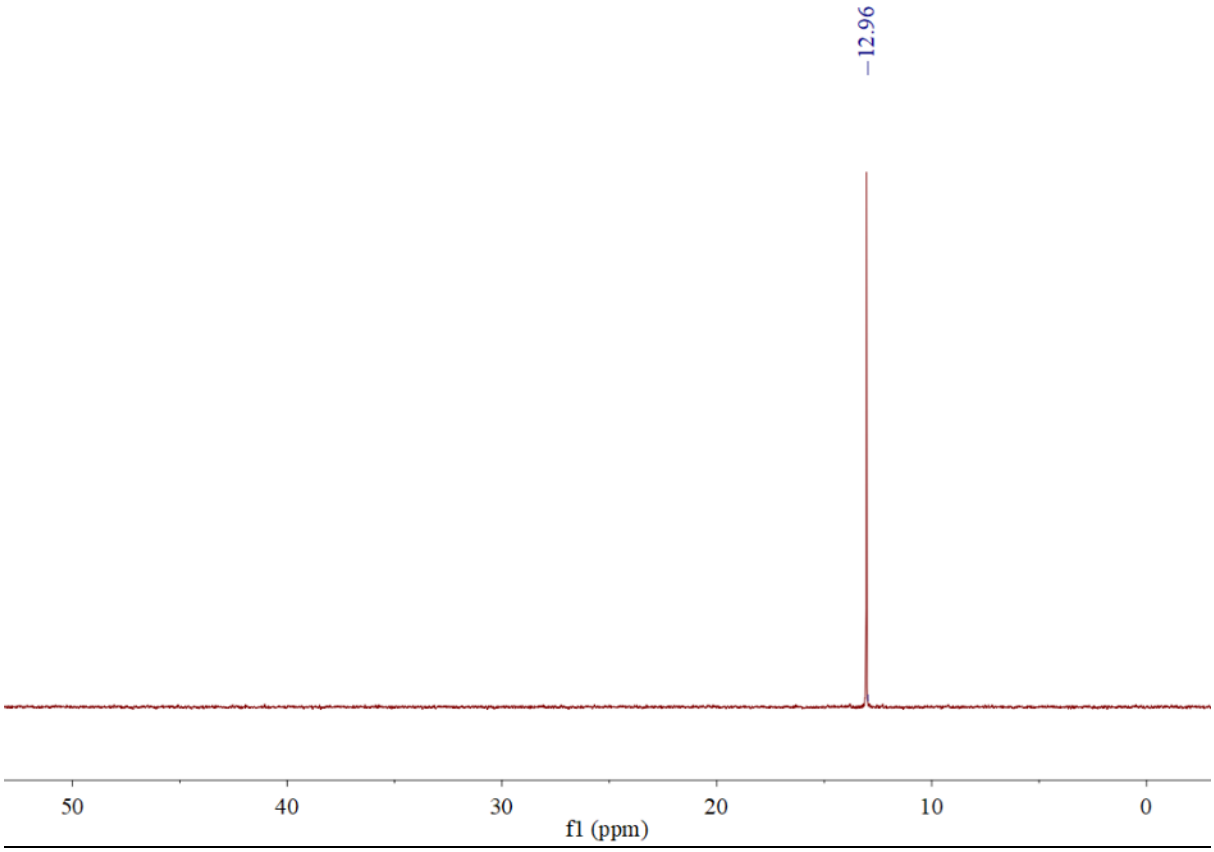

Fig. S21 $^{31}P\{H\}$ NMR (spectrum (in NaOD, DMSO-d_6) of **2**·HCl·H_2O.

4. Zusammenfassung und Ausblick

Die vorliegende Arbeit befasst sich mit drei Forschungsschwerpunkten. In erster Linie wurden die Forschungsergebnisse zu neuem molekularen Zirkonium-Carboxylat-Cluster vorgestellt, die im Zusammenhang mit Koordinationspolymeren von besonderem Interesse sind. Hierbei wurde der Zr_{26}-Oxo-Carboxylat-Cluster synthetisiert, der den größten Zr-Cluster aufweist, der in der bisherigen Literatur bekannt ist. Die mittels Röntgeneinkristalldiffraktometrie aufgeklärte Struktur entspricht der idealisierten Zusammensetzung $[Zr_{26}O_{18}(OH)_{30}(HCOO)_{38}]\cdot 5(HCOOH)\cdot kH_2O$, ($k$ = 2–10). Davor wurde 2017 {Zr_{18}},[77] $[Zr_{18}O_{21}(OH)_2(RCOO)_{28}]$ als größter Zr-oxocluster berichtet. Das Feld der M(IV)-Oxocluster ist benachbart zu dem Gebiet der klassischen Polyoxometallate, kurz POMs, mit der generellen Formel $[X_xM_aO_b]^-$.[75] Hierbei sind die Atome M frühe Übergangsmetalle, wie Vanadium, Niob, Tantal, Molybdän oder Wolfram in ihren hohen bzw. höchsten Oxidationsstufen ($M^{IV, V, VI}$), damit die hohe negative Ladung der Oxo-Anionen im Cluster kompensiert werden kann. Als weitere wichtige Beispiele im Bereich von MOF-SBUs können $M_3OX(RCOO)_6$ (M (III) = Fe, Cr, V, Al, In; X = OH, F) und $Zn_4O(RCOO)_6$ genannt werden, die sich ebenfalls in der Nachbarschaft der M(IV)-Oxocluster befinden.[12] Zr-Oxocluster lassen sich in die folgende Haupttypen unterteilen: der dreieckige {Zr_3} ~ ({Zr_6})$_{1/2}$-,[78] der parallelogrammförmige {Zr_4}-,[79] der unvollständige oktaedrische {Zr_5} ~ {$Zr_{(6-1)}$}-,[77] der archetypische oktaedrische {Zr_6}-,[81] der kubische {Zr_8}-,[82] der {Zr_9} ~ {$Zr_{(6-1+4)}$}-,[83] der {Zr_{10}} ~ {$Zr_{(6+4)}$}-,[77] der pseudo-{Zr_{12}} ~ {Zr_6}$(COO)_4${Zr_6}-, der instabile kubische {Zr_{13}}-[84] sowie der größte {Zr_{18}}-[77]Cluster. Für die Beschreibung all dieser Cluster ist der oktaedrische {Zr_6}-Cluster mit dem invariablen {Zr_6 (μ_3-O/OH)$_8$}-Kern von besonderer Bedeutung. Aus diesem Grund wurden auch große Aggregate mit Hilfe der archetypischen Zr_6-Cluster als Standardbaustein beschrieben, deren Ecken, Kanten oder Flächen geteilt sind. In Folgearbeiten könnte der neue {Zr_{26}}-Cluster als sekundäre Baueinheit zur Synthese von porösen Koordinationspolymeren eingesetzt werden. Dies könnte durch etablierte Methoden zum Ligandenaustausch unter milden Bedingungen eingeführt werden. Die Tatsache, dass solche Strukturen noch nicht beschrieben wurden, könnte durch ihre geringe Löslichkeit und damit Unzugänglichkeit von Einkristallen erklärt werden. Durch Einsatz des supramolekularen Clusters in organisch-anorganischen Hybridmaterialien könnte eine permanente Porosität sowohl bei frisch-synthetisierten als auch bei thermisch behandelten Proben erzeugt werden.
Im zweiten Teil der Arbeit wurde ausgehend von ((Adamantan-1,3,5,7-tetrayl)tetra(phen-4-yl))tetracarbonsäure (H_4L^4, Abbildung 9) über die klassische MOF-Synthese in DMF ein neues MOF **ZRTE-10** hergestellt. Als Modulatoren wurden Ameisensäure und Essigsäure eingesetzt. Das MOF mit der Zusammensetzung $[Zr_6(\mu_3\text{-}O)_4(\mu_3\text{-}OH)_4(L^4)(HL^4)_2(OH)_2(H_2O)_2]$ besitzt eine niedrige Symmetrie (C_2/c) und basiert auf einem seltenen zehnfach-verknüpften Metallknoten. Zwei Drittel der Liganden tragen hierbei eine nicht-deprotonierte Carboxylgruppe. Das Gerüst

weist ein komplexes trinodales $\{4^{14}.6^{24}.8^{7}\}\{4^{3}\}_2\{4^{5}.6\}$-Netz auf. Die überkritische Trocknung mit CO_2 und milde Entgasung bei 120 °C ergab ein poröses Material mit einer BET-Oberfläche von 1190 m^2g^{-1}. Beim Erhitzen auf ~ 200 °C wandelte sich **ZRTE-10** in ein anderes kristallines Gerüst **ZRTE-11** um. Es wurde festgestellt, dass die Topologie von **ZRTE-11** mit der erwarteten Fluorit-Topologie übereinstimmt, die zuvor für andere literaturbekannten MOFs, basiert auf tetraedrischen Liganden beobachtet wurde. **ZRTE-11** mit einer hohen Symmetrie (*I*4/m) basiert auf acht Metallknoten und hat die Formel $[Zr_6(\mu_3\text{-}O)_4(\mu_3\text{-}OH)_4(OH)_4(L^4)_2]$. Die thermisch induzierte Umwandlung von **ZRTE-10** verläuft durch Entfernung eines Liganden pro Zr_6-Knoten in den Poren des Gerüsts, was zu einer relativ niedrigen BET-Oberfläche von 585 m^2g^{-1} für das aktivierte **ZRTE-11** führt. Ein *mixed*-Ligand-Ansatz für **ZRTE-10,11** wurde folglich unter Verwendung von ((Adamantan-1,3,5-triyl)tri(phen-4-yl))tricarbonsäure (H_3L^3, Abbildung 9) versucht, welches ein gestutztes Analogon (*trancated analogou*) zum H_4L^4 ist. Hierbei wurde eine monokristalline Probe von **ZRTE-10** mit einer geringen Ausbeute erhalten. Der Einsatz von HCl als Modulator ermöglicht ferner eine höhere Ausbeute (~80%). Allerdings führt es zu einem nahezu proportionalen Einsatz der Liganden. Röntgenpulverdiffraktogramme der erhaltenen Materialien zeigen die Bildung semiamorpher Materialien. Die thermische Behandlung dieser Materialien erhöht ihre Kristallinität. Jedoch liegen die BET-Oberflächen im Bereich von 400 bis 550 m^2g^{-1} für die Ansätze nur mit H_4L^4 oder H_3L^3. Interessant für weitere Arbeiten wäre, andere *Mixed-Linker*-Ansätze mit verschiedenen Verhältnissen von H_4L^4 und H_3L^3 einzusetzen. Zudem kann auch ein anderer gestutzter Lingand mit zwei fehlenden Carboxylgruppen bzw. ((Adamantan-1,3-diyl)-diphen-4-yl)dicarbonsäure (H_2L^2, Abbildung 9) für das Einfügen der gezielten Defekte verwendet werden. Dabei könnten eine höhere innere Oberfläche sowie eine katalytische Aktivität generiert werden.

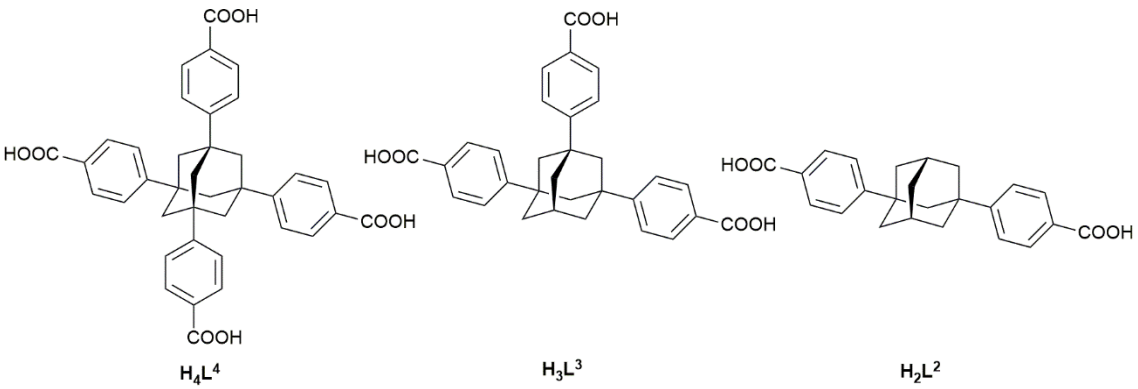

Abbildung 9 Die verwendeten Liganden für die Synthese von MOFs.

Der letzte Schwerpunkt befasst sich mit der Synthese von zwei neuen bifunktionellen Pyrazolat-Phosphonat-Liganden zur potenziellen Synthese von gemischt-Metall MOFs (*mixed-Metal* MOFs). Hierbei wurden 3,5-Dimethyl-4-(4-phosphonophenyl)-1*H*-pyrazol und

4-(4-Phosphonophenyl)-1*H*-pyrazol mittels einer Suzuki-Miyaura Kreuzkupplung, ausgehend von einem Boc-geschützten Pyrazolyl-boronsäureester und Iodo-arylphosphonat synthetisiert, deren Strukturen mittels Röntgeneinkristalldiffraktometrie aufgeklärt wurden. Beide Verbindungen kristallisieren jeweils mit HCl-Molekül in Salzform. Durch H-Brückenbindungen werden im Kristall supramolekulare Netzwerke ausgebildet. Es gibt in der Literatur nur wenige Berichte über Phosphonat-Liganden basierte MOFs mit einer Porosität. Dies könnte durch die Neigung der Phosphonat-Verbindungen zur Bildung von Schichtstrukturen erklärt werden. Zudem sollte Polymorphie dieser Verbindungen, die für Komplexe mit mehrzähnigen Liganden bekannt ist, genannt werden. Außerdem liegen die rasch gebildeten Verbindungen in unlöslicher Form vor, wobei sich keine reversible Reaktion durchführen lässt. Aufgrund dieser Schwierigkeiten war im Rahmen dieser Arbeit nicht möglich, Einkristalle der Metall-Ligand-Verbindungen in einer Güte zu erhalten, welche mittels Einkristalldiffraktometrie untersucht werden konnte. In Folgearbeiten sollten weitere Ansätze in unterschiedlichen Verhältnissen von Liganden zu Metallsalzen in diversen Lösungsmitteln gemacht werden, um Kristalle besserer Qualität zu synthetisieren. Außerdem könnten durch den Einsatz des bifunktionellen Pyrazolat-Phosphonat-Liganden bimetallische Komplexe synthetisiert werden, da nach dem HSAB-Konzept die Pyrazolat-Gruppe eine Affinität zu weicheren Metallionen (wie z.B. Cu^{2+}, Zn^{2+}) und die Phosphonat-Gruppe eine Affinität zu harten Metallionen (wie z.B. Fe^{3+}, Zr^{4+}) aufweist.

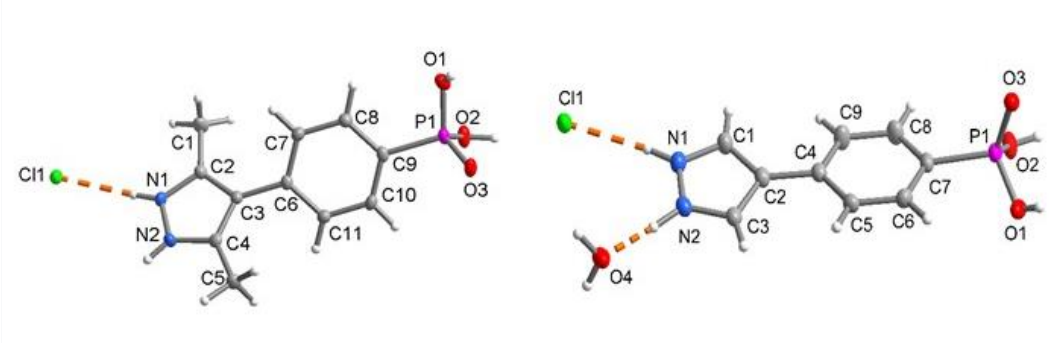

Abbildung 10 Asymmetrische Einheit von 3,5-Dimethyl-4-(4-phosphonophenyl)-1*H*-pyrazol (links), 4-(4-Phosphonophenyl)-1*H*-pyrazol (rechts); (50% thermische Ellipsoide).

5. Literaturverzeichnis

[1] M. E. Davis, Selective binding and removal of guests in a microporous metal–organic framework. *Nature,* **2002**, *417*, 813–821.

[2] S. Kitagawa, R. Kitaura, S. –I. Noro, Functional porous coordination polymers, *Angew. Chem. Int. Ed.*, **2004**, *43*, 2334–2375; S. Kitagawa, R. Kitaura, S. Noro, Funktionale poröse Koordinationspolymere. *Angew. Chem.*, **2004**, *116*, 2388–2430.

[3] F. Schüth, Poröse Materialien im Überblick. *Chem. Ing. Tech.*, **2010**, *82*, 769–777.

[4] K. S. W. Sing, Reporting physisorption data for gas/solid systems with special reference to the determination of surface area and porosity. *Pure Appl. Chem.*, **1985**, *57*, 603–609.

[5] C. Janiak, J. K. Vieth, MOFs, MILs and more: concepts, properties and applications for porous coordination networks (PCNs). *New. J. Chem.*, **2010**, *34*, 2366–2388.

[6] O. M. Yaghi, H. Li, Hydrothermal Synthesis of a Metal-Organic Framework Containing Large Rectangular Channels. *J. Am. Chem. Soc.*, **1995**, *117*, 10401–10402.

[7] S. S. Chui, S. M.-F. Lo, J. P. H. Charmant, A. G. Orpen, I. D. Williams, A chemically functionalizable nanoporous materials, *Science*, **1999**, *283*, 1148–1150.

[8] O. M. Yaghi, H. Li, M. Eddaoudi, M. O'Keeffe, Design and synthesis of an exceptionally stable and highly porous metal-organic framework. *Nature*, **1999**, *402*, 276–279.

[9] H. Furukawa, K. E. Cordova, M. O'Keeffe, O. M. Yaghi, The chemistry and applications of metal-organic frameworks. *Science*, **2013**, *341*, 6149, 1230444.

[10] P. Ramaswamy, N. E. Wong, G. K. H. Shimizu, G. K. H. Shimizu, MOFs as proton conductors-challenges and opportunities. *Chem. Soc. Rev.*, **2014**, *43*, 16, 5913–5932.

[11] X. Wang, N. Ye, Recent advances inmetal-organic frameworks and covalent organic frameworks for sample preparation and chromatographic analysis. *Electrophoresis*, **2017**, *38*, 24, 3053–3180.

[12] D. J. Tranchemontagne, J. L. mendoza-Cortes, M. O' Keeffe, Secondary building units, nets and bonding in the chemistry of metal–organic frameworks. *Chem. Soc. Rev.*, **2009**, *38*, 1257-1283.

[13] J. Bedia, V. Muelas-Ramos, M. Penas-Garzon, A. Gomez-Aviles, J. J. Rodriguez, C. Belver, A Review on the Synthesis and Characterization of Metal Organic Frameworks for Photocatalytic Water Purification. *Catalysts*, **2019**, *9*, 52.

[14] H. K. Chae, D. Y. Siberio-Perez, J. Kim, Y. Go, M. Eddaoudi, A. J. Matzger, M. O'Keeffe, O. M. Yaghi, A route to high surface area, porosity and inclusion of large molecules in crystals. *Nature*, **2004**, *427*, 523–527.

[15] T. G. Glover, G. W. Peterson, B. J. Schindler, D. Britt, O. Yaghi, MOF-74 building unit has a direct impactt on toxic gas adsoption. *Chemical engineering Science*, **2011**, *66*, 163–170.

[16] D. –A. Yang, H. –Y. Cho, J. Kim, S. –T. Yang, W. –S. Ahn, CO_2 capture and conversion using Mg-MOF-74 prepared by a sonochemical method. *Energy Environ. Sci.*, **2012**, *5*, 6465–6473.

[17] N. Reimer, B. Gil, B. Marszalek, N. Stock, Thermal post-synthetic modification of Al-MIL-53-COOH: Systematic investigation of the decarboxylation and condensation reaction. *CrystChemComm*, **2012**, *14*, 4119–4125.

[18] T. Wittmann, R. Siegel, N. Reimer, W. Milius, N. Stock, J. Senker, Enhancing the Water Stability of Al-MIL-101-NH_2 via Postsynthetic Modification. *J. Chem. Eur. J.*, **2015**, *21*, 314-323.

[19] A. Schneemann, V. Bon, I. Schwendler, I. Senkovska, S. Kaskel, R. A. Fischer, Flexible metal–organic frameworks. *Chem. Soc. Rev.*, **2014**, *43*, 6062–6069.

[20] S. Bourrelly, P. L. Llewellyn, C. Serre, F. Millange, T. Loiseau, G. Ferey, Different Adsorption Behaviors of Methane and Carbon Dioxide in the Isotypic Nanoporous Metal Terephthalates MIL-53 and MIL-47. *J. Am. Chem. Soc.*, **2005**, *127*, 13519–13521.

[21] D. Tanaka, K. Nakagawa, M. Higuchi, S. Horike, Y. Kubota, T. C. Kobayashi, M. Takasi, S. Kitagawa, Kinetic Gate-Opening Process in a Flexible Porous Coordination Polymer. *Angew. Chem. Int. Ed.* **2008**, *47*, 3914–3918.

[22] M. Alhamami, H. Doanm, C. H. Cheng, A Review on Breathing Behaviors of Metal-Organic-Frameworks (MOFs) for Gas Adsorption. *Materials*, **2014**, *7*, 3198–3250.

[23] J. Zhang, M. M. Matsushita, X. X. Kong, J. Abe, T. Iyoda, Photoresponsive Coordination Assembly with a Versatile Logs-Stacking Channel Structure Based on Redox-Active Ligand and Cupric Ion. *J. Am. Chem.* Soc. 2001, 123, 12 105–12 106.

[24] M. M. Matsushita, M. Morikawa, T. Kawai, T. Iyoda, Metal coordination complexes composed of photo-electrochemically active ligands. Mol. Cryst. Liq. Cryst. 2000, 343, 87-96.

[25] G. J. E. Davidson, S.J. Loeb, Channels and cavities lined with interlocked components: Metal-based polyrotaxanes that utilize pyridinium axles and crown ether wheels as ligands. *Angew. Chem. Int. Ed.*, **2003**, *42*, 74–77.

[26] M. –L. Tong, X. –M. Chen, X. L-. Yu, T. C. W. Mak, A novel two-dimensional rectangular network. Synthesis and structure of {[Cu(4,4'-bpy)(pyz)(H_2O)$_2$][PF_6]$_2$}$_n$. *J. Chem. Soc, Dalton Trans.*, **1998**, 5–6.

[27] S. Decurtins, H. W. Schmalle, P. Schneuwly, L.-M. Zheng, J. Ensling, A. Hauser, Synthesis, Crystal Structure, and Optical and Magnetic Properties of a Novel Two-Dimensional Copper(II) Network Formed Conjointly with μ-Bipyrimidine, μ-Oxalato, and μ-Chloro Ligands. *Inorg. Chem*. **1995**, *34*, 5501–5506.

[28] S. Kawata, S. Kitagawa, M. Enomoto, H. Kumagai, M. Katada, Mixed ligand copper(II) coordination polymers constructed by Cu-bpm-Cu dimer unit (bpm = 2,2′-bipyrimidine) as a building block. Crystal structures and magnetic properties of [Cu(bpm)(SO_4)] (H_2O)$_n$,

$[Cu_2(bpm)(suc)_{0.5}(ClO_4)_2(OH)(H_2O)_2]_n$ and $[Cu(bpm)_{1.5}(suc)_{0.5}](ClO_4)(H_2O)_{2n}$ (suc = succinate). *Inorg. Chim.* Acta **1998**, *283*, 80–90.

[29] O. M. Yaghi, M. O'Keeffe, N. W. Ockwig, H. K. Chae, M. Eddaoudi, J. Kim, Reticular synthesis and the design of new materials. Nature, **2003**, *423*, 705.

[30] M. O'Keeffe, M. Eddaoudi, H. Li, T. Reineke, O. M. Yaghi, Frameworks for extended solids: Geometrical design principles. J. Solid State Chem. **2000**, *152*, 3.

[31] L. Pauling, The principles determining the structure of complex ionic crystals. J. Am. Chem. Soc. **1929**, *51*, 4, 1010–1026.

[32] S. Kaskel, Poren per Baukasten. *Nachr. Chem.*, **2005**, *53*, 394–399.

[33] M. Eddaudi, J. Kim, N. Rosi, D. vodak, J. Wachter, M. O'Keeffe, O. M. Yaghi, Systematic Design of Pore Size and Functionality in Isoreticular MOFs and Their Application in Methane Storage. *Science*, **2002**, *295*, 469–472.

[34] A. Nuri, N. Vucetic, J. –H. Smatt, Y. Mansoori, J. –P. Mikkola, D. Y. Murzin, Pd Supported IRMOF-3: Heterogeneous, Efficient and Reusable Catalyst for Heck Reaction. *Cat. Letters*, **2019**, *149*, 1941–1951.

[35] P. Ryan, L. J. Broadbelt, R. Q. Snurr, Is catenation beneficial for hydrogen storage in metal-organic frameworks? *Chem. Commun.*, **2008**, 4132–4134.

[36] Mansoori, J. –P. Mikkola, D. Y. Murzin, Pd Supported IRMOF-3: Heterogeneous, Efficient and Reusable Catalyst for Heck Reaction. *Cat. Letters*, **2019**, *149*, 1941–1951.

[37] S. -H. Cho, B. Ma, S. T. Nguyen, J. T. Hupp, T. E. Albert-Schmitt, A metal–organic framework material that functions as an enantioselective catalyst for olefin epoxidation. *Chem. Commun.*, **2006**, 2563–2565.

[38] M. Banerjee, S. Das, M. Yoon, H. J. Choi, M. H. Hyun, S. M. Park, G. Seo, K. Kim, Postsynthetic modification switches an achiral framework to catalytically active homochiral metal−organic porous materials. *J. Am. Chem. Soc.,* **2009**, *131*, 7524–7525.

[39] E. D. Bloch, D. Britt, C. Lee, C. J. Doonan, F. J. Uribe-Romo, H. Furukawa, J. R. Long, O. M. Yaghi, Metal insertion in a microporous metal-organic framework lined with 2,2'-bipyridine, *J. Am. Chem. Soc.,* **2010**, *132*, 14382–14384.

[40] H. Deng, S. Grunder, K. E. Cordova, C. Valente, H. Furukawa, M. Hmadeh, F. Gandara, A. C. Whalley, Z. Liu, S. Asahina, H. Kazumori, M. O'Keeffe, O. Terasaki, J. F. Stoddart, O. M. Yaghi, Large-pore apertures in a series of metal-organic frameworks. *Science*, **2012**, *336*, 1018–1023.

[41] C. Wang, X. Liu, N. Keser Demir, J. P. Chen, K. Li, Applications of water stable metal-organic frameworks. *Chem. Soc. Rev.* **2016**, *45*, 5107–5134.

[42] T. Devic, C. Serre, High valence 3p and transition metal based MOFs. *Chem. Soc. Rev.*, **2014**, *43*, 6097–6115.

[43] Y. Bai, Y. B. Dou, L. H. Xie, W. Rutlrdge, J. R. Li, H. C. Zhou, Zr-based metal-organic frameworks: Design, synthesis, structure and applications. *Chem. Soc. Rev.*, **2016**, *45*, 2327–2367.

[44] J. H. Cavka, S. Jakobsen, U. Olsbye, N. Guillou, C. Lamberti, S. Bordiga, K. P. Lillerud, A new zirconium inorganic building brick forming metal organic frameworks with exceptional stability. *J. Am. Chem. Soc.*, **2008**, *130*, 13850–13851.

[45] M. Dan-Hardi, C. Serre, T. Frot, L. Rozes, G. Maurin, C. Sanchez, G. Ferey, A new photoactive crystalline highly porous titanium(IV) dicarboxylate. *J. Am. Chem. Soc.*, **2009**, *131*, 10857–10859.

[46] S. Yuan, J., -S, Qin, C. T. Lollar, H., -C. Zhou, Stable metal−organic frameworks with group 4 metals: Current status and trends. *ACS Cent. Sci.*, **2018**, *4*, 440–450.

[47] J. Ma, L. D. Tran, A. J. Matzger, Toward topology prediction in Zr-based microporous coordination polymers: The role of linker geometry and flexibility. *Cryst. Growth Des.*, **2016**, *16*, 4148–4153.

[48] J. B. De Coste, G. W. Peterson, H. Jasuja, T. G. glover, Y. G., Huang, K. S. Walton, Stability and degradation mechanisms of metal–organic frameworks containing the $Zr_6O_4(OH)_4$ secondary building unit. *J. Mater. Chem.*, **2013**, *1*, 5642–5650.

[49] J. E. Mondloch, M. J. Katz, N. Planas, D. Semrouni, L. Gagliardi, J. T. Hupp, O. K. Farha, Are Zr_6-based MOFs water stable? Linker hydrolysis vs. capillary-force-driven channel collapse. *Chem. Commun.*, **2014**, *50*, 8944–8946.

[50] A. Schaate P. Roy, A. Godt, J. Lippke, F. Waltz, M. Wiebcke, P. Behrens, Modulated synthesis of Zr-based Metal-organic frameworks: From nano to single crystals. *Chem. Eur. J.*, **2011**, *17*, 6643–6651.

[51] H. Reinsch, B. Bueken, F. Vermoortele, I. Stassen, A. Lieb, K.-P. Lillerud and D. De Vos, Green synthesis of zirconium-MOFs. *CrystEngComm.*, **2015**, *17*, 4070–4074.

[52] V. Guillerm, F. Ragon, M. Dan-Hardi, T. Devic, M. Vishnuvarthan, B. Campo, A. Vimont, G. Clet, Q. Yang, G. Maurin, G. Férey, A. Vittadini, S. Gross, C. Serre, A series of isoreticular, highly stable, porous zirconium oxide based metal-organic frameworks. *Angew. Chem. Int. Ed.*, **2012**, *51*, 9267–9271.

[53] M. J. Cliffe, E. Castillo-Martínez, Y. Wu, J. Lee, A. C. Forse, F. C. N. Firth, P. Z. Moghadam, D. Fairen-Jimenez, M. W. Gaultois, J. A. Hill, O. V. Magdysyuk, B. Slater, A. L. Goodwin, C. P. Grey, Metal–organic nanosheets formed via defect-mediated transformation of a hafnium metal–organic framework. *J. Am. Chem. Soc.*, **2017**, *139*, 5397–5404.

[54] C. Chizallet, S. Lazare, D. Bazer-Bachi, F. Bonnier, V. Lecocq, E. Soyer, A. Quoineaud, N. Bats, Catalysis of Transesterification by a Nonfunctionalized Metal−Organic Framework: Acido-basicity at the external surface of ZIF-8 probed by FTIR and ab Initio calculations. *J. Am. Chem. Soc.* **2010**, *132*, 12365–12377.

[55] F. X. Llabrés I Xamena, F. G. Cirujano, A. Corma, An unexpected bifunctional acid base catalysis in IRMOF-3 for Knoevenagel condensation reactions. *Microporous Mesoporous Mater.* **2012**, *157*, 112–117.

[56] S. Yuan, W. Lu, Y.-P. Chen, Q. Zhang, T.-F. Liu, D. Feng, X. Wang, J. Qin, H.-C. Zhou, Sequential linker installation: Precise placement of functional groups in multivariate metal–organic frameworks. *J. Am. Chem. Soc.*, **2015**, *137*, 3177–3180.

[57] V. Bon, I. Senkovska, I. A. Baburin, S. Kaskel, Zr- and Hf-based metal–organic frameworks: Tracking down the polymorphism. *Cryst. Growth Des.*, **2013**, *13*, 1231–1237.

[58] D. Feng, Z.-Y. Gu, J.-R. Li, H.-L. Jiang, Z. Wie, H.-C. Zhou, Zirconium-metalloporphyrin PCN-222: Mesoporous metal–organic frameworks with ultrahigh stability as biomimetic catalysts. *Angew. Chem. Int. Ed.*, **2012**, *51*, 10307–1031.

[59] V. Bon, I. Senkovska, M. S. Weiss, S. Kaskel, Tailoring of network dimensionality and porosity adjustment in Zr- and Hf-based MOFs. *CrystEngComm*., **2013**, *15*, 9572–9577.

[60] G. C. Shearer, S. Chavan, S. Bordiga, S. Svelle, U. Olsbye, K. P. Lillerud, Defect engineering: Tuning the porosity and composition of the metal-organic framework UiO-66 via modulated synthesis. *Chem. Mater.*, **2016**, *28*, 3749−3761.

[61] M. J. Katz, Z. J. Brown, Y. J. Colon, P. W. Siu, K. A. Scheidt, R. Q. Snurr, J. T. Hupp, O. K. Farha, A facile synthesis of UiO-66, UiO-67 and their derivatives. *Chem. Commun.* (Cambridge, U. K.), **2013**, *49*, 9449−9451.

[62] A. B. Cairns, A. L. Goodwin, Structural disorder in molecular framework materials. *Chem. Soc. Rev.*, **2013**, *42*, 4881–4893.

[63] Z. Fang, B. Bueken, D. E. De Vos, R. A. Fischer, Defect-engineered metal–organic frameworks. *Angew. Chem. Int. Ed.*, **2015**, *54*, 7234–7254.

[64] H. –H. Mautschke, F. Drache, I. Senkovska, S. Kaskel, F. X. Llabres i Xamena, Catalytic properties of pristine and defectengineered Zr-MOF-808 metal organic frameworks. *Catal. Sci. Technol.*, **2018**, *8*, 3610–3616.

[65] H. G. T. Nguyen, N. M. Schweitzer, C.-Y. Chang, T. L. Drake, M. C. So, P. C. Stair, O. K. Farha, J. T. Hupp, S. T. Nguyen, Vanadium-node-functionalized UiO-66: A thermally stable MOF supported gatalyst for the gas-phase oxidative dehydrogenation of cyclohexene. *ACS Catal.*, **2014**, *4*, 2496−2500.

[66] J. Jiang, F. Gandara, Y.-B. Zhang, K. Na, O. M. Yaghi, W. G. Klemperer, Superacidity in sulfated metal-organic framework-808. *J. Am. Chem. Soc.*, **2014**, *136*, 12844−12847.

[67] Z. Wang, S. M. Cohen, Postsynthetic modification of metal–organic frameworks. *Chem. Soc. Rev.*, **2009**, *38*, 1315–1329.

[68] Y. K. Hwang, D. Hong, J. Chang, S. H. Jhung, Y. Seo, J. Kim, A. Vimont, M. Daturi, C. Serre, G. Ferey, Amine grafting on coordinatively unsaturated metal centers of MOFs: Consequences for catalysis and metal encapsulation. *Angew. Chem. Int. Ed.*, **2008**, *47*, 4144–4148.

[69] F. Jeremias, A. Khutia, S. K. Henninger, C. Janiak, MIL-100(Al, Fe) as water adsorbents for heat transformation purposes—a promising application. *J. Mater. Chem.*, **2012**, *22*, 10148–10151.

[70] M. Kim, S. M. Cohen, Discovery, development, and functionalization of Zr(IV)-based metal-organic frameworks. *CrystEngComm*., **2012**, *14*, 4096–4104.

[71] Z. Fang, J. P Dürholt, M. Kauer, W. Zhang, C. Lochenie, B. Jee, B. Albada, N. Metzler-Notle, A. Pöppl, B. Weber, M. Muhler, Y. Wang, R. Schmid, R. A. Fischer, Structural complexity in metal–organic frameworks: Simultaneous modification of open metal sites and hierarchical porosity by systematic doping with defective linkers. *J. Am Chem. Soc.*, **2014**, *136*, 9627–9636.

[72] F. Vermoortele, B. Bueken, G. Le Bars, B. V. de Voorde, M. Vandichel, K. Houthoofd, A. Vimont, M. Daturi, M. Waroquier, V. Van Speybroeck, C. Kirschhock, D. E. De Vos, Synthesis modulation as a tool to increase the catalytic activity of metal–organic frameworks: The unique case of UiO-66(Zr). *J. Am. Chem. Soc.*, **2013**, *135*, 11465–11468.

[73] H. Wu, Y. S. Chua, V. Krungleviciute, M. Tyagi, P. Chen, T. Yildirim, W. Zhou, Unusual and highly tunable missing-linker defects in zirconium metal–organic framework UiO-66 and their important effects on gas adsorption. *J. Am. Chem. Soc.*, **2013**, *135*, 10525–10532.

[74] F. Vermoortele, M. Vandichel, B. Van de Voorde, R. Ameloot, M. Waroquier, V. Van Speybroeck, D. E. De Vos, Electronic effects of linker dubstitution on Lewis acid catalysis with metal–organic frameworks. *Angew. Chem. Int. Ed.*, **2012**, *51* ,4887–4890.

[75] T. Xu, X. Hou, Y. Wang, J. Zhang, J. Zhang and B. Liu, A gigantic polyoxozirconate with visible photoactivity. *Dalton Trans.*, **2017**, *46*, 10185–10188.

[76] M. T. Pope, *Encyclopedia of Inorganic and Bioinorganic Chemistry*, John Wiley & Sons, Chichester, UK, **2011**, pp. 1–11.

[77] W.-H. Fang, L. Zhang, J. Zhang, Synthetic investigation, structural analysis and photocatalytic study of a carboxylate–phosphonate bridged Ti_{18}-oxo cluster. *J. Am. Chem. Soc.*, **2016**, *138*, 7480–7483.

[78] U. Thewalt, K. Döppert, W. Lasser, Darstellung und Struktur des dreikernigen, Sauerstoff-zentrierten, ionischen Cyclopentadienylzirkonium-Carboxylatokomplexes $[Zr_3(\mu_3\text{-}O)(\mu_2\text{-}OH)_3(\mu_2\text{-}C_6H_5COO)_3(\eta^5\text{-}C_5H_5)_3]^+]$ $C_6H_5COO^-\cdot O(C_2H_5)_2$. *J. Organomet. Chem.*, **1986**, *308*, 303-309.

[79] G. Kickelbick, U. Schubert, Oxozirconium methacrylate clusters: $Zr_6(OH)_4O_4(OMc)_{12}$ and $Zr_4O_2(OMc)_{12}$ (OMc = Methacrylate). *Chem. Ber.*, **1997**, *130*, 473–478.

[80] G. Kickelbick, D. Holzinger, C. Brick, G. Trimmel, E. Moons, Hybrid inorganic-organic core-shell nanoparicles from surface-functionalized titanium, zirconium, and vanadium oxo clusters. *Chem. Mater.*, **2002**, *14*, 4382–4389.

[81] G. Kickelbick, U. Schubert, Hydroxy carboxylate substituted oxozirconium clusters. *J. Chem. Soc., Dalton Trans.*, **1999**, 1301–1306.

[82] D. Feng, H.-L. Jiang, Y.-P. Chen, Z.-Y. Gu, Z. Wie, H.-C. Zhou, Metal-organic frameworks based on previously unknown Zr_8/Hf_8 cubic clusters. *Inorg. Chem.*, **2013**, *52*, 12661–12667.

[83] C. Artner, M. Czakler, U. Schubert, New zirconium and zirconium–titanium oxocluster types by expansion or metal substitution of the octahedral Zr_6O_8 structural motif. *Inorg. Chim. Acta.*, **2015**, *432*, 208–212.

[84] B. Morosin, Molecular configuration of a tridecazirconium oxide-methoxide complex. *Acta Crystallogr., Sect. B: Struct. Crystallogr. Cryst. Chem.*, **1977**, *33*, 303–305.

[85] A. Müller, F. Peters, M. T. Pope, D. Gatteschi, Polyoxometalates: Very Large Clusters-Nanoscale Magnets. *Chem. Rev.*, **1998**, *98*, 239–272.

[86] B. Nateghi, I. Boldog, K. V. Domasevitch, C. Janaik, More versatility than thought: large {Zr_{26}} oxocarboxylate cluster by corner-sharing of standard octahedral subunits. *CrystengComm.*, **2018**, *20*, 5132–5136.

[87] C. N. R. Rao, S. Natarajan, R. Vaidhyanathan, Metal carboxylates with open architectures. *Angew. Chem. Int. Ed.*, **2004**, *43*, 1466−1496.

[88] M. Eddaoudi, D. B. Moler, H. Li, B. Chen, T. M. Reineke, M. O'Keeffe, O. M. Yaghi, Modular chemistry: Secondary building units as a basis for the design of highly porous and robust metal-organic carboxylate frameworks. *Acc. Chem. Res.*, **2001**, *34*, 319−330.

[89] G. Ferey, C. Mellot-Draznieks, C. Serre, F. Millange, J. dutour, S. Surble, I. Margiolaki, A Chromium Terephthalate-Based Solid with Unusually Large Pore Volumes and Surface Area. *Science*, **2005**, *309*, 2040−2042.

[90] W. Lu, D. Yuan, T. A. Makal, Z. Wei, J.-R. Li, H.-C. Zhou, Highly porous metal-organic framework sustained with 12-connected nanoscopic octahedra. *Dalton Trans.*, **2013**, *42*, 1708−1714.

[91] Y. Wang, D. Zhao, Beyond equilibrium: Metal-organic frameworks for molecular sieving and kinetic gas separation. *Cryst. Growth Des.*, **2017**, *17*, 2291−2308.

[92] M.-X. Wu, Y.-W. Yang, Metal-organic framework (MOF)-based drug/cargo delivery and cancer therapy. *Adv. Mater.*, **2017**, *29*, 1606134.

[93] Y.-B. Huang, J. Liang, X.-S. Wang, R. Cao, Multifunctional metal-organic framework catalysts: Synergistic catalysis and tandem reactions. *Chem. Soc. Rev.*, **2017**, *46*, 126−157.

[94] W. P. Lustig, S. Mukherjee, N. D. Rudd, A. V. Desai, J. Li, S. K. Ghosh, Metal-organic frameworks: Functional luminescent and photonic materials for sensing applications. *Chem. Soc. Rev.*, **2017**, *46*, 3242−3285.

[95] S. J. Garibay, S. M. Cohen, Isoreticular synthesis and modification of frameworks with the UiO-66 topology. *Chem. Commun.*, **2010**, *46*, 7700−7702.

[96] T.-F. Liu, D. Feng, Y.-P. Chen, L. Zou, M. Bosch, S. Yuan, Z. Wei, S. Fordham, K. Wang, H.-C. Zhou, Topology-guided design and syntheses of highly stable mesoporous porphyrinic zirconium metal-organic frameworks with high surface area. *J. Am. Chem. Soc.*, **2015**, *137*, 413−419.

[97] M. Zhang, Y.-P. Chen, M. Bosch, T. Gentle, K. Wang, D. Feng, Z. U. Wang, H.-C. Zhou, Symmetry-guided synthesis of highly porous metal-organic frameworks with fluorite topology. *Angew. Chem. Int. Ed.*, **2014**, *53*, 815−818.

[98] D. Feng, W.-C. Chung, Z. Wei, Z.-Y. Gu, H.-L. Jiang, Y.-P. Chen, D. J. Darensbourg, H.-C. Zhou, Construction of ultrastable porphyrin Zr metal-organic frameworks through linker elimination. *J. Am. Chem. Soc.*, **2013**, *135*, 17105−17110.

[99] H.-L. Jiang, D. Feng, K. Wang, Z.-Y. Gu, Z. Wei, Y.P. Chen, H.-C. Zhou, An exceptionally stable, porphyrinic Zr metal-organic framework exhibiting PH-dependent fluorescence. *J. Am. Chem. Soc.*, **2013**, *135*, 13934−13938.

[100] Y. Bai, Y. Dou, L.-H, Xie, W. Rutledge, J.-R. Li, H.-C. Zhou, Zr-based metal–organic frameworks: design, synthesis, structure, and applications. *Chem. Soc. Rev.*, **2016**, *45*, 2327−2367.

[101] M. Zhang, Y.-P. Chen, M. Bosch, T. Gentle III, K. Wang, D. Feng, Z. U. Wang, H.-C. Zhou. Symmetry-guided synthesis of highly porous metal–organic frameworks with fluorite topology. *Angew. Chem. Int. Ed.*, **2014**, *53*, 815−818.

[102] T. Zhao, C. Heering, I. Boldog, K. V. Domasevitch, C. Janiak, A view on systematic truncation of tetrahedral ligands for coordination polymers. *CrystEngComm.*, **2017**, *19*, 776−780.

[103] A. Clearfield, K. Demadis, T. Albrecht-Schmitt, B. Bujoli, C. Cahill, R. Murugavel, J. Rocha, G. Hix, G. Shimizu, J. Zubieta, J. Zon, E. Brunet, R. Vivani, M. A. G. Aranda, J. G. Mao, N. Stock, R. Winpenny, P. A. Wright, L. –M. Zheng, Metal Phosphonate Chemistry. Royal Society of Chemistry, **2012**.

[104] G. Alberti, U. Costantino, S. Allulli, N. Tomassini, Crystalline $Zr(R\text{-}PO_3)_2$ and $Zr(R\text{-}OPO_3)_2$ compounds (R = organic radical): A new class of materials having layered structure of the zirconium phosphate type. *J. Inorg. Nucl. Chem.*, **1978**, *40*, 1113−1117.

[105] M. B. Dines, R. E. Cooksey, P. C. Griffith, R. H. Lane, Mixed-component layered tetravalent metal phosphonates/phosphates as precursors for microporous materials. *Inorg. Chem.*, **1983**, *22*, 6**,** 1003−1004.

[106] A. Clearfield, Unconventional metal organic frameworks: Porous cross-linked phosphonates. *Dalton Trans.*, **2008**, *44*, 6089–6102.

[107] P. Deria, D. A. Gomez-Gualdron, W. Bury, H. T. Schaef, T. C. Wang, P. K. Thallapally, A. A. Sarjeant, R. Q. Snurr, J. T. Hupp, O. K. Farha, Ultraporous, Water stable, and breathing

zirconium-based metal–organic frameworks with ftw topology. *J. Am. Chem. Soc.*, **2015**, *137*, 40, 13183–13190.

[108] I. O. Benitez, B. Bujoli, L. J. Camus, C. M. Lee, F. Odobel, D. R. Talham, Monolayers as models for supported catalysts: Zirconium phosphonate films containing manganese(III) porphyrins. *J. Am. Chem. Soc.*, **2002**, *124*, 16, 4363–4370.

[109] M. Taddei, A. Donnadio, F. Costantino, R. Vivani, M. Casciola, Synthesis, srystal structure, and proton conductivity of one-dimensional, two-dimensional, and three-dimensional zirconium phosphonates based on glyphosate and glyphosine. *Inorg. Chem.*, **2013**, *52*, 20, 12131–12139.

[110] K. J. Gagnon, H. P. Perry, A. Clearfield, Conventional and unconventional metal–organic frameworks based on phosphonate ligands: MOFs and UMOFs. *Chem. Rev.*, **2012**, *112*, 2, 1034–1054.

[111] C.-Y. Gao, J. Ai, H.-R. Tian, D. Wu, Z.-M. Sun, An ultrastable zirconium-phosphonate framework as bifunctional catalyst for highly active CO_2 chemical transformation. *Chem. Commun.*, **2017**, *53*, 1293–1296.

[112] J. E. Mondloch, W. Bury, D. Fairen-Jimenez, S. Kwon, E. J. DeMarco, M. H. Weston, A. A. Sarjeant, S. T. Nguyen, P. C. Stair, R. Q. Snurr, O. K. Farha, J. T. Hupp, Vapor-phase metalation by atomic layer deposition in a metal–organic framework. *J. Am. Chem. Soc.*, **2013**, *135*, 28, 10294–10297.

[113] M. Taddei, F. Costantiono, F. Marmottini, A. Comotti, P. Sozzani, R. Vivani, The first route to highly stable crystalline microporous zirconium phosphonate metal–organic frameworks. *Chem. Commun.*, **2014**, *50*, 14831–14834.

[114] T. Zheng, Z. Yang, D. Gui, Z. Liu, X. Wang, X. Dai, S. Liu, L. Zhang, Y. Gao, L. Chen, D. Sheng, Y. Wang, J. Diwu, J. Wang, R. Zhou, Z. Chai, T. E. Albrecht-Schmitt, S. Wang, Overcoming the crystallization and designability issues in the ultrastable zirconium phosphonate framework system. *Nature Commun.*, **2017**, *8*, 15369.

[115] M. Taddei, F. Costantino, R. Vivani, S. Sabatini, S.-H. Lim, S. M. Cohen, The use of a rigid tritopic phosphonic ligand for the synthesis of a robust honeycomb-like layered zirconium phosphonate framework. *Chem. Commun.*, **2014**, *50*, 5737–5740.

[116] J.-P., Zhang, Y.-B. Zhang, J.-B. Lin, X.-M. Chen, Metal Azolate Frameworks: From Crystal Engineering to Functional Materials. *Chem. Rev.*, **2012**, *112*, 2, 1001–1033.

[117] S. Trofimenko, Boron-pyrazole chemistry. II. Poly(1-pyrazolyl)-borates. *J. Am. Chem. Soc.*, **1967**, *89*, 3170–3177.

[118] S. Trofimenko, Coordination chemistry of pyrazole-derived ligands. *Chem. Rev.*, **1972**, *72*, 497–509.

[119] G. Noe I, J.C. Roder, S. Dechert, H. Pritzkow, L. Bolk, S. Mecking, F. Meyer, Nickel(II) complexes– a bimetallic approach in olefin polymerisation. *Adv. Synth. Catal.*, **2006**, *348*, 887–897.

[120] F. M. Woodward, P. J. Gibson, G. B. Jameson, C. P. Landee, M. M. Turnbull, R. D. Willett, Two-dimensional heisenberg antiferromagnets: Syntheses, X-ray structures, and magnetic behavior of $[Cu(pz)_2](ClO_4)_2$, $[Cu(pz)_2](BF_4)_2$, and $[Cu(pz)_2(NO_3)](PF_6)$. *Inorg. Chem.*, **2007**, *46*, p. 4256–4266.

[121] F. K. Keter, J. Darkwa, Perspective: the potential of pyrazole-based compounds in medicine. *Biometals*, **2012**, *25*, 9–21.

[122] S. Fustero, M. Sánchez-Roselló, P. Barrio, A. Simón-Fuentes, From 2000 to mid-2010: A fruitful decade for the synthesis of pyrazoles. *Chem. Rev.*, **2011**, *111*, 6984–7034.

[123] G. Aromí, L. A. Barrios, O. Roubeau, P. Gamez, Triazoles and tetrazoles: Prime ligands to generate remarkable coordination materials. *Coord. Chem. Rev.*, **2011**, *55*, 485–546.

[124] F. G. Bordwell, Equilibrium acidities in dimethyl sulfoxide solution. *Acc. Chem. Res.*, **1988**, *21*, 456–463.

[125] J. J. Low, A. I. Benin, P. Jakubczak, J. F. Abrahamian, S. A. Faheem, R. R. Willis, Virtual high throughput screening confirmed experimentally: Porous coordination polymer hydration. *J. Am. Chem. Soc.*, **2009**, *131*, 15834–15842.

[126] D. J. Tranchemontagne, K. S. Park, H. Furukawa, J. Eckert, C. B. Knobler, O. M. Yaghi, Hydrogen storage in new metal–organic frameworks. *J. Phys. Chem. C*, **2012**, *116*, 13143-13151.

[127] C. Heering, I. Boldog, V. Vasylyeva, J. Sanchiz, C. Janiak, Bifunctional pyrazolate-carboxylate ligands for isoreticular cobalt and zinc MOF-5 analogs with magnetic analysis of the $\{Co_4(\mu_4\text{-}O)\}$ node. *CrystEngComm.*, **2013**, *15*, 9757–9768.

[128] P. O. Adelani, L. J. Jouffret, J. E. S. Szymanowski, P. C. Burns, Correlations and differences between uranium(VI) arsonates and phosphonates. *Inorg. Chem.*, **2012**, *51*, 12032–12040.

[129] P. O. Adelani, G. E. Sigmon, P. C. Burns, Hybrid Uranyl Arsonate Coordination Nanocages. *Inorg. Chem.*, **2013**, *52*, 6245–6247.

[130] M. O'Keeffe, Design of MOFs and intellectual content in reticular chemistry: a personal view. *Chem. Soc. Rev.*, **2009**, *38*, 1215–1217.

[131] M. O'Keeffe, O. M. Yaghi, Deconstructing the Crystal Structures of Metal–Organic Frameworks and Related Materials into Their Underlying Nets. *Chem. Rev.*, **2012**, *112*, 675-702.

[132] J. Dechnik, A. Nuhnen, C. Janiak, Mixed-Matrix Membranes of the Air-Stable MOF-5 Analogue $[Co_4(\mu_4\text{-}O)(Me_2pzba)_3]$ with a Mixed-Functional Pyrazolate-Carboxylate Linker for CO_2/CH_4 Separation. *Cryst. Growth Des.*, **2017**, *17*, 4090–4099.

[133] C. Heering, B. Francis, B. Nateghi, G. Makhloufi, S. Luedeke, C. Janiak, Syntheses, structures and properties of group 12 element (Zn, Cd, Hg) coordination polymers with a mixed-functional phosphonate-biphenyl-carboxylate linker. *CrystEngComm*, **2016**, *18*, 5209-5223.